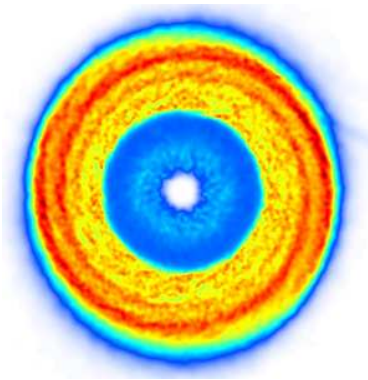


# **Accretion onto stellar mass black holes**

A thesis submitted for the degree of  
Doctor of Philosophy  
at the University of Leicester.

by

**Patrick Deegan**



Theoretical Astrophysics Group  
Department of Physics and Astronomy  
University of Leicester  
UK

March 2009

© Patrick Deegan 2009.

This thesis is copyright material and no quotation from it may be published without proper acknowledgement.

# Accretion onto stellar mass black holes

by

**Patrick Deegan**

## *Abstract*

I present work on the accretion onto stellar mass black holes in several scenarios.

Due to dynamical friction stellar mass black holes are expected to form high density cusps in the inner parsec of our Galaxy. These compact remnants may be accreting cold dense gas present there, and give rise to potentially observable X-ray emission. I build a simple but detailed time-dependent model of such emission. Future observations of the distribution and orbits of the gas in the inner parsec of Sgr A\* will put tighter constraints on the cusp of compact remnants.

GRS 1915+105 is an LMXB, whose large orbital period implies a very large accretion disc and explains the extraordinary duration of its current outburst. I present smoothed particle hydrodynamic simulations of the accretion disc. The models includes the thermo-viscous instability, irradiation from the central object and wind loss. I find that the outburst of GRS 1915+105 should last a minimum of 20 years and up to  $\sim 100$  years if the irradiation is playing a significant role in this system. The predicted recurrence times are of the order of  $10^4$  years, making the duty cycle of GRS 1915+105 to be a few 0.1%.

I present a simple analytical method to describe the observable behaviour of long period black hole LMXBs, similar to GRS 1915+105. Constructing two simple models for the surface density in the disc, outburst and quiescence times are calculated as a function of orbital period. LMXBs are an important constituent of the X-ray light function (XLF) of giant elliptical galaxies. I find that the duty cycle can vary considerably with orbital period, with implications for modelling the XLF.

*To all those people who helped me..... you know who you are!*

## *Acknowledgements*

OK, first off I would like to thank all of the fellow postgrads who lived down in the cave during my time in Leicester. First off Paul, who kindly shared with me the templates and style files used in this thesis. Yohann, Matthew, Jal, Alex, Lee, Uğur, Pete, Fergus, Dave and Fabrizio were the best office mates a guy could ask for and made the three (and a bit) years of of my PhD a lot of fun.

Now the postdocs: Jim, Emma, Lynette, Dean, James, Chris, Seung-Hoon and Andreas, all at one point or another helped me out, thanks guys. Special mention goes to Martin who helped me so much in the early days when I was finding my feet. Another special mention goes to Céline who kindly provided me with (lots of) feedback, this thesis is is much improved because of her.

Moving on to the permanent staff Andrew, Walter, Mark and Giuseppe who I learnt so much from. I would like to thank Lisa for generally organising my life; Sergei for giving me an excellent introduction to my PhD life; and Graham for always giving me help and guidance when I most needed it.

Finally I'd like to thank all the friends and family that got me up to this point in my life.

# Contents

<b>1</b>	<b>Introduction</b>	<b>1</b>
1.1	Black holes . . . . .	2
1.1.1	Theoretical argument . . . . .	2
1.1.2	Observational evidence for black holes . . . . .	3
1.2	Accretion . . . . .	4
1.2.1	Accretion as an energy source . . . . .	4
1.2.2	Eddington limit . . . . .	6
1.2.3	Viscosity . . . . .	7
1.2.4	Viscous spreading in an accretion disc . . . . .	9
1.3	Low mass X-ray binaries . . . . .	14
1.3.1	Binary systems . . . . .	14
1.3.2	X-ray binaries . . . . .	19
1.3.3	The disc instability model . . . . .	22
1.4	The Galactic centre . . . . .	26
<b>2</b>	<b>Numerical methods</b>	<b>29</b>
2.1	Smoothed Particle Hydrodynamics . . . . .	30
2.2	SPH Derivation . . . . .	31
2.2.1	Interpolant . . . . .	31
2.2.2	Derivative . . . . .	32

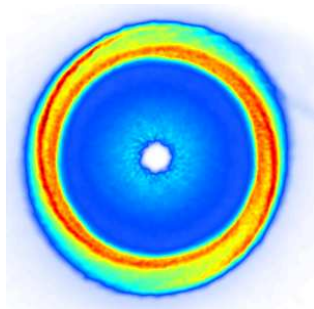
2.2.3	The kernel . . . . .	32
2.2.4	Smoothing length . . . . .	33
2.3	Fluid Equations . . . . .	34
2.3.1	Equations of fluid dynamics . . . . .	34
2.3.2	SPH equations in an accretion disc . . . . .	35
2.3.3	Artificial Viscosity . . . . .	35
2.4	Nearest Neighbours . . . . .	37
2.4.1	Neighbour table . . . . .	37
2.4.2	Monotonic logical Grid . . . . .	37
2.4.3	Hierarchical Tree . . . . .	37
2.4.4	Link list . . . . .	38
2.4.5	Link list example . . . . .	39
2.5	Time stepping . . . . .	44
2.5.1	Courant-Friedrichs-Lewy condition . . . . .	46
2.6	SPH code overview . . . . .	46
2.7	Viscous Particle ring . . . . .	47
<b>3</b>	<b>Constraining the number of compact remnants near Sgr A*</b>	<b>51</b>
3.1	Introduction . . . . .	52
3.2	Numerical approach . . . . .	53
3.2.1	Time-dependent disc accretion . . . . .	54
3.2.2	Orbital evolution of accretors . . . . .	55
3.2.3	The model for the Minispiral . . . . .	56
3.3	Results . . . . .	57
3.3.1	Emission from individual black holes . . . . .	57
3.3.2	Representative cases . . . . .	60
3.3.3	Search in the $N, \zeta$ parameter space . . . . .	61
3.3.4	Sensitivity of results to the properties of the Minispiral . . . . .	64

3.3.5	Comparison to related previous work and result uncertainties . . .	65
3.3.6	A neutron star cusp . . . . .	66
3.4	Conclusions . . . . .	67
<b>4</b>	<b>GRS 1915+105</b>	<b>72</b>
4.1	Introduction . . . . .	73
4.2	Physical ingredients . . . . .	74
4.2.1	The disc instability model . . . . .	74
4.2.2	Irradiation . . . . .	75
4.2.3	Wind Loss . . . . .	76
4.3	Numerical Method . . . . .	77
4.3.1	Particle injection and rejection . . . . .	77
4.3.2	Triggering the disc instability . . . . .	77
4.3.3	Models using a massive disc . . . . .	79
4.3.4	Models using an under-massive disc . . . . .	80
4.3.5	Under-massive disc with scaled $R_{\text{irr}}$ . . . . .	81
4.3.6	Scaling outburst and recurrence timescales . . . . .	82
4.4	Results . . . . .	85
4.4.1	Typical Behaviour . . . . .	85
4.4.2	Changing $\alpha_{\text{hot/cold}}$ . . . . .	91
4.4.3	Changing $K_{\text{max/min}}$ . . . . .	96
4.4.4	Changing $\epsilon$ and $\lambda$ . . . . .	102
4.5	Discussion . . . . .	103
4.5.1	Comparisons to other work . . . . .	103
4.5.2	Central accretion rate and the need for a wind . . . . .	107
4.5.3	Conclusion . . . . .	109

<b>5</b>	<b>Long period LMXBs</b>	<b>110</b>
5.1	Introduction . . . . .	111
5.2	The outburst . . . . .	112
5.2.1	Determination of the disc radius, $R_{\text{disc}}$ . . . . .	113
5.2.2	Outburst duration . . . . .	114
5.2.3	A Different model for the disc surface density profile . . . . .	117
5.3	The quiescence time . . . . .	119
5.3.1	Mass transfer rate . . . . .	121
5.3.2	Period range . . . . .	123
5.4	Exploring the parameter space . . . . .	124
5.4.1	Model 1 . . . . .	124
5.4.2	Model 2 . . . . .	128
5.5	Comparisons with observations . . . . .	133
5.6	GRS 1915+105 . . . . .	138
5.7	Discussion . . . . .	139
<b>6</b>	<b>Conclusions</b>	<b>145</b>
<b>A</b>	<b>Results</b>	<b>149</b>

# Chapter 1

## *Introduction*



“They can chew you up, but they gotta spit  
you out.”  
- McNulty

*The Wire: Collateral Damage [2.02]*

The work in this thesis deals with accretion onto black holes. In this section I will begin by introducing the concept of black holes and discuss the evidence for their existence. I will then spend some time going over the mechanism of the accretion process in detail: the concepts discussed here will be used throughout this volume. Finally I will cover two situations in which accretion onto black holes can take place: low mass X-ray binaries and in the Galactic Centre.

## 1.1 Black holes

### 1.1.1 Theoretical argument

Of the four forces in nature (the strong force, weak force, the electromagnetic force and gravity) gravity is the weakest. However, it is the dominant force in the Universe on large scales. The effects of gravity are most prominent around the objects known as black holes. In 1705, Isaac Newton's *Opticks* was published: it stated that light was of a particle nature. If this was the case, light should be influenced by gravity. This thought occurred to the amateur astronomer John Michell (Michell 1784). He calculated that if a star existed with a radius 500 times that of the Sun and the same average density, then its escape velocity would be equal to the speed of light. Simply equating the escape velocity of a star to the speed of light results in an expression for the radius of a star.

$$v_{\text{esc}} = \sqrt{\frac{2GM}{R_{\star}}} \Rightarrow R_{\star} = \frac{2GM}{c^2}, \quad (1.1)$$

where  $c$ ,  $v_{\text{esc}}$ ,  $M$  and  $R_{\star}$  are the speed of light, escape velocity, mass and radius of the star respectively. Equation (1.1) produces answers that, at the time, seemed absurdly small and this generated little interest among the scientific community. For example, the Sun's mass ( $M_{\odot} \sim 2 \times 10^{33}\text{g}$ ) results in  $R_{\star} \sim 29\text{ km}$ .

The idea of what were to become known as black holes was not revisited until the 20<sup>th</sup> century. By 1915 Albert Einstein had developed his theory of general relativity (Einstein 1915) and had argued that gravity does influence light, due to the curvature of spacetime<sup>1</sup>. Karl Schwarzschild solved Einstein's field equations to describe the gravitational field outside a spherical, non-rotating mass and showed that a black hole was theoretically possible. However, the process leading up to their formation was still a mystery.

<sup>1</sup>N.B. Einstein used entirely different arguments to the ones used by Michell (1784)

In the 1930s several physicists, such as Chandrasekhar and Oppenheimer, were working on the ultimate fate of stars. Oppenheimer and Snyder described the gravitational collapse of a star that had exhausted all of its nuclear fuel (Oppenheimer & Snyder 1939). Subsequently Oppenheimer & Volkoff (1939) theorised that there may be a limit on the mass of a neutron star (the most dense object known at the time) and a star exceeding this limit may have a final collapse. As a consequence, black holes are thought to be the ultimate stage of development in the evolution of massive stars.

A thorough examination of black holes is beyond the scope of this work, however some general facts will be useful. The radius described in eq. (1.1) is known as the Schwarzschild radius,  $R_{\text{Schw}}$ . This can be thought of as the surface of a black hole, called the event horizon. Within the event horizon all of the mass is located at a single point: the singularity. This is a point of infinite density where spacetime is infinitely curved, which nothing (including light) can escape from.

### 1.1.2 Observational evidence for black holes

By the 1940s the theory behind black holes was, for the most part, understood. There was one problem however: there was no evidence for them. This is unsurprising since by their very nature black holes are impossible to observe directly. It was not until the 1970's that indirect observational evidence began to emerge<sup>2</sup>. The first black hole candidate was in the system Cygnus X-1 (Cyg X-1). Discovered in X-rays in 1964, Cyg X-1 is one of the brightest X-ray sources that can be seen from Earth with X-ray luminosities of  $4.6 \times 10^{37} \text{ erg s}^{-1}$  in the 0.7-300 keV band (Makishima et al. 2008).

The optical counterpart was subsequently discovered to be a blue supergiant variable star, incapable of producing a significant X-ray flux. If the blue supergiant could not produce the observed X-rays something else must. The first clues that Cyg X-1 contained some sort of compact object was from the satellite Uhuru (Oda et al. 1971). Extended observations showed that the source of the X-rays was rapidly varying. This suggested that the source must be small due to the speed of light restricting “communication” between differing regions. This led to speculation that Cyg X-1 was a binary system consisting of a giant star and a compact object of some description. Webster & Murdin (1972) and Bolton (1972) discovered a 5.6 day orbital period of the supergiant; based on the period, the mass function and the mass of the supergiant (obtained from its spectral identifica-

---

<sup>2</sup>This observational evidence was the result of matter accreting onto black holes, see §1.2

tion<sup>3</sup>) the mass of the compact object was found to be too large for a neutron star<sup>4</sup>. The most recent mass estimate of the compact object is  $8.7 M_{\odot}$  (Iorio 2008). The only way the X-rays could be produced is for some material to fall onto what is now widely regarded as a black hole. This process is known as accretion and is discussed in §1.2.1. It appears that Cyg X-1 consists of a black hole accreting from a supergiant star. A second candidate, LMC X-3, for a black hole was identified by Cowley et al. (1983). Cyg X-1 and LMC X-3 are just two examples of a class of objects called X-ray binaries, which all consist of a compact object (a neutron star or black hole) accreting in some manner from a secondary star. The subclasses of X-ray binaries will be discussed in §1.3.

## 1.2 Accretion

### 1.2.1 Accretion as an energy source

In §1.1.2 it was alluded to that accretion was the source of the high energy X-rays emanating from the source Cyg X-1. Accretion is an efficient source of energy and powers many of the highest energy sources in the Universe. Consider a body of mass  $M$  and radius  $R_{\star}$ , the gravitational potential energy extracted by a mass  $m$  falling onto its surface is,

$$\Delta E_{\text{acc}} = \frac{GMm}{R_{\star}}. \quad (1.2)$$

It is clear from eq. (1.2) that the efficiency of the accretion process is dependent on the ratio of  $M/R_{\star}$ . This ratio is greatest when dealing with compact objects such as neutron stars and black holes. Assuming all of the energy released by infalling matter is converted into radiation at the stellar surface and matter accretes at a rate  $\dot{M}$ , the accretion luminosity produced is

$$L_{\text{acc}} = \frac{GM\dot{M}}{R_{\star}} \quad (1.3)$$

Equation (1.3) is only valid when the accretor has a solid surface, such as a white dwarf or neutron star. When the accretor is a black hole, eq. (1.3) is not strictly valid, some

---

<sup>3</sup>A star's mass can be estimated by looking at its spectra. The temperature of the star's atmosphere is related to the mass of the star. The temperature also affects the ionisation states of atoms in its atmosphere resulting in differing stellar spectra.

<sup>4</sup>In a neutron star the weight of the star is supported by short-range repulsive interactions between neutrons governed by the strong force and quantum degeneracy pressure of the neutrons. If a compact object has a mass greater than  $\sim 1.5 - 3.0 M_{\odot}$  these forces will be unable to prevent the object collapsing to some denser form.

of the material can simply fall in past the event horizon and add to the black hole mass rather than producing observable radiation. This uncertainty can be parameterised by the inclusion of a dimensionless quantity  $\eta$  (the accretion efficiency)

$$\begin{aligned} L_{\text{acc}} &= \frac{2\eta GM\dot{M}}{R_{\star}} \\ &= \eta\dot{M}c^2, \end{aligned} \quad (1.4)$$

where  $R_{\star}$  was replaced with the Schwarzschild radius from eq. (1.1) and  $\eta$  has a typical value  $\sim 0.1$  (see §7.8 in Frank, King & Raine (2002)).

The simplest astrophysical accretion problem is steady, spherically symmetric accretion onto a star of mass  $M$ . This situation was considered by Hoyle & Lyttleton (1939), Bondi & Hoyle (1944) and Bondi (1952); it is a reasonable approximation to a star accreting from a gas cloud or the interstellar medium and it provides a useful upper estimate of the accretion rate on a star. The derivation begins with the equations of gas dynamics, specifically the continuity equation for a steady flow

$$\frac{1}{r^2} \frac{d}{dr}(r^2 \rho v) = 0, \quad (1.5)$$

where  $r$ ,  $v$  and  $\rho$  are position, velocity and density of the gas. This integrates to,

$$\begin{aligned} r^2 \rho v &= C \\ 4\pi r^2 \rho(-v) &= \dot{M}. \end{aligned} \quad (1.6)$$

as  $\rho(-v)$  is an inward flux of material the integration constant  $C$  can be related to an accretion rate  $\dot{M}$ . If all gas within a distance of  $r_{\text{acc}}$  is assumed to be captured and accreted by the star then

$$\dot{M} = 4\pi r_{\text{acc}}^2 \rho(-v). \quad (1.7)$$

There are two extreme conditions that can determine the size of  $r_{\text{acc}}$ : when the motion of the star in the gas is supersonic and when the star is at rest with respect to the gas. Hoyle & Lyttleton (1939) studied the first regime and found  $r_{\text{acc}} \sim 2GM/v^2$ , while Bondi (1952) found  $r_{\text{acc}} \sim 2GM/c_s^2$  in the second regime, where  $c_s$  is the sound speed of the

gas. There are now two forms for the mass accretion rate<sup>5</sup>

$$\begin{aligned}\dot{M} &= 4\pi\rho\frac{(GM)^2}{v^3} \\ \dot{M} &= 4\pi\rho\frac{(GM)^2}{c_s^3}.\end{aligned}\tag{1.8}$$

Finally Bondi (1952) proposed an interpolation formula to bridge the gap between the two extremes

$$\dot{M} = 4\pi\rho\frac{(GM)^2}{(\Delta v^2 + c_s^2)^{3/2}},\tag{1.9}$$

where  $\Delta v^2$  is the relative velocity between the star and the gas. Further details of the derivation can be found in the papers cited above or alternatively in Frank et al. (2002).

The above is only valid if the infalling gas has no intrinsic angular momentum. In general this is not the case and the specific angular momentum causes the gas to orbit around the accretor: this will result in an accretion disc. The specific angular momentum of a body in orbit of radius  $R$  about a central body of mass  $M$  is

$$j = (GMR)^{1/2}.\tag{1.10}$$

As a body moves closer to the central mass its angular momentum decreases, conversely if  $R$  increases  $j$  also rises. Since the total angular momentum of the disc has to be conserved, the angular momentum loss of the mass falling onto the accretor has to be accompanied by an angular momentum gain of the mass in the outer disc, i.e, angular momentum needs to be transported outwards for matter to accrete.

Accretion discs occur in a wide variety of phenomena and on varying size scales, from active galactic nuclei (AGN) to gamma ray bursts and binary systems. Accretion discs are also thought to be necessary for star and planet formation. In this thesis I am mainly concerned with discs around stellar mass black holes contained within binary systems. The mechanics of binary systems and accretion discs are discussed in the following sections of this introduction.

## 1.2.2 Eddington limit

The form of eqs. (1.3) and (1.4) suggests that the luminosity of an object will increase indefinitely if  $\dot{M}$  rises. This fails to account for the effect the radiation of the accretor

---

<sup>5</sup>The velocity in eq. (1.7) differs depending on the conditions. In the supersonic case  $v$  is the relative velocity of the gas. When the star is at rest  $v \rightarrow c_s$ .

has on the infalling matter, which imposes a limit on  $\dot{M}$ . Assuming the infalling matter is comprised entirely of ionised hydrogen, the gravitational force on the electron-proton pairs is,

$$F = \frac{GM(m_p + m_e)}{r^2} \sim \frac{GMm_p}{r^2}, \quad (1.11)$$

where  $m_p$  and  $m_e$  are the mass of the proton and the electron respectively ( $m_p \gg m_e$ ). This inward force is opposed by the outward force of radiation pressure on the ions. The radiation pressure mainly affects the electrons through Thomson scattering<sup>6</sup>. The attractive Coulomb force between the ions means that the electrons will drag the protons outward. The force on the electrons is equal to the rate at which they absorb momentum,

$$F = \frac{L\sigma_T}{4\pi cr^2}, \quad (1.12)$$

where  $\sigma_T$  is the Thomson scattering cross-section for electrons and  $L$  is the luminosity. Equating eqs. (1.11) and (1.12),

$$L_{\text{Edd}} = \frac{4\pi GMm_p c}{\sigma_T} \sim 1.3 \times 10^{38} (M/M_\odot) \text{erg s}^{-1}, \quad (1.13)$$

gives the value for the luminosity at which the gravitational force and the radiative force are equal. This is known as the Eddington limit and imposes a maximum limit on the accretion rate onto any object. Note this is only an order of magnitude estimate assuming a steady spherically symmetric accretion flow. The mass accretion rate at the Eddington limit for black holes is given by combining eqs. (1.4) and (1.13),

$$\dot{M}_{\text{Edd}} = \frac{1.3 \times 10^{38}}{\eta c^2} \frac{M}{M_\odot} \text{g s}^{-1}, \quad (1.14)$$

### 1.2.3 Viscosity

When some material is gravitationally captured by a massive body it will not be accreted immediately. This is due to the angular momentum of the material, which will go into orbit about the body forming what is known as an accretion disc. Figure 1.1 depicts the general idea behind the accretion disc. Around the central accretor there is a rotating disc of gas moving with a characteristic angular velocity. In addition to this, viscous forces cause the disc to spread in the radial direction. The mechanism by which gas ends up in an accretion disc is discussed in §1.3.1. In this and following sections I will go into some details about the mechanisms behind accretion discs. For a more in depth discussion the

<sup>6</sup>When charged particles elastically scatter photons

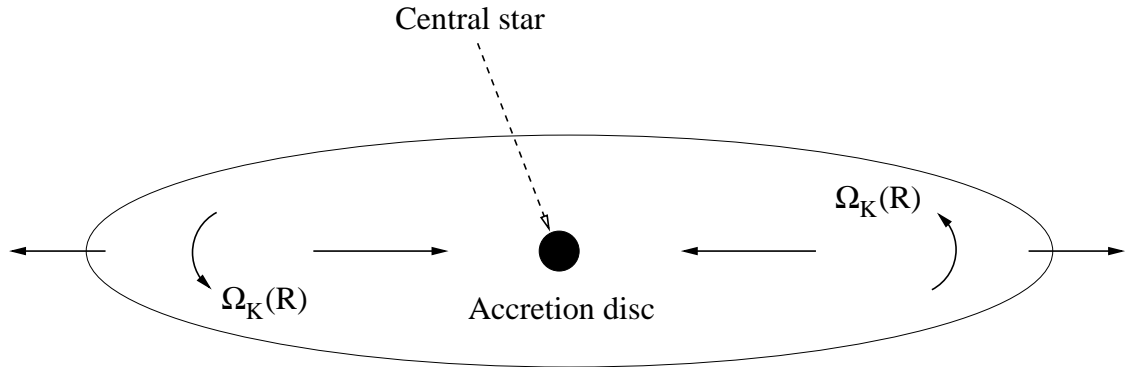


FIGURE 1.1. Standard picture of an accretion disc. Solid arrows depict the direction of motion of the disc.

reader is referred to Frank et al. (2002) or Pringle (1981). The mass of an accretion disc is typically much smaller than that of the accretor. If this is indeed the case, the self gravity of the accretion disc can be ignored and the disc orbits the central body of mass  $M$  with a Keplerian angular velocity,

$$\Omega_K(R) = \left( \frac{GM}{R^3} \right)^{1/2}, \quad (1.15)$$

where  $R$  is the distance from  $M$ . This implies differential rotation in the accretion disc i.e. material closer to  $M$  will have a higher angular velocity than material at a larger radius. When two neighbouring annuli slide past each other, random thermal motions of the gas result in angular momentum transport perpendicular to the circular velocity of the gas. This process is called *shear viscosity*.

Assuming a speed  $\tilde{v}$  for the random motions and a typical length scale between element interaction  $\lambda$ , the kinematic viscosity is,

$$\nu = \lambda \tilde{v}. \quad (1.16)$$

A large shear viscosity is necessary for the angular momentum transport during the lifetime of an accretion disc. However the process behind the viscosity is still open for debate. The *Reynolds number* is a ratio of the inertial and viscous forces in a fluid. If a fluid is dominated by viscous forces the Reynolds number is less than one. For an accretion disc, which relies on molecular collisions, the Reynolds number has been calculated to be as high as  $10^{14}$ . It appears that molecular collisions are insufficient to provide the shear viscosity needed. There is a critical value of the Reynolds number in every system above which turbulent motions begin. The large values calculated for accretion discs suggest that the material in an accretion disc is turbulent, which could provide the nec-

essary shear viscosity. Assuming that turbulence is the cause of the shear viscosity in accretion discs eq. (1.16) can be modified,

$$\nu_{\text{turb}} = \lambda_{\text{turb}} v_{\text{turb}}. \quad (1.17)$$

The values  $\lambda_{\text{turb}}$  and  $v_{\text{turb}}$  represent the size and velocity of the largest turbulent motions respectively. This does not at first appear to be any improvement on eq. (1.16), indeed, a complete description of turbulence is still elusive. Shakura & Sunyaev (1973) parameterised all of the ignorance involving turbulence in their relation,

$$\nu = \alpha c_s H, \quad (1.18)$$

known as the  $\alpha$ -prescription of shear viscosity. Shakura and Sunyaev reasoned that the largest turbulent motions cannot exceed the height of the disc  $H$  and that the motions cannot be supersonic, hence a maximum speed is the sound speed of the gas  $c_s$ . Equation (1.18) is a useful form for the shear viscosity, it has encouraged the comparison between theory and experiment to determine the magnitude of  $\alpha$ . The magnitude of  $\alpha$  while expected to be  $\lesssim 1$  is still the subject of much debate. The physical mechanism behind viscosity also remains uncertain. The magnetorotational instability (Balbus & Hawley 1991, Balbus 2003) (MRI) is the current favoured model to explain the viscosity in accretion discs. Consider a rotating disc in the presence of a vertical magnetic field. Two neighbouring fluid elements can behave as though they are connected by a ‘spring’, due to the magnetic tension. In a Keplerian disc the inner fluid element has a larger velocity than the outer element, causing the “spring” to stretch. The inner fluid element is then forced by the spring to slow down, hence reducing its angular momentum and causing the inner fluid element to move a lower orbit. The outer fluid element is forced by the spring to speed up, increasing its angular momentum and will therefore move to a higher orbit. Theoretically this could provide the necessary viscosity to explain the observed accretion rates in accretion discs.

## 1.2.4 Viscous spreading in an accretion disc

### Viscous torque

In §1.2.3 the concept of shear viscosity was introduced. I shall now briefly explain the mechanism by which a ring of matter spreads due to this viscous force. Consider the situation depicted in fig. 1.2. There are two neighbouring annuli each of width

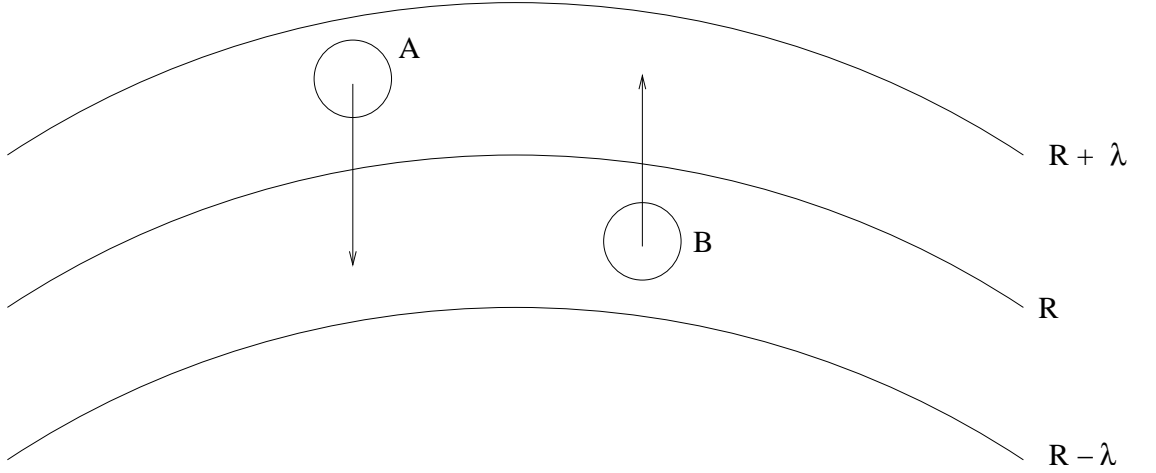


FIGURE 1.2. Mass transfer between adjacent annuli in an accretion disc.

$\lambda$ , the average distance between interactions of the gas elements. When gas elements are exchanged across the surface  $R$  they carry differing amounts of angular momentum. Element A will on average carry the angular momentum equivalent to a position of  $R + \lambda/2$ . Similarly, element B has an angular momentum equivalent to a position of  $R - \lambda/2$ . Matter crosses the surface  $R$  equally in both directions due to chaotic motions. For every unit arc length the mass flux in both directions is of the order  $H\rho\tilde{v}$ , where  $\rho$  is the mass density. While the mass flux is identical in both directions, the same cannot be said for the angular momentum. This results in a transport of angular momentum due to the random motions. The difference of the outward and inward angular momentum flux gives the torque exerted on the outer annulus by the inner annulus per unit arc length and is of the order  $-H\rho\tilde{v}\lambda R^2\Omega'$ , where  $\Omega' = d\Omega/dR$  (Frank et al. 2002). The total torque exerted by the outer annulus on the inner annulus is therefore,

$$G(R) = 2\pi R\nu\Sigma R^2\Omega', \quad (1.19)$$

where eq. (1.16) has been used and the *surface density* of the disc is defined as

$$\Sigma = \int_0^H \rho \, dz = \rho H, \quad (1.20)$$

for a constant density. Assuming a Keplerian angular velocity (see eq. (1.15))  $\Omega'$  is always negative. From the form of eq. (1.19), the inner annulus loses angular momentum to the outer annulus.

### Dissipation

Now consider a ring of gas of thickness  $dR$  at a distance  $R$  from a mass  $M$ . The inner and outer edges of the disc will experience different torques, the net of which is,

$$G(R + dR) - G(R) = \frac{\partial G}{\partial R} dR. \quad (1.21)$$

This torque is acting in the presence of the angular velocity  $\Omega(R)$ , hence a rate of work being performed (power)

$$\Omega \frac{\partial G}{\partial R} dR = \left[ \frac{\partial}{\partial R} (G\Omega) - G\Omega' \right] dR. \quad (1.22)$$

The term  $G\Omega' dR$  represents the rate at which mechanical energy is lost to the gas. The energy lost ends up as heat energy, i.e. the torque causes dissipation in the accretion disc and locally heats the gas. Defining the dissipation rate per unit surface area  $D(R)$  so that

$$D(R) = \frac{G\Omega'}{4\pi R} = \frac{1}{2} \nu \Sigma (R\Omega')^2. \quad (1.23)$$

Where each ring has a surface area of  $2 \times 2\pi R dR$  and eq. (1.19) has been used. If a Keplerian velocity is assumed eq. (1.15) then

$$D(R) = \frac{9}{8} \nu \Sigma \frac{GM}{R^3}. \quad (1.24)$$

### Viscous ring

Consider a thin (close to  $z = 0$ ) disc in a Keplerian orbit about a central star of mass  $M$ . The disc will have a circular velocity of,

$$v_\phi = R\Omega_K(R). \quad (1.25)$$

In addition to the circular velocity, there is a small radial drift velocity  $v_r$ , which is negative for small  $R$  due to matter falling towards  $M$ . The expression for the mass of an annulus of the disc of width  $\lambda$  is,

$$\Delta m = 2\pi R \Sigma \lambda. \quad (1.26)$$

Similarly the angular momentum of the annulus is given by  $2\pi R\Sigma R^2\Omega_K\lambda$ . Again following Frank et al. (2002), the rate of change of mass for an annulus is,

$$\frac{\partial}{\partial t}(2\pi R\lambda\Sigma) = \begin{aligned} &v_r(R, t)2\pi R\Sigma(R, t) \\ &-v_r(R + \lambda, t)2\pi(R + \lambda)\Sigma(R + \lambda, t). \end{aligned} \quad (1.27)$$

In the limit  $\lambda \rightarrow 0$ , eq. (1.27) reduces to

$$R\frac{\partial\Sigma}{\partial t} + \frac{\partial}{\partial R}(R\Sigma v_r) = 0. \quad (1.28)$$

When considering the angular momentum, the net effects of the viscous torques need to be included,

$$\begin{aligned} \frac{\partial}{\partial t}(2\pi R\lambda\Sigma R^2\Omega_K) = &v_r(R, t)2\pi R\Sigma(R, t)R^2\Omega_K(R) \\ &-v_r(R + \lambda, t)2\pi(R + \lambda)\Sigma(R + \lambda, t) \\ &\times (R + \lambda)^2\Omega_K(R + \lambda) + \frac{\partial G}{\partial R}\lambda. \end{aligned} \quad (1.29)$$

Again in the limit  $\lambda \rightarrow 0$ ,

$$R\frac{\partial}{\partial t}(\Sigma R^2\Omega_K) + \frac{\partial}{\partial R}(R\Sigma v_r R^2\Omega_K) = \frac{1}{2\pi} \frac{\partial G}{\partial R}. \quad (1.30)$$

Combining eqs. (1.28), (1.30) and (1.19) results in,

$$\frac{\partial\Sigma}{\partial t} = \frac{3}{R} \frac{\partial}{\partial R} \left( R^{1/2} \frac{\partial}{\partial R} (\nu\Sigma R^{1/2}) \right). \quad (1.31)$$

This is the basic equation describing the time evolution of the surface density in a Keplerian disc. Assuming that  $\nu$  is a constant enables a relatively simple analytic solution. Provided an initial mass distribution of

$$\Sigma(R, t = 0) = \frac{m}{2\pi R_0} \delta(R - R_0), \quad (1.32)$$

i.e. a ring of matter at radius  $R_0$  and following the method outlined in Frank et al. (2002) an expression for the surface density is,

$$\Sigma(x, \tau) = \frac{m}{\pi R_0^2} \tau^{-1} x^{-1/4} e^{-\frac{(1+x^2)}{\tau}} I_{1/4}(2x/\tau). \quad (1.33)$$

Where  $x = R/R_0$  and  $\tau = 12\nu t R_0^{-2}$  and  $I_{1/4}$  is a modified Bessel function. Figure 1.3 shows the form of eq. (1.33) for several values of  $\tau$ . The viscosity of the disc, has the

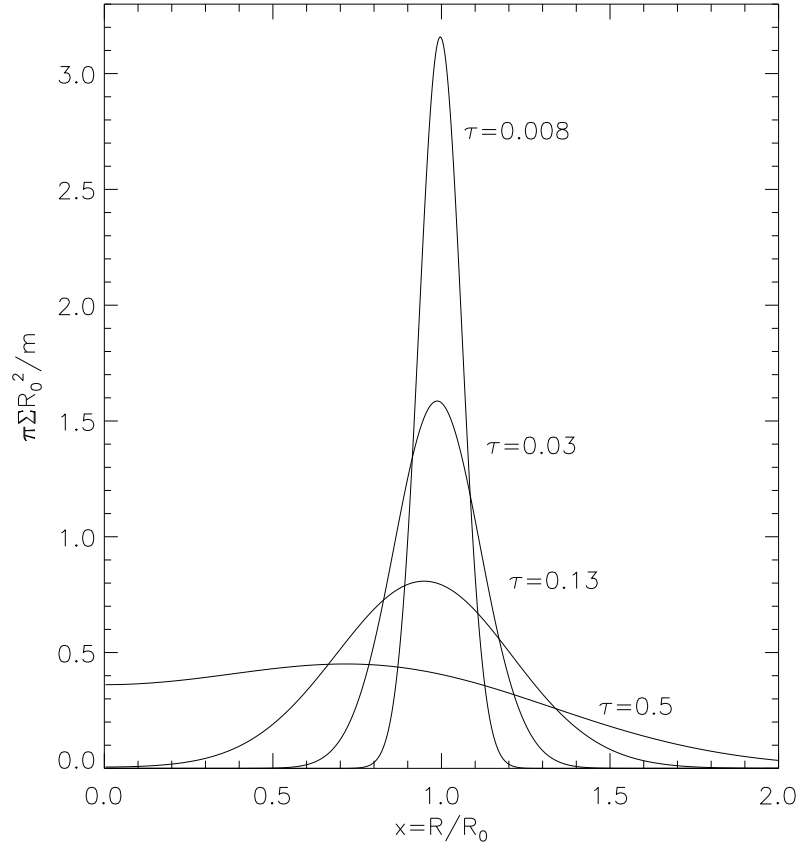


FIGURE 1.3. A ring of matter of mass  $m$  placed in a Keplerian orbit (at  $R = R_0$ ) spreads out due to viscosity. The surface density is given by eq. (1.33)

effect of spreading the ring on a time scale

$$t_{\text{visc}} \sim \frac{R^2}{\nu}. \quad (1.34)$$

Examining fig. 1.3, it is possible to gain an insight into how an accretion disc functions. After a long time,  $\tau > 1$ , the vast majority of the mass originally in the disc has been accreted onto the central object. The angular momentum of the mass in the disc has been carried away to a large radii by a small fraction of the mass. This is the basic principle behind all accretion discs, whether they are found around stellar mass black holes, AGN or protostars.

## 1.3 Low mass X-ray binaries

### 1.3.1 Binary systems

A binary star is a system that consists of two stars orbiting around their centre of mass. It has been suggested that a large percentage of stars are part of systems with two or more stars (Duquennoy & Mayor 1991, Fischer & Marcy 1992). Binary star systems are of large importance, by observing their orbits it is possible to calculate orbital period of the system. This information can be used to determine the masses of the individual stars<sup>7</sup>. The stars in binary systems can also influence each other's evolution producing many and varied astrophysical objects.

#### Binary Geometry

Before discussing the specifics of low mass X-ray binaries, I describe the basic geometry of a binary star system. Consider the system depicted in fig. 1.4, containing two stars of mass  $M_1$  and  $M_2$  (in this work it is assumed that  $M_1 > M_2$ ) respectively orbiting about a centre of mass (COM). The separation of the stars  $a$  can be determined by Kepler's third law,

$$4\pi^2 a^3 = G(M_1 + M_2)P_{\text{orb}}^2, \quad (1.35)$$

where  $P_{\text{orb}}$  is the orbital period in the binary. The total potential of the system has three constituent parts; the gravitational potential of the two stars and the effect of the Coriolis force. The potential at a point  $\mathbf{r}$  in a binary with an angular velocity of  $\Omega$  is described by the Roche potential

$$\Phi(\mathbf{r}) = -\frac{GM_1}{|\mathbf{r} - \mathbf{r}_1|} - \frac{GM_2}{|\mathbf{r} - \mathbf{r}_2|} - \frac{1}{2}(\Omega \wedge \mathbf{r})^2 \quad (1.36)$$

where  $\mathbf{r}_1$  and  $\mathbf{r}_2$  are the position vectors of the centres of  $M_1$  and  $M_2$  respectively. Figure 1.5 shows eq. (1.36) plotted on the line of centres of the system. Three local maxima are apparent in the potential: they are known as the first three Lagrangian points.

Further insight into accretion problems in binary systems can be gained by plotting equipotentials of  $\Phi(\mathbf{r})$  in the orbital plane, fig. 1.6. The equipotentials are heavily dependent on the mass ratio  $q = M_1/M_2$ . When a test particle is close to either of the stars, its motion is largely determined by the nearest star. Similarly a test particle at a large

---

<sup>7</sup>Provided the radial velocities of the stars are known and the inclination of the system with respect to the observer is known.

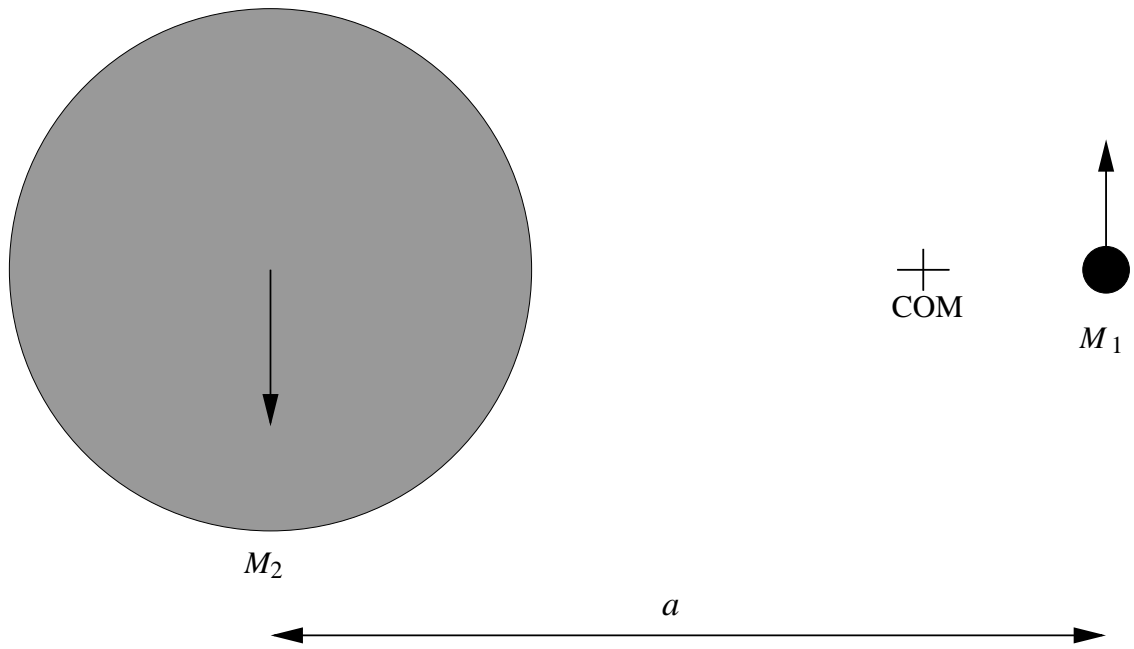


FIGURE 1.4. A binary system consisting of a compact star  $M_1$  and a secondary star  $M_2$  orbiting around their COM with a binary separation  $a$ . Arrows indicate the direction of motion.

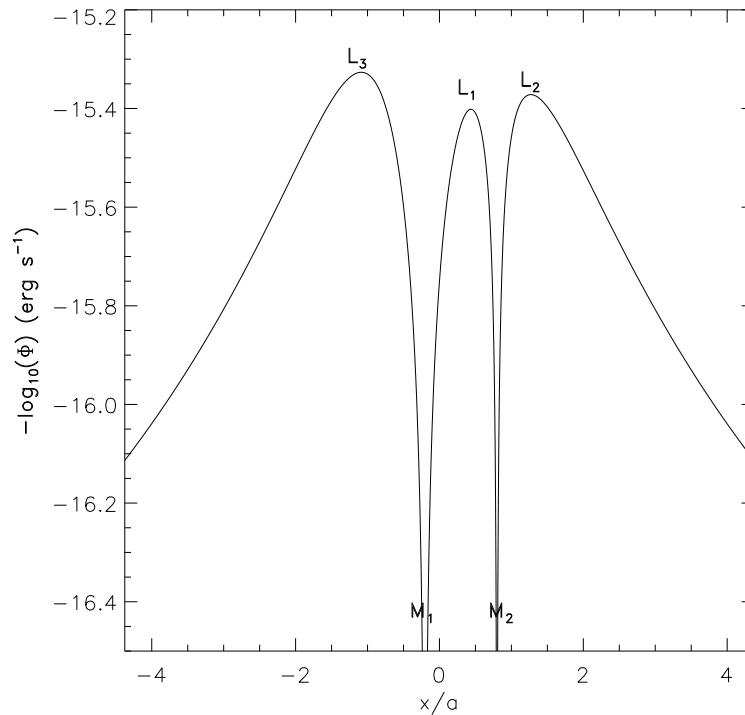


FIGURE 1.5. Roche potential  $\Phi(\mathbf{r})$  along the line of centres (the line connecting the centres of mass) for a binary system with a mass ratio  $q = 1/4$ , shown are the  $L_1$ ,  $L_2$  and  $L_3$  points and the positions of  $M_1$  and  $M_2$ .

distance from the primary only feels the force from a single mass centred on the centre of mass (COM) of the system. More important is the area surrounding the  $L_1$  point, the equipotentials in this region resembling a figure-of-eight. The critical equipotential surrounding both stars and passing through the  $L_1$  point is known as the *Roche lobe*. If the secondary star somehow fills its Roche lobe, matter may be transferred to the primary star via the  $L_1$  point. As demonstrated by fig. 1.5 the “path of least resistance” is via the  $L_1$  point, an unstable local maxima (actually a saddle point in 3D). Matter is then transferred, in a process called Roche lobe overflow (RLO), to the primary’s Roche lobe.

To examine the Roche lobes in more detail a measure of their size is needed. Due to the form of eq. (1.36) the lobes are not spherical. A common approximation is to consider a sphere of radius  $R_2$  that has the same volume as the lobe. The non trivial nature of eq. (1.36) means there is no exact formula describing  $R_2$ , but Eggleton (1983) describes a analytic approximation for all values of  $q$ ,

$$\frac{R_2}{a} = \frac{0.49q^{2/3}}{0.6q^{2/3} + \ln(1 + q^{1/3})}. \quad (1.37)$$

This calculates the radius of the lobe sphere for the secondary. In the range  $q \lesssim 0.8$  a simpler form (Paczynski 1971) is

$$\frac{R_2}{a} = \frac{2}{3^{4/3}} \left( \frac{q}{1+q} \right)^{1/3}. \quad (1.38)$$

An interesting consequence of this: combining eqs. (1.35) and eq. (1.38), the average density of a lobe filling star is determined by the orbital period of the binary (expressed in hours),

$$\bar{\rho} = \frac{3M_2}{4\pi R_2^3} = \frac{3^5}{8} \frac{\pi}{GP_{\text{orb}}^2} \sim 110P_{\text{orb}}^{-2}(\text{hr}) \text{ g cm}^{-3} \quad (1.39)$$

### Mass transfer

The means of mass transfer onto the primary depends on the evolution of the secondary star, which is largely determined by its mass. If the secondary is a high mass star such as an O or B type it will have a significant stellar wind. A fraction of this wind can be captured by the primary, form an accretion disc and subsequently accrete onto the primary. For a lower mass secondary, mass transfer cannot proceed until the star, somehow, fills its Roche lobe. Then, mass can be transferred via the  $L_1$  point. Gas initially at the  $L_1$  point settles into an orbit of radius  $R_{\text{circ}}$  around the primary with the same angular momentum that it possessed at the  $L_1$  point. The material settles into the lowest energy

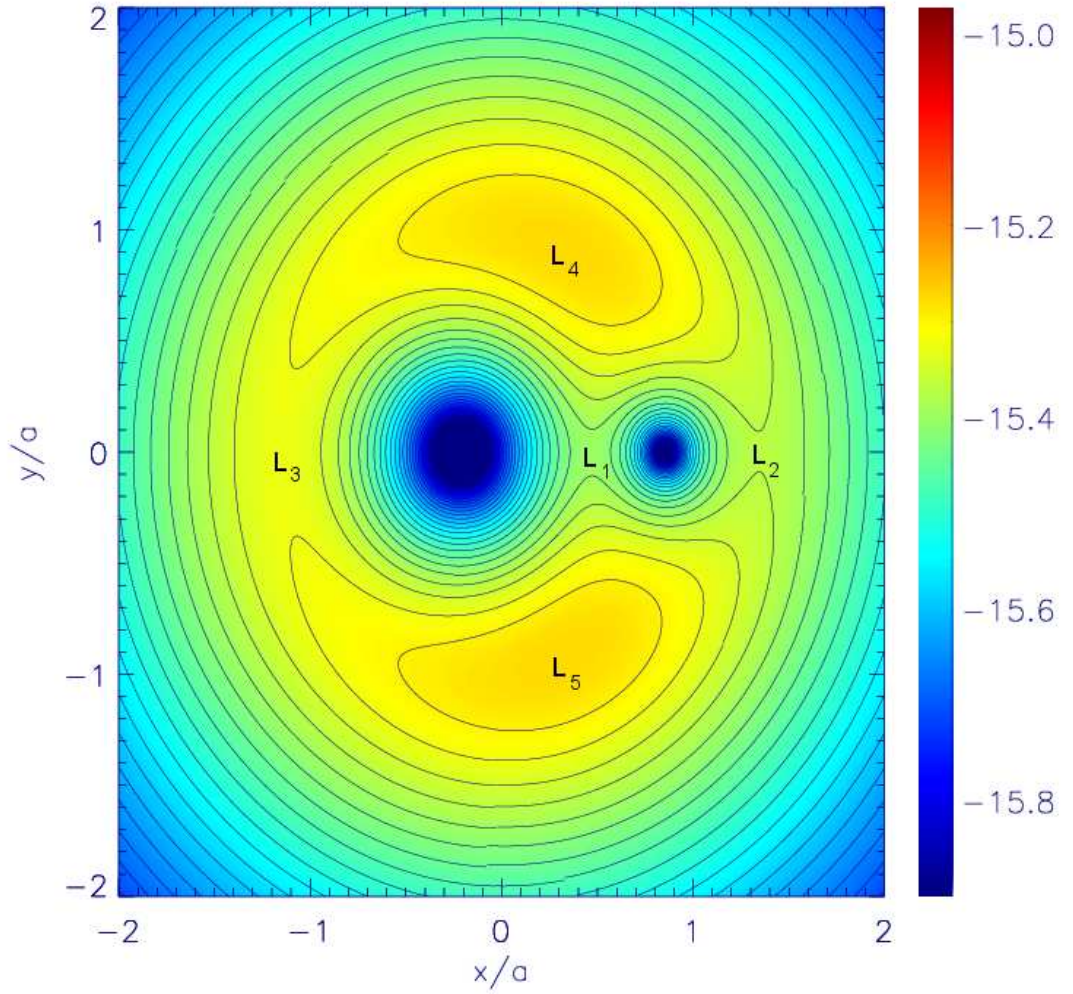


FIGURE 1.6. Roche equipotentials  $\Phi(\mathbf{r}) = \text{constant}$ , for a binary system with a mass ratio  $q = 1/4$ . Shown are the five Lagrangian points  $L_1 - L_5$ . The inner Lagrangian point  $L_1$  is a saddle point in the potential surface. If the secondary star evolves and fills its Roche lobe, mass can be transferred to the primary star. The colour scale represents  $-\log_{10}(\Phi)$  and is in units of  $\text{erg s}^{-1}$ .

orbit for a given angular momentum i.e. circular, because of dissipation when the stream of matter interacts with itself. From the conservation of angular momentum,

$$R_{\text{circ}} v_{\phi}(R_{\text{circ}}) = R_{L_1} v_{\perp} \quad (1.40)$$

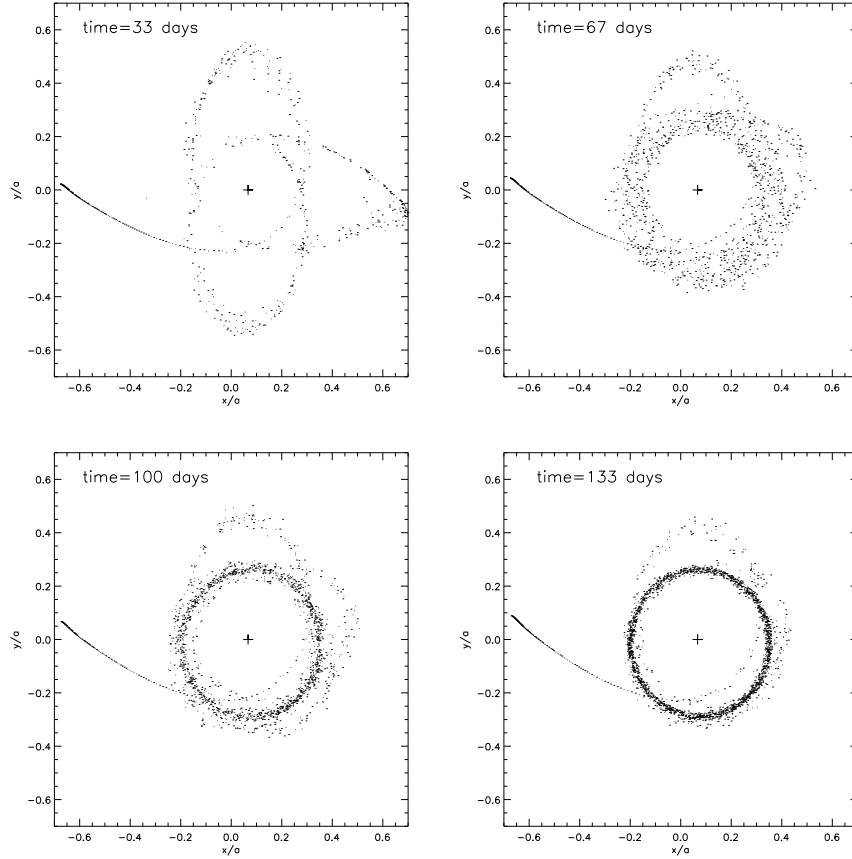


FIGURE 1.7. A particle simulation of disc formation in the system GRS 1915+105 with  $a \sim 7.5 \times 10^{12}$  cm,  $P_{\text{orb}} = 33.5$  days,  $M_1 = 14 M_{\odot}$  and  $M_2 = 1.0$ . The cross represents the position of  $M_1$ , the secondary red giant is not shown. Particles are emitted from the  $L_1$  point.

where  $R_{L_1}$  is the distance from  $M_1$  to  $L_1$ ,  $v_{\phi}(R_{\text{circ}})$  is the circular velocity at  $R_{\text{circ}}$ , given by

$$v_{\phi}(R_{\text{circ}}) = \left( \frac{GM_1}{R_{\text{circ}}} \right)^{1/2} \quad (1.41)$$

and  $v_{\perp}$  is the velocity (in a non-rotating frame) perpendicular to the line of centres at the  $L_1$  point. As gas is transferred from the secondary, it accumulates at  $R_{\text{circ}}$  forming a ring which spreads out due to collisions, shocks and viscous dissipation to form an accretion disc, the mechanics of which have been discussed in §1.2.4. An example of a numerical simulation showing the formation of an accretion disc is shown in fig. 1.7.

For the process of mass transfer via Roche lobe overflow to begin one of two things must occur. The lobe of the star can shrink until it is equal to the stellar radius or the star can expand to fill the Roche lobe. Starting by looking at the orbital angular momentum,

$J$ , of the binary

$$J = (M_1 a_1^2 + M_2 a_2^2) \frac{2\pi}{P_{\text{orb}}}. \quad (1.42)$$

Where  $a_1 = (M_2/M_1)a$  and  $a_2 = (M_1/M_2)a$  are the distances of  $M_1$  and  $M_2$  from the COM respectively, simplifying with  $M_T = M_1 + M_2$  and using eq. (1.35) gives

$$J = M_1 M_2 \left( \frac{Ga}{M_T} \right)^{1/2}. \quad (1.43)$$

If it is assumed that all of the mass lost by the secondary ( $\dot{M}_2 < 0$ ) is gained by the primary then,  $\dot{M}_T = 0$  and  $\dot{M}_1 = -\dot{M}_2$ . Logarithmic differentiation of eq. (1.43) then gives

$$\frac{\dot{a}}{a} = \frac{2\dot{J}}{J} - \frac{2\dot{M}_2}{M_2}(1 - q). \quad (1.44)$$

Due to  $q < 1$  and  $\dot{M}_2 < 0$ , for conservative mass transfer (no loss of mass or angular momentum  $\dot{J} = 0$ ) the LHS of the equation is always positive and the orbital separation must increase. Logarithmic differentiation of eq. (1.38) gives

$$\frac{\dot{R}_2}{R_2} = \frac{\dot{a}}{a} + \frac{\dot{M}_2}{3M_2}, \quad (1.45)$$

combing this with eq. (1.44) gives an expression for the change in the lobe radius of the secondary

$$\frac{\dot{R}_2}{R_2} = \frac{2\dot{J}}{J} - \frac{2\dot{M}_2}{M_2} \left( \frac{5}{6} - q \right). \quad (1.46)$$

Again for conservative mass transfer any system with  $q < 5/6$  will result in the Roche lobe expanding away from the star, stopping any mass transfer if the star does not similarly expand.

### 1.3.2 X-ray binaries

A simple approximation of a blackbody spectrum allows an estimate of the optimum wavelength an accreting black hole should be observable in. Define a temperature  $T_{\text{bb}}$  that the black hole would have if it radiated as a blackbody,

$$T_{\text{bb}} = \left( \frac{L_{\text{acc}}}{4\pi R_{\star}^2 \sigma} \right)^{1/4}, \quad (1.47)$$

where  $\sigma$  is the Stefan-Boltzmann constant. Assuming a black hole mass of  $5 M_{\odot}$ , using eq. (1.1) and assuming the luminosity is equal to its Eddington luminosity ( $6.5 \times$

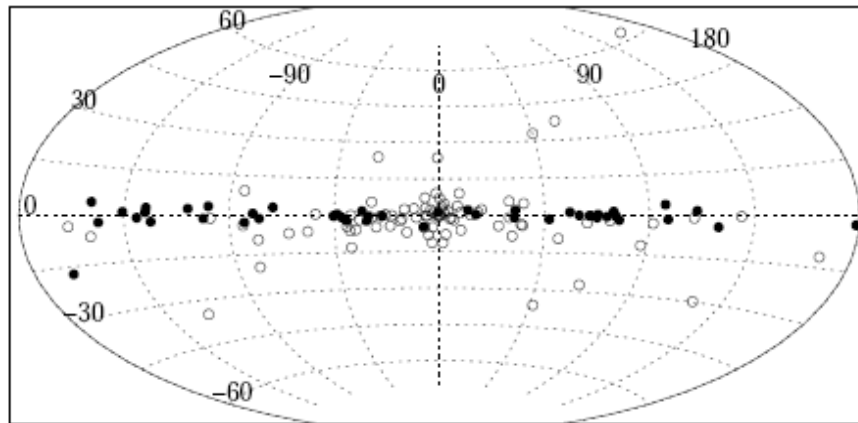


FIGURE 1.8. Distribution of HMXB (filled circles) and LMXB (empty circles) within the Milky Way (Grimm et al. 2003).

$10^{38} \text{erg s}^{-1}$ ), gives  $T_{\text{bb}} \sim 4 \times 10^7 \text{ K}$ . This temperature would result in photons with an energy of  $kT_{\text{bb}} \sim 1 \text{ keV}$  (where  $k$  is the Boltzmann constant). At this energy, a black hole is a source of X-rays. A note of caution, this result is no more than an order of magnitude estimate. Assuming the Eddington luminosity in eq. (1.47) is only viable because of the insensitivity of  $T_{\text{bb}}$  to the luminosity. Similar arguments can be used to show neutron stars also radiate largely in X-rays. The previous sections have shown that, accretion can be a source of energy (§1.2.1), mass can be transferred from a secondary star to a primary compact star (§1.3.1) and that this mass will form an accretion disc that will spread due to viscosity (§1.2.4). In addition the emitted spectrum of black holes and neutron stars will be in the X-ray band. This has led systems containing a black hole/neutron star accreting from a secondary star to be classified as X-ray binaries.

X-ray binaries are typically separated into two categories: high mass X-ray binaries (HMXB) and low mass X-ray binaries (LMXB). HMXBs typically consist of a black hole/neutron star and a high mass companion. Accretion can take place due to the wind of the massive companion star or due to Roche lobe overflow. They have a hard X-ray spectra ( $kT \gtrsim 15 \text{ keV}$ ) and are known to be concentrated in the Galactic plane (see fig. 1.8). LMXBs are binaries where a neutron star/black hole is present, along with a low mass main sequence star, or a evolved giant star filling its Roche lobe. Mass can only be transferred to the primary via Roche lobe overflow. The mass ratio  $q$  in these systems can be low, referring to eq. (1.46) the secondary star must expand<sup>8</sup> for mass transfer to proceed. In contrast to HMXBs, LMXBs have a softer X-ray spectra ( $kT \lesssim 10 \text{ keV}$ ) and are associated with the Galactic bulge. The lifetime of an O or B type star is of the order of  $10^{6-7} \text{ yrs}$ , resulting in HMXB being found in star forming regions (i.e. the Galactic

<sup>8</sup>Assuming that  $\dot{J} = 0$ , which is not always the case, particularly in systems with a low orbital period

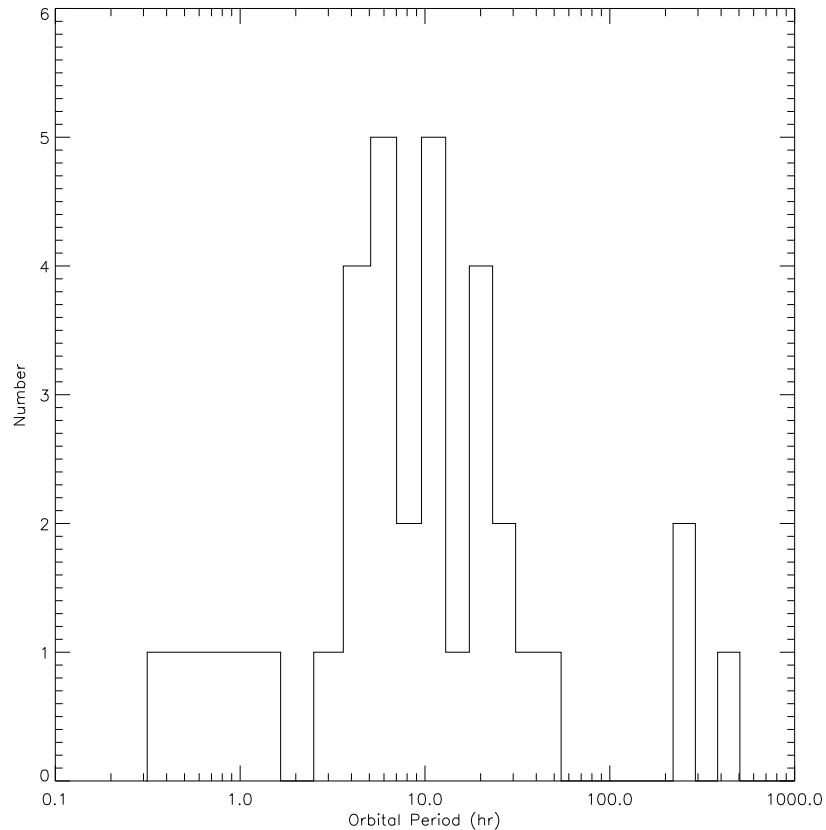


FIGURE 1.9. Orbital period distribution of 33 well defined LMXB (White et al. 1995)

plane). The lifetime of LMXBs on the other hand is much longer ( $\sim 10^{10}$  yrs); therefore LMXBs are found throughout the Galaxy and are also associated with globular clusters (Clark 1975).

Figure 1.9 shows the orbital distribution of 33 well measured LMXBs. The peak in the distribution appears to be  $\sim 10$  hrs. This is in contrast to orbital periods in main sequence binaries which are of the order of years. The process of forming a LMXB must decrease the orbital separation and hence decrease the orbital period. Assuming a binary begins with two main sequence stars, the more massive primary star evolves quicker and enters the giant phase first. As the primary star expands it will transfer mass to the secondary via the  $L_1$  point (see §1.3.1). As the primary continues to expand the secondary becomes engulfed resulting in a common envelope phase. Frictional forces between the stars and the common envelope causes the orbital separation to shrink and the common envelope to be ejected. The end result is a reduced orbital separation and a primary star that is now a helium core, which will in turn collapse into a neutron star/black hole in a supernova. If the binary survives the supernova it will consist of a

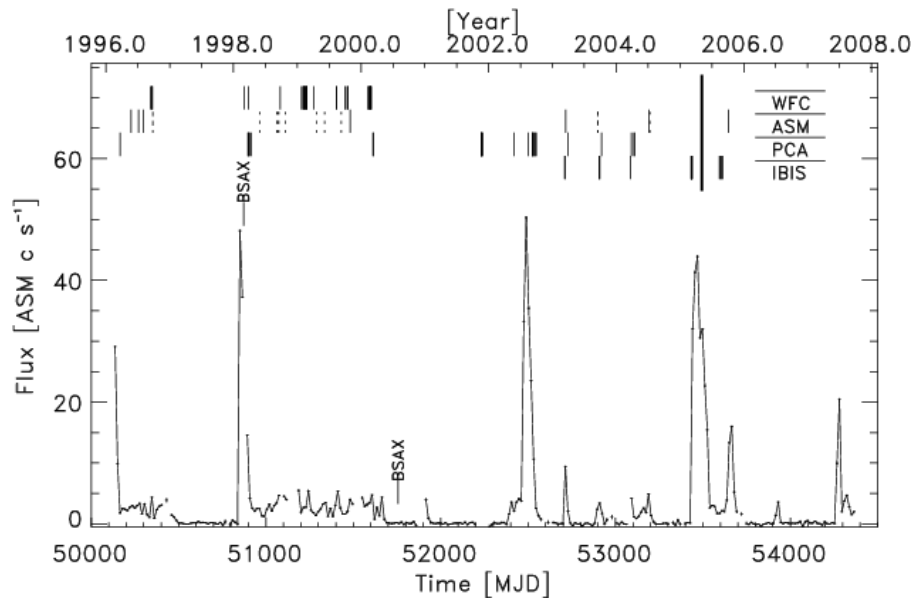


FIGURE 1.10. 1.5-12 keV light curve of 4U 1608-522 at a 2-week time resolution (Keek et al. 2008)

compact object and a main sequence star, the progenitor of an LMXB. This also explains the few LMXBs with longer orbital periods: these systems never entered the common envelope phase and they remained at a large orbital separation.

Some LMXBs exhibit transient behaviour: they show long periods of inactivity interrupted by periods of increased luminosity. Figure 1.10 shows the X-ray lightcurve of the LMXB 4U 1608-522. The X-ray flux can increase by an order of magnitude or more for short periods. Referring to eq. (1.3), the mass accretion onto the compact object must be somehow be increased. The two possibilities to achieve this are an increase in the mass transfer from the secondary star or an increase in the mass being transported in the disc. The first possibility can be ruled out based on observations of the secondary star and the hot spot (where the gas stream impacts the disc) in the disc. The second possibility explains the transient behaviour of LMXBs via an instability in the accretion disc which temporarily increases  $\dot{M}$  through the disc. This model which became known as the disc instability model (DIM) has had great success explaining the observations of LMXBs along with other outbursting systems such as cataclysmic variables.

### 1.3.3 The disc instability model

The disc instability model was first proposed by Hōshi (1979) to explain dwarf novae. It has since been developed for LMXBs, for a review see Lasota (2001) and Dubus, Hameury & Lasota (2001). Firstly I will go over the basic ideas involved in the DIM

and how it explains outbursts. Secondly the mathematical reasoning underpinning the DIM will be discussed. A relation between the surface density of the disc  $\Sigma$  and the temperature  $T$  results in the *S-curve* shown in fig. 1.11. The curve represents the regime in which an annulus of the disc can remain in thermal equilibrium. To the right of the curve energy generation due to viscosity is greater than the energy losses from the surface of the disc, hence the disc heats up. The opposite is true on the left of the curve.

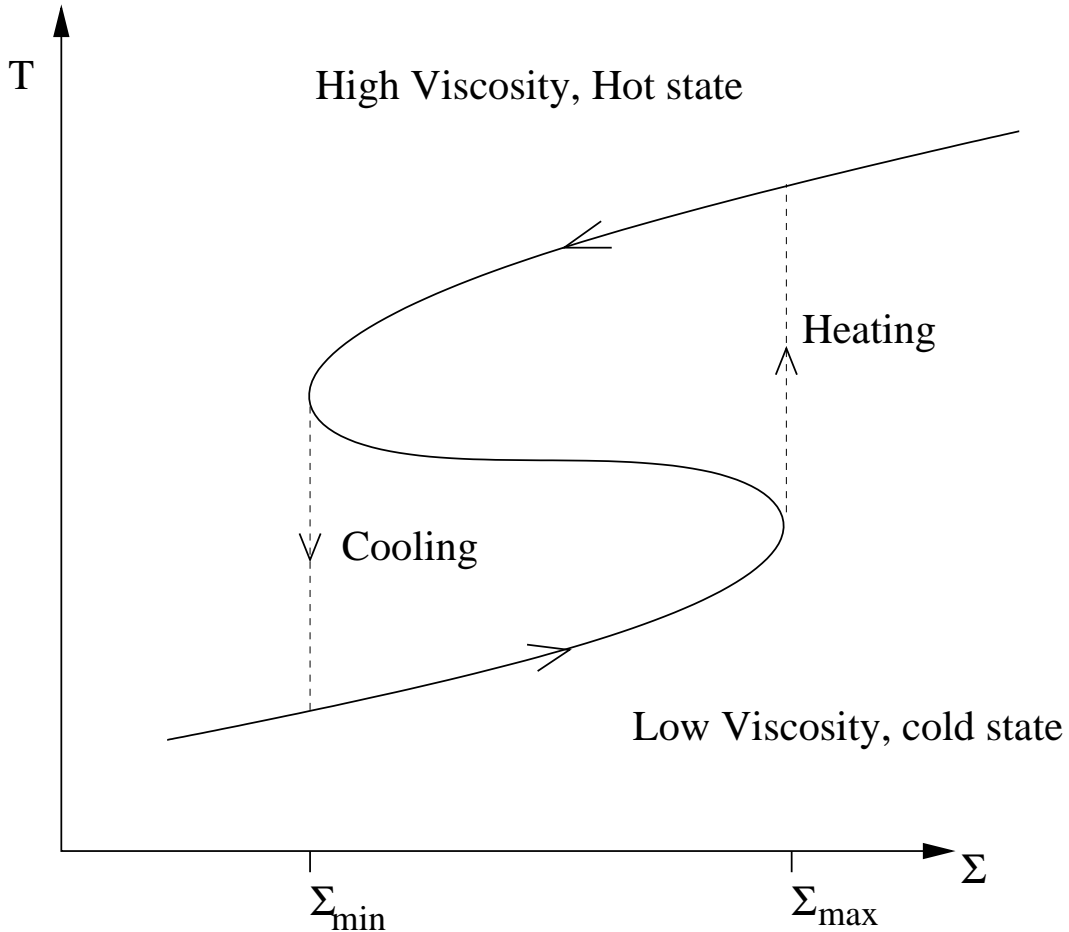


FIGURE 1.11. The *S-curve* for a given annulus of an accretion disc. The annulus has a limit-cycle behaviour between hot and cold states.

The physical mechanism that underlines the DIM is the ionisation of hydrogen and the extreme sensitivity of the opacity function in this temperature region which results in an instability. In the *S-curve* the lower cold state corresponds to low opacity neutral hydrogen, while the higher hot state corresponds to high opacity ionised hydrogen. The critical value for the surface density above which the hydrogen in the disc is ionised ( $T \sim 6500$  K) is denoted  $\Sigma_{\max}$ . The solution which has a negative gradient ( $\partial T / \partial \Sigma < 0$ ) is unstable, resulting in limit-cycle behaviour when the disc heats and cools at the critical points  $\Sigma_{\max}$  and  $\Sigma_{\min}$ .

The changes in the annulus are assumed to be followed by a change in the viscosity. An increase in the ionisation of an annulus could in theory result in an increased viscosity, if the viscosity is wholly or partially the result of magnetic fields. The increase in viscosity is associated with an increase of angular momentum transfer within the disc. This causes a matter wave to propagate in the disc pushing the surface density of neighbouring annuli above  $\Sigma_{\max}$ . Thus, the instability is likewise propagated through the disc. An increase in the mass transferred within the disc would account for the increasing  $\dot{M}$  and hence the increase in luminosity during the hot states. The DIM has been successful in explaining many astrophysical phenomena. However the uncertainty over the physical mechanism behind viscosity in accretion discs means its validity remains uncertain. Nevertheless the fact remains that the DIM is the currently the only theory to successfully explain observations of CVs and LMXBs. As mentioned in §1.2.3 the effect of magnetic fields on the disc is expected to give rise to the MRI leading to viscosity in the disc. Simulations using magnetohydrodynamics (MHD) may provide further evidence backing this theory (for a review see Balbus & Hawley (2003)).

The central premise of the DIM is the *S-curve*. To understand the origin of the curve I will follow the reasoning of Frank et al. (2002). Starting with eq. (1.31), let  $\mu = \nu\Sigma$  and perturb the surface density so that  $\Sigma = \Sigma_0 + \Delta\Sigma$  resulting in,

$$\frac{\partial\Delta\Sigma}{\partial t} = \frac{3}{R} \frac{\partial}{\partial R} \left( R^{1/2} \frac{\partial}{\partial R} (\Delta\mu R^{1/2}) \right). \quad (1.48)$$

Frank et al. (2002) show that the viscosity  $\nu$  is a function of the surface density and radius only, hence  $\mu$  is also, meaning

$$\Delta\Sigma = \frac{\partial\Sigma}{\partial\mu} \Delta\mu. \quad (1.49)$$

Using this in eq. (1.48) gives a relation describing how the perturbation in  $\mu$  evolves with time,

$$\frac{\partial\Delta\mu}{\partial t} = \frac{\partial\mu}{\partial\Sigma} \frac{3}{R} \frac{\partial}{\partial R} \left( R^{1/2} \frac{\partial}{\partial R} (\Delta\mu R^{1/2}) \right). \quad (1.50)$$

The important result from this is that  $\partial\Delta\mu/\partial t \propto \partial\mu/\partial\Sigma$ . If  $\partial\mu/\partial\Sigma > 0$  then eq. (1.50) exhibits behaviour similar to that shown in fig. 1.3, i.e. the perturbation decays on a viscous timescale. However the perturbations grow if the condition  $\partial\mu/\partial\Sigma < 0$  is satisfied.

To gain a better understanding of this instability  $\mu$  must be related to a more intuitive quantity. Use the conservation equations for mass eq. (1.28) and angular momentum

eq. (1.30) and assume a steady state ( $\partial/\partial t = 0$ ) disc rotating with a Keplerian velocity. From eq. (1.28) and using the same arguments used as in eq. (1.6) gives

$$\begin{aligned} R\Sigma v_R &= C \\ 2\pi R\Sigma(-v_R) &= \dot{M}. \end{aligned} \quad (1.51)$$

Similarly from eq. (1.30) and using eq. (1.19) gives

$$-\nu\Sigma\Omega'_K = \Sigma(-v_R)\Omega_K + \frac{C}{2\pi R^3}, \quad (1.52)$$

where  $C$  is a constant of integration. The second term on the RHS is identified as rate at which angular momentum is lost from the disc to the accretor. At the beginning of the boundary layer  $\Omega'_K = 0$  and  $\Omega_K \sim \Omega_K(R_*)$ , where  $R_*$  is the radius of the accretor. Along with eq. (1.51) this gives the value of the integration constant as  $C = -\dot{M}(GM R_*)^{1/2}$ . Finally, using eq. (1.15) relates  $\mu$  to the local mass transfer rate

$$\nu\Sigma = \mu = \frac{\dot{M}}{3\pi} \left( 1 - \left( \frac{R_*}{R} \right)^{1/2} \right). \quad (1.53)$$

Therefore the instability is in the region where  $\partial\dot{M}/\partial\Sigma < 0$ . This describes the behaviour of the disc in the unstable regime: when  $\Sigma$  decreases the local mass transfer rate increases, leading to the fragmentation of the disc as unstable regions are emptied of mass.

To show the dependency of the instability on the opacity of the disc the mass accretion rate needs to be related the temperature of the disc. If the disc is assumed to be optically thick in the  $z$  direction then it will radiate as a blackbody. This energy loss will be equal to the viscous dissipation in the disc

$$\sigma T^4(R) = \frac{9}{8}\nu\Sigma\frac{GM}{R^3}, \quad (1.54)$$

where eq. (1.24) has been used. To obtain the desired relation, substitute eq. (1.53) into the above

$$T^4(R) = \frac{3\dot{M}GM}{8\pi R^3\sigma} \left( 1 - \left( \frac{R_*}{R} \right)^{1/2} \right). \quad (1.55)$$

Meaning  $\dot{M} \propto T^4(R)$ , this recovers the instability condition originally stated and depicted in fig. 1.11, namely  $\partial T/\partial\Sigma$ . To proceed any further a relation between  $\Sigma$  and  $T$

is needed. Given an opacity of  $\kappa_R \propto \rho T_c^n$  Frank et al. (2002) show that

$$T \propto \Sigma^{\frac{13-2n}{4(7-2n)}}, \quad (1.56)$$

for a given central temperature ( $z = 0$ ). The gradient of which is negative when  $7/2 < n < 13/2$ , given the form of the opacity above this corresponds to the range in which hydrogen is ionised, giving the physical cause of the *S-curve*. The simple *S-curve* in fig. 1.11 is an idealised version to explain the basics of the DIM. In reality there are two *S-curves* corresponding to the different values of  $\alpha$ . This was implemented early in the development of the DIM to explain the duration of outbursts in dwarf nova. An example of a calculated *S-curve* is shown in fig. 1.12.

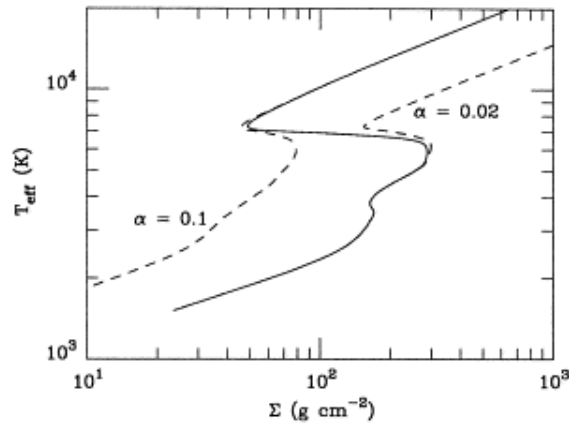


FIGURE 1.12. An example of a calculated *S-Curve*. The dashed lines have a constant  $\alpha$  and the solid line is the result with different  $\alpha$ 's on the upper and lower parts of the curve (Lasota 2001).

## 1.4 The Galactic centre

In §1.3 the black holes in question are no more than several  $M_\odot$  in mass. There are however black holes in existence which are several orders of magnitude more massive. Lynden-Bell & Rees (1971) speculated that there may be a large central mass within the Galaxy which would probably be a black hole. The first evidence for this central black hole was a bright radio source in the central parsec (Balick & Brown 1974). It has since been named *Sagittarius A\** (Sgr A\*) and is now widely believed to be a  $\sim 4 \times 10^6 M_\odot$  black hole (Schödel et al. 2002). Sgr A\* is part of a group of aptly named objects called super massive black hole (SMBH) believed to reside in the centre of most if not all galaxies.

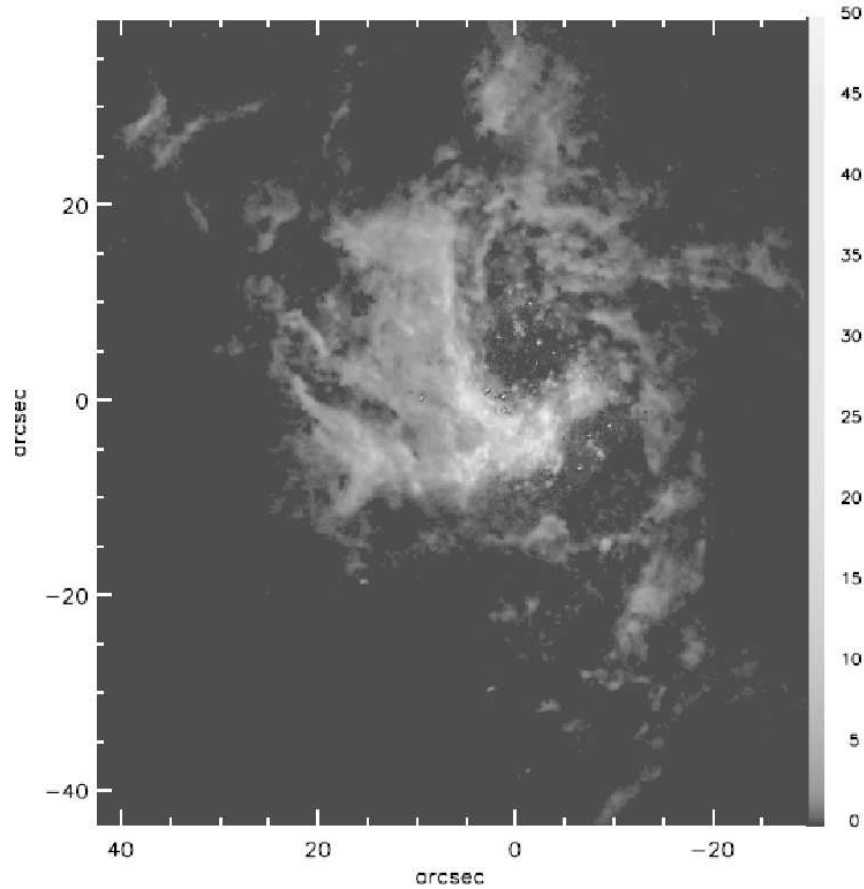


FIGURE 1.13. Pa $\alpha$  in the Galactic centre showing the feature known as the Minispiral. The gray scale units are  $10^{16}$  erg cm $^{-2}$  s $^{-1}$  per pixel, and spatial offsets are relative to Sgr A\* (Scoville et al. 2003).

The central parsec around Sgr A\* contains thousands of stars. Most are old red main sequence stars. Within the central half-parsec however the power output is dominated by young massive stars (Krabbe et al. 1995) which appear to have been formed *in situ* despite the large tidal shear due to Sgr A\*. More puzzling is the so called S-stars<sup>9</sup> which are found  $\sim 0.03$  parsecs from Sgr A\*. How such young stars formed isotropically around Sgr A\* is still open to debate. In addition to these massive young stars there is the strong possibility that a significant number of compact remnants are located in the nucleus of the Galaxy. Dynamical friction should result in massive stellar remnants transferring closer to Sgr A\* and less massive stars being ejected from the Galactic centre entirely (Morris 1993).

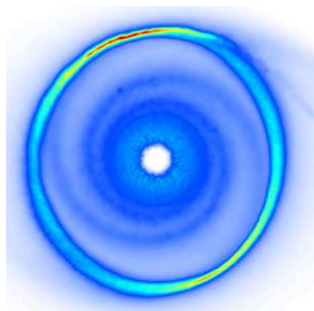
In addition to stars and compact objects the inner few parsecs of the Galaxy also con-

<sup>9</sup>The S-stars were first described by Eckart & Genzel (1997). They are young ( $< 10$  Myr), a factor of 10 closer to the SMBH than the closest stellar population previously known, and move around Sgr A\* on randomly oriented orbits that are highly eccentric.

tains a significant amount of ionised gas. In projection the gas features appear to have a spiral shape (see fig. 1.13), resulting in the collective name the Minispiral. The structure of the Minispiral is believed to consist of as many as nine components (Paumard, Maillard & Morris 2004). The origin of the gas is still unclear, the hyperbolic orbits (Yusef-Zadeh, Roberts & Biretta 1998) of the feature known as the northern arm suggest that some of the gas is a temporary feature in the inner Galaxy. The presence of the Minispiral and the expected compact objects leads to the possibility that black holes (and neutron stars) could accrete gas from the Minispiral, via Bondi-Hoyle accretion (eq. (1.9)), and be observable. I consider this possibility in Chapter 3.

# Chapter 2

## *Numerical methods*



“The bigger the lie, the more they believe.”  
- Bunk

*The Wire: More With Less [5.01]*

## 2.1 Smoothed Particle Hydrodynamics

In this chapter I will introduce the concept of smoothed particle hydrodynamics (SPH) which will be used extensively in §4. There are two basic ways to computationally model fluid flows, with and without a grid. The standard grid method involves a fixed grid in space where fluid quantities and derivatives are computed using finite difference methods. This approach runs into resolution difficulties when it is confronted with problems that span many orders of magnitude in space or density. This leads to a refinement of the standard grid approach: the adaptive mesh refinement (AMR) method solves many of the problems that plague the fixed grid method by refining the grid in regions of interest.

In the SPH approach, instead of using a grid the fluid quantities are carried by several interpolation points called particles. These particles trace the fluid motion and fluid quantities and derivatives are calculated by interpolating over neighbouring particles. This method became known as smoothed particle hydrodynamics. The Lagrangian nature (the coordinates move with the particles) inherent to SPH is extremely useful in problems that grid codes had difficulty with because the resolution of the SPH method is automatically adjusted with respect to the particle positions. SPH was first described by Lucy (1977) and Gingold & Monaghan (1977) and has been used in a wide variety of astrophysical problems:

- Supernovae explosions
- Star formation
- Galaxy collisions
- Gas dynamics
- Planet formation
- Star collisions
- Accretion discs

In this thesis I use an SPH code written by James Murray (Murray 1995, Murray 1996). The code has been modified by myself for this work and others (Truss et al. 2000, Murray, Truss & Wynn 2002). For a comprehensive review of SPH see Monaghan (1992). In the following section, I describe the SPH formalism and how it is implemented in the code.

## 2.2 SPH Derivation

### 2.2.1 Interpolant

Start with the trivial identity

$$Q(\mathbf{r}) = \int Q(\mathbf{r}')\delta(|\mathbf{r} - \mathbf{r}'|)d\mathbf{r}', \quad (2.1)$$

where  $\delta$  is the Dirac delta function and  $Q$  is a function that is defined in the coordinates  $\mathbf{r}$ . This can be approximated using,

$$\lim_{h \rightarrow 0} W(\mathbf{r} - \mathbf{r}', h) = \delta(\mathbf{r} - \mathbf{r}'), \quad (2.2)$$

where  $W$  is a smoothing kernel with a characteristic smoothing length  $h$ .  $Q$  is then given by

$$Q(\mathbf{r}) = \int Q(\mathbf{r}')W(|\mathbf{r} - \mathbf{r}'|, h)d\mathbf{r}' + \mathcal{O}(h^2), \quad (2.3)$$

where  $W$  has been expanded in a Taylor series about  $\mathbf{r}$  and is normalised to

$$\int W(\mathbf{r} - \mathbf{r}', h)d\mathbf{r}' = 1. \quad (2.4)$$

The integral in eq. (2.3) is then changed to a sum over a set of discrete points (the particles) which the interpolation is performed over and the mass element  $\rho dV$  is replaced with the particle mass  $m$

$$\begin{aligned} Q(\mathbf{r}) &= \int \frac{Q(\mathbf{r}')}{\rho(\mathbf{r}')} W(\mathbf{r} - \mathbf{r}', h) \rho(\mathbf{r}') d\mathbf{r}' + \mathcal{O}(h^2) \\ &\sim \sum_{i=1}^N m_i \frac{Q_i}{\rho_i} W(\mathbf{r} - \mathbf{r}', h), \end{aligned} \quad (2.5)$$

where  $i$  refers to quantity being evaluated at the position of particle  $i$ . Equation (2.5) is the basis for SPH, as it allows us to find an approximation to any physical quantity of a fluid. A common example of the SPH method is finding the density at any point in the fluid. Let  $Q(\mathbf{r}) \rightarrow \rho(\mathbf{r})$  then eq. (2.5) becomes,

$$\rho(\mathbf{r}) = \sum_{i=1}^N m_i W(\mathbf{r} - \mathbf{r}', h). \quad (2.6)$$

This is the origin of the term SPH, the mass of each particle is smoothed over the smoothing length resulting in a continuous density distribution of the fluid.

### 2.2.2 Derivative

Using eq. (2.5) the derivative of the fluid quantities can be obtained. This is highly desirable, calculating the derivatives at points in the fluid enables calculation of pressure and viscous forces within the fluid. The particle positions are then updated according to these forces. From eq. (2.3),

$$\nabla Q(\mathbf{r}) = \int \nabla Q(\mathbf{r}') W(\mathbf{r} - \mathbf{r}', h) d\mathbf{r}', \quad (2.7)$$

integration by parts gives

$$\nabla Q(\mathbf{r}) = \int_S Q(\mathbf{r}') W(\mathbf{r} - \mathbf{r}', h) \mathbf{n} da + \int Q(\mathbf{r}') \nabla W(\mathbf{r} - \mathbf{r}', h) d\mathbf{r}', \quad (2.8)$$

where  $\mathbf{n}$  and  $da$  are the unit normal and area element respectively of a surface  $S$ . The first term on the LHS of the equation is a surface integral and in practice can be ignored as long as either  $Q(\mathbf{r})$  or  $W$  are zero at some point in space. With this assumption in mind and changing the integral to a series of interpolation points as before results in,

$$\nabla Q(\mathbf{r}) = \sum_{i=1}^N \frac{m_i}{\rho(\mathbf{r})} Q(\mathbf{r}') \nabla W(\mathbf{r} - \mathbf{r}', h). \quad (2.9)$$

Assuming that the derivative of the kernel is non zero, the derivative of any physical quantity can be calculated.

### 2.2.3 The kernel

When SPH was first developed the kernels used were simple Gaussian functions of the form

$$W(r, h) = \frac{1}{\pi^{3/2} h^3} e^{-x^2}, \quad (2.10)$$

where  $r = \mathbf{r} - \mathbf{r}'$  and  $x = r/h$  (Gingold & Monaghan 1977). This approach, however, implies that all of the particles in the simulation are used to evaluate a physical quantity, no matter how little a given particle contributes. This is a waste of computing resources and motivated the use of spline kernels in later work (Monaghan & Lattanzio 1985),

$$W(r, h) = \frac{\sigma}{h^\nu} \begin{cases} 1 - \frac{3}{2}x^2 + \frac{3}{4}x^3 & \text{where } 0 \leq x < 1 \\ \frac{1}{4}(2-x)^3 & \text{where } 1 \leq x \leq 2 \\ 0 & \text{where } x > 2 \end{cases} \quad (2.11)$$

where  $\nu$  is the number of dimensions and  $\sigma$  is a normalisation factor given by,

$$\sigma = \begin{cases} \frac{2}{3} & \text{when } \nu = 1 \\ \frac{10}{7\pi} & \text{when } \nu = 2 \\ \frac{1}{\pi} & \text{when } \nu = 3. \end{cases} \quad (2.12)$$

From eq. (2.11) the derivative of the kernel follows

$$\nabla W(r, h) = \frac{\sigma}{h^\nu} \begin{cases} 3x + \frac{9}{4}x^2 & \text{where } 0 \leq x < 1 \\ -\frac{3}{4}(2-x)^2 & \text{where } 1 \leq x \leq 2 \\ 0 & \text{where } x > 2. \end{cases} \quad (2.13)$$

This ensures that only neighbouring particles within  $2h$  contribute to a quantity. Assuming the smoothing length has been chosen correctly, only particles with significant contributions are used when performing any calculation. This dramatically reduces the cost in computing time.

#### 2.2.4 Smoothing length

The accuracy and speed of any SPH calculation is heavily dependent on the choice of the smoothing length. If  $h$  is too great the number of neighbours of the particles in high density regions is unnecessarily large and the calculation is computationally expensive. Conversely if the smoothing length is too small, particles in areas of low density may find themselves with no other particles within  $2h$ , causing the SPH calculation to break down. To resolve this, it is necessary to introduce variable smoothing lengths, specific to each particle. This approach would ensure areas of high density have high spatial resolutions while areas of low density are also accounted for. The errors introduced by allowing the smoothing length to vary are shown to be of the order of  $h^2$ , the same as those when making the initial SPH approximation (Hernquist & Katz 1989). The smoothing length is generally adjusted so that each particle has a given number of neighbours within  $2h$ . One caveat when varying the smoothing length, to ensure that momentum is conserved, it is necessary to ensure that the smoothing length used to calculate the force on particle  $i$  due to particle  $j$  is the same as that used to calculate the force on particle  $j$  due to particle  $i$ . This is achieved by using the average smoothing length of the two particles (Benz 1990).

$$h_{ij} = \frac{h_i + h_j}{2}. \quad (2.14)$$

## 2.3 Fluid Equations

### 2.3.1 Equations of fluid dynamics

Consider a fluid with density  $\rho$  and a velocity  $\mathbf{v}$ . The behaviour of the gas can be described by three conservation equations: mass, momentum and energy. The conservation of mass is described by the continuity equation

$$\frac{\partial \rho}{\partial t} + \nabla \cdot (\rho \mathbf{v}) = 0. \quad (2.15)$$

The  $\partial \rho / \partial t$  term describes the density changing with time and the  $\nabla \cdot (\rho \mathbf{v})$  term describes the flux of mass into a volume. For an incompressible flow eq. (2.15) reduces to  $\nabla \cdot \mathbf{v} = 0$ . The conservation of momentum is described by the Euler equation

$$\rho \frac{\partial \mathbf{v}}{\partial t} + \rho (\mathbf{v} \cdot \nabla) \mathbf{v} = -\nabla P + \mathbf{f}, \quad (2.16)$$

where  $\mathbf{f}$  represents external forces acting on the fluid and  $P$  is the pressure at a given point. In the vast majority of astrophysical problems  $P$  can be expressed using the perfect gas law, an equation of state relating the pressure, density and the temperature  $T$  of the fluid

$$P = \frac{\rho k T}{\mu m_H}, \quad (2.17)$$

$\mu$  is the mean molecular weight and  $m_H$  is the mass of hydrogen. Equation (2.16) is analogous to Newton's second law, i.e. forces on the fluid result in an acceleration. From the discussion in §1 viscosity is an important consideration for accretion discs. The Navier-Stokes equation describes a compressible fluid with a constant shear viscosity  $\nu$

$$\rho \frac{\partial \mathbf{v}}{\partial t} + \rho (\mathbf{v} \cdot \nabla) \mathbf{v} = -\nabla P + \mathbf{f} + \nu \nabla^2 \mathbf{v} + \frac{1}{3} \nu [\nabla (\nabla \cdot \mathbf{v})]. \quad (2.18)$$

Finally the conservation of energy is governed by

$$\frac{\partial}{\partial t} \left( \frac{1}{2} \rho v^2 + \rho \psi \right) + \nabla \cdot \left[ \left( \frac{1}{2} \rho v^2 + \rho \psi + P \right) \mathbf{v} \right] = \mathbf{f} \cdot \mathbf{v} - \nabla \cdot \mathbf{F}_{\text{rad}} - \nabla \cdot \mathbf{q}. \quad (2.19)$$

Here  $\psi$  is the internal energy per unit mass for the fluid. The quantity  $1/2 \rho v^2 + \rho \psi$  is the energy of a gas element and has two constituents: the kinetic energy per unit volume ( $1/2 \rho v^2$ ) and the internal energy per unit volume ( $\rho \psi$ ). On the right hand side of the equation there are several source/sink terms due to radiation ( $\nabla \cdot \mathbf{F}_{\text{rad}}$ ) and a conductive flux of heat ( $\nabla \cdot \mathbf{q}$ ). The above equations can completely describe a fluid in

an astrophysical system.

### 2.3.2 SPH equations in an accretion disc

I have introduced the equations of fluid dynamics and will now detail how they are implemented in SPH. Mass conservation is an inherent property of SPH so an explicit SPH expression for the continuity equation is unnecessary. To obtain an expression that governs how particles behave we start with the momentum conservation (eq. (2.16)), neglecting any external forces

$$\frac{\partial \mathbf{v}}{\partial t} + (\mathbf{v} \cdot \nabla) \mathbf{v} = -\frac{\nabla P}{\rho}. \quad (2.20)$$

Using the techniques in §2.2,

$$\int \left( \frac{\partial \mathbf{v}}{\partial t} + (\mathbf{v} \cdot \nabla) \mathbf{v} \right) W(|\mathbf{r} - \mathbf{r}'|, h) d\mathbf{r}' = - \int \frac{\nabla P}{\rho} W(|\mathbf{r} - \mathbf{r}'|, h) d\mathbf{r}' \quad (2.21)$$

and proceeding in a way identical to (Benz 1990) we achieve an expression for momentum conservation suitable for implementation in SPH,

$$\frac{d\mathbf{v}_i}{dt} = - \sum_{j=1}^N m_j \left( \frac{P_i}{\rho_i^2} + \frac{P_j}{\rho_j^2} \right) \nabla_i W(|\mathbf{r} - \mathbf{r}'|, h), \quad (2.22)$$

where  $\nabla_i$  denotes the gradient with respect to the coordinates of particle  $i$ . Similarly

$$\frac{d\psi_i}{dt} = \frac{P_i}{\rho_i^2} \sum_{j=1}^N m_j \mathbf{v}_{ij} \cdot \nabla_i W(|\mathbf{r} - \mathbf{r}'|, h) \quad (2.23)$$

is the SPH energy conservation equation (Benz 1990).

### 2.3.3 Artificial Viscosity

Equation (2.22) is only valid for a inviscid fluid. In a real fluid the viscosity allows the conversion of kinetic energy into heat. This is especially important in the treatment of shocks, which is where viscosity is most significant in astrophysical problems. In SPH an artificial viscosity is introduced to attempt to model for this

$$\frac{d\mathbf{v}_i}{dt} = - \sum_{j=1}^N m_j \left( \frac{P_i}{\rho_i^2} + \frac{P_j}{\rho_j^2} + \Pi_{ij} \right) \nabla_i W(|\mathbf{r} - \mathbf{r}'|, h). \quad (2.24)$$

The total energy is not conserved by eq. (2.23) when artificial viscosity is included. Another term must be included that accounts for the heating of the fluid due to shocks,

$$\frac{d\psi_i}{dt} = \frac{P_i}{\rho_i^2} \sum_{j=1}^N m_j \mathbf{v}_{ij} \cdot \nabla_i W(|\mathbf{r} - \mathbf{r}'|, h) + \frac{1}{2} \sum_{j=1}^N m_j \Pi_{ij} \mathbf{v}_{ij} \cdot \nabla_i W(|\mathbf{r} - \mathbf{r}'|, h). \quad (2.25)$$

Several forms of  $\Pi_{ij}$  have been tried with the most widely used being

$$\Pi_{ij} = \begin{cases} -\frac{\alpha c_{ij} \mu_{ij} + \beta \mu_{ij}^2}{\rho_{ij}} & \text{where } \mathbf{v}_{ij} \cdot \mathbf{r}_{ij} < 0 \\ 0 & \text{where } \mathbf{v}_{ij} \cdot \mathbf{r}_{ij} > 0, \end{cases} \quad (2.26)$$

where

$$\mu_{ij} = \frac{h \mathbf{v}_{ij} \cdot \mathbf{r}_{ij}}{\mathbf{r}_{ij}^2 + \eta}, \quad (2.27)$$

and  $c_{ij}$  and  $\rho_{ij}$  are the average sound speed and density of two particles. The numerical factor  $\eta$  prevents  $\mu_{ij}$  becoming singular when  $\mathbf{r}_{ij} \rightarrow 0$  and is set to  $\eta = 0.01h^2$ . The quantities  $\alpha^1$  and  $\beta$  are free parameters that control the strength of the viscosity. The  $\alpha$  term primarily deals with the bulk viscosity of the fluid, while the second order  $\beta$  term becomes significant in shocks. From eq. (2.26),  $\Pi_{ij} \neq 0$  only when  $\mathbf{v}_{ij} \cdot \mathbf{r}_{ij} < 0$ , i.e. the viscous force only acts when two particles are approaching one another. This formalism is used when  $\Pi_{ij}$  was only necessary in the treatment of shocks. In this work we are interested in the shear viscosity so receding and approaching particles do interact. Therefore eq. (2.26) is changed to,

$$\Pi_{ij} = \begin{cases} -\frac{\alpha c_{ij} \mu_{ij} + \beta \mu_{ij}^2}{\rho_{ij}} & \text{where } \mathbf{v}_{ij} \cdot \mathbf{r}_{ij} < 0 \\ -\frac{\alpha c_{ij} \mu_{ij}}{\rho_{ij}} & \text{where } \mathbf{v}_{ij} \cdot \mathbf{r}_{ij} > 0. \end{cases} \quad (2.28)$$

---

<sup>1</sup>N.B. This is not equivalent to the  $\alpha$  described in §1.2.3. The link between the artificial viscosity  $\alpha$  and the Shakura-Sunyaev  $\alpha$  is discussed in §2.7

## 2.4 Nearest Neighbours

With the introduction of a kernel of the form of eq. (2.11) we only consider particles within  $2h$  of any particle  $i$ . These particles are known as the nearest neighbours of particle  $i$ . There are many ways to find the nearest neighbours of a given particle,

1. Neighbour table
2. Monotonic logical Grid
3. A Tree
4. Link list

I will present the basics of the first three methods and give an example of the link list used by the code.

### 2.4.1 Neighbour table

For every particle  $i$ , all the labels of neighbouring particles within  $2h$  are stored in an array. If we have  $N$  particles and every particle has  $N_n$  nearest neighbours, then an array of dimension  $N \times N_n$  is needed. This array has to be updated after every time step in the simulation, unless the particles' positions are not changing significantly with time. If  $N$  and  $N_n$  are large the resulting size of the array may be problematic.

### 2.4.2 Monotonic logical Grid

Similar to the neighbour table, this method relies on storing information about the particles neighbours in an array. All of the properties of the particles are stored in an array, the order they are stored in the array relates to their physical position in the simulation. Therefore finding the nearest neighbours is simply a matter of searching through the array.

### 2.4.3 Hierarchical Tree

This approach is mainly used in problems that require self gravity. Indeed the information used to calculate the self gravity in a fluid is the same as that required for the nearest

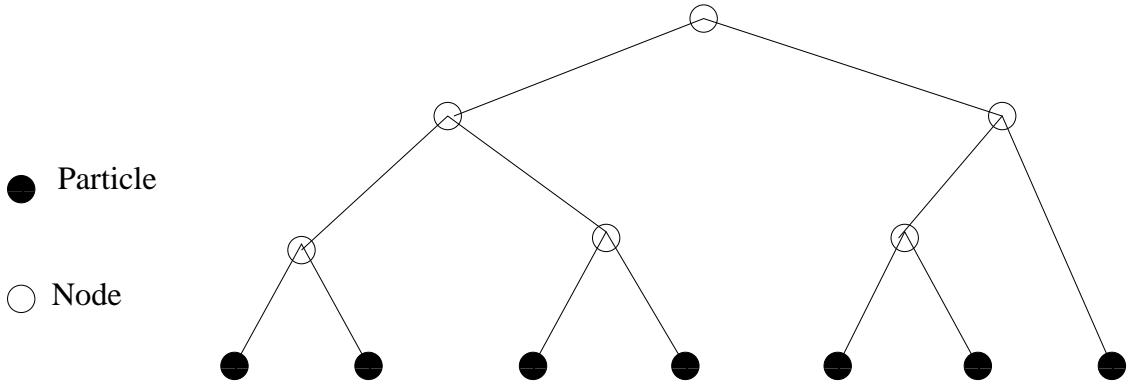


FIGURE 2.1. A simple example of a hierarchical tree, note the number of particles  $N = 7$  and the number of nodes  $2N - 1 = 13$ .

neighbours. In a tree, particles are grouped together in nodes, these nodes then interact with one another. Once a node has been formed, its position is defined as the centre of mass of all the internal nodes/particles contained within it. The number of nodes depends on the number of particles,  $2N - 1$ , see fig. 2.1.

A node is considered to be an effective “particle” in its own right. This is only accurate when considering particles some distance from the node. When considering a node particle interaction it may be necessary to open up the node to reveal its constituent parts, (see fig. 2.2). When

$$\frac{R_n}{R_{pn}} < \theta_{crit}, \quad (2.29)$$

the node is opened up and the particles interaction is considered with all the nodes constituents. Trees effectively cut down the computing time needed when considering particle particle interactions from  $\mathcal{O}N^2$  to  $\mathcal{O}N\log N$ . When  $\theta_{crit} \rightarrow 0$  all nodes are open and the calculation returns to  $\mathcal{O}N^2$ .

#### 2.4.4 Link list

When using this method a grid is overlaid on the computational domain. The particles are assigned to a cell and a list is constructed with the labels of every particle in that cell. Finding the nearest neighbours then consists of searching through neighbouring cells for particles. The link list consists of two arrays one which records the label of the last particle in that cell, if there are  $n_{cell}$  cells, this array needs to be of length  $n_{cell}$ . The second array is of length  $N$  and records the label of the previous particle in that cell. A combination of these two arrays records what cell every particle is in. This method

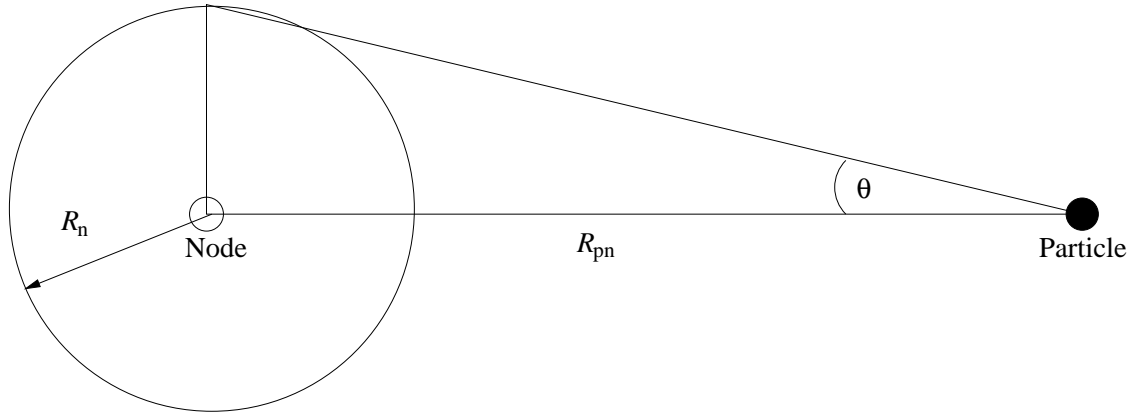


FIGURE 2.2. Diagram showing node opening angle,  $R_{pn}$  is the distance between the node and particle and  $R_n$  is the radius of the node.

is very memory efficient when compared to a Neighbour Table, however setting up and accessing the link list are recursive operations.

### 2.4.5 Link list example

Figure (2.3) shows a simplified 2D example with 8 particles. Firstly we want to know the extent of the computational domain. The particles 1, 3, 5 and 8 define the maximum extent of the domain in the  $x, y$  plain,

$$\begin{aligned} x_{\text{side}} &= x_{\text{max}} - x_{\text{min}} \\ y_{\text{side}} &= y_{\text{max}} - y_{\text{min}}. \end{aligned} \quad (2.30)$$

The lengths  $x_{\text{side}}$  and  $y_{\text{side}}$  are divided by  $2h_{\text{max}}$ , where  $h_{\text{max}}$  is the maximum smoothing length allowed for a particle. This gives the size of the computational domain in terms of the maximum smoothing length,

$$\begin{aligned} l_x &= x_{\text{side}}/2h_{\text{max}} = 4 \\ l_y &= y_{\text{side}}/2h_{\text{max}} = 3 \\ l_{xy} &= l_x l_y = 12. \end{aligned} \quad (2.31)$$

The resulting grid is “unpacked” into a 1D array using the relation,

$$l_{\text{cell}} = l_{\text{xcell}} + (l_{\text{ycell}} - 1)l_x + (l_{\text{zcell}} - 1)l_{xy}, \quad (2.32)$$

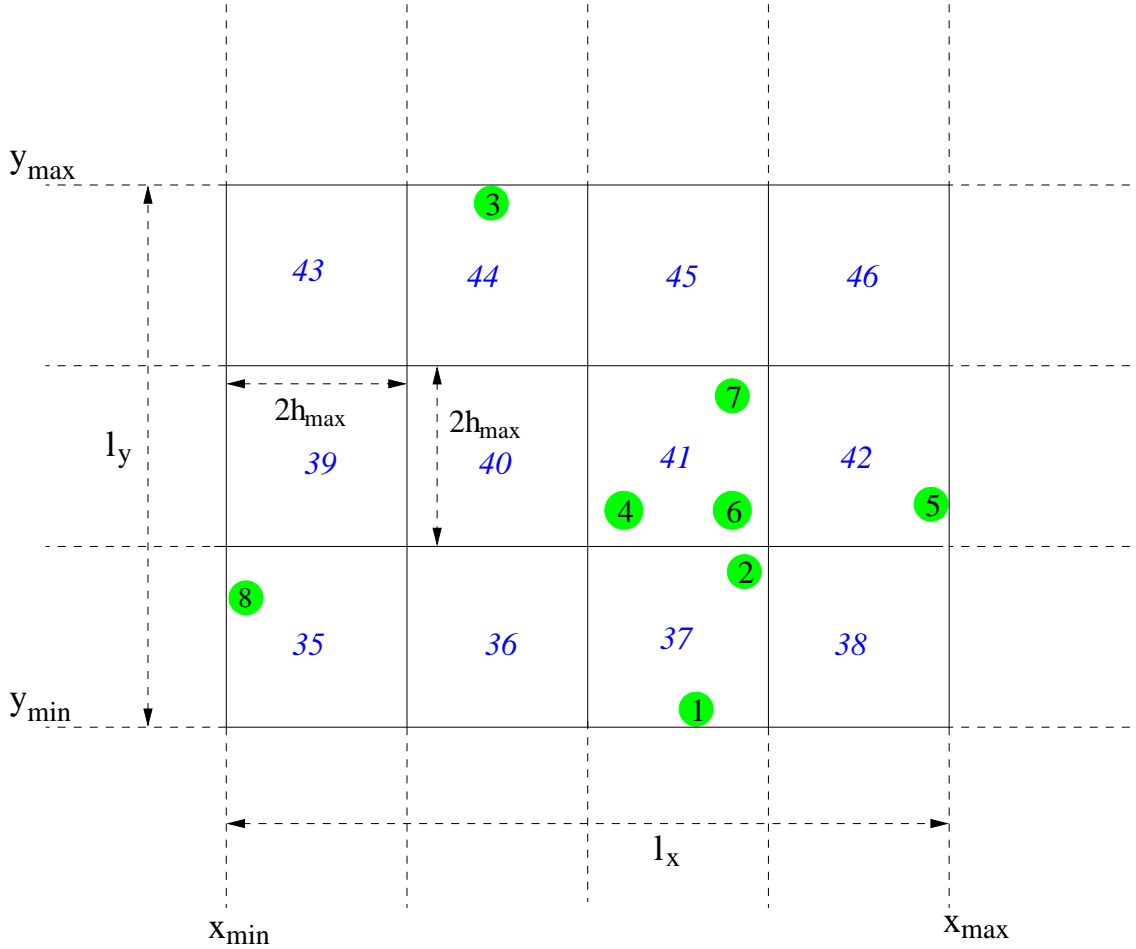


FIGURE 2.3. Simplified 2D computational domain with 8 particles. A grid has been overlaid as described in section (2.4.4).

where

$$\begin{aligned}
 l_{x\text{cell}} &= \mathbb{N}\{(x(i) - x_{\min})/2h_{\max}\} + 3 \\
 l_{y\text{cell}} &= \mathbb{N}\{(y(i) - y_{\min})/2h_{\max}\} + 3 \\
 l_{z\text{cell}} &= \mathbb{N}\{(z(i) - z_{\min})/2h_{\max}\} + 3.
 \end{aligned} \tag{2.33}$$

The values  $x(i)$ ,  $y(i)$  and  $z(i)$  refer to the  $x$ ,  $y$  and  $z$  coordinates of the  $i$ 'th particle. Equations (2.33) locates which grid square each particle  $i$  is located. The + 3 accounts for the fact that the initial two values of  $l_{x\text{cell}}$  and  $l_{y\text{cell}}$  denote cells which are never occupied. The link list itself is simple to construct, using two arrays,  $ll$ , and  $ihoc$ . The code to implement the link list is relatively simple and is shown below.

```

do i = 1, n
  ll(i) = ihoc(lcell)
  ihoc(lcell) = i
end do
    
```

We proceed as follows:

1. first loop  $i = 1$

$$\left. \begin{array}{l} l_{xcell} = 5 \\ l_{ycell} = 3 \\ l_{zcell} = 3 \end{array} \right\} \Rightarrow l_{cell} = 37$$

Particle 1 is in cell number 37. We now update the link list

ll =	1	2	3	4	5	6	7	8				
	0	0	0	0	0	0	0	0				
ihoc =	35	36	37	38	39	40	41	42	43	44	45	46
	0	0	1	0	0	0	0	0	0	0	0	0

FIGURE 2.4. Link list after particle 1

2. Second loop  $i = 2$

$$\left. \begin{array}{l} l_{xcell} = 5 \\ l_{ycell} = 3 \\ l_{zcell} = 3 \end{array} \right\} \Rightarrow l_{cell} = 37$$

Particle 2 is in cell number 37, the same as particle 1, again we update the link list

ll =	1	2	3	4	5	6	7	8				
	0	1	0	0	0	0	0	0				
ihoc =	35	36	37	38	39	40	41	42	43	44	45	46
	0	0	2	0	0	0	0	0	0	0	0	0

FIGURE 2.5. Link list after particle 2

3. Third loop  $i = 3$

$$\left. \begin{array}{l} l_{xcell} = 4 \\ l_{ycell} = 5 \\ l_{zcell} = 3 \end{array} \right\} \Rightarrow l_{cell} = 44$$

Particle 3 is in cell number 44, we now update the link list

4. Fourth loop  $i = 4$

$$\left. \begin{array}{l} l_{xcell} = 5 \\ l_{ycell} = 4 \\ l_{zcell} = 3 \end{array} \right\} \Rightarrow l_{cell} = 41$$

Particle 4 is in cell number 41, we now update the link list

ll =	1	2	3	4	5	6	7	8				
	0	1	0	0	0	0	0	0				
ihoc =	35	36	37	38	39	40	41	42	43	44	45	46
	0	0	2	0	0	0	0	0	0	3	0	0

FIGURE 2.6. Link list after particle 3

ll =	1	2	3	4	5	6	7	8				
	0	1	0	0	0	0	0	0				
ihoc =	35	36	37	38	39	40	41	42	43	44	45	46
	0	0	2	0	0	0	4	0	0	3	0	0

FIGURE 2.7. Link list after particle 4

5. Fifth loop  $i = 5$

$$\left. \begin{aligned} l_{xcell} &= 6 \\ l_{ycell} &= 4 \\ l_{zcell} &= 3 \end{aligned} \right\} \Rightarrow l_{cell} = 42$$

Particle 5 is in cell number 42, we now update the link list

ll =	1	2	3	4	5	6	7	8				
	0	1	0	0	0	0	0	0				
ihoc =	35	36	37	38	39	40	41	42	43	44	45	46
	0	0	2	0	0	0	4	5	0	3	0	0

FIGURE 2.8. Link list after particle 5

6. Sixth loop  $i = 6$

$$\left. \begin{aligned} l_{xcell} &= 5 \\ l_{ycell} &= 4 \\ l_{zcell} &= 3 \end{aligned} \right\} \Rightarrow l_{cell} = 41$$

Particle 6 is in cell number 41, the same as particle 4, we now update the link list

ll =	1	2	3	4	5	6	7	8				
	0	1	0	0	0	4	0	0				
ihoc =	35	36	37	38	39	40	41	42	43	44	45	46
	0	0	2	0	0	0	6	5	0	3	0	0

FIGURE 2.9. Link list after particle 6

7. Seventh loop  $i = 7$

$$\left. \begin{aligned} l_{x\text{cell}} &= 5 \\ l_{y\text{cell}} &= 4 \\ l_{z\text{cell}} &= 3 \end{aligned} \right\} \Rightarrow l_{\text{cell}} = 41$$

Particle 7 is in cell number 42, the same as particle 6 and particle 4, we now update the link list

$ll =$	1	2	3	4	5	6	7	8						
	0	1	0	0	0	4	6	0						
$ihoc =$	35	36	37	38	39	40	41	42	43	44	45	46		
	0	0	2	0	0	0	7	5	0	3	0	0		

FIGURE 2.10. Link list after particle 7

8. Eighth loop  $i = 8$

$$\left. \begin{aligned} l_{x\text{cell}} &= 3 \\ l_{y\text{cell}} &= 3 \\ l_{z\text{cell}} &= 3 \end{aligned} \right\} \Rightarrow l_{\text{cell}} = 35$$

Particle 8 is in cell number 35, we now update the link list

$ll =$	1	2	3	4	5	6	7	8						
	0	1	0	0	0	4	6	0						
$ihoc =$	35	36	37	38	39	40	41	42	43	44	45	46		
	8	0	2	0	0	0	7	5	0	3	0	0		

FIGURE 2.11. Link list after particle 8

To calculate the nearest neighbours of, for example, particle 6 is as follows. Firstly we look at the cell at which particle 6 is in, looking at element 41 in the array  $ihoc$  we see the last particle that was known to be in the cell was particle 7. Now look at the seventh element in the array  $ll$ , we see the particle 6 was in the cell previously. Look at the sixth element of  $ll$  we can see that previously to particle 6, particle 4 was in the cell. Finally looking at the fourth element of  $ll$ , which is zero, we see that particle 4 was the first particle in the cell. We now know that particles 7, 6 and 4 are in the cell labelled 41.

Now we examine the neighbouring cells, in this simplified example there are 8 cells surrounding the home cell of particle 6. In 3D this increases to 26 neighbouring cells. The neighbouring cells are: 36, 37, 38, 40, 42, 44, 45 and 46. Looking in the array  $ihoc$  we can see that elements 36, 38, 40, 45 and 46 are equal to zero; meaning that these cells

currently have no particles in. Looking at the cells 42 and 44, we see in *ihoc* that particles 5 and 3 are in these cells respectively. Looking at array *ll* we see that these particles are the only ones in these cells. The remaining cell is 37, proceeding in a manner similar to cell 41 we know that particles 1 and 2 are in this cell. Hence, the nearest neighbours of particle 6 which are particles 1, 2, 3, 4, 5 and 7.

## 2.5 Time stepping

The accretion discs that have been described thus far evolve due to two forces: viscous forces that have the effect of viscously spreading the disc and pressure forces. As seen in §1.2.4 the viscous forces act to spread the disc on a time scale given by eq. (1.34). The dynamics of the disc are also influenced by gravity. For a typical time scale due to the force of gravity, consider a test partial  $m$  in a Keplerian orbit about a central object  $M$  ( $M \gg m$ ) at a distance of  $R$ . Using eq. (1.35) the orbital period at a point  $R$  is

$$P_{\text{orb}} \sim 2\pi \left( \frac{R^3}{GM} \right)^{1/2}. \quad (2.34)$$

This can be the basis for a dynamical gravitation time  $t_{\text{grav}}$ . Typically the dynamical time scale is much shorter than the viscous/pressure time scales and an accretion disc can vary in radial extent by several orders of magnitude resulting in a large range of dynamical times. This difference in  $t_{\text{grav}}$  creates problems when considering the length of the time step in a simulation. The vast majority of the mass in the disc (and therefore most of the particles) will be located in the outer disc. Here the orbital velocities are low. If a global time step was chosen appropriate for the few particles in the inner disc which need their positions and velocities to be updated frequently, the positions of particles in the outer disc would be updated needlessly.

To avoid such inefficient use of computing resources the SPH code uses a method called operator splitting. An important part of this method is using the fact that the gravity calculation<sup>2</sup> is relatively simple (only a few lines of code are needed). Far more computational time is needed to calculate the nearest neighbours, density and viscosity. From the discussion above, the dynamical time scale is much shorter than the viscous time scale. This suggests it is possible to reduce the frequency with which the pressure and viscosity forces are calculated but still calculate the gravity as required. This is the origin of the name operator splitting. On each particle there are two accelerations acting

---

<sup>2</sup>In the standard thin disc approximation the self gravity of the disc is ignored. Particles in all the simulations presented here have no particle-particle gravitational interaction.

on it. One is the acceleration due to the pressure/viscous forces  $\mathbf{a}_p$  and the other is the acceleration due to gravity  $\mathbf{a}_{\text{grav}}$ ,

$$\frac{d\mathbf{v}}{dt} = \mathbf{a}_p + \mathbf{a}_{\text{grav}} \quad (2.35)$$

The quantity  $\mathbf{a}_{\text{grav}}$  is easy to calculate whereas  $\mathbf{a}_p$  is more involved. Operator splitting ensures that calculation of  $\mathbf{a}_p$  is minimised. The scheme used by Murray in his SPH code is a drift-kick-drift scheme. Firstly the velocity of the particles are integrated over a half pressure force time step,  $\Delta t_p$ ,

$$\frac{\mathbf{v}_{l+\frac{1}{2}} - \mathbf{v}_l}{\frac{1}{2}\Delta t_p} = \mathbf{a}_p(r_l, v_l), \quad (2.36)$$

where the initial time is  $t_l$ . The positions of the particles are not updated at this stage. Now a full pressure time step is taken to update the positions and velocities using only the gravity force. During this stage the code goes through many dynamical time steps. The initial velocity at  $k = 0$  is equal to  $\mathbf{v}_{l+\frac{1}{2}}$ .

$$\frac{\mathbf{r}_{k+1} - \mathbf{r}_k}{\Delta t_{\text{grav}}} = \mathbf{v}_{k+1} \quad (2.37)$$

$$\frac{\mathbf{v}_{k+1} - \mathbf{v}_k}{\Delta t_{\text{grav}}} = \mathbf{a}_{\text{grav}}(r_k, v_k). \quad (2.38)$$

Due to  $\Delta t_{\text{grav}} \ll \Delta t_p$  the code goes through several iterations of  $k$  for each  $l$ . After  $n_k$  gravity time steps the code has advanced one pressure time step, where  $n$  is an integer. Finally a second half pressure time step using only the pressure forces is calculated using the positions and velocities from the last gravity time step.

$$\frac{\mathbf{v}_{l+1+\frac{1}{2}} - \mathbf{v}_{nk}}{\frac{1}{2}\Delta t_p} = \mathbf{a}_p(r_{nk}, v_{nk}). \quad (2.39)$$

While the operator splitting can be performed in two stages, one for the pressure forces and one for the gravity force, this approach with three stages is used. This three step approach conserves physical quantities more accurately over long integrations. The pressure calculations are performed using a simple leapfrog integrator. This calculates positions and velocities alternately, resulting in them “leaping” over each other. The gravity calculations are performed with a fourth order Runge-Kutta integration scheme. This is accurate to  $\mathcal{O}dt^4$ , which is more than adequate. A scheme with greater accuracy (Press et al. 1992), but a corresponding increasing in the use of computing resources

is unnecessary. The limiting factor is the use of the kernel (see §2.2.1) in the pressure calculation, which is only accurate to  $\mathcal{O}h^2$ .

### 2.5.1 Courant-Friedrichs-Lewy condition

The Courant-Friedrichs-Lewy (CFL) condition is to ensure the time step of a simulation is less than a certain time to prevent unphysical effects. For example, if a particle is moving a characteristic length  $L$ , then the time step  $dt$  must be less than the time required for the particle to move a distance equal to  $L$ . When  $L$  is reduced, the upper limit for the time step is correspondingly decreased. Simply put the CFL condition is a characteristic length scale of a simulation divided by a characteristic velocity,

$$dt < \frac{L}{v_p}, \quad (2.40)$$

where the particle has a speed  $v_p$ . In Murray’s SPH code, the CFL condition for the viscosity time control takes the form

$$dt = \frac{h}{c_s + 0.6(2\alpha c_s + \beta\mu_{ij})}, \quad (2.41)$$

$\alpha$  and  $\beta$  are the artificial viscosity parameters,  $c_s$  is the sound speed,  $h$  is the smoothing length and  $\mu_{ij}$  is given by eq. (2.27).

## 2.6 SPH code overview

In previous sections I have gone into some detail about SPH in general and specifically how the code by Murray works. I will now give an overview of the code to show how all the constituent “parts” fit together.

- Select the system parameters. All masses are scaled to the system mass and all lengths are scaled to the binary separation,  $a$ . The code is also scaled so that the orbital angular frequency is equal to one,  $2\pi/P_{\text{orb}} = 1$ . This results in a velocity unit of  $2\pi a/P_{\text{orb}}$ .
- All particles are initially set to the cold (less viscous) state.
- A particle is injected from the  $L_1$  point.

- The positions of the primary and secondary stars are located and changed as needed.
- The link list is built.
- Solve the momentum and thermal energy equation for each particle using all neighbouring particles within  $2h$ . Neighbours are located via the link list.
- The velocity of all the particles is advanced a half pressure time step using only the pressure forces.
- The gravity force is now used to update both positions and velocities forwards one pressure time step.
- A new link list is built to sort the new positions of the particles.
- The density at each particle is calculated using all particles within  $2h$ . If conditions are satisfied then the particles have their viscosities switched into the hot state. For more detail on how this is achieved see §4.
- Again the velocities of all the particles are advanced a half pressure time step using only the pressure forces.
- Any particles that are within  $0.04a$  of the primary are considered to be accreted and are removed from the system. If any return to the secondary's Roche lobe or if they are at a distance  $r > a$  with a velocity greater than the escape velocity they are also removed.
- Particles that are considered to be accreted provide a mass transfer rate onto the primary. This is used to calculate an irradiation radius, which also switches particles contained within into the hot state. Further details are in §4.
- Finally a new link list is created and particles are located.
- Another particle is injected from the  $L_1$  point and the process repeats itself.

## 2.7 Viscous Particle ring

In §2.3.3 the concept of artificial viscosity was introduced. In order to compare the artificial viscosity  $\alpha$  to the Shakura-Sunyaev  $\alpha_{ss}$ <sup>3</sup>, I look at the problem of a ring of matter which spreads due to viscous forces. This problem has a relatively simple analytic

---

<sup>3</sup>The Shakura-Sunyaev  $\alpha$  has been renamed to  $\alpha_{ss}$  in this section to prevent confusion

solution and can be compared to results from the SPH code, see §1.2.4. As introduced in §1.2.3 the  $\alpha$ -prescription (Shakura & Sunyaev 1973) is as follows,

$$\nu = \alpha_{ss} c_s H \quad (2.42)$$

Using eq. (1.33) it is possible to equate the artificial viscosity introduced in section (2.3.3) to  $\alpha_{ss}$ . Figure (2.12) shows a simulation of 20000 particles placed in a thin ring of width 1/40 of the initial smoothing length of the particles. The ring spreading can be clearly seen. During the simulation the  $\beta$  term in the artificial viscosity was set to zero, as there are no shocks in this problem, only the viscous torque exerted on the inner ring by the outer ring. The surface density of the ring simulation was compared to theoretically derived curves using eq. (1.33) with sound speed of  $7.8 \times 10^5 \text{ cm s}^{-1}$  and a disc scale height given by,

$$H = \frac{c_s}{\Omega}. \quad (2.43)$$

Figure 2.13 shows the results of the comparisons for four different values of  $\alpha_{ss}$  after eight equally spaced time intervals, between 2250 and 7500 time steps. As can be seen from fig. 2.13, none of the values of  $\alpha_{ss}$  exactly fit the curve generated by the SPH code. To quantitatively state which value of  $\alpha_{ss}$  best fits the SPH code result, a  $\chi^2$  test was performed, (see fig. 2.7. This determined that an SPH  $\alpha = 1.0$  was best described by an  $\alpha_{ss} \sim 0.9$ , i.e. there is almost a one to one relation between the two  $\alpha$ s.

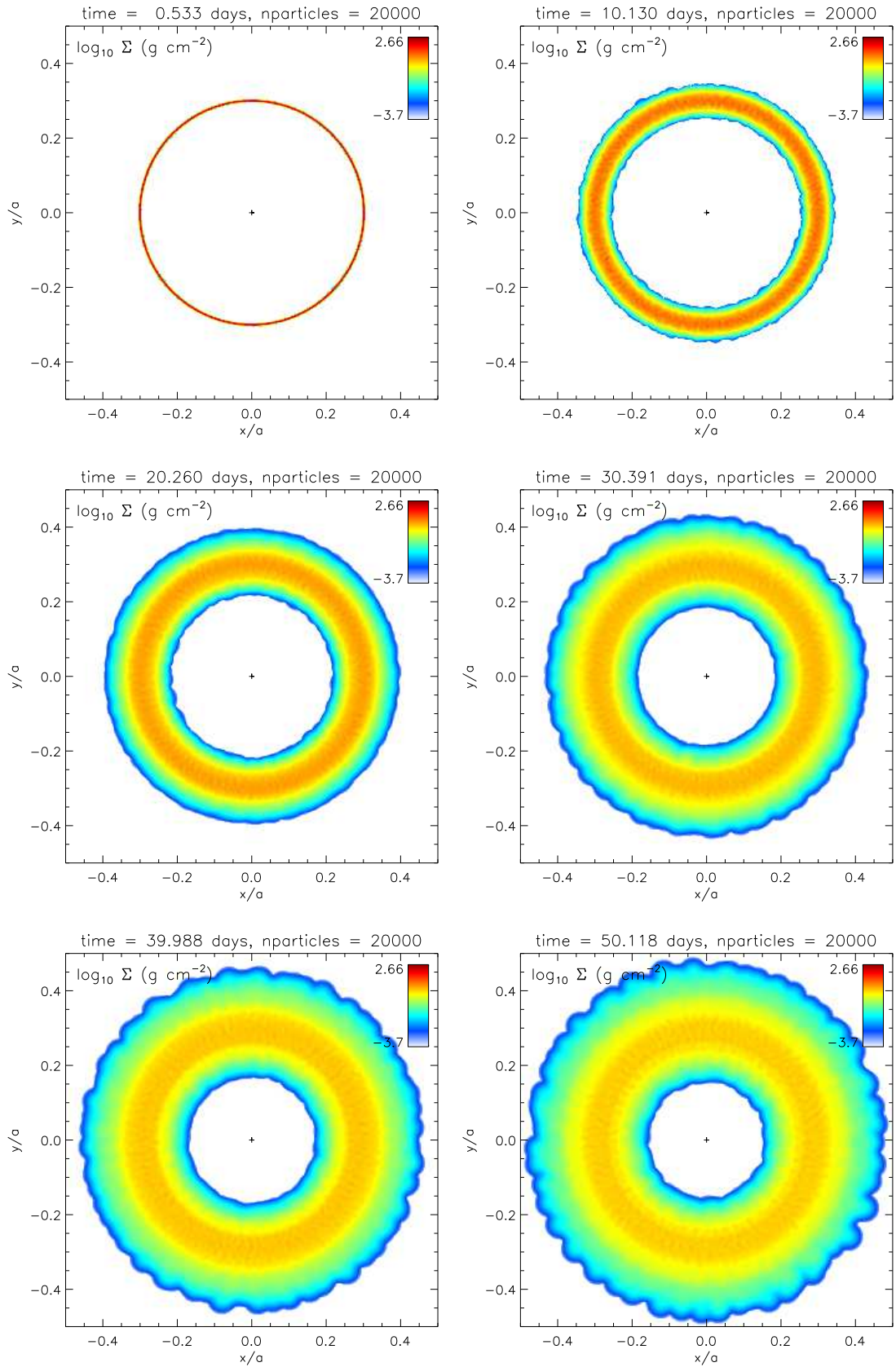


FIGURE 2.12. Snapshots of the evolution of a ring of matter in a Keplerian orbit about a central mass, the ring was at an initial radius of  $0.3a$

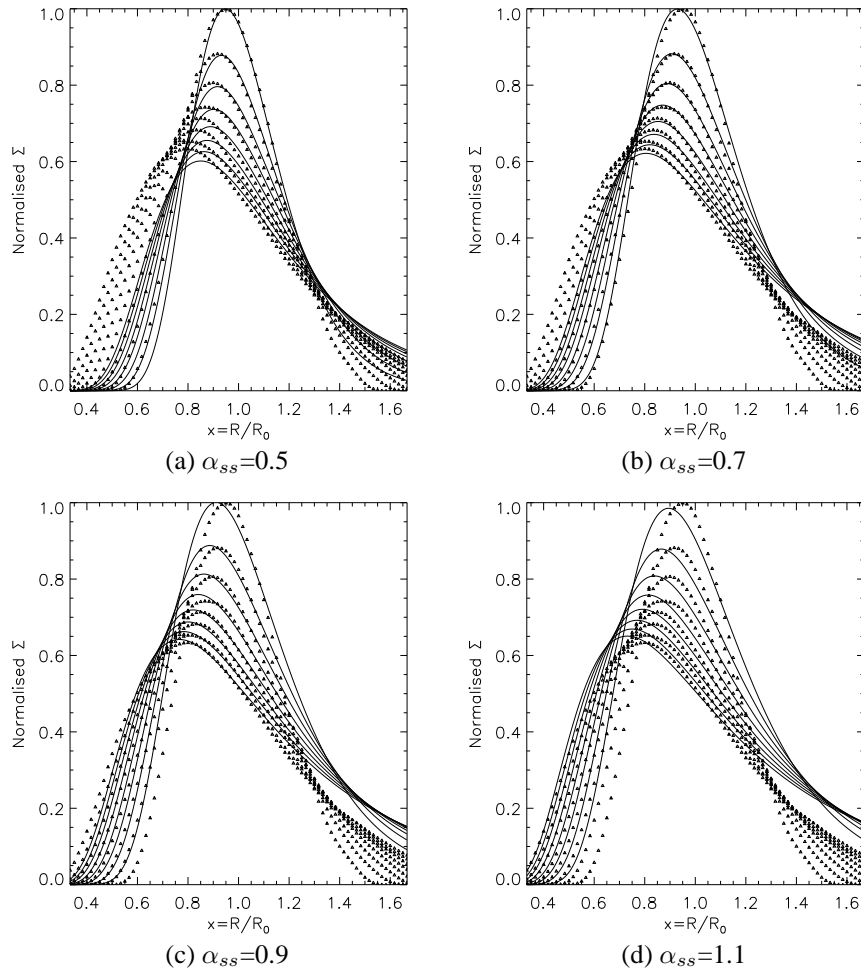


FIGURE 2.13.  $\alpha = 1.0$  disk evolution ( $\Delta$ ) plotted at 2250 to 7500 time steps compared to a normalised theoretical derived density curve (solid lines).

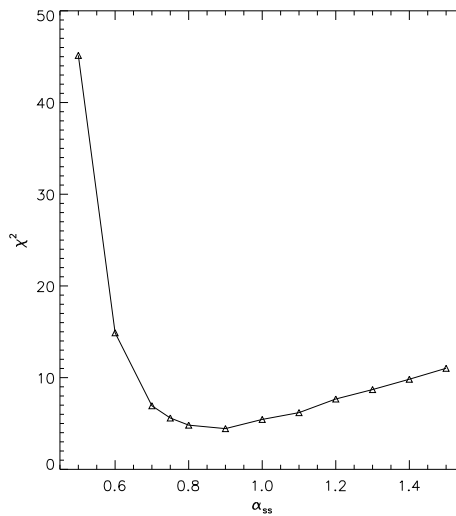
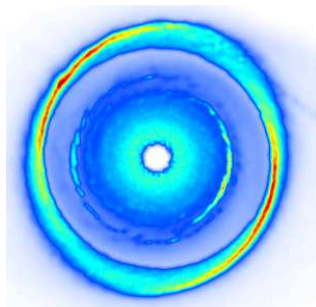


FIGURE 2.14.  $\chi^2$  test comparing a SPH  $\alpha$  to various values of Shakura-Sunyaev  $\alpha_{ss}$ .

# Chapter 3

*Constraining the number of compact remnants near Sgr A\**



“You cannot lose if you do not play.”  
- Marla Daniels

*The Wire: The Detail [1.02]*

### 3.1 Introduction

Theoretical calculations predict a cusp of  $\sim 20000$  stellar mass black holes in the central parsec of our Galaxy (Morris 1993, Miralda-Escudé & Gould 2000) and a similar number of neutron stars (Freitag, Amaro-Seoane & Kalogera 2006, Hopman & Alexander 2006). X-ray observations reveal a highly significant overabundance of transients in the same region (Muno et al. 2005*b*) when compared with the region of  $\sim$  several tens of parsecs from Sgr A\*, the super-massive black hole (SMBH) of mass  $M_{\text{smbh}} \sim 4 \times 10^6 M_{\odot}$  in the Galactic Centre (GC) (Schödel et al. 2002, Ghez et al. 2003). Several methods to constrain the population of these remnants are discussed in the literature. In particular, one might look for dynamical signatures of these remnants on the orbits of stars near Sgr A\* (Rubilar & Eckart 2001, Mouawad et al. 2005, Alexander & Livio 2004) and by gravitational lensing (Chanamé, Gould & Miralda-Escudé 2001, Alexander & Loeb 2001). Also young neutron stars might be detectable as pulsars (Chanamé & Gould 2002, Pfahl & Loeb 2004). Each of these methods come with its own set of observational difficulties and limitations.

Nayakshin & Sunyaev (2007) proposed an alternative method to detect the compact remnant’s cusp. They suggested that these compact remnants may be accreting gas at relatively high rates when they happen to travel through a dense ionised gas observed to exist in the GC (Morris 1993). They calculated a simple time-averaged model for X-ray emission from such a cusp, and concluded that the total emission of the cusp could be as high as  $\gtrsim 10^{35}$  erg s $^{-1}$ , i.e. very significant observationally.

On the other hand, a time-independent treatment does not take into account the complexity of the problem. Despite the high total number of black holes, due to a small volume filling fraction of cold gas in the GC, only a few of the black holes will be moving within the gas clouds and possess a small enough relative velocity to be visible to *Chandra*<sup>1</sup>. Here I extend the model of (Nayakshin & Sunyaev 2007) in several ways. Firstly, I allow time-dependency in the problem by explicitly following realistic Keplerian orbits of the compact objects. Secondly, the formation and evolution of small scale accretion discs around the accretors is modelled, as such discs will form due to the excess angular momentum of the accreting gas. An attempt is made to model (in a rather basic manner) the observed distribution of ionised gas from which the compact objects might be accreting, “the Minispiral” (see §1.4). Non-circular gas orbits are also considered with a simplified approach.

---

<sup>1</sup>*Chandra* is a X-ray Observation satellite launched in 1999. It was a great improvement over previous X-ray telescopes with an angular resolution of 0.5 arcsecond, several orders of magnitude greater than the first orbiting X-ray telescopes. *Chandra* operates in the 0.1 - 10 keV band.

The model shows a large intrinsic time-dependence of the accretion on the compact objects and the X-ray emission it produces. Despite that, and despite uncertainties in the model (exact gas orbits, circularisation radius parameter, radiative efficiency, etc.), certain conclusions can be drawn. In particular, with the  $\sim 20000$  compact remnants expected in the central parsec, at least several X-ray sources with X-ray luminosity greater than  $10^{33}$  erg s $^{-1}$  should be present. Such sources, which could be called “fake X-ray binaries”, can potentially contribute to the sources observed by (Muno et al. 2005b) in the central parsec. Conversely, it appears that a cusp significantly more populous, i.e., with 40000 compact remnants, would over-produce the X-ray emission as compared to the observations, and should thus be ruled out.

## 3.2 Numerical approach

A stellar mass black hole of mass  $M_{\text{bh}}$  travelling through a gas cloud or a disc with density  $\rho$  is capturing gas in a *small scale disc about it* (see below) at the Bondi-Hoyle accretion rate (Bondi & Hoyle 1944):

$$\dot{M}_{\text{capt}} = 4\pi\rho \frac{(G M_{\text{bh}})^2}{(\Delta v^2 + c_s^2)^{3/2}}, \quad (3.1)$$

introduced in §1.2 where  $c_s$  and  $\Delta v$  are the gas sound speed and the relative velocity between the black hole and the gas, respectively. The above picture is complicated by the presence of the SMBH. The area of influence of the stellar mass black holes is limited by the Hill radius. The Hill radius is a measure of the extent of a body’s gravitational influence on its surroundings. For an order of magnitude estimate, equate the orbital velocity around the black hole  $\Omega_{\text{bh}}$  to the orbital velocity of the black hole around the SMBH  $\Omega_{\text{smbh}}$ . This gives the radius at which the gravitational influence of the black hole and the SMBH are equal, using eq. (1.15),

$$\sqrt{\frac{GM_{\text{bh}}}{r_{\text{H}}^3}} = \sqrt{\frac{GM_{\text{smbh}}}{R^3}}, \quad (3.2)$$

hence

$$r_{\text{H}} = R \left( \frac{M_{\text{bh}}}{M_{\text{smbh}}} \right)^{1/3} \quad (3.3)$$

where  $R$  is the distance between the stellar mass black hole and the SMBH. A rigorous derivation gives Hill’s radius to be,  $r_{\text{H}} = R(M_{\text{bh}}/3M_{\text{smbh}})^{1/3}$  (Hamilton & Burns 1991). This imposes a limit on the capture rate, given by the Hill accretion rate,  $\dot{M}_{\text{H}} = 4\pi r_{\text{H}}^2 \rho c_s$ .

Hence,

$$\dot{M}_{\text{capt}} = \min[\dot{M}_{\text{capt}}, \dot{M}_{\text{H}}] \quad (3.4)$$

where  $\dot{M}_{\text{capt}}$  on the right hand side of the equation is defined in eq. (3.1).

### 3.2.1 Time-dependent disc accretion

The captured gas may have a net angular momentum resulting in the formation of a disc around the stellar mass black hole. The disc size is of the order of the circularisation radius for the gas flow,  $r_c$ , which is unknown. The maximum value of  $r_c$  is the capture radius,  $r_{\text{capt}}$ , which is

$$r_{\text{capt}} = \min \left[ r_{\text{H}}, \frac{GM_{\text{bh}}}{\Delta v^2 + c_s^2} \right]. \quad (3.5)$$

I thus parametrise the circularisation radius as

$$r_c = \zeta r_{\text{capt}}, \quad (3.6)$$

where  $\zeta$  is a parameter less than unity. The viscous time scale in such a disc around the stellar mass black hole is (Pringle 1981)

$$t_{\text{visc}} = \frac{1}{\alpha \Omega_{\text{d}}} \left( \frac{r_c}{h} \right)^2, \quad (3.7)$$

where  $\alpha$  is the viscosity parameter,  $\Omega_{\text{d}} = \sqrt{GM_{\text{bh}}/r_c^3}$  is the angular velocity of the disc and  $h$  is the scale height of the disc. Numerically using the standard results  $h = c_s r_c^{3/2} / (GM_{\text{bh}})$ ,  $c_s^2 = P/\rho$  and  $P = \rho kT / \mu m_p$  (see §5.2 in Frank et al. (2002)),

$$t_{\text{visc}} = 1.5 \times 10^3 \text{ yrs } \alpha_{0.01}^{-1} \mu_{\text{d}}^{1/2} r_{c,12}^{-1/2} T_{\text{d},3}^{-1}, \quad (3.8)$$

where  $T_{\text{d},3}$  is the disc temperature in units of  $10^3$  K, the viscosity parameter is  $\alpha = 0.01\alpha_{0.01}$ ,  $\mu_{\text{d}}$  is the mean molecular mass in units of hydrogen mass ( $m_p$ ) and  $r_{c,12}$  is the circularisation radius in  $10^{12}$  cm. This is to be compared with the period (the orbital time) about the SMBH:

$$P = \frac{2\pi}{\Omega_{\text{K}}} = 2900 \text{ yrs } R_{0.1}^{3/2} M_6^{-1/2}. \quad (3.9)$$

Here,  $\Omega_{\text{K}}$  is the Keplerian angular frequency for the black hole orbiting the super-massive one:  $\Omega_{\text{K}} = \sqrt{GM_{\text{smbh}}/R^3}$ . The corresponding Keplerian velocity is  $v_{\text{K}} = R\Omega_{\text{K}}$ .

Thus, the gas captured in the small-scale disc accretes on the black hole after a delay

of a fraction of to a few (black hole around the SMBH) orbital times. The evolution of the disc mass is given by the rate at which the mass is added,  $\dot{M}_{\text{capt}}$ , minus the mass accreted onto the black hole,  $\dot{M}_{\text{acc}}$ :

$$\frac{dM_d}{dt} = \dot{M}_{\text{capt}} - \dot{M}_{\text{acc}}. \quad (3.10)$$

The black hole accretion rate is calculated as

$$\dot{M}_{\text{acc}} = \frac{M_d}{t_{\text{visc}}} e^{-t_{\text{visc}}/12t} \quad (3.11)$$

(see §5.2 in Frank et al. (2002)). Finally, the luminosity of the accretion flow is modelled in the same way as in Nayakshin & Sunyaev (2007). Namely, I write  $L_X = \eta \dot{M}_{\text{acc}} c^2$ , where  $\eta$  is given by

$$\eta = 0.01 \frac{\dot{M}_{\text{acc}}}{\dot{M}_0 + \dot{M}_{\text{acc}}}, \quad (3.12)$$

where  $\dot{M}_0 = 0.01 M_{\text{Edd}}$  is the critical accretion rate where the switch from the radiatively efficient to radiatively inefficient regime occurs (Esin, McClintock & Narayan 1997). It is also assumed that X-ray emission visible in the *Chandra* band constitutes 10% of the bolometric efficiency, which would be a lower limit for typical spectra of X-ray binaries in their hard state.

### 3.2.2 Orbital evolution of accretors

The velocity and space distribution of stellar mass black holes is modelled as a cusp that follows the Bahcall & Wolf (1976) distribution for heavier species in a mass-segregated cusp. This distribution results in the black hole number density and velocity distribution obeying power laws of the form  $R^{-7/4}$  and  $f_0$  respectively, where,

$$f_0 \propto R^{-1/4} \left( 1 - \frac{v^2}{v_{\text{esc}}^2} \right)^{1/4}. \quad (3.13)$$

Both space and velocity distributions are isotropic. The most recent Monte-Carlo simulations (Freitag et al. 2006) broadly support these classical results. However a recent Fokker-Planck study (Hopman & Alexander 2006) predicts a somewhat steeper power-law density dependence for the black hole cusp,  $\rho_{\text{BH}} \propto R^{-2}$ . However, this level of detail is left for future investigations.

The black hole cusp is sharply cut at  $R = 0.7$  pc (Miralda-Escudé & Gould 2000). The artificial cut of the black hole distribution at the outer cusp radius is a crude ap-

proximation to the more complicated broken power-law structure of the cusp found by (Freitag et al. 2006). It is also not entirely self-consistent as black holes do follow their orbits hence changing their radial position. To determine the significance of this the structure of the cusp was examined  $10^4$  years after it was set up (see fig. 3.1). The density profile did in fact change. Some black holes on eccentric orbits with large semi-major axes were found at radii much larger than the outer cusp radius. However, the maximum change in the black hole density profile was no more than 30%. Furthermore, the black holes on very eccentric orbits will be those that accrete gas at a low rate unless the gas in the inner parsec moves on similar eccentric orbits. Therefore, emission from these black holes might be neglected in any event.

Generating a series of orbits consistent with this space-velocity distribution, the initial phases of the black holes were randomly set along their orbits, and then their spatial motion was followed. The instantaneous gas capture rate for each black hole was also recorded. When one of these orbits intersects the disc of the Minispiral, the black hole in question starts capturing gas and builds up a disc around it as described in §3.2.1.

### 3.2.3 The model for the Minispiral

Paumard et al. (2004) suggests that the Minispiral is a dynamical feature in a state of almost free fall onto Sgr A\*. However, if this was the case then Sgr A\* itself would be accreting from the Minispiral. This would result in accretion rates far above that from the stellar winds (Cuadra et al. 2006), and would contradict the X-ray observations (Baganoff et al. 2003). More realistically, the gas in the Minispiral follows an eccentric orbit which does not enter the inner arcsecond ( $\sim 0.03$  parsec) of the GC.

In my simple model, the Minispiral is modelled as half of a disc in a local Keplerian circular rotation around Sgr A\* with the total gas mass of  $M_{\text{disc}} = 50M_{\odot}$ , in accord with estimates in Paumard et al. (2004). It extends from a radius of 0.1 pc from the SMBH to a radius of 0.5 pc. The disc scale height,  $H$ , is assumed to have a fixed ratio to the radius,  $R$ :  $H/R = 0.1$ . The gas density is given by  $\rho(R) = M_{\text{disc}}/(2\pi R^2 H)$ .

The dynamical age of the Minispiral is a few thousand years. Therefore, the calculations ran for 3000 years with these assumptions, and then the Minispiral was instantaneously “removed”. This is done as a rough model of time evolution of the system in the case where the gas apocenter is larger than 0.5 parsecs, so that the Minispiral would leave the inner 0.5 parsec after a dynamical time. In §3.3.4 I vary some of the above assumptions about the structure of the Minispiral to estimate the sensitivity of

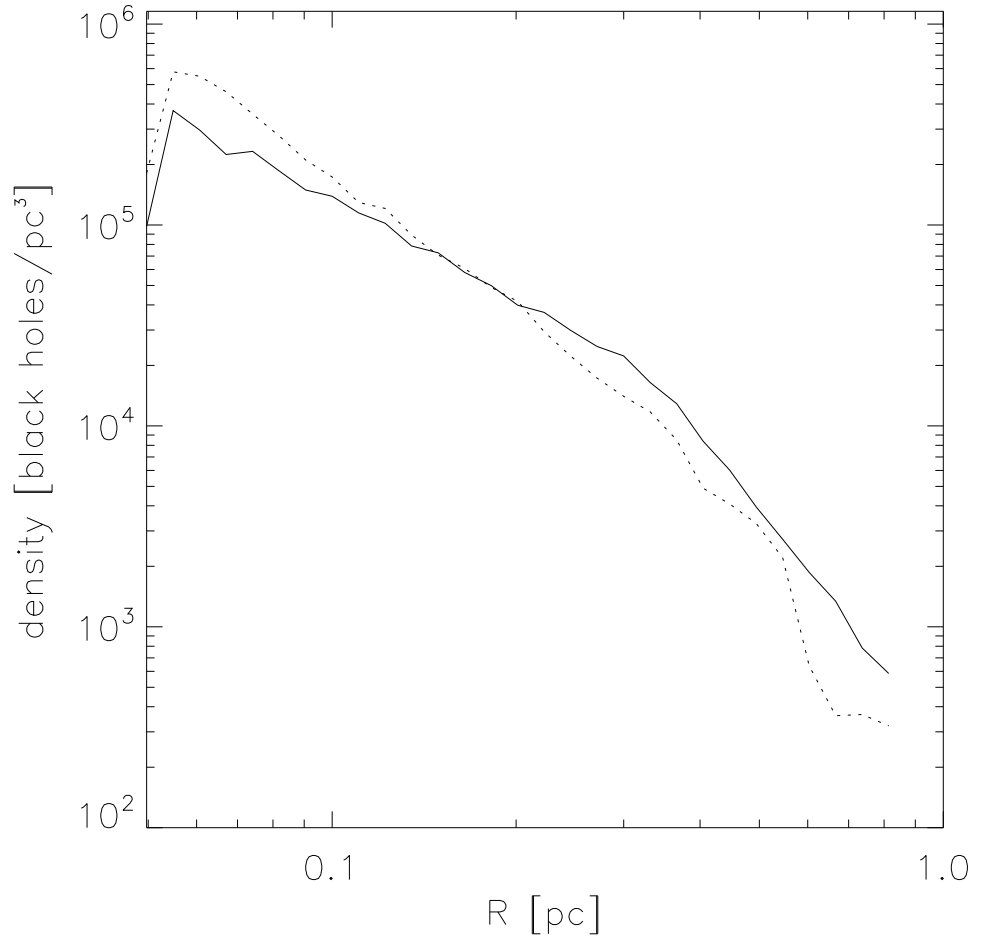


FIGURE 3.1. Density profile of the black hole cusp; the solid line and the dotted line correspond to  $t = 0$  and  $t = 10^4$  yr respectively

my results to these assumptions. In future work, a more complicated, but unavoidably model-dependent dynamics of the Minispiral should be included.

## 3.3 Results

### 3.3.1 Emission from individual black holes

To motivate the study of X-ray emission from black hole cusps in this work, the emission from individual black holes was examined. For simplicity of discussion in this section only, the “half-disc” described in §3.2.3 is replaced with a full disc, with other parameters unchanged, the only exception being the mass of the Minispiral, which was doubled. The

black holes follow Keplerian orbits (§3.2.2) that are characterised by the values of the semi-major axis and the eccentricity (see Table 3.1). The inclination of the orbit to the midplane of the disc,  $i$ , is also essential in determining the accretion history of the black hole in question. The orbital parameters of the test cases are summarised in Table 3.1. Figure 3.2 shows the resulting light curves for the four tests explored. The circularisation parameter is fixed at  $\zeta = 0.1$  for all of the tests.

Table 3.1. Orbital parameters of individual black hole orbits (see §3.3.1). The inclination of the orbit is with respect to the midplane of the Minispiral. The last column shows the time-averaged X-ray luminosity of the source.

Black hole	Inclination ( $^{\circ}$ )	Eccentricity	Semi-major axis (pc)	$\langle L_x \rangle$ erg s $^{-1}$
T1	6	0.1	0.1	$1.78 \times 10^{36}$
T2	11	0.2	0.1	$2.97 \times 10^{34}$
T3	1	0.6	0.3	$1.34 \times 10^{34}$
T4	29	0.5	0.08	$1.28 \times 10^{32}$

T1 in Table 3.1 is shown with the solid curve in fig. 3.2 is the most luminous case. Low inclination and eccentricity of the orbit ensure that the black hole spends all of its time inside the disc. The near circular orbit ensures a low relative velocity between the black hole and the gas in the disc. Hence, the gas capture rate is relatively high, as is the X-ray luminosity. The few kinks in the lightcurve are caused by periodic variations in the relative velocity due to the eccentricity of the orbit.

The black hole in test T2 is on a slightly more eccentric and more inclined orbit. The relative black hole-gas velocity is larger than in test T1, and hence the gas capture rate is reduced (see eq. (3.1)). The black hole spends a significant amount of time inside the disc, but there are periods of time when it exits the disc through one of its faces. Half of the dips in the lightcurve correspond to time spent outside the disc, and the other to the time when the relative velocity  $\Delta v$  reaches the highest value along the trajectory. Due to a relatively large size of the accretion disc (the “small scale” one discussed in §3.2.1) that builds up around the black hole, the viscous time is comparable to the duration of time spent outside of the disc, and hence the dips are relatively minor. The X-ray light curve of the source reaches a quasi-steady state with the luminosity  $L_x \sim \text{few} \times 10^{34}$  erg s $^{-1}$  after  $\sim 10^4$  years.

In test T3, the black hole is on a more eccentric orbit, with eccentricity  $e = 0.6$ , and a larger semi-major axis. The high eccentricity of the orbit results in a high relative

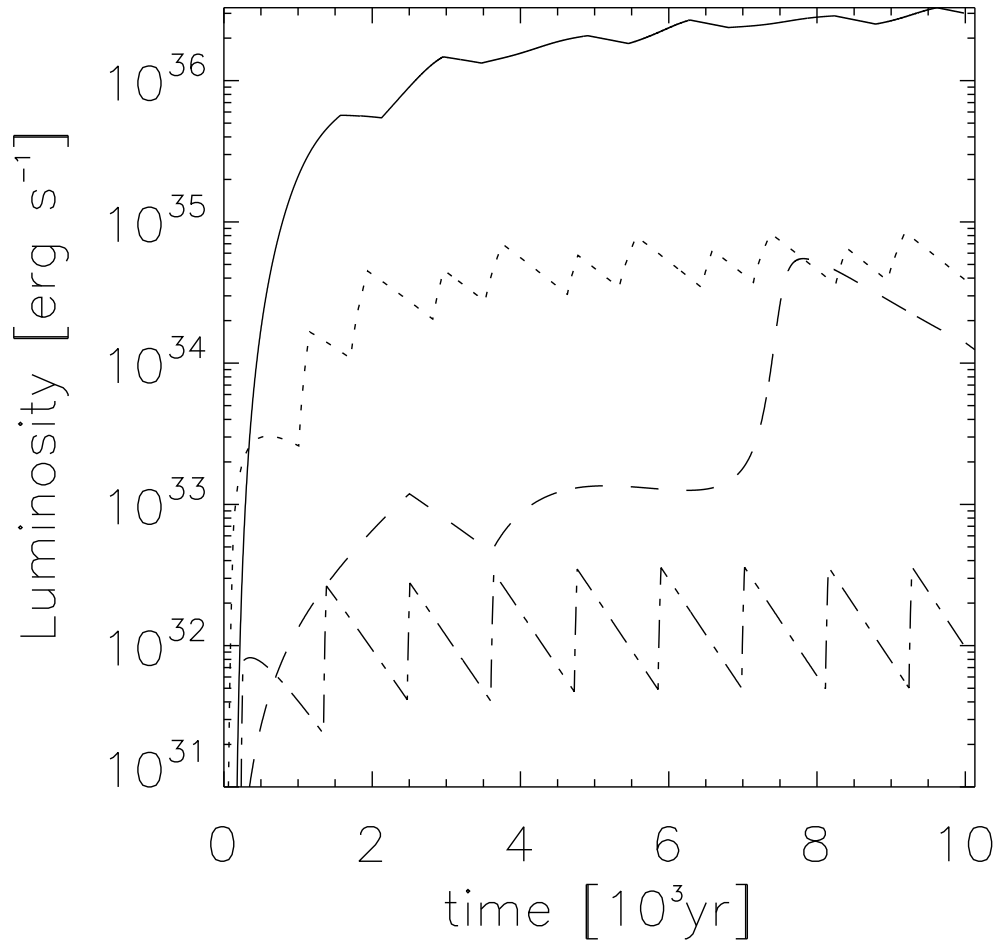


FIGURE 3.2. X-ray light curves of the four individual black holes described in §3.3.1; the solid, dotted, dashed and dotted-dashed lines correspond to T1, T2, T3, and T4 respectively.

velocity which limits the gas capture rate. For most of the orbit,  $L_X < 10^{33} \text{ erg s}^{-1}$ . The luminosity of the black hole increases dramatically at  $t \sim 8000$  years. At this moment in time, the relative velocity is near a minimum while the gas density in the disc is close to the maximum reached on this orbit, yielding the maximum capture rate. The accretion luminosity approaches that of case T2.

Finally, test T4 is close to the worst case scenario as far as the gas capture rate is concerned. A high inclination and eccentricity orbit imply that the black hole spends little time inside the disc. Accumulation of gas in the small scale accretion disc happens in a burst-like manner when the black hole is inside the disc. Also note that since the

relative velocity is high, the gas capture radius (see eq. (3.5)) is smaller than it is in tests T1 and T2, and hence the disc viscous time is shorter (see eq. (3.8)). This results in shorter decay times for the “bursts” in the lightcurve. The X-ray luminosity is never larger than  $\text{few} \times 10^{32} \text{ erg s}^{-1}$ .

These simple tests indicate that the black holes may be expected to produce a detectable X-ray emission in one of the two following ways: (i) a few black holes may be on orbits essentially co-moving with the gas, producing a few bright point sources; (ii) the dim majority of high inclination and/or high eccentricity orbits may not produce individually bright sources but may be collectively bright, producing an unresolvable “diffuse” X-ray emission.

To estimate an upper-limit of the mass accreted by these black holes over the lifetime of the Minispiral assume that all the black holes have capture rates equal to T1 (highly unlikely). T1 is the most luminous case and has a capture rate of  $\sim 10^{-9} M_{\odot} \text{ yrs}^{-1}$ . If one were to assume the lifetime of the Minispiral was  $\sim 1000 \text{ yrs}$  then 20000 black holes would accrete  $\sim 0.02 M_{\odot}$ , negligible compared to the total mass of the Minispiral.

### 3.3.2 Representative cases

Having considered the individual accretors’ case in the previous section we move on to the problem of the total black hole cusp emission with the Minispiral model. A black hole distribution consistent with the (Bahcall & Wolf 1976) distribution as described in §3.2.2 is generated. The orientation of orbits is drawn randomly from an isotropic distribution.

The upper panels in fig. 3.3 display the total X-ray luminosity of a cluster of  $N = 5000$  black holes as a function of time for two values of the circularisation radius parameter,  $\zeta$ , 0.1 and 0.001, left and right, respectively. The lower panels show the number of X-ray sources with luminosity higher than  $10^{33} \text{ erg s}^{-1}$  for the tests shown in the panels above. Such sources could be observed by *Chandra*. Several conclusions can be made. With a larger value of  $\zeta = 0.1$ , the accretion discs around black holes are larger, and thus viscous times are long. As a result, the X-ray emission varies smoothly with time, first increasing as the discs are built up, and then decreasing on  $\sim$  a thousand years time scale. Thus the sources are rather steady in time, and are also dim.

For the smaller value of  $\zeta = 0.001$ , viscous times in small scale discs are much shorter. Therefore, the X-ray emission from the sources varies on much shorter time scales, i.e., of a few years to tens of years. The sources are also brighter as the peak

accretion rates are higher – each individual source shines much brighter for a shorter time, as compared with the larger  $\zeta$  case. Both the upper and the lower panels provide us with largely independent predictions which may be compared to X-ray observations.

Figure 3.4 shows the same experiments as fig. 3.3 but for 20000 black holes. Comparison between the two different values of  $\zeta$  shows similar trends as before. It is interesting to compare the figs. 3.3 and 3.4. While the results depend significantly on the unknown value of  $\zeta$ , both low and high  $\zeta$  tests show the same tendency of a significant luminosity increase with increase in the number of black holes. In fact, the luminosity increased by a larger factor than the black hole number did. The higher the number of accretors, the larger the chance to have sources with small  $\Delta v$ , hence increasing the luminosity of the cusp with increasing  $N$  in a non-linear fashion. The number of sources above the chosen luminosity threshold also increased. These tendencies hold for all values of  $\zeta$ . This suggests that by performing tests across all reasonable parameter space for  $\zeta$  the maximum allowed number of stellar mass black holes in the cusp may be determined.

### 3.3.3 Search in the $N, \zeta$ parameter space

Following this idea, a number of models for a range of values of  $\zeta$  and for the total black hole numbers of  $N = 5, 10, 20$  and 40 thousand were tested. During the time period modelled, the results vary considerably in each test. For example, it is possible for just one single source to dominate the X-ray luminosity output of the cluster. In order to reduce and estimate the statistical noise of the results, for each of the values of  $\zeta$  and the total black hole number considered here, the tests were repeated three times, each time generating a new random black hole orbit distribution. The mean value for the observables for the three runs were calculated as were the deviations from the mean values. The averaging was done between time  $2000 < t < 3000$  years to look at a state that may be similar to the present state of the Minispiral, given its estimated dynamical time.

A summary of the results is presented in Table 3.2. Several quantities were defined specifically, the average total X-ray luminosity of the black hole cluster and the number of black holes brighter than  $10^{33}$  erg s<sup>-1</sup>,  $N_X$ , as such sources would have been resolved by *Chandra* into separate point sources. Time-dependent variants of these quantities were plotted in figs. 3.3 and 3.4. In addition to these, the probabilities that the total

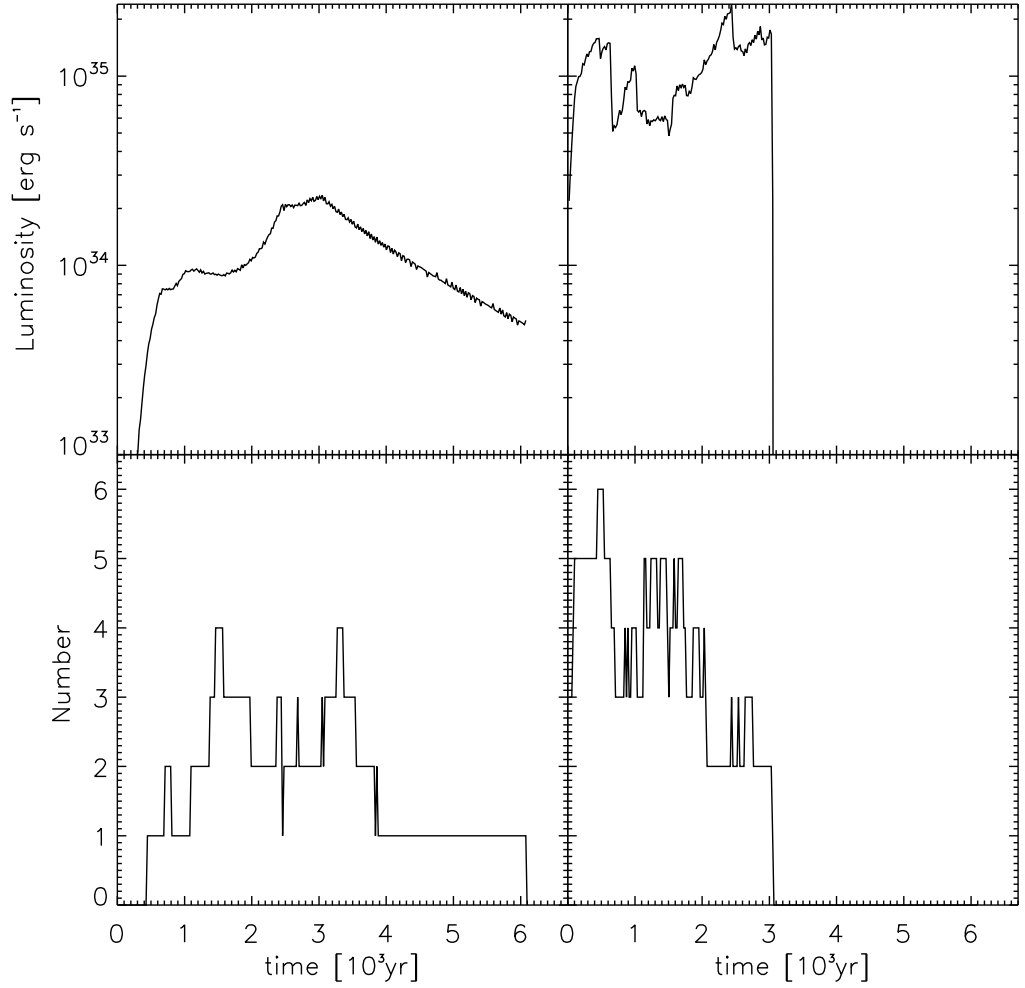


FIGURE 3.3. X-ray light curves (top panels) and number of individual sources (bottom panels) where  $L_x > 10^{33} \text{ erg s}^{-1}$ , when the total number of black holes in the inner parsec is 5000. The left and right panels correspond to  $\zeta = 0.1$  and  $\zeta = 0.001$  respectively.

luminosity of the cusp exceeds  $10^{35}$  and  $10^{36} \text{ erg s}^{-1}$  were defined:

$$P(L_X > 10^{35}) = \frac{1}{t_f - t_i} \int_{L_X > 10^{35}} dt, \quad (3.14)$$

and similarly for  $10^{36} \text{ erg s}^{-1}$ ,  $t_i$  and  $t_f$  are 2000 and 3000 years respectively. The probability of the number of individual sources brighter than  $L_X > 10^{33}$  being larger

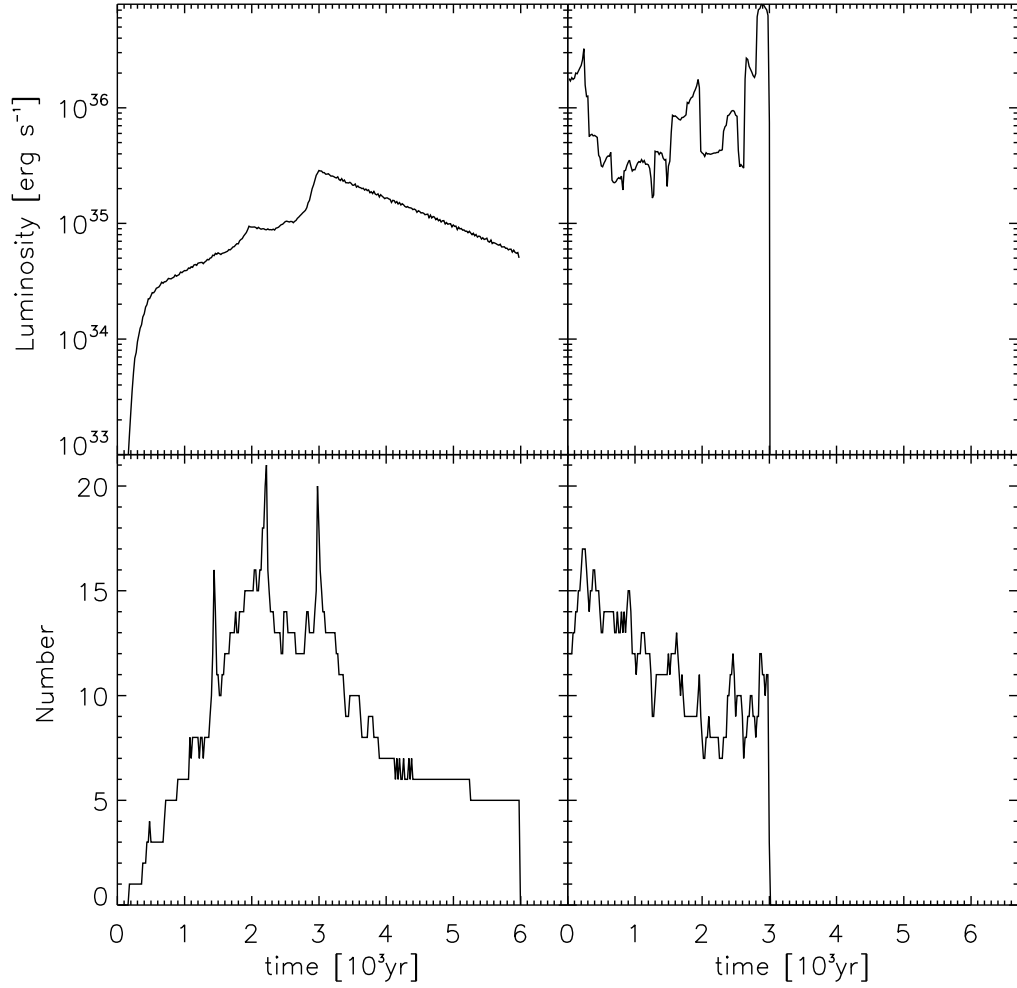


FIGURE 3.4. X-ray light curves and number of individual sources where  $L_x > 10^{33}$  erg  $s^{-1}$ , when the total number of black holes in the inner parsec is 20000. The left and right panels correspond to  $\zeta = 0.1$  and  $\zeta = 0.001$  respectively.

than 3, 10 and 20 at a given time is defined in a similar way, e.g.,

$$P(N_X > 10) = \frac{1}{t_f - t_i} \int_{N_X > 10} dt. \quad (3.15)$$

These values can be compared to the number of discrete X-ray sources in the inner parsec as detected by *Chandra*.

Observations of the inner parsec by *Chandra* have placed upper limits on the total luminosity of sources of approximately  $10^{35}$  erg  $s^{-1}$  (Baganoff et al. 2003) and the number of individual X-ray sources with a luminosity greater than  $10^{33}$  erg  $s^{-1}$  of a dozen or

so (F. Baganoff, private communication, *Galactic Centre Workshop 2006*). With these constraints in mind the possibility that the cusp contains 40000 black holes can be immediately ruled out. For any reasonable value of  $\zeta$ , the total luminosity and the number of individual sources with  $L_X > 10^{33}$  erg s<sup>-1</sup> are too large compared to observations. A cusp containing 20000 black holes is not very likely but cannot be ruled out completely at this time. In particular, only the larger  $\zeta$  case is acceptable for  $N = 20000$ . Even though the average total cusp luminosity is  $\sim 10^{36}$  erg s<sup>-1</sup> for this test, i.e., too large, the probability  $P(L_X > 10^{35})$  is only  $\sim 0.66$ . Cusps with  $N = 5000$  or 10000 black holes is well within the limits imposed by observations.

### 3.3.4 Sensitivity of results to the properties of the Minispiral

A rather simple model for the Minispiral is used (§3.2.3), partially because it is not yet clear what a better model for this gas would be. Currently the origin of this gaseous feature and the precise three-dimensional distribution of gas and velocity field is unknown (Paumard et al. 2004).

To test the sensitivity of the conclusions to the properties of the Minispiral, several of the assumptions made in §3.2.3 were varied. Table 3.3 summarises these tests. In particular, in one of the series of tests the Minispiral was assumed to be three times more massive, i.e., contain  $150 M_\odot$  of gas, with all other assumptions unchanged. In this case the luminosity of the cusp increases significantly at a given number of black holes, and even the  $N = 10^4$  case is too luminous for the smaller values of the circularisation parameter  $\zeta$ . Hence the upper limit on the number of black holes is around  $10^4$ .

Another likely complication is that the gas may be on a parabolic or an eccentric trajectory rather than a circular one, as assumed in this work until now. For such orbits, the gas velocity can be both larger and smaller than the local Keplerian value, depending on where exactly on the orbit the gas is. Observationally, the Minispiral seems to be closer to the pericenter of its orbit rather than the apocenter (Paumard et al. 2004). To test the significance of non-Keplerian orbits, the gas velocity was set to 1.2 and 1.4 times the local Keplerian value in the two series of tests presented in Table 3.3. Clearly this model is not geometrically self-consistent as the half-disc we use for the Minispiral should then deform in a complicated way. The larger gas velocity should result in a decrease in the number of black holes travelling at a low relative speed through the Minispiral, which should reduce the average gas capture rate (eq. 3.1).

Table 3.3 shows that increasing the gas velocity to 1.2 of the local Keplerian value results in a marked drop in average luminosity of black holes, to the point that a cusp

containing 40000 black holes cannot be ruled out for the larger value of the circularisation parameter,  $\zeta = 0.1$ . On the other hand, realistically, the sources would have a distribution in values of  $\zeta$ , and hence a fair number of sources would have  $\zeta \sim 0.01$  or less, which would then be ruled out.

Moving on to the gas velocity  $1.4v_K$ , a further drop in the luminosity of the cusp and the number of sources detectable by *Chandra* (Table 3.3) is noted. Even the  $N = 40000$  is allowed. However this model strongly over-simplifies the situation in the Galactic Centre. The Minispiral should be a feature bound to Sgr A\* (or else the fact that it is crossing the innermost region of the parsec now would be a coincidence), and hence it is rather implausible that the gas is on a radial trajectory for which one would have  $v = \sqrt{2}v_K \sim 1.4v_K$ . I believe the case where  $v = 1.2v_K$  is the one that better represents reality

Finally, the last entries in Table 3.3 are the tests with the Minispiral mass of  $M_{\text{disc}} = 150 M_\odot$  and  $v = 1.2v_K$ . A cusp of 40000 black holes is clearly inconsistent with the observations, whereas the  $N = 20000$  is not completely ruled out.

### 3.3.5 Comparison to related previous work and result uncertainties

Blaes & Madau (1993) and Perna et al. (2003) considered the related question of observing isolated neutron stars of the Galaxy in X-rays as they accrete gas passing through molecular clouds. Agol & Kamionkowski (2002) studied the same issue for isolated stellar mass black holes. In particular, the latter study concluded that radiative efficiency of accreting black holes needs to be very small, i.e.,  $\eta = 10^{-5}$ , in order to not contradict the available X-ray data.

My model differs from Agol & Kamionkowski (2002) in two important aspects. Firstly, the viscous disc evolution is modelled in a simplified manner whereas these authors assumed that the instantaneous Bondi-Hoyle capture rate is also the instantaneous accretion rate onto the black hole. If the disc viscous time is long, my model predicts a smaller accretion rate onto the black hole but for a longer period of time. Thus, with the same radiative efficiency, I would in general predict fewer high luminosity sources but a higher number of low luminosity sources.

Secondly, rather than use a constant radiative efficiency factor, eq. (3.12) is used, in which  $\eta \propto \dot{M}$  for  $\dot{M} \ll 0.01$ . While this prescription is quite reasonable on both theoretical and observational grounds (Esin et al. 1997), it is by no means the only one possible. To assess the magnitude of the possible changes in the results, a cusp of  $N =$

40000 was considered, in a similar test to those in Table 3.2. With the constant  $\eta = 10^{-4}$  value, and an instantaneous accretion model as in Agol & Kamionkowski (2002), the number of detectable sources was about 15, and the cusp total average luminosity was around  $2 \times 10^{35} \text{ erg s}^{-1}$ . The number of detectable sources is thus comparable to what I find with my standard assumptions.

On the other hand, if one uses the radiative efficiency as low as  $\eta = 10^{-5}$ , then there is only  $N_X \sim 3$  observable sources. Such a low radiative efficiency would hence allow a cusp with  $N = 40000$  black holes. However,  $\eta = 10^{-5}$  is extreme and is unlikely at least for the sources with higher accretion rates as these are in the parameter space of observed moderately bright accreting X-ray binaries, where  $\eta$  is clearly larger than  $10^{-5}$  (Esin et al. 1997).

### 3.3.6 A neutron star cusp

The mechanism that produces an overabundance of black holes in the Galactic Centre also applies to neutron stars, as they are also more massive than an average star. Simulations by Freitag et al. (2006) predict that a cusp of neutron stars will have a number density profile quite similar to that of stellar mass black holes. These neutron stars would be accreting gas in a similar manner to the black holes, with modifications only due to the smaller mass ( $M_{\text{ns}} = 1.4 M_{\odot}$ ) and the existence of a surface.

Using the method outlined in §1.3.2 I approximate the emission of an accreting neutron star as a black-body with temperature  $T_{\text{ns}}$  from the surface area  $4\pi R_{\text{ns}}^2$ , where  $R_{\text{ns}} = 10 \text{ km}$  is the radius of the neutron star. Most of the radiation flux will be emitted at wavelengths corresponding to photon energy  $E = 3kT_{\text{ns}}$ :

$$E \sim 0.8 L_{34}^{1/4} \text{ keV} , \quad (3.16)$$

where  $L_{34}$  is the X-ray luminosity in units of  $10^{34} \text{ erg s}^{-1}$ . Due to the quite large absorbing column density to the GC,  $N_{\text{H}} \sim 10^{23} \text{ cm}^{-2}$  (Baganoff et al. 2003), soft X-ray emission below  $\sim 1 \text{ keV}$  is practically unobservable. Hence the minimum observable total X-ray luminosity of a neutron star was set at  $10^{34} \text{ erg s}^{-1}$ , rather than  $10^{33} \text{ erg s}^{-1}$  for the black hole case.

Assuming that the radiative efficiency of an accreting neutron star with negligible magnetic fields is constant at  $\eta \sim 0.1$ , the luminosity of an accreting neutron star is simply

$$L_X = 0.1 \dot{M}_{\text{acc}} c^2 . \quad (3.17)$$

With these modifications, I can use the method developed in §3.2 to calculate the X-ray emission from the cusp containing neutron stars. The results are presented in a way identical to the black hole cusp in Table 3.4. As with the black hole cusp case, the  $N = 40000$  case is strongly ruled out on account of too large a number of detectable point sources,  $N_X$ , and the total X-ray luminosity of the cusp. The  $N = 20000$  cusp also appears to be a bit too high in terms of both the total luminosity and the number of sources.

However, the assumption that all of the captured material makes it onto the neutron star surface (see eq. (3.17)) is uncertain. It is well known that the “propeller effect” may reduce the X-ray luminosity of neutron stars by disrupting the flow far from the stellar surface (Menou et al. 1999). In fact Perna et al. (2003) showed that the radiative efficiency of accreting isolated neutron stars in the Galaxy should not exceed  $\eta \sim 10^{-3}$  on average, or else observational constraints would be violated. If  $\eta \sim 10^{-3}$  is adopted, the total X-ray luminosity of the neutron star cusp with  $N = 40000$  is only  $\text{few} \times 10^{34} \text{ erg s}^{-1}$ . Hardly any individual sources would radiate above the chosen detection threshold of  $10^{33} \text{ erg s}^{-1}$ .

### 3.4 Conclusions

Stellar mass black holes and neutron stars are predicted to clutter the central parsec of our Galaxy (Morris 1993, Miralda-Escudé & Gould 2000, Freitag et al. 2006, Hopman & Alexander 2006). While these predictions seem to be very robust, observational confirmation of the existence of a stellar remnant cusp is only indirect at the moment (Muno et al. 2005*b*). Nayakshin & Sunyaev (2007) suggested that these sources, accreting *cold* gas episodically from the Minispiral or other molecular or ionised gas features found in the central parsec, may be bright enough both collectively and individually to be observable with *Chandra*. I performed a more elaborate study, where a time-dependent disc accretion onto the compact sources was considered. Also taken into account was the fact that at low accretion rates, the radiative efficiency of black holes appears to be drastically reduced (Esin et al. 1997), and I used a Monte-Carlo like approach to randomly initialise the cusp of compact remnants.

The main effort in this work was to set the upper limit on the number of compact remnants. Whereas the models have internal uncertainties, such as the value of circularisation parameter  $\zeta$ , and observational uncertainties (the mass and precise orbit of the Minispiral), a cusp of black holes with  $N \gtrsim 40000$  seems to be ruled out, bar-

ring the possibility that radiative efficiency of these sources is extremely low. A cusp with  $N \sim 20000$  black holes, as theoretically predicted (Freitag et al. 2006, Hopman & Alexander 2006), is broadly consistent with the data. Future efforts should improve these upper limits. The constraints on the neutron star cusp are weaker as the propeller effect could realistically make radiative efficiency too small for most sources.

On the basis of my calculations, it is quite realistic that some of the X-ray sources visible in the central parsec (Baganoff et al. 2003, Munro et al. 2005*b*) may be isolated black holes and neutron stars accreting gas from the Minispiral. Such sources should be preferentially found close to the Minispiral if the viscous time is short ( $\zeta$  is small). In addition, binary systems containing a black hole and a normal low mass star can also accrete gas in roughly the same way as I calculated here. In the case of low values of circularisation parameter,  $\zeta$ , the size of the disc around the primary (the black hole) can be smaller than the size of the binary itself. Thus, these systems may appear as “fake X-ray binaries”, where the gas supply comes from outside rather than from the low mass secondary. Observational signatures of such systems might be warped and out of binary plane accretion discs, “too short” or “too weak” accretion outbursts for the size of the binary.

Table 3.2. Characteristics of black hole cusp averaged between 2000–3000 years (see §3.3.3).

Number <sup>a</sup> [10 <sup>3</sup> ]	$\zeta^b$	$\langle L_X \rangle^c$ [10 <sup>35</sup> erg s <sup>-1</sup> ]	P( $L_X > 10^{36}$ ) <sup>d</sup>	P( $L_X > 10^{35}$ ) <sup>e</sup>	$\langle N_X \rangle^f$	P( $N_X > 20$ ) <sup>g</sup>	P( $N_X > 10$ ) <sup>h</sup>	P( $N_X > 3$ ) <sup>i</sup>
5	0.001	1.85 ± 0.51	0	0.53 ± 0.46	2.76 ± 0.75	0	0	0.33 ± 0.8
5	0.01	2.75 ± 1.33	0.42 ± 0.2	0.72 ± 0.1	4.2 ± 0.4	0	0	0.63 ± 0.13
5	0.1	0.73 ± 0.6	0	0.24 ± 0.21	2.23 ± 0.2	0	0	0.18 ± 0.11
10	0.001	15.91 ± 2.70	0.33 ± 0.13	0.90 ± 0.07	4.44 ± 0.28	0	0	0.71 ± 0.06
10	0.01	1.03 ± 0.24	0	0.45 ± 0.16	5.36 ± 0.26	0	0	0.90 ± 0.04
10	0.1	0.51 ± 0.28	0	0.31 ± 0.22	4.53 ± 1.52	0	0.01 ± 0.00	0.45 ± 0.21
20	0.001	19.97 ± 5.87	0.57 ± 0.05	0.99 ± 0.01	8.87 ± 0.81	0	0.19 ± 0.11	1.00 ± 0.00
20	0.01	9.67 ± 1.94	0.34 ± 0.14	0.99 ± 0.00	12.26 ± 1.40	0.01 ± 0.01	0.69 ± 0.17	1.00 ± 0.00
20	0.1	9.88 ± 4.49	0.34 ± 0.22	0.66 ± 0.23	13.11 ± 1.25	0.01 ± 0.00	0.74 ± 0.16	1.00 ± 0.00
40	0.001	40.37 ± 1.75	1.00 ± 0.00	1.00 ± 0.00	19.40 ± 0.37	0.34 ± 0.05	1.00 ± 0.00	1.00 ± 0.00
40	0.01	100.53 ± 62.13	0.77 ± 0.08	0.99 ± 0.00	24.66 ± 0.50	0.85 ± 0.05	1.00 ± 0.00	1.00 ± 0.00
40	0.1	6.50 ± 1.83	0.20 ± 0.14	1.00 ± 0.00	24.59 ± 2.18	0.72 ± 0.14	1.00 ± 0.00	1.00 ± 0.00

The columns list:

<sup>a</sup> Total number of black holes in the cusp

<sup>b</sup> Circularisation parameter (§3.2.1)

<sup>c</sup> Time-averaged luminosity of the cusp

<sup>d–e</sup> Probability that the total luminosity of the cusp is greater than 10<sup>36</sup> or 10<sup>35</sup> erg s<sup>-1</sup>, respectively.

<sup>f</sup> Average number of sources with X-ray luminosity greater than 10<sup>33</sup> erg s<sup>-1</sup> ( $N_X$ )

<sup>g–i</sup> Probability that  $N_X$  is greater than 20, 10 and 3, respectively

Table 3.3. Same as Table 3.2, but for different models of the Minispiral

Number [ $10^3$ ]	$\zeta$	$\langle L_X \rangle$ [ $10^{35} \text{ erg s}^{-1}$ ]	$P(L_X > 10^{36})$	$P(L_X > 10^{35})$	$\langle N_X \rangle$	$P(N_X > 20)$	$P(N_X > 10)$	$P(N_X > 3)$
<b>3 M<sub>gas</sub><sup>a</sup></b>								
5	0.01	28.13 ± 11.54	0.62 ± 0.15	0.84 ± 0.08	5.81 ± 0.95	0	0.03 ± 0.02	0.84 ± 0.06
5	0.1	1.53 ± 4.45	0	0.67 ± 0.40	7.04 ± 0.47	0	0.06 ± 0.04	1.00 ± 0.00
10	0.01	35.21 ± 12.01	0.63 ± 0.17	1.00 ± 0.00	9.24 ± 0.93	0	0.36 ± 0.13	1.00 ± 0.00
10	0.1	2.06 ± 0.74	0	0.56 ± 0.16	14.12 ± 0.51	0.02 ± 0.00	0.98 ± 0.01	1.00 ± 0.00
20	0.01	24.53 ± 6.02	0.77 ± 0.13	1.00 ± 0.00	18.95 ± 1.25	0.40 ± 0.16	1.00 ± 0.00	1.00 ± 0.00
20	0.1	5.47 ± 0.41	0.01 ± 0.00	1.00 ± 0.00	29.38 ± 2.06	0.90 ± 0.07	1.00 ± 0.00	1.00 ± 0.00
<b>1.2 v<sub>K</sub><sup>b</sup></b>								
5	0.01	0.93 ± 0.55	0.02 ± 0.01	0.14 ± 0.07	1.85 ± 0.36	0	0	0.10 ± 0.04
5	0.1	0.05 ± 0.03	0	0	0.44 ± 0.20	0	0	0
10	0.01	0.45 ± 0.10	0	0.13 ± 0.05	3.47 ± 0.42	0	0	0.49 ± 0.13
10	0.1	0.38 ± 0.25	0	0.17 ± 0.12	2.45 ± 1.42	0	0	0.31 ± 0.22
20	0.01	4.86 ± 1.63	0.14 ± 0.05	0.43 ± 0.15	6.65 ± 0.08	0	0.03 ± 0.01	0.91 ± 0.04
20	0.1	0.35 ± 0.07	0	0	4.24 ± 0.08	0	0	0.76 ± 0.07
40	0.01	40.65 ± 1.66	0.56 ± 0.14	0.94 ± 0.04	13.42 ± 0.23	0.02 ± 0.01	0.74 ± 0.06	1.00 ± 0.00
40	0.1	1.05 ± 0.37	0	0.18 ± 0.13	10.27 ± 0.62	0	0.44 ± 0.80	1.00 ± 0.00
<b>1.4 v<sub>K</sub><sup>c</sup></b>								
5	0.01	0.07 ± 0.02	0	0	0.71 ± 0.15	0	0	0
5	0.1	0.02 ± 0.00	0	0	0.37 ± 0.26	0	0	0
10	0.01	0.12 ± 0.04	0	0	1.17 ± 0.21	0	0	0
10	0.1	0.05 ± 0.01	0	0	0.83 ± 0.32	0	0	0
20	0.01	0.32 ± 0.48	0	0.03 ± 0.02	3.66 ± 0.43	0	0	0.49 ± 0.13
20	0.1	0.03 ± 0.00	0	0	0.11 ± 0.05	0	0	0
40	0.01	0.64 ± 0.14	0	0.18 ± 0.09	5.37 ± 0.60	0	0.04 ± 0.01	0.72 ± 0.07
40	0.1	0.12 ± 0.03	0	0	1.34 ± 0.36	0	0	0.01 ± 0.01
<b>3 M<sub>gas</sub> &amp; 1.2 v<sub>K</sub><sup>d</sup></b>								
20	0.01	9.79 ± 0.93	0.34 ± 0.06	1.00 ± 0.00	15.47 ± 0.25	0.07 ± 0.02	0.98 ± 0.01	1.00 ± 0.00
20	0.1	2.89 ± 1.03	0.09 ± 0.06	0.86 ± 0.10	13.72 ± 0.25	0.04 ± 0.01	0.91 ± 0.03	1.00 ± 0.00
40	0.01	12.17 ± 0.96	0.59 ± 0.02	1.00 ± 0.00	25.02 ± 0.78	0.90 ± 0.05	1.00 ± 0.00	1.00 ± 0.00
40	0.1	6.43 ± 1.76	0.29 ± 0.10	0.93 ± 0.05	19.63 ± 1.82	0.50 ± 0.16	1.00 ± 0.00	1.00 ± 0.00

<sup>a</sup> Mass of the Minispiral has been tripled to  $150 M_\odot$

<sup>b</sup> Velocity of the gas has been increased to  $1.2 v_K$ , where  $v_K$  is the local Keplerian velocity

<sup>c</sup> Velocity of the gas has been increased to  $1.4 v_K$

<sup>d</sup> Mass of the Minispiral has been tripled to  $150 M_\odot$  and the velocity of the gas has been increased to  $1.2 v_K$

Table 3.4. Same as Table 3.2 but for a neutron star cusp.

Number <sup>a</sup> [10 <sup>3</sup> ]	$\zeta^b$	$\langle L_X \rangle^c$ [10 <sup>35</sup> erg s <sup>-1</sup> ]	P( $L_X > 10^{36}$ ) <sup>d</sup>	P( $L_X > 10^{35}$ ) <sup>e</sup>	$\langle N_X \rangle^f$	P( $N_X > 20$ ) <sup>g</sup>	P( $N_X > 10$ ) <sup>h</sup>	P( $N_X > 3$ ) <sup>i</sup>
5	0.001	3.23 ± 5.24	0.08 ± 0.06	0.79 ± 0.11	2.84 ± 0.43	0	0	0.32 ± 0.10
5	0.01	2.43 ± 0.76	0	0.67 ± 0.12	2.78 ± 0.81	0	0	0.38 ± 0.16
5	0.1	1.44 ± 0.18	0	0.85 ± 0.11	2.90 ± 0.67	0	0	0.34 ± 0.20
10	0.001	4.17 ± 0.90	0.02 ± 0.01	0.99 ± 0.01	6.25 ± 0.45	0	0.03 ± 0.02	0.94 ± 0.02
10	0.01	5.89 ± 1.38	0.18 ± 0.08	0.99 ± 0.01	4.53 ± 0.34	0	0	0.72 ± 0.10
10	0.1	6.69 ± 3.59	0.30 ± 0.21	0.83 ± 0.12	3.32 ± 0.15	0	0	0.47 ± 0.05
20	0.001	8.13 ± 1.34	0.27 ± 0.11	1.00 ± 0.00	11.52 ± 1.15	0	0.57 ± 0.15	1.00 ± 0.00
20	0.01	9.73 ± 1.73	0.32 ± 0.12	1.00 ± 0.00	7.32 ± 0.30	0	0.11 ± 0.08	0.97 ± 0.02
20	0.1	7.17 ± 2.15	0.27 ± 0.19	1.00 ± 0.00	9.00 ± 0.35	0	0.19 ± 0.05	1.00 ± 0.00
40	0.001	41.60 ± 12.71	0.99 ± 0.01	1.00 ± 0.00	21.99 ± 0.52	0.69 ± 0.07	1.00 ± 0.00	1.00 ± 0.00
40	0.01	18.62 ± 4.46	0.87 ± 0.07	1.00 ± 0.00	15.82 ± 0.48	0.04 ± 0.02	0.99 ± 0.00	1.00 ± 0.00
40	0.1	17.91 ± 3.74	0.86 ± 0.10	1.00 ± 0.00	21.34 ± 0.34	0.66 ± 0.05	1.00 ± 0.00	1.00 ± 0.00

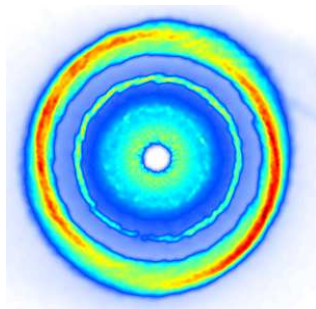
<sup>a</sup> – <sup>e</sup> see Table 3.2 caption.

<sup>f</sup> Average number of neutron stars with  $L_X$  greater than  $10^{34}$ erg s<sup>-1</sup> ( $N_X$ ). Only sources with  $L_X > 10^{34}$  are visible, see §3.3.6.

<sup>g</sup> – <sup>i</sup> see Table 3.2 caption.

# Chapter 4

*GRS 1915+105*



“Don’t matter how many times you get  
burnt, you just keep doin’ the same.”  
- Bodie

*The Wire: Time after Time [3.01]*

## 4.1 Introduction

GRS 1915+105 is a member of a class of objects called low mass X-ray binaries (LMXB). As described in §1.3, they consist of a black hole/neutron star primary and a low mass secondary star which is filling its Roche lobe. Mass is transferred from the secondary star via the L1 point and forms an accretion disc around the primary. The accretion disc may become unstable due to the thermal-viscous instability resulting in an increase in the accretion rate onto the primary. These sudden accretion events lead to a brightening of the source in X-rays for several months.

GRS 1915+105 is one of the brightest X-ray sources visible in the sky. It was first discovered in 1992 (Castro-Tirado, Brandt & Lund 1992) when it went into outburst and has been extensively studied ever since (for a review see Fender & Belloni (2004)). The outburst which led to the system's detection in 1992 is still proceeding to this day, lasting 20 times longer than for any other LMXB. The X-ray light curve of GRS 1915+105 is one of the more complex that has been observed with large variability on a variety of time scales (Greiner, Morgan & Remillard 1996, Belloni et al. 1997).

A radio counterpart was observed by Mirabel et al. (1993) and was discovered to have components moving away from GRS 1915+105 with an apparent superluminal velocity (Mirabel & Rodriguez 1994). This, combined with a distance estimate of 12.5 kpc, means that GRS 1915+105 became the first source in our Galaxy to exhibit superluminal motion. This had previously only been associated with jets from super-massive black holes in active galactic nuclei and led to GRS 1915+105 being classed as a microquasar.

Identification of the optical counterpart to GRS 1915+105 was hindered by over 30 magnitudes of absorption in the optical band separating us from the source (Mirabel et al. 1994). Infrared spectroscopy identified the secondary as a K or M type giant (Greiner et al. 2001), which confirmed that GRS 1915+105 was a LMXB. Radial velocity measurements confirmed the presence of a black hole of  $\sim 14 M_{\odot}$  and obtained an orbital period of 33.5 days (Greiner, Cuby & McCaughrean 2001). The most recent observations suggest a  $14.0 \pm 4.4 M_{\odot}$  black hole and a secondary of  $0.8 \pm 0.5 M_{\odot}$  (Harlaftis & Greiner 2004). The longevity of GRS 1915+105 outbursts can possibly be explained by its long orbital period which results in an extremely large accretion disc forming around the black hole,  $R_{\text{disc}} \sim 2 \times 10^2 \text{ cm}$  (Truss & Done 2006). This ensures there is a large reservoir of mass in the disc and results in the long outburst time observed.

In this work I concentrate on the long term behaviour of GRS 1915+105, specifically

the duty cycle, i.e. the fraction of the time the system is in outburst,

$$\text{duty cycle} = \frac{t_{\text{out}}}{t_{\text{out}} + t_{\text{q}}}. \quad (4.1)$$

Where  $t_{\text{out}}$  and  $t_{\text{q}}$  are the outburst and quiescent times respectively. Additionally the recurrence time will also be discussed in this work  $t_{\text{rec}} = t_{\text{out}} + t_{\text{q}}$ . Analytic estimates of the duration of an outburst were performed by Truss & Done (2006). However these simplified estimates could not include effects such as tidal interactions and mass loss from the disc, which may dramatically effect any outburst.

The mass transfer rate,  $-\dot{M}_2$ , from the secondary is significantly smaller than the accretion rate onto the black hole during an outburst. As a result the time between outbursts is expected to be far larger than the outburst itself: the disc is depleted during an outburst and needs to build up in mass again before another outburst is triggered. Hence GRS 1915+105 and other systems like it are expected to spend most of their lives in the quiescent phase and will be difficult to detect. This raises the question, how many GRS 1915+105 like objects are in our Galaxy and the local Universe?

In section 4.3 I present the features of the smooth particle hydrodynamics (SPH) code I use and introduce the parameters that determine the behaviour of the simulations. In section 4.4 I will present the results and determine the parameters effects on the duty cycle. Finally in section 4.5 the implications of the work are discussed.

## 4.2 Physical ingredients

In this section I will go into the physical ingredients used in the code in some detail. The SPH code by Murray (1995) has been modified to include the following physical effects: the disc instability model (DIM), irradiation of the accretion disc by a central source of X-rays and Eddington wind loss from the disc.

### 4.2.1 The disc instability model

This was introduced in §1.3.3 and was devised to explain the outbursts in dwarf novae. The disc vertical equilibrium solution, at a given radius, results in a relation between the surface density of the disc  $\Sigma$  and the temperature  $T$ , the *S-curve* shown in fig. 1.11. The solution is unstable on the middle branch resulting in limit-cycle like behaviour when the

disc heats and cools at the critical densities  $\Sigma_{\max}$  and  $\Sigma_{\min}$ . Such a solution is calculated using the Shakura-Sunyaev viscosity prescription, see §1.2.3,

$$\nu = \alpha c_s H, \quad (4.2)$$

where  $\alpha$  is a free parameter.

Historically, in order to reproduce observed outbursts, the two- $\alpha$  model was introduced:  $\alpha$  takes different values ( $\alpha_h$  and  $\alpha_c$ ) on the hot and cold branch of the S-curve. This translates into  $\Sigma_{\max} = \Sigma_{\max}(R, \alpha_c)$  and  $\Sigma_{\min} = \Sigma_{\min}(R, \alpha_h)$ . If somewhere in the disc  $\Sigma(R) > \Sigma_{\max}(R)$ , the annulus enters the hot, high-viscous state, which propagates to nearby annuli. The front propagating inward forces the disc into the hot viscous state on its way. The high viscosity implies a high accretion rate onto the central object, leading to an X-ray outburst. The disc returns to quiescence (low viscosity, small accretion rate) once  $\Sigma(R) < \Sigma_{\min}$ . It has been found by integration of the vertical disc structure that  $\Sigma_{\max}$  and  $\Sigma_{\min}$  scale linearly with radius (Cannizzo, Shafer & Wheeler 1988):

$$\Sigma_{\max}(R) = 11.4 R_{10}^{1.05} M_1^{-0.35} \alpha_c^{-0.86} \text{ g cm}^{-2}, \quad (4.3)$$

and

$$\Sigma_{\min}(R) = 8.25 R_{10}^{1.05} M_1^{-0.35} \alpha_h^{-0.8} \text{ g cm}^{-2}, \quad (4.4)$$

where  $M_1$  is the primary mass in solar masses, and  $R_{10}$  is the radius in units of  $10^{10}$  cm. Equations (4.3) and (4.4) are used in our numerical setup, but it is noted that some slightly different prescriptions exist, e.g. Dubus et al. (2001).

## 4.2.2 Irradiation

As stated above, wherever  $\Sigma(R) > \Sigma_{\max}(R)$  the disc is in the hot viscous state. However, these are not the only grounds for the disc entering the hot state. The X-ray radiation generated when matter falls into the black hole (see §1.3) can keep the hydrogen ionised and the disc in the hot state out to a certain radius  $R_{\text{irr}}$ . This does not take place in dwarf novae which typically do not emit significantly in X-rays and have smaller luminosities than LMXBs.

To estimate the region of the disc that is affected by irradiation of the central source, the ionisation temperature of hydrogen,  $T_H$ , is used in the Stefan-Boltzmann law

$$\epsilon L_X = 4\pi\sigma R_{\text{irr}}^2 T_H^4, \quad (4.5)$$

where  $\sigma$  is the Stefan-Boltzmann constant and  $\epsilon$  is a constant containing all of the unknown information about the nature of the X-ray source, the geometry of the disc and the albedo of the gas within the disc. If no assumptions about the accretion or irradiation efficiency are made then

$$\begin{aligned} R_{\text{irr}} &= \left( \frac{\epsilon \eta \dot{M} c^2}{4\pi \sigma T_H^4} \right)^{1/2} \\ &= 2.7 \times 10^{11} \left( \frac{\epsilon}{10^{-3}} \right)^{1/2} \left( \frac{\eta}{0.1} \right)^{1/2} \dot{M}_{18}^{1/2} \text{ cm.} \end{aligned} \quad (4.6)$$

where  $\epsilon$  is defined as the irradiation efficiency,  $\eta$  is the accretion efficiency and  $\dot{M}_{18}$  is the central accretion rate in units of  $10^{18} \text{ g s}^{-1}$ .

### 4.2.3 Wind Loss

Local mass loss due to the local mass transfer rate exceeding the Eddington limit is also included. The local accretion rate at radius  $R$  is given by,

$$\dot{M}(R) = -2\pi R v_R(R) \Sigma(R) \quad (4.7)$$

where  $v_R(R)$  is the radial velocity. The Eddington rate at the same radius is,

$$\dot{M}_{\text{Edd}}(R) = \lambda \frac{R L_{\text{Edd}}}{G m_1}, \quad (4.8)$$

where  $L_{\text{Edd}}$  is the Eddington luminosity,  $m_1$  is the black hole mass and  $\lambda$  is a free parameter usually set to 1. If  $\dot{M}(R) > \dot{M}_{\text{Edd}}(R)$  a wind carries away the excess mass at a rate  $\dot{M}_{\text{wind}}$ . The parameter  $\lambda$  allows us to depart from the Eddington limit<sup>1</sup> (when  $\lambda = 1$ ): the smaller  $\lambda$ , the easier it is to remove particles from the disc. This is just a simple way to parametrise the wind efficiency. These three mechanisms contain the free parameters that are varied throughout this work in order to reveal their relative effects, namely:  $\alpha_h$ ,  $\alpha_c$ ,  $\epsilon$  and  $\lambda$ . Note also that the expressions for  $\Sigma_{\text{max}}$  and  $\Sigma_{\text{min}}$  are estimates only and that I allow for a change in their normalisations which results in two extra parameters. This is detailed in the numerical setup below.

<sup>1</sup>Recall the assumptions made when deriving the Eddington limit in §1.2.2, a steady spherically symmetric accretion comprised entirely of Hydrogen.

## 4.3 Numerical Method

I study the long term evolution of GRS 1915+105 using the smooth particle hydrodynamic (SPH) code detailed in §2. It includes the thermal viscous instability, wind loss, disc irradiation as described in §4.2. Moreover, the full binary potential is included and hence any tidal effects that may arise.

### 4.3.1 Particle injection and rejection

In the simulations particles are injected from the L1 point, and into the primary's potential, with the transfer rate given by Ritter (1999),

$$-\dot{M}_2 \sim 7.3 \times 10^{-10} \left( \frac{M_2}{M_\odot} \right)^{1.74} \left( \frac{P_{\text{orb}}}{1 \text{ day}} \right)^{0.98} M_\odot \text{ yr}^{-1}. \quad (4.9)$$

Using GRS 1915+105 system characteristics, this gives  $-\dot{M}_2 \sim 2 \times 10^{-8} M_\odot \text{ yr}^{-1}$ . For more detail on the mass transfer rate in binary systems see §1.3.1.

Particles are removed from the simulation when they are within  $0.04a$  ( $a$  is the binary separation) of the black hole, if they return to the secondary's Roche lobe or if they are at a distance  $r > a$  from the black hole with a velocity greater than the escape velocity. The first condition implies that the accretion rates derived are not the accretion rates onto the black hole (as  $0.04a \gg R_{\text{Schw}}$ ). Some material may still be blown away in a wind before it reaches the black hole surface but resolution and timescale issues prevent us from studying the most inner regions of the accretion disk.

### 4.3.2 Triggering the disc instability

The disc is divided into one hundred annuli in which the mean surface density is evaluated. When the surface density of one of these annuli is greater than  $\Sigma_{\text{max}}(R)$ ,  $\alpha$  is switched into the hot state ( $\alpha = \alpha_h$ ). Conversely, the disc switches back to the cold state ( $\alpha = \alpha_c$ ) wherever  $\Sigma(R) < \Sigma_{\text{min}}(R)$ . Using eqs. (4.3) and (4.4) with the parameters of GRS 1915+105 and the typical values of the Shakura-Sunyaev  $\alpha$  parameter  $\alpha_h = 0.1$  and  $\alpha_c = 0.01$ ,

$$\Sigma_{\text{max}} = K_{\text{max}} \left( \frac{R}{a} \right)^{1.05} \sim 2.5 \times 10^5 \left( \frac{R}{a} \right)^{1.05} \text{ g cm}^{-2}, \quad (4.10)$$

$$\Sigma_{\min} = K_{\min} \left(\frac{R}{a}\right)^{1.05} \sim 2.2 \times 10^4 \left(\frac{R}{a}\right)^{1.05} \text{ g cm}^{-2}. \quad (4.11)$$

In practice, we cannot use the values of  $K_{\max/\min}$  shown in eqs. (4.10) and (4.11). Using  $K_{\max} \sim 2.5 \times 10^5 \text{ g cm}^{-2}$ , triggering an outburst would take a prohibitive amount of time. Typical values used were  $K_{\max}^{\text{sph}} = 55$  and  $K_{\min}^{\text{sph}} = 4.7853$ . The reasons behind this are discussed in §4.3.3-§4.3.5 and its effects are discussed in §4.3.6. The quantities  $K_{\max}$  and  $K_{\min}$  are also to be varied to explore how a less or more massive disk would behave. For the same reasons,  $\alpha_h$  and  $\alpha_c$  are also increased from their canonical values given above, in order to speed up the outburst and quiescence times. Doing so allows the system to relatively quickly reach steady-state and undergo several outburst events during a single run. The draw-back is that results need to be scaled in order to get actual quiescence and outburst times, this is detailed in §4.3.6.

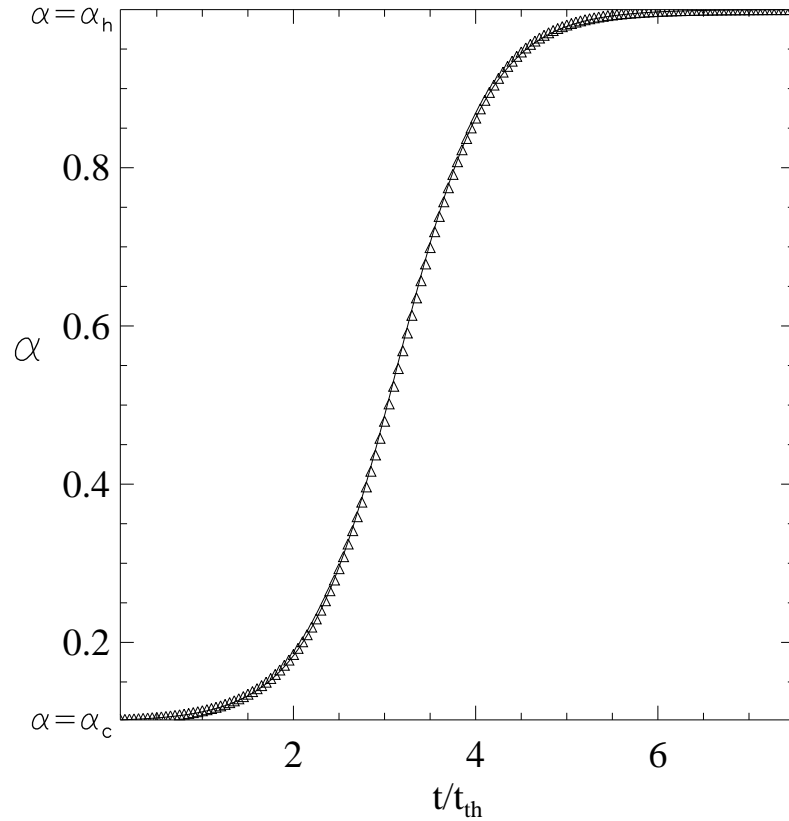


FIGURE 4.1. Functional form of the viscous switch, eq. (4.13). The viscosity is switched after a few thermal time scales. A comparison is made between eq. (4.13) solid line and eq. (4.15) points

The last technical point is that of the disc transition between the cold and hot states. It is performed following the method described in Truss et al. (2000), Murray et al.

(2002) and Truss & Wynn (2004). Particles are switched from the cold into the hot state smoothly on the thermal time scale,  $t_{\text{th}}$ , of the system. The thermal time is given by a ratio of the heat content per unit area of the disc,  $\sim \rho kT/\mu m_p \sim \Sigma c_s^2$  and the rate of energy loss (dissipation) per unit area of the disc,  $9\nu\Sigma GM_1/4R^3$  (see §1.2.4). This results in a thermal time scale of

$$t_{\text{th}} = \frac{4}{9\alpha\Omega_K} \quad (4.12)$$

where I have used eq. (1.15) and the fact that  $H/c_s \sim t_\phi \sim \Omega_K^{-1}$ , the dynamical time scale in the disc (§5.8 in Frank et al. (2002)). Once a switch is triggered,  $\alpha$  follows

$$\alpha(t) = \alpha^+ \pm \alpha^- \tanh\left(\frac{t}{t_{\text{th}}} - \pi\right), \quad (4.13)$$

where

$$\alpha^\pm = \frac{(\alpha_h \pm \alpha_c)}{2}. \quad (4.14)$$

The change in viscosity parameter ( $\delta\alpha$ ) in a time-step ( $\delta t$ ) is therefore given by,

$$\delta\alpha = \frac{\delta t}{t_{\text{th}}} \alpha^- \left[ 1 - \left( \frac{\alpha - \alpha^+}{\alpha^-} \right)^2 \right]. \quad (4.15)$$

Fig. 4.1 compares the forms of eqs. (4.13) and (4.15).

### 4.3.3 Models using a massive disc

In the first attempt to model GRS 1915+105, the physical values for  $K_{\text{max}}$  and  $K_{\text{min}}$  were used from eqs. (4.10) and (4.11). One disadvantage of this method was the mass and time resolutions of the simulations was poor. Limited computational time means it is desirable to keep the number of particles in the disc to  $N \sim 10^5$ . A typical simulation with  $10^5$  particles takes  $\sim 3000$  computer hours, any significant increase in the particle number and this time becomes prohibitively long. A rough estimate of the particle mass can be found by approximating the mass of the disc immediately before an outburst

$$M_{\text{disc}} \sim \int_0^{R_{\text{out}}} 2\pi R \Sigma_{\text{max}}(R) dR \sim \frac{2\pi K_{\text{max}}}{a^{1.05}} \int_0^{R_{\text{out}}} R^{2.05} dR \quad (4.16)$$

and dividing by the number of particles,  $m_p = M_{\text{disc}}/N$ . With a  $R_{\text{out}} \sim 0.4a$  the particle mass is  $m_p = 1.7 \times 10^{25}$ g. This demonstrates how the particle mass is related to the

choice of  $K_{\max}$  used in the code,  $m_p \propto K_{\max}$ . The global time steps used in the code are

$$t_{\text{step}} = \frac{t_{\text{res}} P_{\text{orb}}}{2\pi} \quad (4.17)$$

with a time resolution of  $t_{\text{res}}$ . Assuming one particle is emitted from the  $L_1$  point per time step then,

$$\begin{aligned} m_p &= \dot{M}_2 t_{\text{step}} \\ t_{\text{res}} &= \frac{2\pi m_p}{P_{\text{orb}} \dot{M}_2} \end{aligned} \quad (4.18)$$

To ensure the correct mass transfer rate ( $-\dot{M}_2 \sim 2 \times 10^{-8} M_{\odot} \text{ yr}^{-1}$ ) and using  $m_p = 1.7 \times 10^{25} \text{ g}$ , a time resolution of  $\sim 30$  is needed. In effect one particle is emitted once every  $\sim 5$  orbits. To speed up the code the viscosity in the disc is a factor of ten greater than is typically assumed both during outburst and quiescence, leading to a higher rate of particle accretion. This slow rate of particle injection coupled with the higher rate of particle accretion can result in an entirely empty disc. To prevent this, the rate of particle injections was increased effectively increasing  $-\dot{M}_2$  by a  $\sim$  few thousand. Fig. 4.2 shows a sample of the output of the code.

#### 4.3.4 Models using an under-massive disc

To avoid the problems discussed in §4.3.3 one possibility is to scale down the mass of the disc while the particle number remains constant. If a reduced value of  $K_{\max}^{\text{sph}} = 55 \text{ g cm}^{-2}$  is used, an approximate particle mass is  $\sim 3.5 \times 10^{21} \text{ g}$ , following the steps outlined in §4.3.3. The values for  $K_{\max}^{\text{sph}}$  and  $K_{\min}^{\text{sph}}$  were chosen to have the same ratio as  $K_{\max}/K_{\min}$ . This allows for a significantly improved mass and time resolution of the code. Using eq. (4.18)  $t_{\text{res}} \sim 0.005$ , resulting in a global time step of  $\sim 2300 \text{ s}$ . However the resulting  $R_{\text{irr}}$  during outburst is too small (fig. 4.3 compared to fig. 4.2). GRS 1915+105 is expected to be accreting at the Eddington limit, using eq. (1.14) results in an irradiation radius of

$$R_{\text{Edd}} = 3.24 \times 10^{11} \left( \frac{\epsilon}{10^{-3}} \right)^{1/2} \left( \frac{M_1}{M_{\odot}} \right)^{1/2} \text{ cm}. \quad (4.19)$$

For  $\epsilon = 7 \times 10^{-4}$  (value used by Truss & Done (2006)),  $R_{\text{Edd}} \sim 0.14a$ , a value that is greater than any produced by this version of the code. Scaling the irradiation efficiency up to approximate the system more accurately will be necessary.

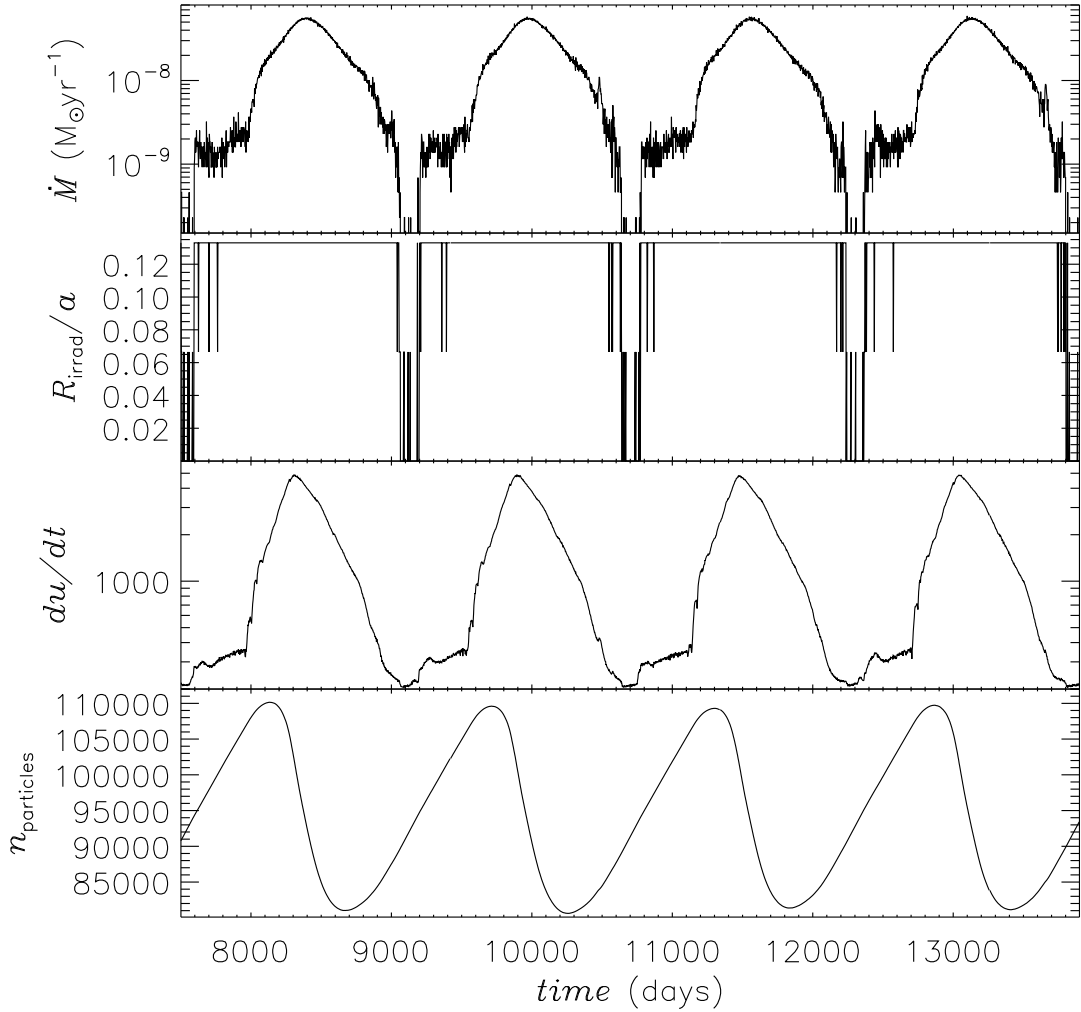


FIGURE 4.2. Plot of central accretion rate, irradiation radius, dissipation (code units) and number of particles as a function of time with  $\Sigma_{\text{max}}$  and  $\Sigma_{\text{min}}$  given by eqs. (4.10) and (4.11)

### 4.3.5 Under-massive disc with scaled $R_{\text{irr}}$

To rectify the smaller than expected irradiation radius, an allowance for the under-massive disc must be made. Upon accretion the mass of the particles are scaled up when calculating  $R_{\text{irr}}$ . When  $K_{\text{max}} = 2.5 \times 10^5 \text{ g cm}^{-2}$  and  $K_{\text{max}}^{\text{sph}} = 55 \text{ g cm}^{-2}$  then the particle masses were scaled up by a factor of  $K_{\text{max}}/K_{\text{max}}^{\text{sph}} \sim 4500$ . The output of the code is shown in fig. 4.4. A comparison between the output of the code for the unscaled and scaled irradiation radii is shown in fig. 4.5. A larger  $R_{\text{irr}}$  prolongs the outburst and its exponential decay, as expected for an irradiated disc (King & Ritter 1998), has a longer

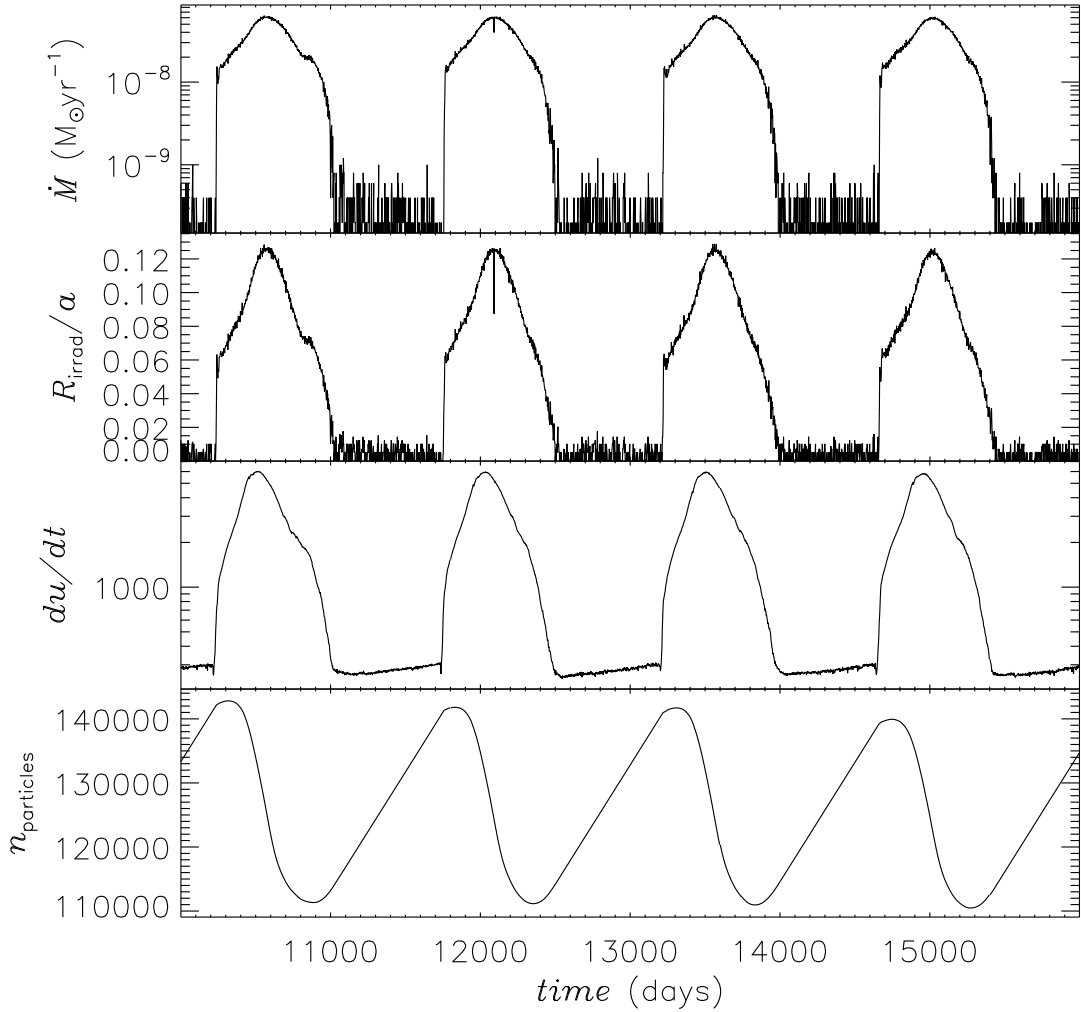


FIGURE 4.3. Plot of central accretion rate, irradiation radius, dissipation (code units) and number of particles as a function of time. Values of  $K_{\text{max}}^{\text{sph}} = 55 \text{ g cm}^{-2}$  and  $K_{\text{min}}^{\text{sph}} = 4.7853 \text{ g cm}^{-2}$  are used.

timescale.

### 4.3.6 Scaling outburst and recurrence timescales

As we have stated in section 4.3, for reasons of computational time, we are forced to use  $\Sigma_{\text{max/min}}$  and  $\alpha_{\text{hot/cold}}$  values which are different from their “true” values. In this section we consider how to scale the outburst and quiescent timescales from the simulations to produce predictions of the true timescales.

In the code we use a  $\Sigma_{\text{max}}$  proportional to  $R$ . During an outburst most of the mass

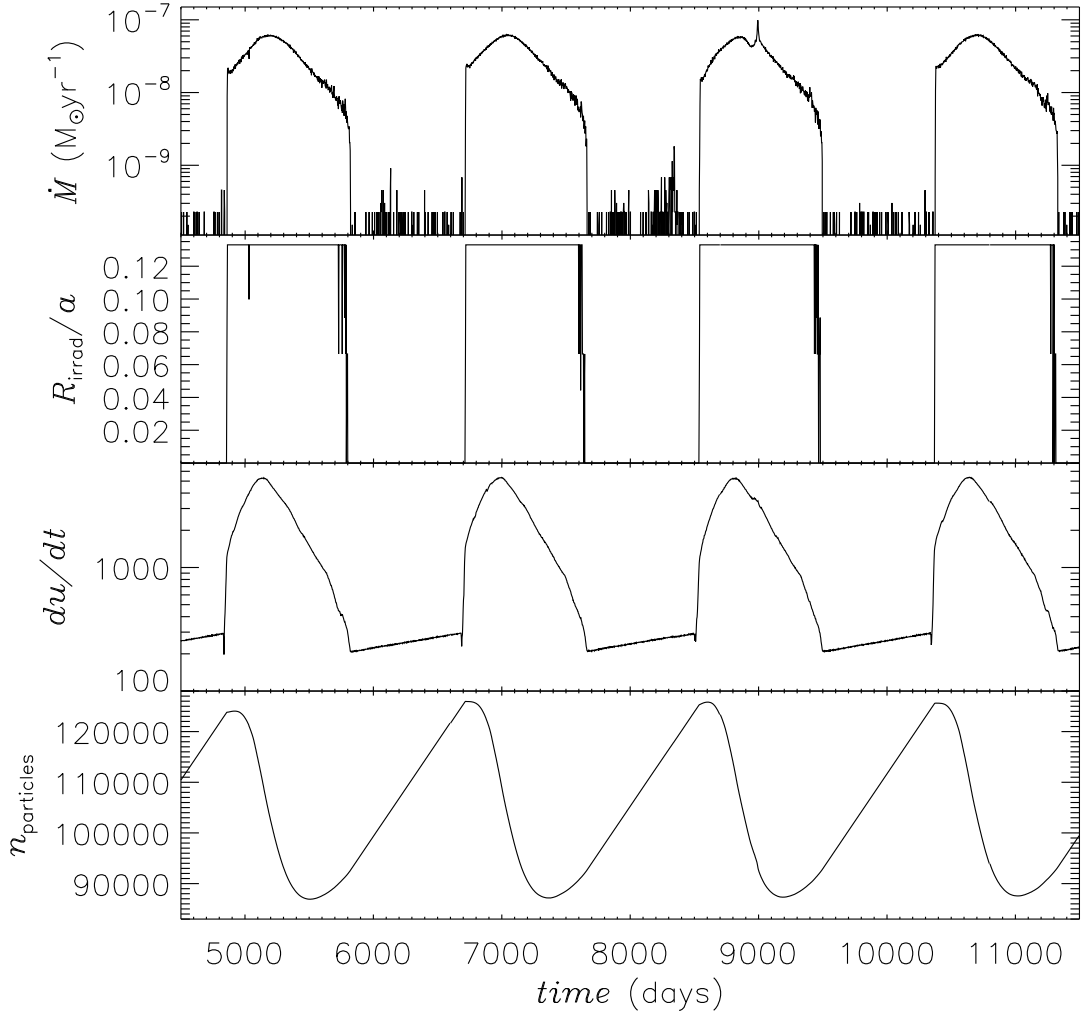


FIGURE 4.4. Plot of central accretion rate, irradiation radius, dissipation (code units) and number of particles as a function of time. Values of  $K_{\text{max}}^{\text{sph}} = 55 \text{ g cm}^{-2}$  and  $K_{\text{min}}^{\text{sph}} = 4.7853 \text{ g cm}^{-2}$  are used and  $R_{\text{irr}}$  has been scaled.

inside a certain radius ( $R_{\text{out}}$ ) will be accreted. At the start of the outburst the surface density inside this radius will be near  $\Sigma_{\text{max}}$ . The outburst timescale is then given by

$$t_{\text{out}} = \frac{M}{\dot{M}} \quad (4.20)$$

where  $\dot{M}$  is the rate at which the mass in the region  $R < R_{\text{out}}$  changes and  $M$  is the mass in the same region, given by,

$$M \sim \int_0^{R_{\text{out}}} 2\pi R \Sigma_{\text{max}}(R) dR - \int_0^{R_{\text{out}}} 2\pi R \Sigma_{\text{min}}(R) dR. \quad (4.21)$$

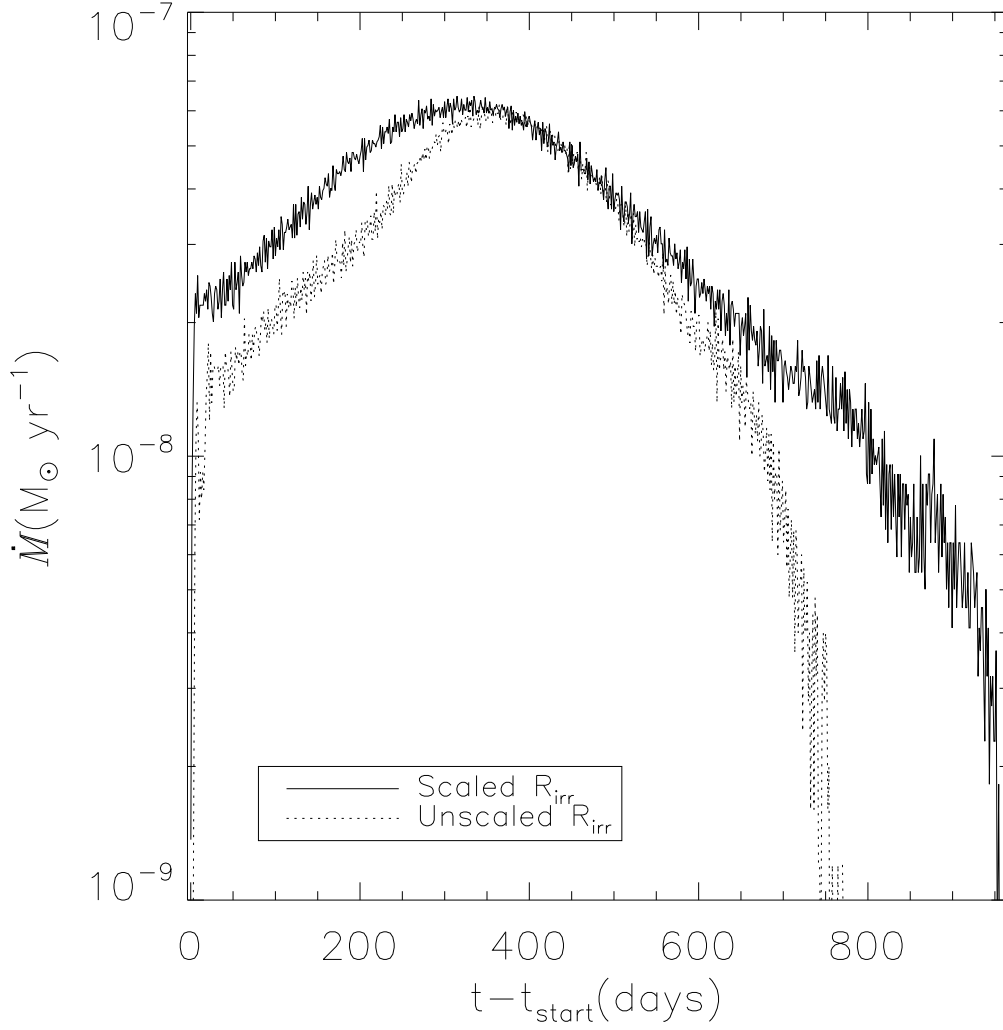


FIGURE 4.5. Comparison between the output of the code with a scaled and unscaled  $R_{\text{irr}}$ . The time has been normalised to the start of the outburst

Simplifying using eqs. (4.3) and (4.4) gives,

$$M \sim \frac{2\pi R_{\text{out}}^2}{3.05} (\Sigma_{\text{max}}(R_{\text{out}}) - \Sigma_{\text{min}}(R_{\text{out}})). \quad (4.22)$$

Eqs. (4.10), (4.11) and (4.22) can then be used to show,

$$M \propto (K_{\text{max}} - K_{\text{min}}). \quad (4.23)$$

Given that (see eq. (1.53)),

$$\dot{M} \propto \alpha_h \Sigma_{\text{max}} \propto \alpha_h K_{\text{max}} \quad (4.24)$$

then

$$t_{\text{out}} \propto \frac{(K_{\text{max}} - K_{\text{min}})}{\alpha_h K_{\text{max}}} \quad (4.25)$$

This provides a way to scale the results we obtain from our SPH code. The ratio of the “real” outburst time to the simulated outburst time is therefore,

$$\frac{t_{\text{out}}}{t_{\text{out}}^{\text{sph}}} = \frac{(K_{\text{max}} - K_{\text{min}})\alpha_h^{\text{sph}} K_{\text{max}}^{\text{sph}}}{(K_{\text{max}}^{\text{sph}} - K_{\text{min}}^{\text{sph}})\alpha_h K_{\text{max}}}. \quad (4.26)$$

Where  $K_{\text{max}}$  and  $K_{\text{min}}$  are the physical values and  $K_{\text{max}}^{\text{sph}}$  and  $K_{\text{min}}^{\text{sph}}$  are the values used in the SPH simulation. Similarly we can also scale the quiescent times by using,

$$t_{\text{q}} = \frac{M}{-\dot{M}_2} \quad (4.27)$$

where  $M$  is given by eq. (4.23), hence,

$$t_{\text{q}} \propto \frac{K_{\text{max}} - K_{\text{min}}}{-\dot{M}_2} \quad (4.28)$$

which gives the ratio of the “real” quiescent time to the quiescent time in the simulation as,

$$\frac{t_{\text{q}}}{t_{\text{q}}^{\text{sph}}} = \left( \frac{K_{\text{max}} - K_{\text{min}}}{K_{\text{max}}^{\text{sph}} - K_{\text{min}}^{\text{sph}}} \right) \left( \frac{-\dot{M}_2^{\text{sph}}}{-\dot{M}_2} \right). \quad (4.29)$$

The *standard* simulation has the following parameters  $K_{\text{max}} = 55$ ,  $K_{\text{min}} = 4.785$  (all subsequent references to  $K_{\text{max}/\text{min}}$  refer to the values used in the code),  $\alpha_h = 1$ ,  $\alpha_c = 0.1$ ,  $\eta = 0.1$  and  $\lambda = 1.0$ . When exploring the parameter space, only one of these variables was changed at any one time, the rest took these values. In §2.7 I determined the relation between the Shakura-Sunyaev  $\alpha_{ss}$  and the artificial viscosity  $\alpha$ , because of the approximate one-to-one relation between the two they can be used interchangeably. However, to remove ambiguity, unless stated otherwise  $\alpha$  in this section refers to the artificial viscosity parameter.

## 4.4 Results

### 4.4.1 Typical Behaviour

As previously stated in §4.3.1 particles are injected from the L1 point and proceed to build up in a disc around the accreting black hole. The particle mass and  $K_{\text{max}}$  were

chosen to ensure approximately  $10^5$  particles were in the disc before an outburst was triggered. The simulations were permitted to go through several outbursts until the disc achieved a steady state.

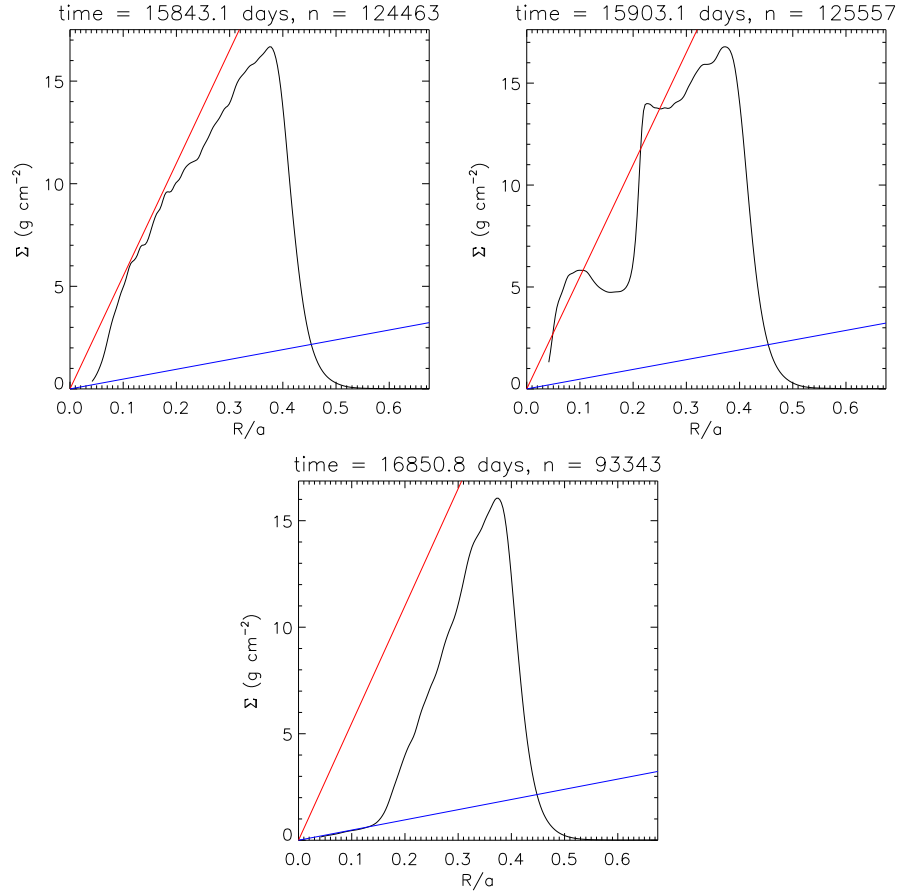


FIGURE 4.6. Evolution of azimuthally averaged surface density before outburst (top left panel) during outburst (top right panel) and after outburst (bottom panel). Red and blue lines represent  $\Sigma_{\max}$  and  $\Sigma_{\min}$  respectively, see eqs. (4.10), (4.11). Binary separation for GRS1515+105 is  $a \sim 7.5 \times 10^{12}$  cm

Fig. 4.6 shows the evolution of the azimuthally averaged surface density in a disc for a typical simulation. In the snapshot immediately prior to the outburst (top left panel), the surface density in the inner disc closely follows the form of eq. (4.10) with  $K_{\max} = 55$ . Exceeding this limit at  $R \sim 0.1a$  is the trigger for entry into the hot viscous state and hence the trigger for the outburst. The annulus that enters the hot state begins to spread, its particles drift into neighbouring annuli increasing their surface density. This process repeats itself if the surface density of the neighbouring annuli rises above  $\Sigma_{\max}(R)$ . In this way a significant portion of the disc enters the hot state. The top right panel in fig. 4.6 shows the disc in the initial stages of an outburst. The increased viscosity in the inner disc has already caused particles to be transferred to the inner regions of the disc, where

they will be removed from the simulation and said to be accreted by the black hole. To further illustrate the changes in the disc during an outburst, fig. 4.7 displays the average artificial viscosity parameter in the disc during the initial stages of an outburst. The inner disc is in the hot state, conversely the outer disc is in the cold state.

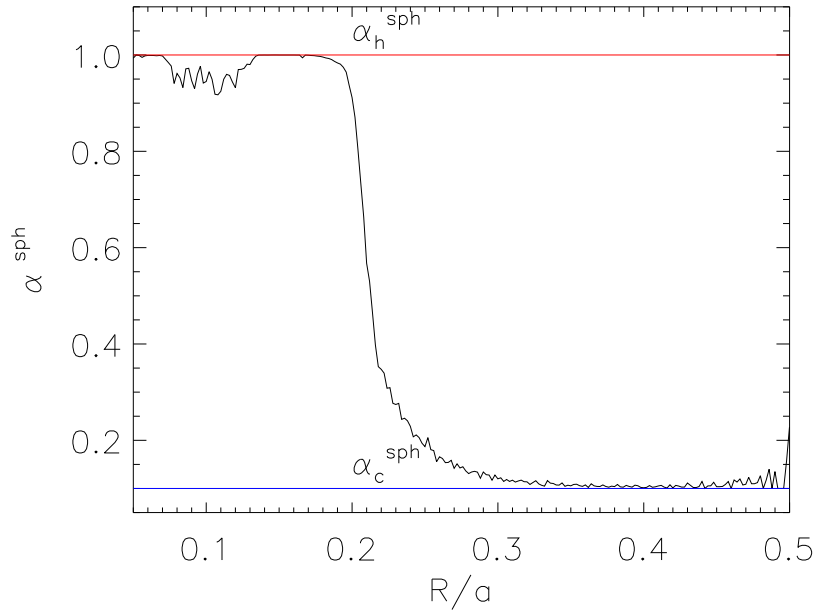


FIGURE 4.7. Radial profile of the artificial viscosity parameter during an outburst. For comparison the  $\alpha$  in the hot and cold states is displayed.

Typically 20-30% of the particles in the disc are accreted onto the black hole during an outburst. The bottom panel in fig. 4.6 shows the disc immediately after the outburst. Comparing to the top panel, it is apparent that the inner disc has lost a substantial number of particles. The surface density in the inner disc is now approximately equal to eq. (4.11) with  $K_{\min} = 4.79$ . During quiescence the disc regains the mass it lost in outburst and the cycle repeats.

Figures 4.8 and 4.9 show snapshots of the evolution of the surface density and viscous dissipation in the disc during an outburst and fig. 4.10 the mass accretion rate onto the black hole during the outburst. The first snapshot is immediately before the outburst. The outburst is triggered in the inner disc and a density wave moves outwards and inwards pushing more of the disc into the hot state. In this way a significant fraction of the disc is accreted. During the outburst there is far more azimuthal variability in the disc, this is particularly apparent in the surface density plot where spiral “arms” can be seen. Consequently the range in surface density is greater during an outburst. The dissipation in the disc is larger during an outburst with much of the additional dissipation

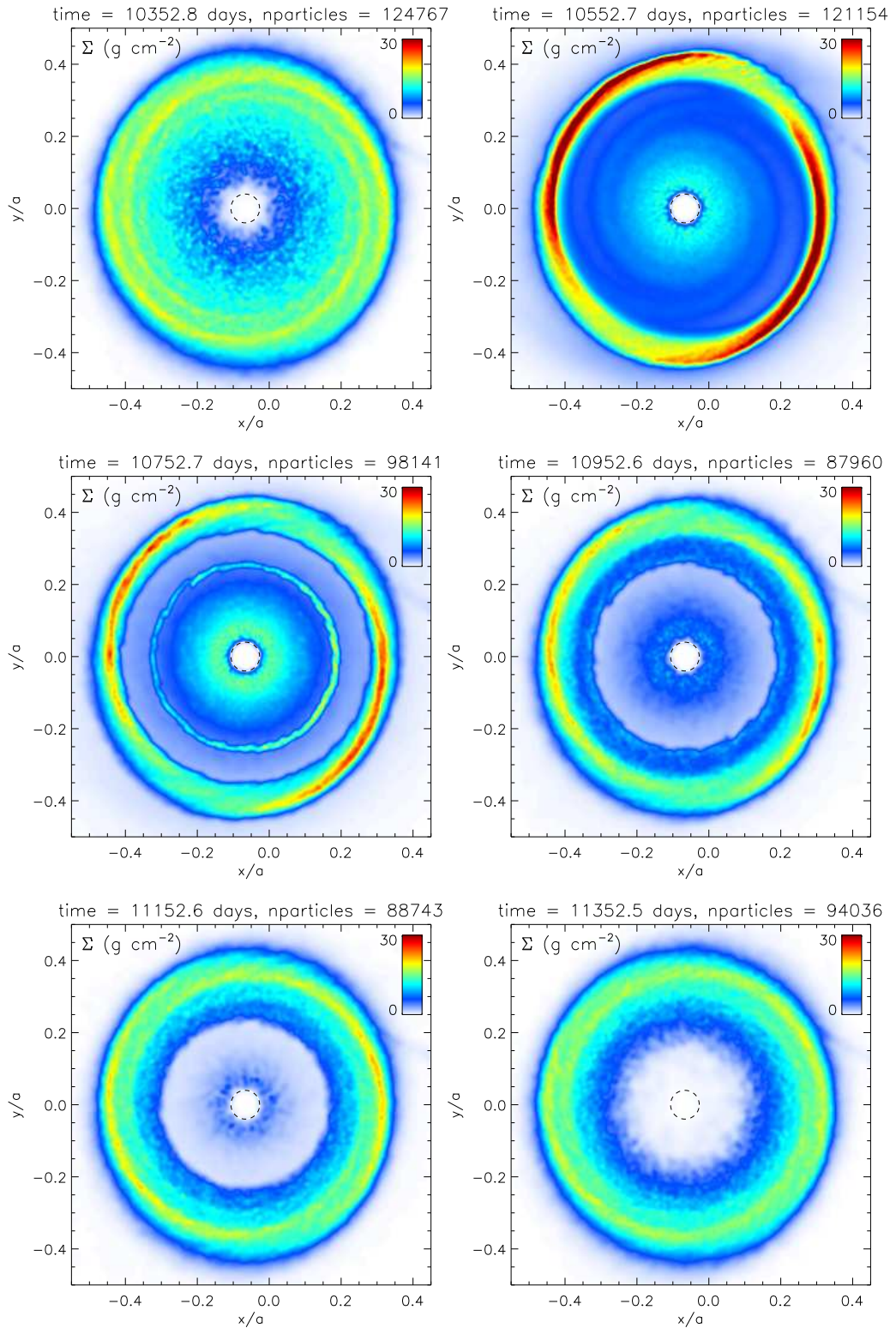


FIGURE 4.8. Snapshots of the Surface density ( $\text{g cm}^{-2}$ ) through an outburst at 200 day intervals. Note the central part of the disc (dashed circle) is not modelled in the simulation.

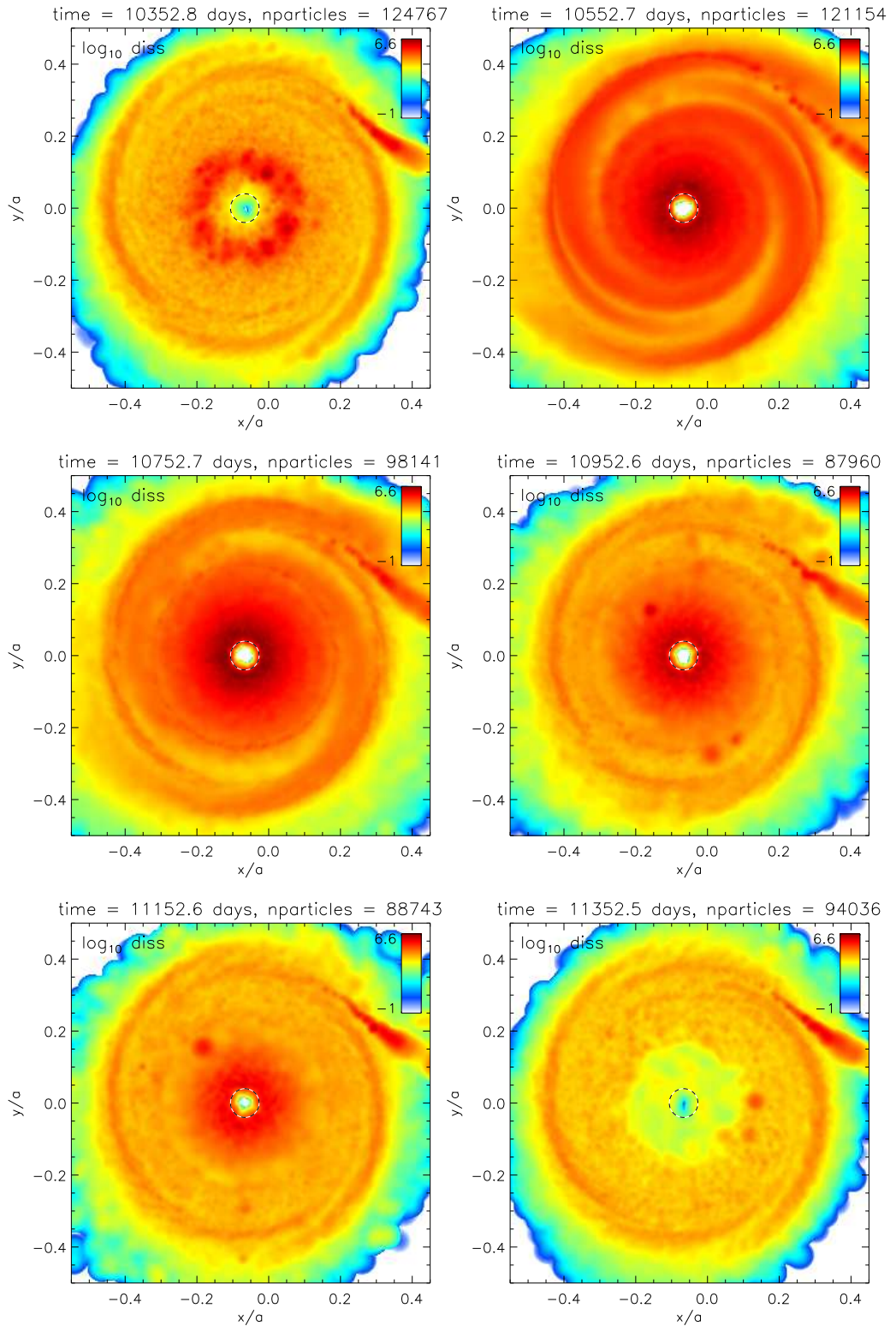


FIGURE 4.9. Snapshots of the viscous dissipation in the disc through an outburst at 200 day intervals. Colour scale is in log code units.

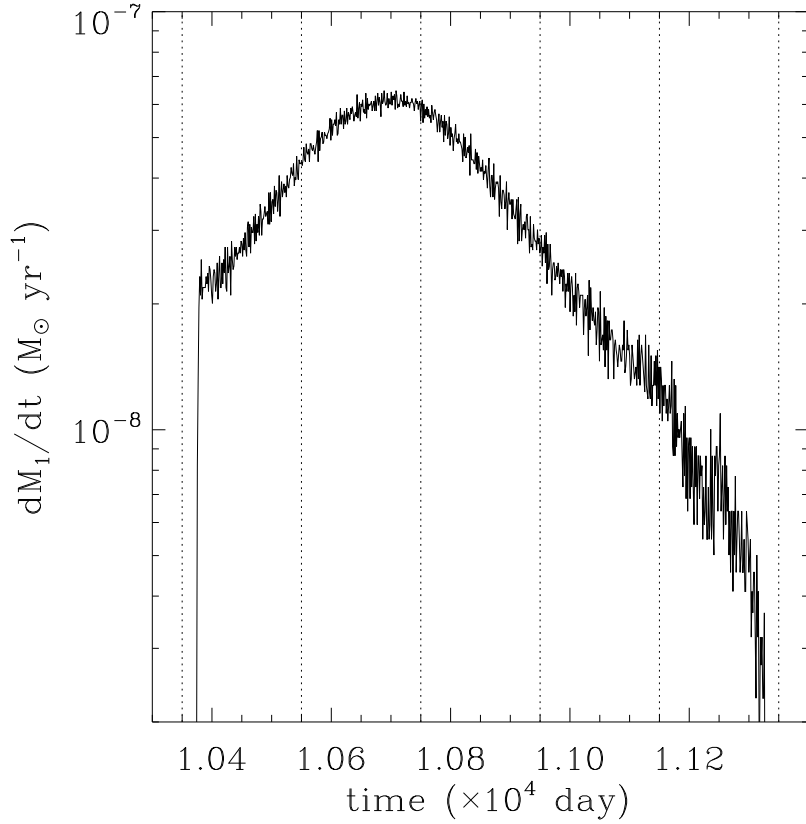


FIGURE 4.10. Mass accretion rate onto the black hole during the outburst depicted in figs. 4.8 and 4.9. Dotted lines denote the time of the snapshots.

in the inner disc. This is what one would expect. The accretion rate is non-uniform, local density variations particularly evident in the middle left panel of fig. 4.8 lead to a variable accretion rate. As in fig. 4.6 the depletion of the inner disc can be clearly seen. Figure 4.11 shows the history of a simulation once it has reached a steady state where approximately the same fraction of the disc is lost during an outburst. The mass accretion rates as functions of time of all the simulations in this work are in §A. Figure 4.11 is the raw output from the code which must be scaled by the methods described in §4.3.6. The effects of increasing  $\alpha_{h/c}$  and decreasing the disc mass is to compress both the outburst time and the quiescent time. Indeed, in contrast fig. 4.11 the quiescent time is several orders of magnitude greater than the outburst time, in effect  $t_{\text{rec}} \sim t_{\text{q}}$ . Additionally the mass accretion rate onto the black hole is also affected by the changes to the disc mass and viscosity. With particle masses being scaled upwards by a factor of  $K_{\text{max}}/K_{\text{max}}^{\text{sph}} \sim 4500$  and outburst prolonged by a factor of  $\sim \alpha_h^{\text{sph}}/\alpha_h^{\text{real}} = 10$ ,  $\dot{M}_1$  is scaled from few  $10^{-8} M_{\odot} \text{ yr}^{-1}$  to few  $10^{-5} M_{\odot} \text{ yr}^{-1}$ . This is several orders of mag-

nitude greater than the Eddington accretion rate of GRS 1915+105 ( $3 \times 10^{-7} M_{\odot} \text{ yr}^{-1}$ , using eq. (1.14)), hence the plateau observed in  $R_{\text{irr}}$  common to all the simulations<sup>2</sup>.

#### 4.4.2 Changing $\alpha_{\text{hot/cold}}$

Figure 4.12 shows the effect of varying  $\alpha_h$  and  $\alpha_c$  on  $t_{\text{out}}$ ,  $t_{\text{rec}}$  and duty cycle. The results presented are of the simulations alpha h [1 – 4] and alpha c [1 – 3]. The values for the  $\alpha$  displayed in fig. 4.12 are the “real” values of the artificial viscosity parameter, i.e. smaller than the values used in the code by a factor of 10. The timescales are scaled as described in §4.3.6. For numerical reasons it was decided that  $K_{\text{max/min}}$  would not be changed with  $\alpha_{h/c}$ , as demanded by eqs. (4.3) and (4.4). Changing  $K_{\text{max/min}}$  in conjunction with  $\alpha_{h/c}$  would force the disc into a persistent hot state. However the scaling method described can account for this deficiency in the setup.

The outburst time is roughly governed by the viscous time at the outermost part of the outburst and is given by (Pringle 1981),

$$\begin{aligned} t_{\text{out}} &\sim t_{\text{visc}} = \frac{1}{\alpha_h \Omega_K (H/R)^2} \\ &\sim 170 \left( \frac{\alpha_h}{0.1} \right)^{-1} \left( \frac{(H/R)_{\text{out}}}{0.03} \right)^{-2} \left( \frac{R_{\text{out}}}{a} \right)^{3/2} \text{ yrs.} \end{aligned} \quad (4.30)$$

where eq. (1.15) has been used and  $a = 7.5 \times 10^{12} \text{ cm}$ . During the outburst the inner disc is switched into the hot, more viscous, state as described in §1.3.3. One would expect that variations of the viscosity in the cold state to have little impact on  $t_{\text{out}}$  which is confirmed by fig. 4.12. If the approximate values of  $H/R \sim 0.03$  (fig. 4.13a) and  $R_{\text{out}} = 0.3a$  are used then  $t_{\text{out}} \sim 2.8/\alpha_h$ . This simple analytic upper estimate matches the calculated outburst times well (fig. 4.13b) given that  $H/R$  is not constant with  $R$  or time and  $R_{\text{out}}$  is not necessarily the same for each simulation.

The effect of  $\alpha_h$  on the recurrence time is more complicated, with increasing and decreasing  $\alpha_h$  from the value of 0.1 both reducing  $t_{\text{rec}}$ . Examining fig. A.4 the trend with increasing  $\alpha_h$  is shorter outbursts with an increased  $\dot{M}$ . This is mirrored in the number of particles accreted during an outburst, which decreases with  $\alpha_h$ . The disc in the simulations was allowed to reach a steady state, therefore  $t_{\text{rec}}$  can be approximated by the time required to replenish the disc (see eq. (4.27)) and the mass lost in an outburst.

<sup>2</sup>In the simulations we calculate  $\dot{M}_1$  at a radius of  $0.04a > R_{\text{Schw}}$  due to the lack of resolution in the inner disc. This is not the rate at which matter will arrive at  $R_{\text{Schw}}$  as some material will likely be lost in a wind. However the accretion rate is still expected to be super-Eddington at  $R_{\text{Schw}}$

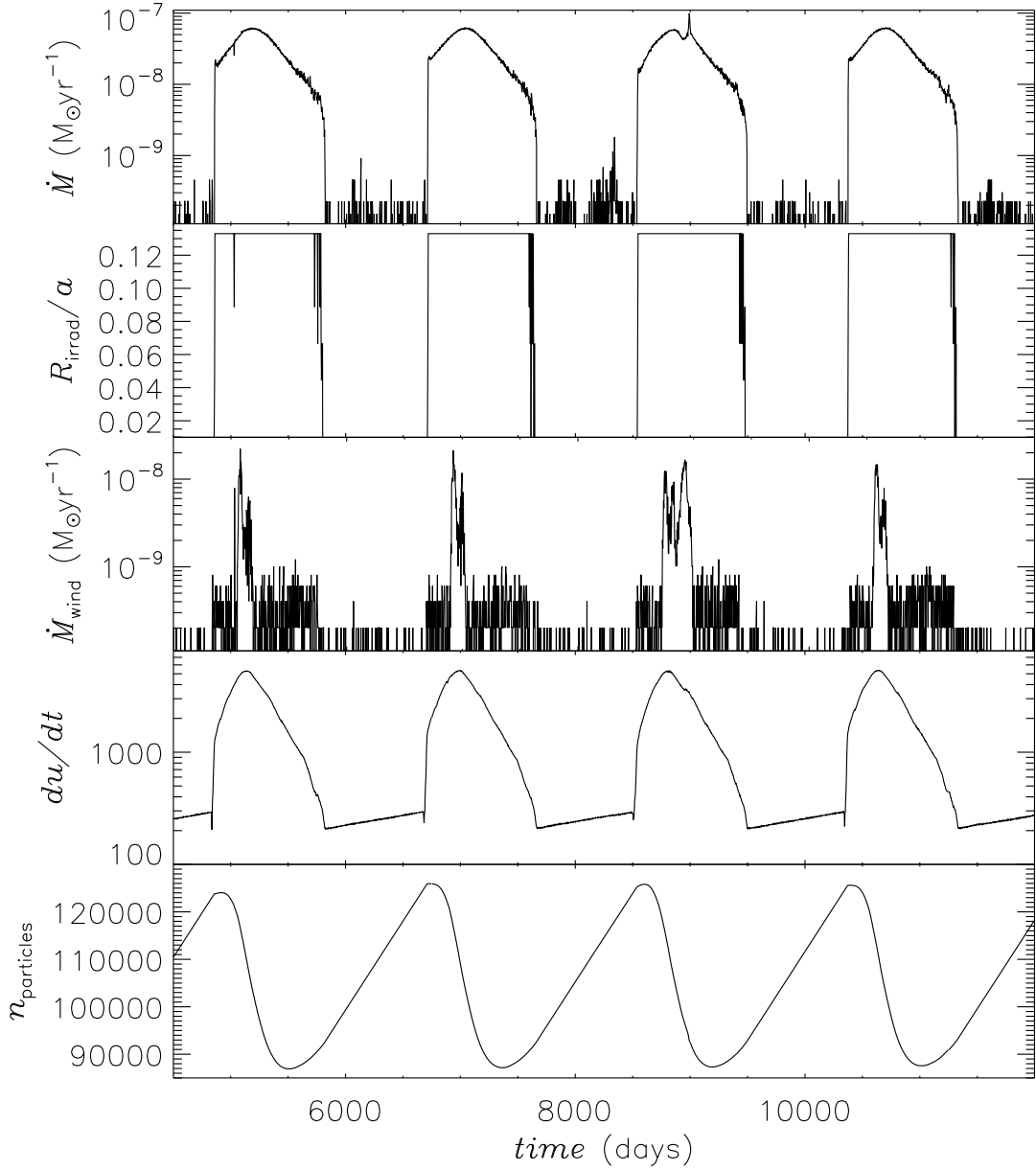


FIGURE 4.11. Plot of central accretion rate, irradiation radius, Eddington wind loss, dissipation (code units) and number of particles in the simulation. With  $K_{\text{max}} = 55$  and  $K_{\text{min}} = 4.79$ , the particle mass is  $\sim 1.1 \times 10^{-12} M_{\odot}$ .

When  $\alpha_h = 0.05$  the disc loses  $\sim 54000$  particles during an outburst, while  $\sim 38000$  particles are lost when  $\alpha_h = 0.15$ . When  $\alpha_h$  is increased the mass/particles in the inner disc are removed from the disc quickly. This limits the matter waves described in §1.3.3

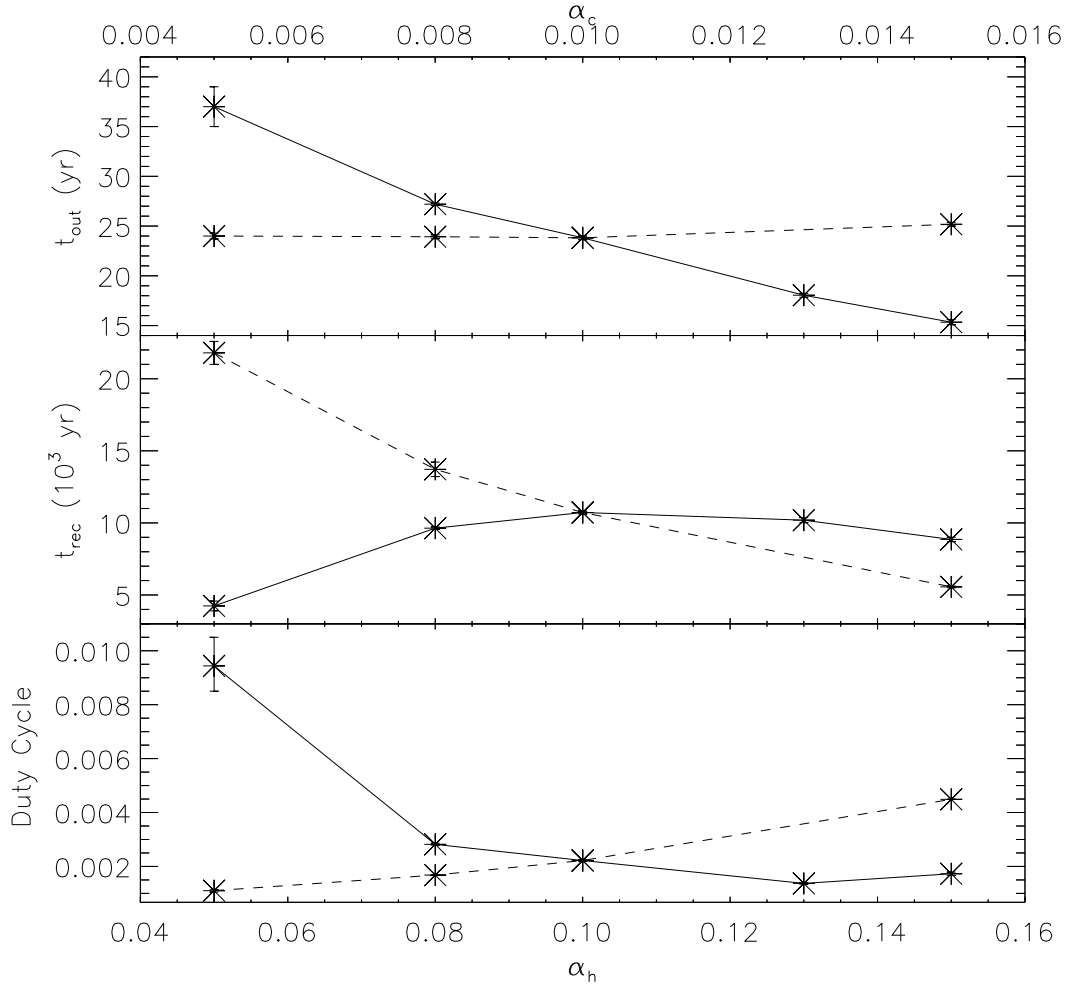
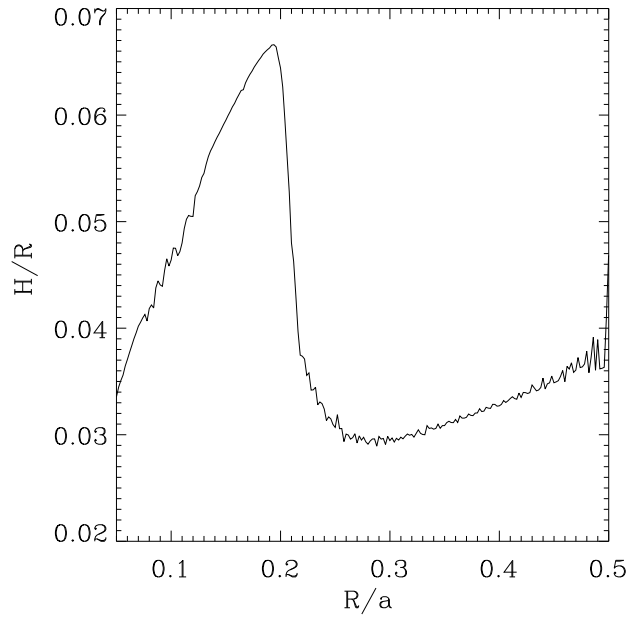
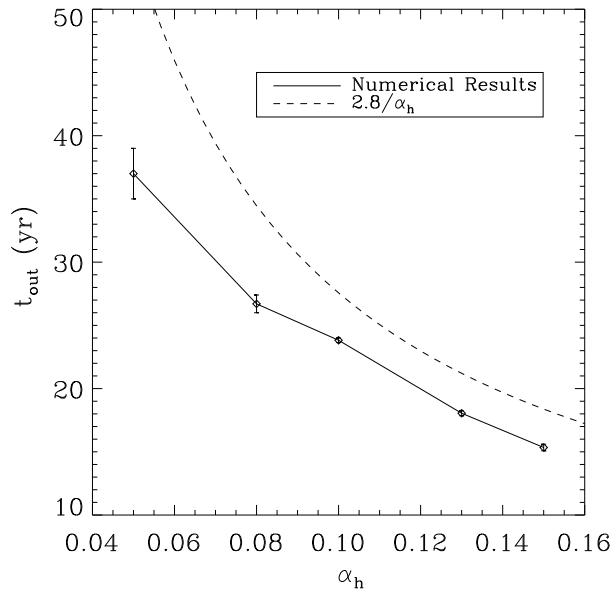


FIGURE 4.12.  $t_{\text{out}}$ ,  $t_{\text{rec}}$  and duty cycle shown as a function of  $\alpha_{\text{hot}}$  (solid line) and  $\alpha_{\text{cold}}$  (dashed line). N.B. the values of  $\alpha$  have been scaled to their correct values ( $\alpha = \alpha^{\text{sph}}/10$ )

that sustain the outburst.

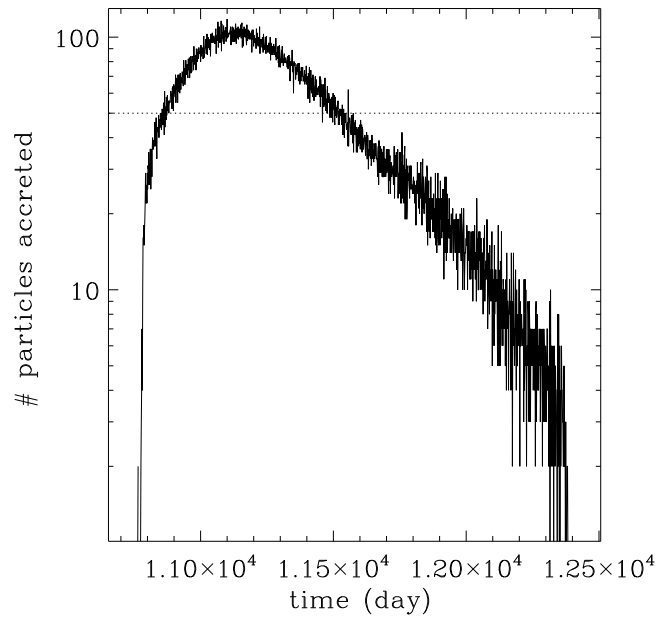
The above explanation satisfactorily explains the behaviour of  $t_{\text{rec}}$  for values of  $\alpha_h > 0.1$ . However at lower values of  $\alpha_h$  the recurrence time exhibits contradictory behaviour. This is a numerical effect caused by the small disc mass. The rate at which the disc is being replenished by  $-\dot{M}_2$  is several orders of magnitude too large for the disc mass in the simulations. This can be taken into account in most cases by the scaling method detailed in §4.3.6. However, certain parameter sets can render the scaling inaccurate. As shown in fig. A.4 (top panel), when  $\alpha_h = 0.05$  the outbursts are characterised by their long duration and low intensity. The rate at which particles are lost from the disc to the primary is lower than the transfer rate from the secondary for a significant portion of the outburst (see fig. 4.14a). This contradicts what is known about LMXBs in outburst,

(a) Plot of  $H/R$  against  $R$  during outburst

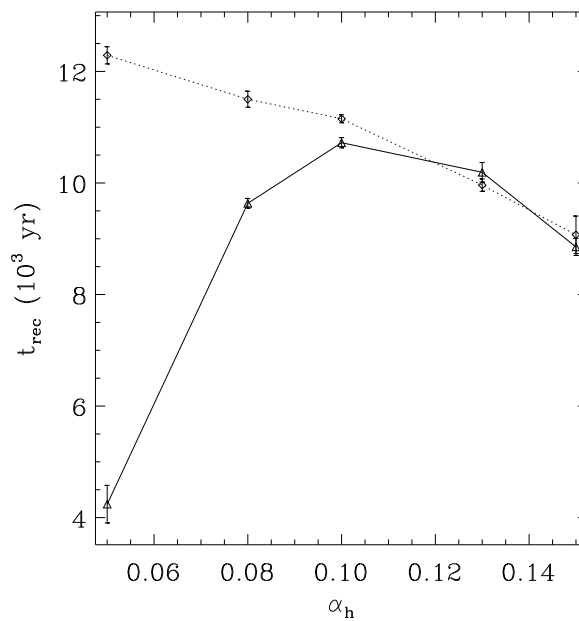
(b) Numerical results compared to an analytic approximation

FIGURE 4.13.

$\dot{M}_1 \gg -\dot{M}_2$ . In the simulation where  $\alpha_h = 0.05$  the disc gains in mass during an outburst. In effect the disc is close to being in a persistent high state and a constant outburst. The simulation alpha c 4 (lower panel in fig. A.5) is another example of a



(a) Comparison between particles accreted by the primary and the particles transferred from the secondary (dotted line) in 50 time steps



(b) Comparison between two different scaling methods for the recurrence time. Solid line depicts scaling method described in §4.3.6 and dotted line is the alternative method described in §4.4.2

FIGURE 4.14.

simulation on the cusp of entering a constant outburst. In this simulation  $\alpha_c = 0.02$ : this results in an increase in the viscosity of the cold state, consequently the mass transfer in the disc was too high for the simulation to reach a steady state.

Another way to estimate the  $t_{\text{rec}}$  is by assuming all of the mass lost in an outburst is regained during the quiescent phase. Knowing the mass transfer rate the quiescent time is given by eq. (4.27). The mass lost during the outburst  $M_{\text{out}}$  is calculated from the particle mass  $m_p \sim 1.1 \times 10^{-12} M_{\odot}$  and a count of the number particles accreted per outburst  $N_{\text{out}}$ , hence  $M_{\text{out}} = N_{\text{out}} m_p$ . Both scaling methods are displayed in fig. 4.14b. The large differences in  $t_{\text{rec}}$  between the two scaling methods when  $\alpha_h < 1.0$  highlight the deficiencies of the scaling method detailed in §4.3.6. The need to stay in the regime where the scaling method of §4.3.6 can be used (when  $\dot{M}_1 > -\dot{M}_2$ ) is the reason for the sometimes restricted range of parameters in this work. The alternative scaling method could be used, it is essentially an analytic method based on the outburst time rather than calculating the recurrence time independently from the code output. An effort was made to use both scaling methods when possible. A reduction in  $\alpha_c$  is associated with an increase in  $\Sigma_{\text{max}}$  (see eq. (4.3)). Making the assumption that the outer radius of the outburst and surface density profile of the disc are unaffected by this change<sup>3</sup> then more mass should be lost in the outburst for smaller values of  $\alpha_c$ . With a fixed  $-\dot{M}_2$  this results in increased recurrence times as seen in fig. 4.12. The lower panel in fig. 4.12 shows the variation of the duty cycle. While similar in amplitude, both  $\alpha_h$  and  $\alpha_c$  affect it in opposite ways. Neglecting the lower values of  $\alpha_h$  the duty cycle spans a limited range from 0.1% to 0.4% which emphasises that GRS 1915+105 spends the vast majority of the time in quiescence.

### 4.4.3 Changing $K_{\text{max/min}}$

The critical density profiles used are given by eq. (4.3) and (4.4) which are fitted to the vertical disc structure obtained by Cannizzo et al. (1988). This is by no means the only fit possible, with many possible models for the disc, other prescriptions can be found in Cannizzo & Wheeler (1984), Hameury et al. (1998) and Dubus et al. (2001) among others. As mentioned in §4.4.2 there is a limited range of  $K_{\text{max/min}}$  that results in transient behaviour of the discs. Figure 4.15 shows the effects of varying the  $K_{\text{max}}$  and  $K_{\text{min}}$  parameters on the duty cycle, outburst and recurrence times (remembering throughout that  $\Sigma_{\text{max/min}}$  are directly proportional to  $K_{\text{max/min}}$ ). Simulations used are sig max[1 – 3] and sig min[1 – 4] in table A.1.

<sup>3</sup>This assumption is examined in §4.4.3

Changing  $K_{\max/\min}$  can effect the outbursts in two ways: altering the mass lost from the disc during an outburst (see fig. 4.16) and changing the position where the outburst is triggered (also  $R_{\text{out}}$ ). The mass transfer rate is constant, therefore the changes in the recurrence time should be explained by the differing amounts of mass being lost from the disc in an outburst. Using eq. (4.21) the mass accreted can be expressed as

$$M_{\text{out}} \sim \frac{2\pi R_{\text{out}}^2}{3.05} (\Sigma_{\text{max}}(R_{\text{out}}) - \Sigma_{\text{min}}(R_{\text{out}})).$$

Hence  $M_{\text{out}} \propto \Sigma_{\text{max}}(R_{\text{out}})$  and  $\propto -\Sigma_{\text{min}}(R_{\text{out}})$ . Assuming for the moment a constant  $R_{\text{out}}$  then  $M_{\text{out}} \propto K_{\text{max}}$  and  $\propto -K_{\text{min}}$ . The middle panel in fig. 4.15 (and fig. 4.16) shows a trend in agreement with the above relation with the caveat that  $R_{\text{out}}$  will likely be different in the simulations.

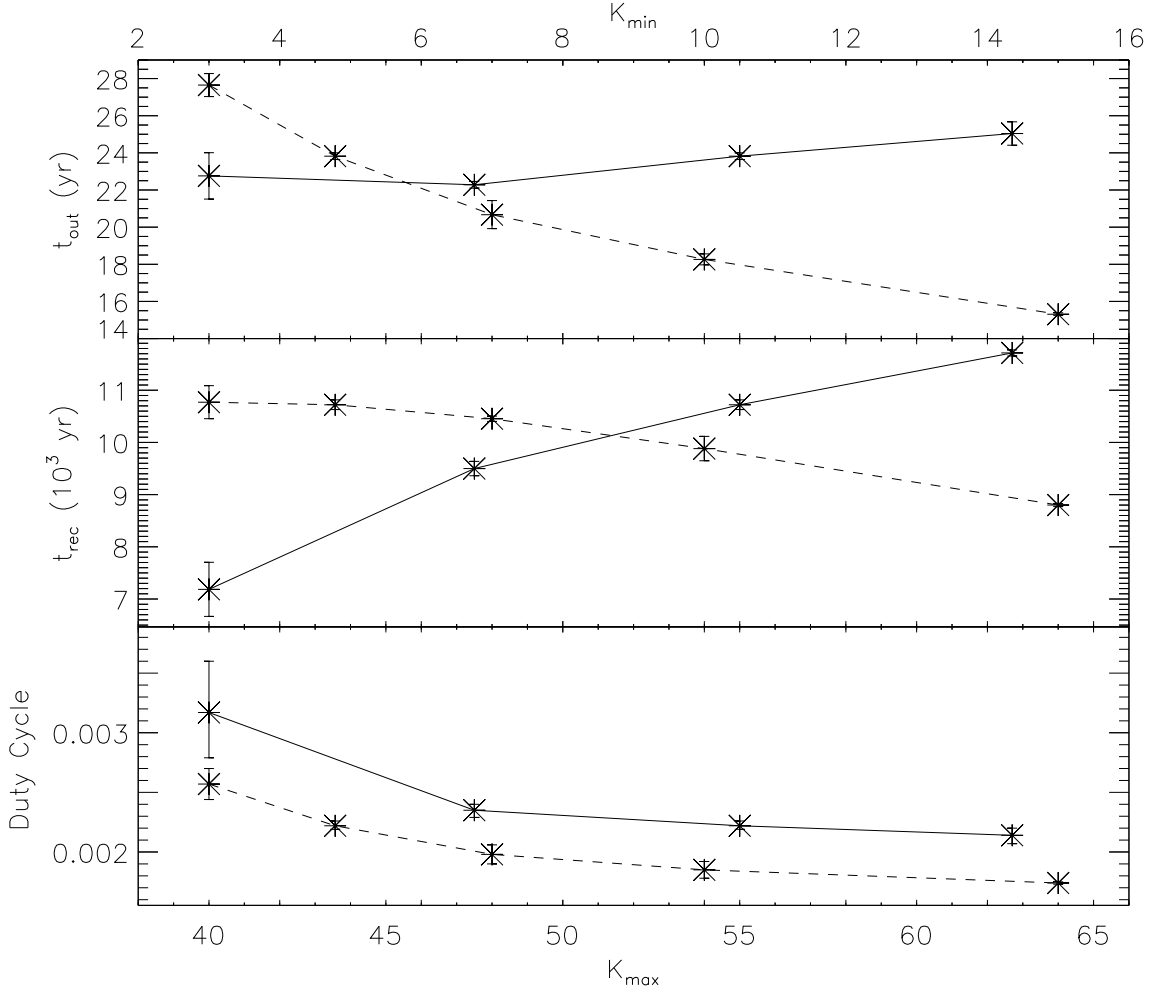


FIGURE 4.15.  $t_{\text{out}}$ ,  $t_{\text{rec}}$  and duty cycle shown as a function of  $K_{\max}$  (solid line) and  $K_{\min}$  (dashed line).

The top panel of fig. 4.15 depicts the variations in the outburst time. Once an outburst

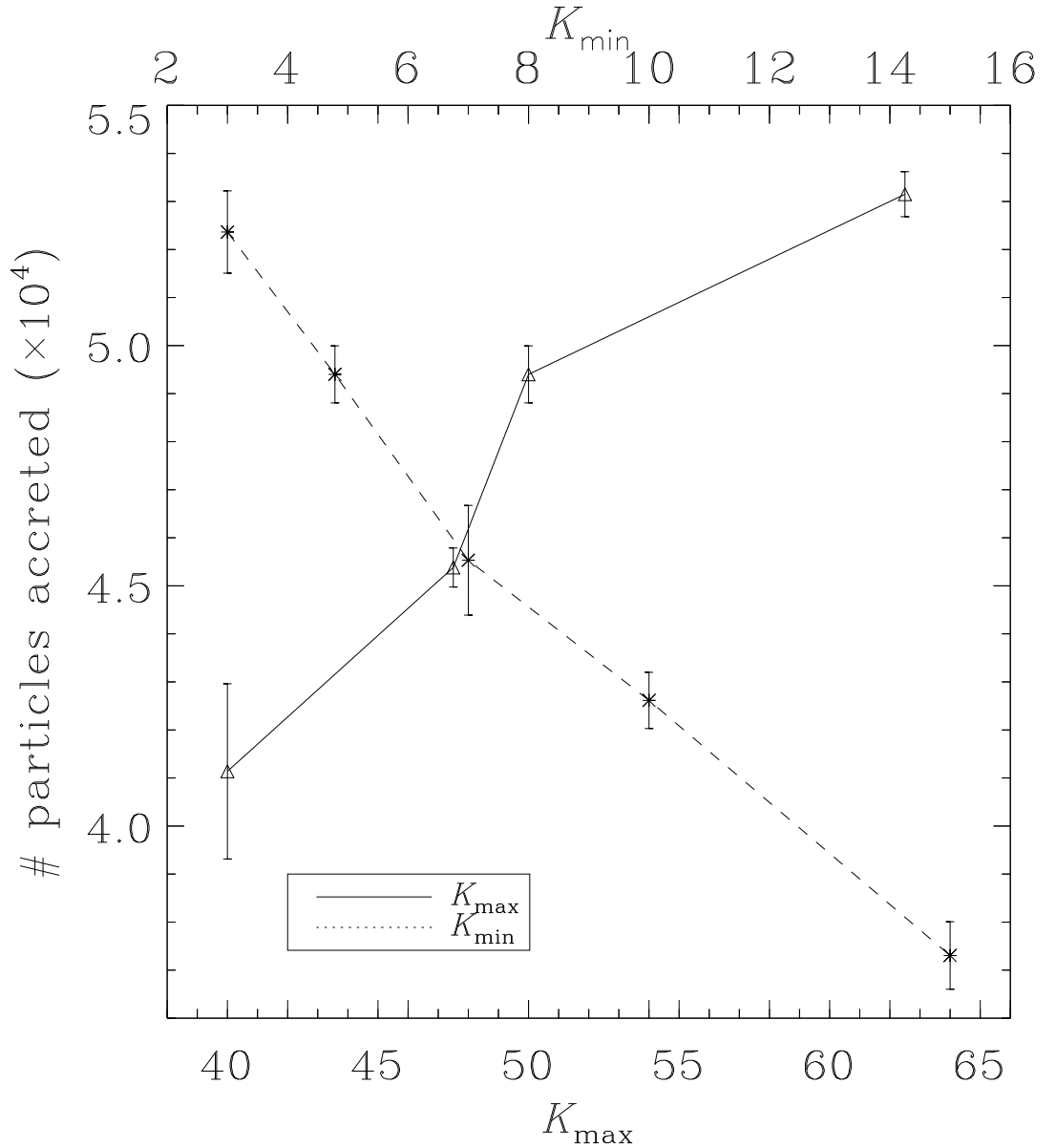


FIGURE 4.16. Plots of the number of particles accreted during an outburst as a function of  $K_{\min}$  and  $K_{\max}$

has been triggered the surface density in the unstable region of the disc drops until it reaches  $\Sigma_{\min}$ . As  $K_{\min}$  is increased the mass remaining in the disc after an outburst is likewise increased. The decrease in the mass accreted in an outburst as a function of  $K_{\min}$  has been discussed previously and is shown in fig. 4.16. Figure 4.17 shows the surface density of two simulations with differing values for  $K_{\min}$ , the snapshots show the surface density at a time when the outburst is  $\sim 80\%$  complete (the outbursts in question are depicted in fig. A.3, simulation names sig min 1 and sig min 4). The  $\Sigma$  profile of the disc has been significantly altered by the change in  $K_{\min}$ . When  $K_{\min} = 15 \text{ g cm}^{-2}$  the

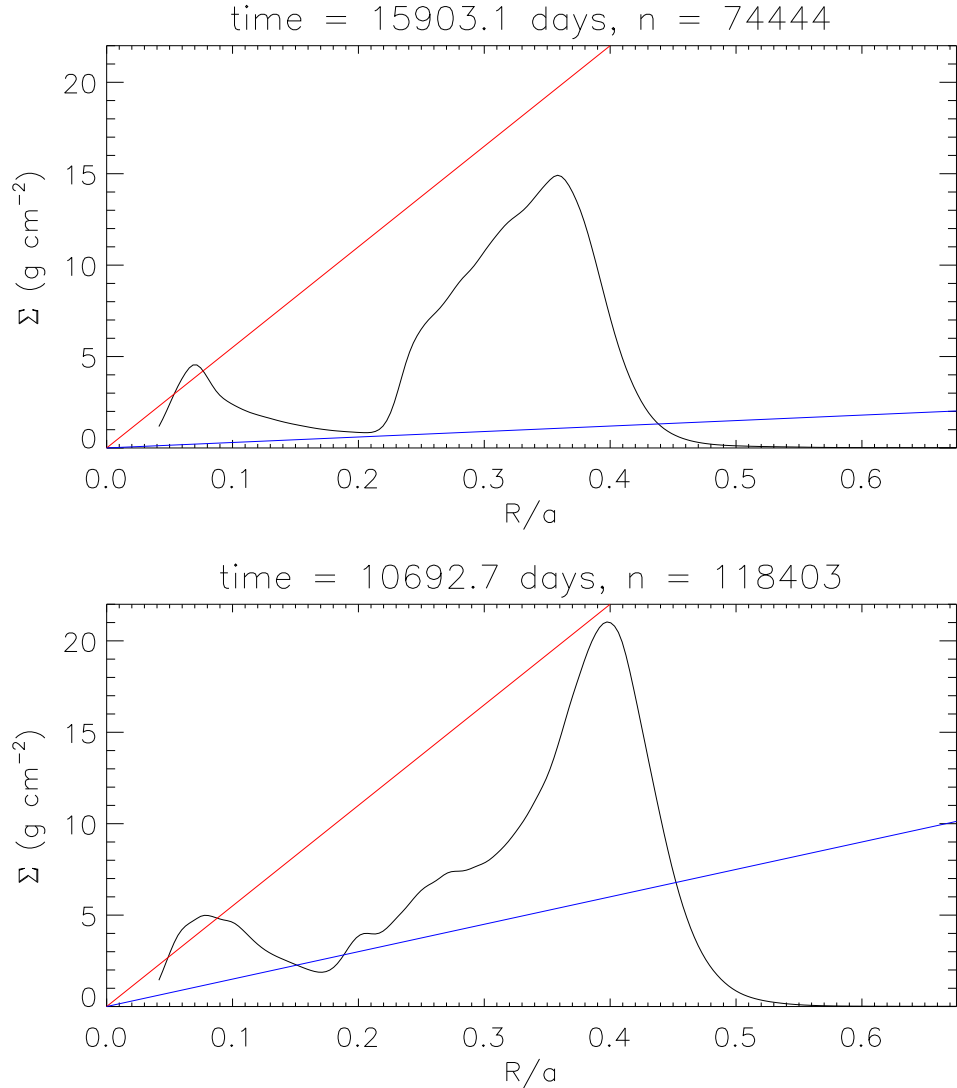


FIGURE 4.17. Top panel shows simulation with  $\Sigma_{\min} = 3(R/a) \text{ g cm}^{-2}$ . Bottom panel shows simulation with  $\Sigma_{\min} = 15(R/a) \text{ g cm}^{-2}$  (blue lines).

outer disc in particular builds up to higher surface densities. The inner disc also retains more mass post outburst, reducing the time taken for the disc to re-enter the cold state and the outburst to end.

The behaviour of the outburst time as a function of  $K_{\max}$  is more complicated. Firstly the location of the trigger for the outburst changes. When the slope of  $\Sigma_{\max}^{\text{sph}}$  is increased the outburst is triggered progressively closer to  $M_1$ . Figure 4.18 depicts the triggering points for outbursts for two different forms of  $\Sigma_{\max}$  (simulations sig max 1 and sig min 3 in fig. A.2). In the upper panel  $K_{\max} = 40$ : the outburst is triggered at  $R_{\text{out}} \sim 0.38a$  and propagates inwards (outside-in). In the lower panel  $K_{\max} = 62.7$ : the outburst is triggered at  $R \sim 0.12a$  and propagates outwards (inside-out) to a radius of  $R_{\text{out}} =$

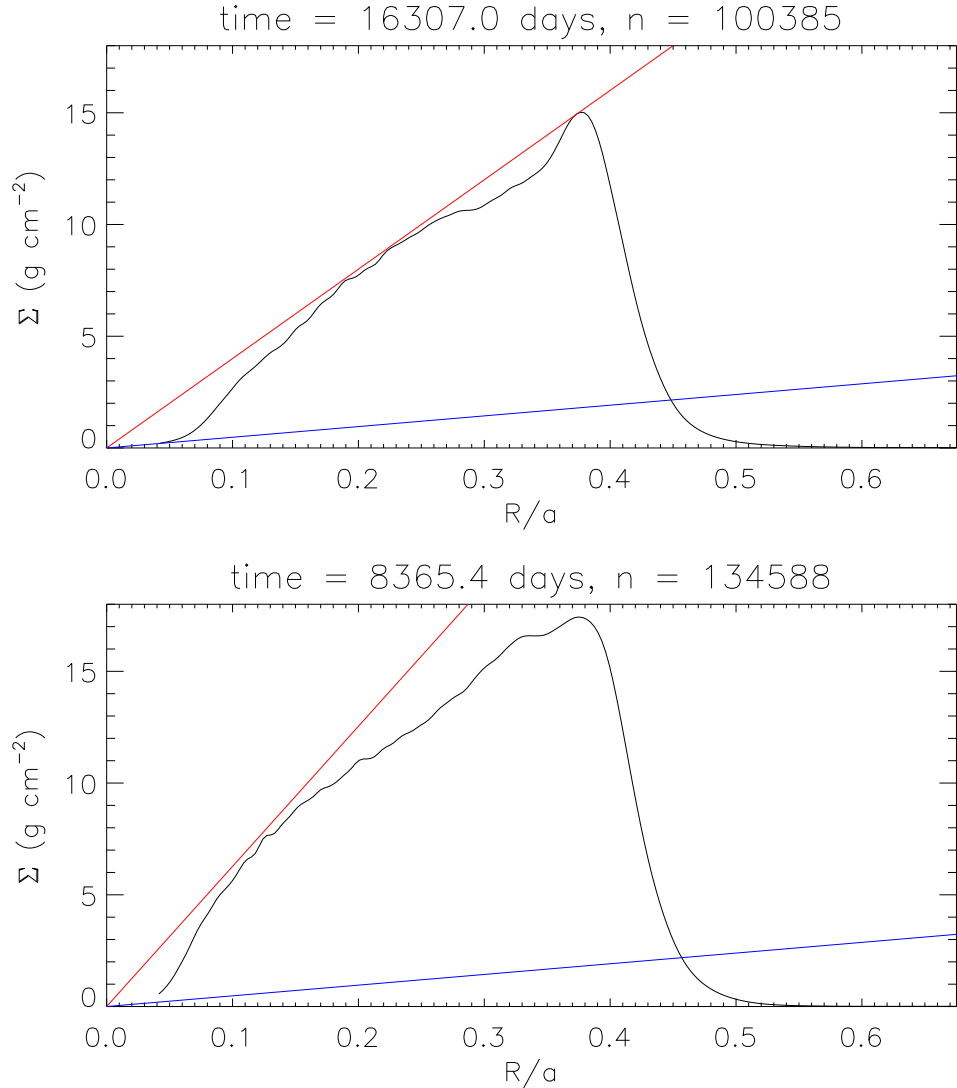


FIGURE 4.18. Top panel shows simulation with  $\Sigma_{\max} = 40(R/a) \text{ g cm}^{-2}$ . Bottom panel shows simulation with  $\Sigma_{\max} = 62.7(R/a) \text{ g cm}^{-2}$  (red lines).

0.3a. This change in outburst behaviour is shown in fig. 4.19. The lower three panels show outbursts in the simulations sig max [2 – 4] and all show a similar trend of an initial, nearly instantaneous increase in  $\dot{M}_1$  followed by a slow increase. In the top panel however, the outburst has a different form with the initial step rise in  $\dot{M}_1$  followed by a fast increase. This fast rise in  $\dot{M}_1$  is expected when outbursts are triggered in the outer disc (Smak 1984). For all the values of  $K_{\max}^{\text{sph}}$  used the outbursts either begin at  $\sim 0.3a$  propagating inwards or are triggered in the inner disc propagating outwards to  $\sim 0.3a$ . This accounts for the limited effect changing  $K_{\max}^{\text{sph}}$  has to the outburst time, keeping in mind eq. (4.30). Again the duty cycle spans a narrow range centred around 0.25%.

The mass transfer history of the simulation named sig max 4 is shown in fig. A.2

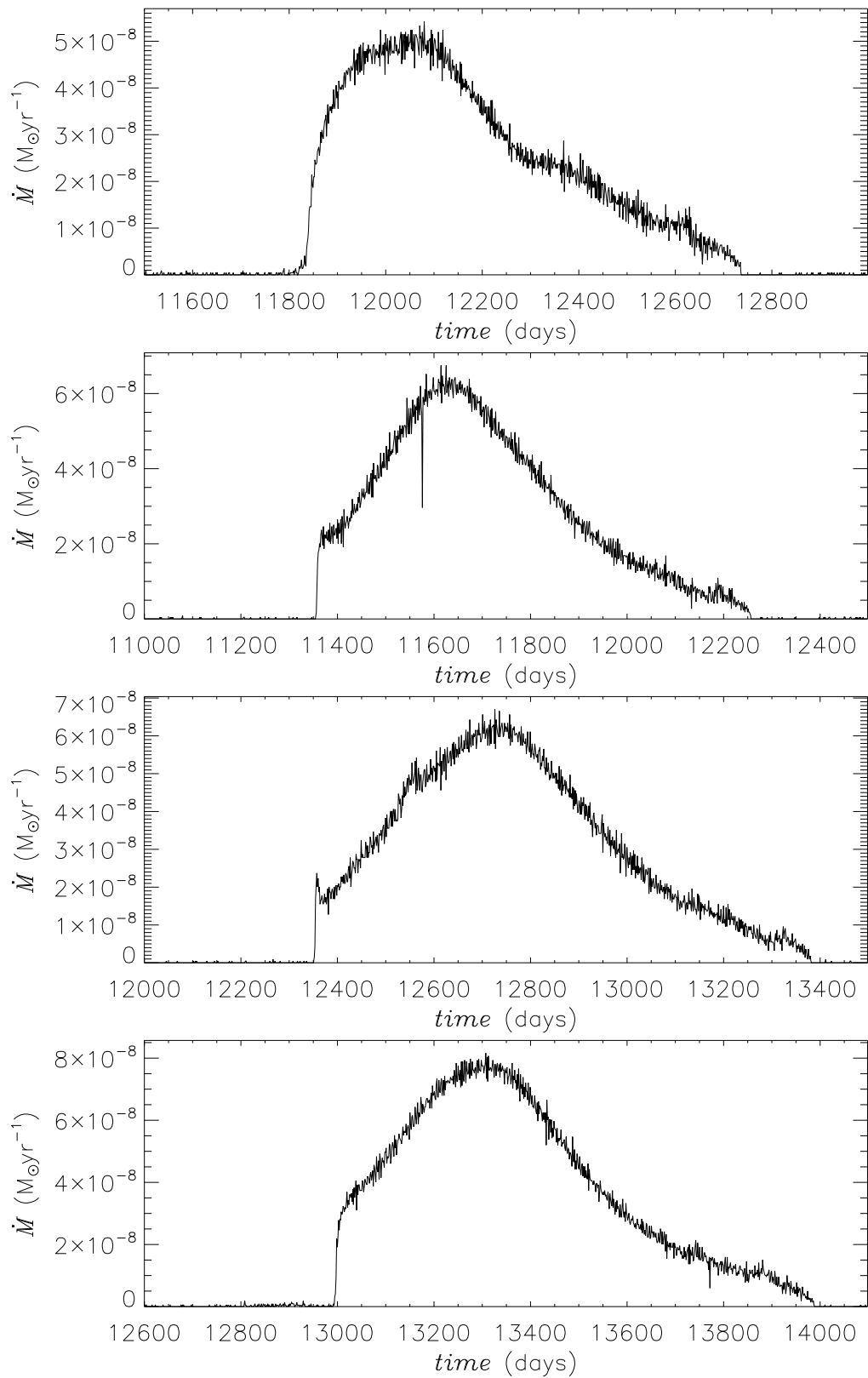


FIGURE 4.19. Individual outbursts in simulations sig max [1 - 4]

(lower panel). It exhibits unusual behaviour when compared to the other simulations discussed previously, particularly it fails to reach a steady state. This is not technically true, a steady state is reached but not one with a common outburst. The accretion history is explained in the following way: an outburst is triggered at a radius of  $\sim 0.2a$  which results in a significant fraction of the disc mass being lost. Following this the disc begins to build up in mass once again. Due to the steep slope of  $K_{\max}^{\text{sph}}$  the inner disc reaches  $\Sigma_{\max}^{\text{sph}}$  quicker than the outer parts of the disc and this time the outburst is triggered at  $\sim 0.1a$ . The outburst does not propagate to the depleted outer disc and a shorter outburst is the result. With the inner disc depleted the next outburst is triggered at a radius of  $\sim 0.2a$  once the outer disc has gained sufficient mass and the process repeats.

#### 4.4.4 Changing $\epsilon$ and $\lambda$

Figure 4.20 shows the effect of varying the  $\epsilon$  and  $\lambda$  parameters (simulations irr [1–4] and wind [2–4]). Similar to sig max 4, the simulation wind 1 exhibited two different outburst types. When increasing  $\lambda$  the higher the threshold, hence a less efficient wind. The efficiency of the wind has no noticeable effect on the outburst time (fig. 4.20 top panel). The surface density profile is not significantly affected by the change in  $\lambda$  and hence the outbursts are triggered and extend to the same  $R_{\text{out}}$ . As  $\lambda$  is decreased more mass is lost in the wind and the amount of mass accreted onto the black hole is correspondingly decreased (see table A.2). However this does not significantly change  $t_{\text{out}}$ , only reducing the mass accretion rate. As more mass is lost from the disc *via* the wind the recurrence time would be expected to increase. This is seen in fig. 4.20. There is a relatively large change in  $t_{\text{rec}}$  when  $\lambda$  becomes less than 1. For values above this limit the mass lost from the disc during quiescence is negligible. As increasing mass is lost from the disc in quiescence the longer the quiescent phase needs to be to ensure the disc build up in mass to trigger the next outburst. The change in  $\dot{M}_{\text{wind}}$  with differing values of  $\lambda$  is shown in fig. 4.21.

The parameter  $\epsilon$  controls the efficiency of the irradiation of the disc. This has two effects, both of which act to increase the duration of the outburst. The first of which is as follows, the surface density of an annulus can drop below  $\Sigma_{\text{min}}$  but the irradiation can keep the annulus in the hot state. This effect can be seen in fig. 4.5. The second effect is when the irradiation radius (see eq. (4.6)) is larger than the outer radius of the outburst would otherwise have been, given no irradiation. This results in areas of the disc entering the hot state which otherwise would remain cold. For values of  $\epsilon \leq 12 \times 10^{-4}$  (solid line and crosses) only the first effect of  $\epsilon$  is noticeable. Outbursts are typically triggered at a

distance of  $0.15 - 0.20a$  within the disc. The lower values of  $\epsilon$  result in an irradiation radius that is within the trigger radius (see triangles in fig. 4.22). Using eq. (4.19) with  $\epsilon = 7 \times 10^{-4}$  and assuming accretion at the Eddington rate for a  $14 M_{\odot}$  black hole gives  $R_{\text{irr}} \sim 0.14a$ . While the irradiation does ensure the exponential decay of the outburst (King & Ritter 1998) it does not have a large affect on the outburst time. Unfortunately, any further increase in the  $\epsilon$  parameter and the disc entered the regime  $\dot{M}_1 \sim -\dot{M}_2$  and a constant hot state. This numerical effect, caused by a mass transfer rate which is unphysically large for the disc mass used in the simulations, was overcome by allowing the disc to build up and then turning off particle injections. This is a valid approach in GRS 1915+105 as  $\dot{M}_1 \gg \dot{M}_2$ , indeed it is actually closer to the physical system than having a relatively high  $\dot{M}_2$  as before. While this would not result in a steady state simulation (and the results should be used with some caution), it does give an indication of the typical outburst times for high values of  $\epsilon$ . The outbursts themselves are shown in fig. 4.23 while the scaled  $t_{\text{out}/\text{rec}}$  and duty cycles are denoted by diamonds in fig. 4.20. In these simulations  $R_{\text{out}} = R_{\text{irr}}$ , using eqs. (4.6) and (4.30) the outburst time should then obey  $t_{\text{out}} \propto \epsilon^{3/4}$ . This is in good agreement with the diamond points which follow an approximate power law of  $t_{\text{out}} \propto \epsilon^{0.7}$ . For the highest value of  $\epsilon$  a substantial fraction of the disc is involved in the outburst with  $\sim 80\%$  of all the particles pre outburst being lost during the outburst. The quiescent time was calculated from the mass accreted using the method described in §4.4.2, the more mass lost from the disc the longer to replenish.

## 4.5 Discussion

### 4.5.1 Comparisons to other work

I have calculated the outburst and recurrence time scales for GRS 1915+105 and have examined the effects of varying various parameters in the system. This work can be viewed as an extension of the paper by Truss & Done (2006), in which they analytically estimated the outburst time scale. In their paper, the outburst time was calculated by considering the mass in the disc,  $M_{\text{disc}}$ ,

$$t_{\text{out}} = \frac{M_{\text{disc}}}{\langle \dot{M}_{\text{disc}} \rangle}. \quad (4.31)$$

From the models by Dubus et al. (2001) the surface density in the disc was thought to follow  $\Sigma_{\text{max}}$  in the inner 10% of the disc before flattening off at larger radii, resulting in

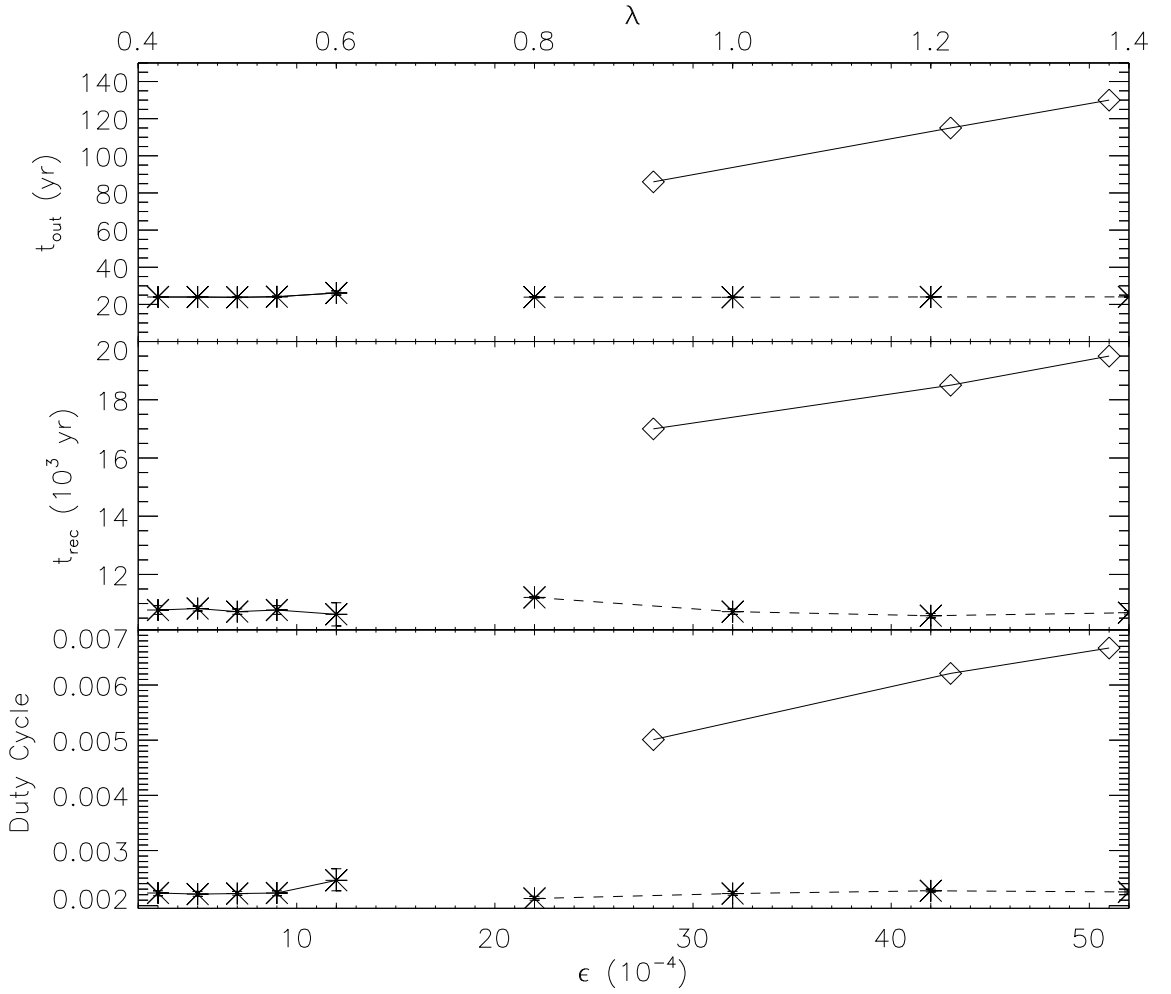


FIGURE 4.20.  $t_{\text{out}}$ ,  $t_{\text{rec}}$  and duty cycle shown as a function of  $\epsilon$  (solid lines) and  $\lambda$  (dashed line)

an approximation for  $M_{\text{disc}}$

$$M_{\text{disc}} = \int_{0.1R_{\text{disc}}}^{R_{\text{out}}} 2\pi R \Sigma_{\text{max}}(0.1R_{\text{disc}}) dR, \quad (4.32)$$

where  $R_{\text{out}}$  was given by eq. (4.6). Truss & Done (2006) approximated the time averaged mass loss from the disc by

$$\langle \dot{M}_{\text{disc}} \rangle = \langle \dot{M}_1 \rangle + \langle \dot{M}_{\text{wind}} \rangle - \dot{M}_2. \quad (4.33)$$

Knowing that  $\dot{M}_2 \ll \langle \dot{M}_1 \rangle$ , the inclusion of  $\langle \dot{M}_{\text{wind}} \rangle$  resulted in a maximum and a minimum length of an outburst for a given irradiation efficiency. The maximum is obtained when  $\langle \dot{M}_{\text{wind}} \rangle = 0$  and the minimum  $\langle \dot{M}_{\text{wind}} \rangle = \langle \dot{M}_1 \rangle = \dot{M}_{\text{Edd}}$ .

Table 4.1 compares this work with the outburst times predicted by Truss & Done

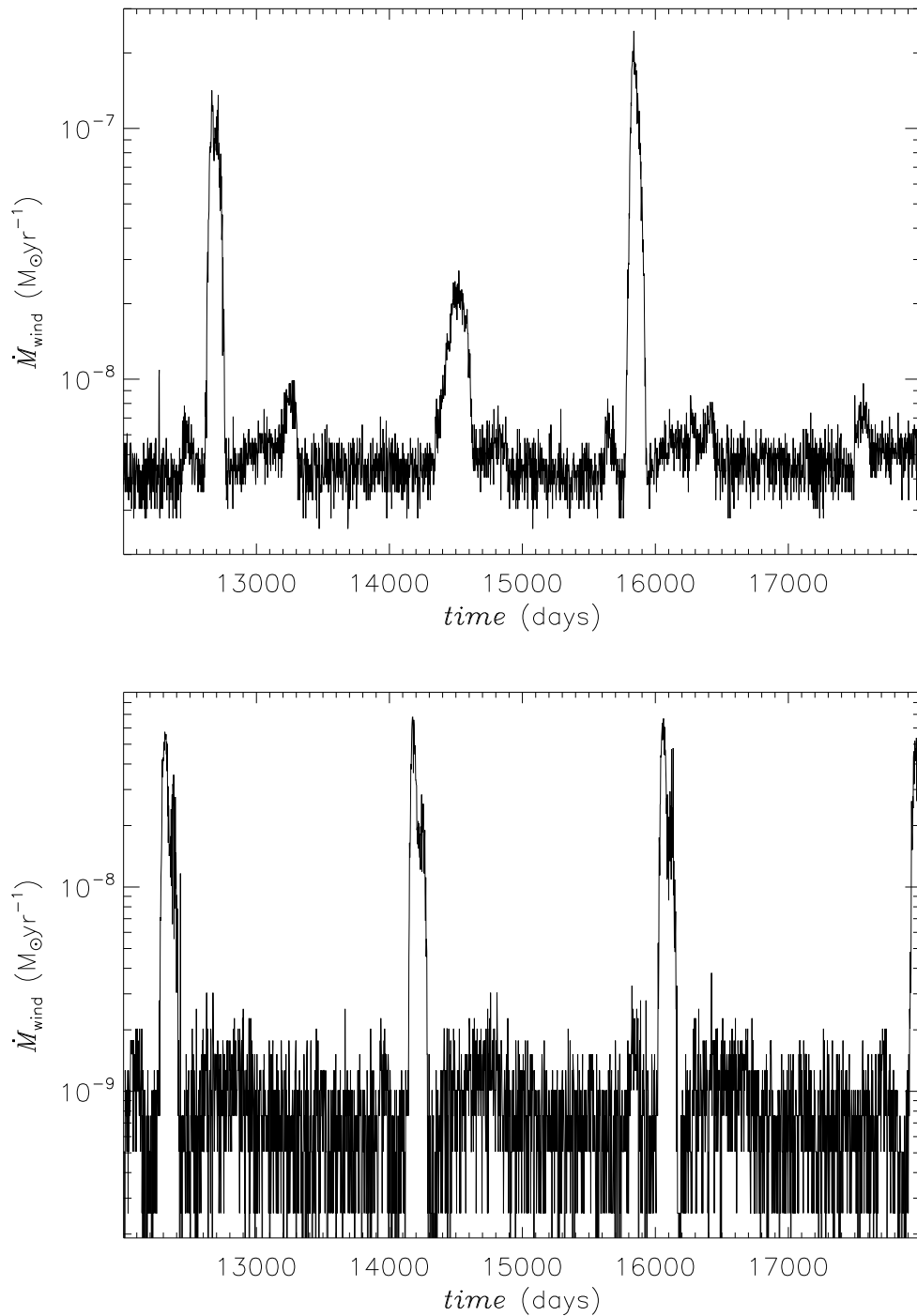


FIGURE 4.21. Plot of the mass lost via wind when  $\lambda = 0.6$  (top panel, wind 1) and  $\lambda = 0.8$  (bottom panel, wind 2)

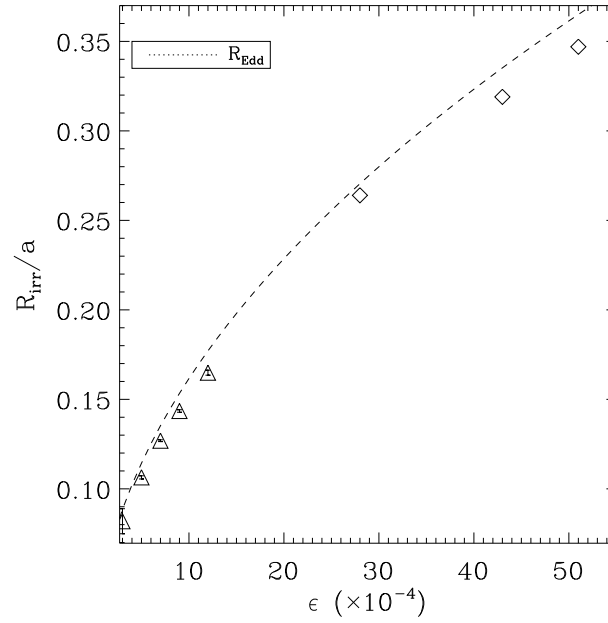


FIGURE 4.22. Plot of the average irradiation radius during an outburst as a function of  $\epsilon$  compared with eq.4.19

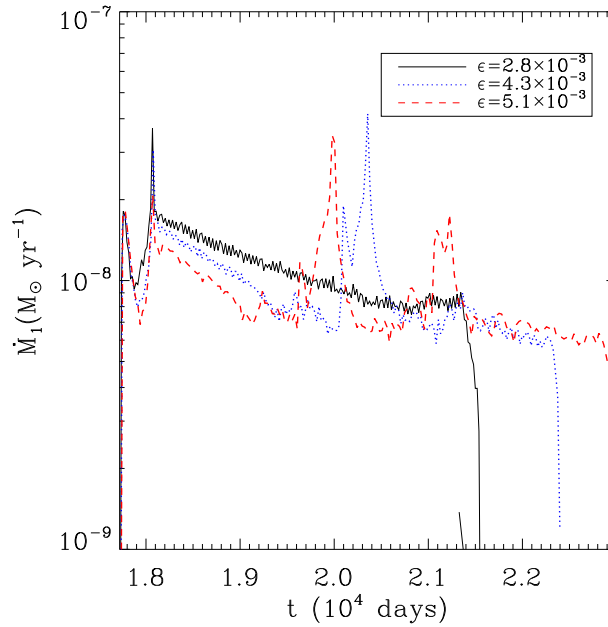


FIGURE 4.23. Plot of  $\dot{M}_1$  against time for 3 values of  $\epsilon$  during an outburst. Larger values of  $\epsilon$  increase the length of the outburst.

Table 4.1. Comparison of the predicted outburst times of Truss & Done (2006) (first set) and this work (second set). Truss & Done (2006) predicted outburst times for  $\langle \dot{M}_{\text{wind}} \rangle = 0$  and  $\langle \dot{M}_{\text{wind}} \rangle = \dot{M}_{\text{Edd}}$  respectively.

	$\epsilon$ ( $\times 10^{-3}$ )	$R_{\text{irr}}$ ( $a$ )	$t_{\text{out}}^{\text{max}}$ (yr)	$t_{\text{out}}^{\text{min}}$ (yr)
T & D	0.17	0.07	4.7	2.3
	0.69	0.13	21	10
	1.6	0.2	47	23
	2.8	0.27	85	42
	4.3	0.33	130	66
	5.1	0.36	160	76
This work	0.3	0.08	$23.9 \pm 0.2$	
	0.5	0.11	$24.0 \pm 0.3$	
	0.7	0.13	$23.8 \pm 0.2$	
	0.9	0.14	$24.1 \pm 0.3$	
	1.2	0.16	$26.1 \pm 1.1$	
	2.8	0.27	86	
	4.3	0.33	115	
	5.1	0.36	130	

(2006). For values of  $\epsilon < 0.7 \times 10^{-3}$  I predict outburst times greater than those by Truss & Done (2006). This is due to their approach of assuming the irradiation radius determines the region of the disc consumed in the outburst. As discussed in §4.4.4 in the low  $\epsilon$  regime the irradiation radius is not the primary factor determining the extent of the outburst, rather it is the triggering point of the outburst (typically at  $0.1\text{-}0.2a$ ). When  $\epsilon \geq 0.9 \times 10^{-3}$  my predictions are comfortably within the limits proposed by Truss & Done (2006). Figure 4.24 displays the data in table 4.1. With the exception of low irradiation efficiencies the results presented here are consistent with Truss & Done (2006). Table 4.1 shows the large variation of the outburst time when  $\epsilon$  is allowed to vary. The duration of the current outburst of GRS 1915+105 in conjunction with these numerical models may provide some evidence of the irradiation efficiency in LMXBs.

## 4.5.2 Central accretion rate and the need for a wind

As mentioned in §4.4.1 the accretion rate measured at the inner boundary of the disc ( $R_{\text{in}} = 0.04a \sim 3 \times 10^{11}$  cm) in the simulations must be scaled up to  $\dot{M}_{\text{in}} \sim 10^{-5} M_{\odot} \text{ yr}^{-1}$ . As discussed, this is much larger than the Eddington rate of the black hole, i.e.  $\dot{M}_1 \sim 10^{-7} M_{\odot} \text{ yr}^{-1}$  at  $R_{\text{Schw}} = 4 \times 10^6$  cm. So far, the outburst of GRS 1915+105 has lasted

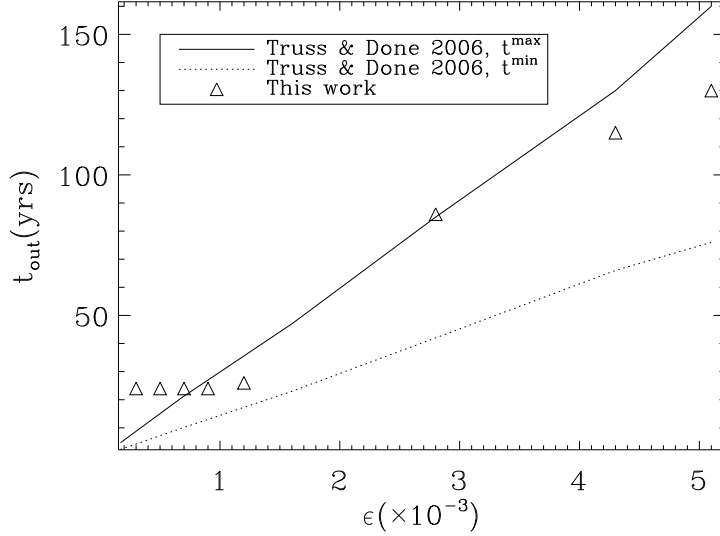


FIGURE 4.24. Comparison between this work and Truss &amp; Done (2006)

17 years. Using eq. (4.30) with  $H/R = 0.03$  and  $\alpha_h = 0.1$  gives a minimum outer radius  $R_{\text{out}} \sim 2 \times 10^{12}$  cm. Assuming the surface density profile of the disc follows  $\Sigma_{\text{max}}$  (given by eq. (4.10)), a rough upper estimate of the mass lost in the outburst is

$$M_{\text{out}} = \int_0^{R_{\text{out}}} 2\pi r \Sigma_{\text{max}}(R) dr \sim 2 \times 10^{-4} M_{\odot}. \quad (4.34)$$

This mass implies a transfer rate through the disc  $\dot{M}_{\text{in}} \sim 10^{-5} M_{\odot} \text{ yr}^{-1}$ , in agreement with the transfer rate we measure at the inner boundary of the simulations. If one were to make a more modest approximation for the disc mass and use eq. (4.32) then the disc mass is  $\sim 5 \times 10^{-5}$ . Implying a mass transfer rate in the disc of  $\sim 3 \times 10^{-6} M_{\odot} \text{ yr}^{-1}$ , still significantly greater than the Eddington limit.

Conversely, if one takes the mass accretion rate that is observationally inferred from the X-ray luminosity ( $\dot{M}_1 \sim 10^{-7} M_{\odot} \text{ yr}^{-1}$ ) as the transfer rate through the disc and use  $t_{\text{out}} = 17$  yrs, one gets  $M_{\text{out}} \sim 10^{-6} M_{\odot}$ . Again assuming the density profiles of eqs. (4.34) and (4.32) this implies an outer radius of between  $\sim 2 - 6 \times 10^{11}$  cm, which may be incompatible with a viscous/outburst time of 17 years. This contradiction implies that a significant fraction of the mass involved in the outburst is actually lost to the system in the form of a wind launched from the innermost regions not modelled in the simulations. Ueda, Yamaoka & Remillard (2009) concluded the existence of a thermally and/or radiation driven disc wind in GRS 1915+105 from the absorption lines in its spectra and inferred a launching radius  $\sim$  few  $R_{\text{Schw}}$ . This corresponds to the innermost regions our simulations. They estimate the mass loss rate in the wind to be

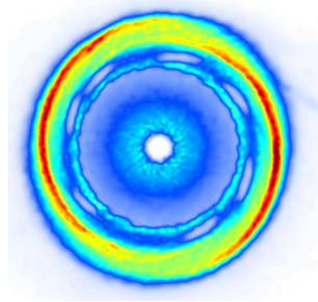
$\sim 5 \times 10^{-7} M_{\odot} \text{ yr}^{-1}$ , of the same order as the inferred accretion rate onto the black hole.

### 4.5.3 Conclusion

In this section I have described the galactic microquasar GRS 1915+105 and have outlined a numerical approach to model the accretion disc around the black hole contained within the system. In this model I described the physical processes that can affect the evolution of the disc and outlined several key parameters that will influence the length of both the outburst and the quiescent periods between the outbursts. From my analysis the length of the outburst is independent of the efficiency of the X-ray irradiation (when  $\epsilon \leq 10^{-3}$ ). With some confidence the outburst can be expected to last at least  $\sim 20 \pm 5$  yr. As the outburst began in 1992 this raises the possibility that the outburst could end in the next decade. If so this would indicate that the X-ray irradiation of the disc is negligible. If however the outburst persists any longer, the conclusion that significant fractions of the outer disc are being irradiated is unavoidable. The length of the outburst (which could last  $\sim 100$  yrs, see table 4.1) will provide information about the disc geometry and how efficient the irradiation is. It may also shed some light on how the disc is being irradiated, i.e. by a central source or by scattered X-rays. GRS 1915+105 can be expected to spend the vast majority of its lifetime in quiescence with a recurrence time calculated that is of the order  $\sim 9500 \pm 2500$  yr. This results in a duty cycle of the order of 0.002, which is lower than shorter period LMXBs ( $\sim 0.01$ ). This may have implications for modelling other long period LMXBs and the X-ray contents of the local Universe, both of which will be examined in §5.

# Chapter 5

## *Long period LMXBs*



“No one wins. One side just loses more slowly.”  
- Prez

*The Wire: Refugees [4.04]*

## 5.1 Introduction

There are 15 confirmed Galactic black hole X-ray binaries. The system known as GRS 1915+105 can be considered to be the most unusual. Discovered in 1992 (Castro-Tirado et al. 1992) it has a relatively long orbital period which sets it apart from all of the other Galactic black hole X-ray binaries, as discussed in §4. The outburst of GRS 1915+105 has been proceeding since 1992, far longer than any other LMXB. GRS 1915+105 has no known counterpart in the Galaxy but there is the possibility that similar objects can be observed in other galaxies.

Irwin (2006) analysed X-ray data from multiple epochs of two elliptical galaxies, M87 and NGC 1399. Despite the *Chandra* observations being carried out over a period of 5.3 yr in the case of M87 and 3.3 yr in the case of NGC 1399 there were several high luminosity sources that were persistent for the entire observation time. Irwin (2006) argues that these sources are most likely black hole LMXBs. Firstly M87 and NGC 1399 are elliptical galaxies with old stellar populations, ruling out any HMXBs (see §1.3). Secondly many of the sources have luminosities greater than  $8 \times 10^{38} \text{ erg s}^{-1}$ . This is the Eddington luminosity for a black hole with a mass of  $\sim 6 M_{\odot}$ . Explaining these sources with neutron stars ( $2 - 3 M_{\odot}$ ) emitting several times their Eddington luminosity is unlikely. Additionally, the high mass accretion rates required to sustain these luminosities rule out persistent sources. A donor star would be consumed in a few million years as all potential high mass donors have long since expired in these old stellar populations. The duration of the outbursts implies there is a large reservoir of mass in the accretion disc, suggesting these LMXBs most likely have long orbital periods and giant secondary stars. Several of these LMXB candidates ( $\sim 85\%$ ) appear to be associated with globular clusters. This is in stark contrast to our Galaxy, where no black hole has been found residing in a globular cluster. This raises the possibility that the potential LMXBs are, in fact, several combined lower luminosity ( $< 10^{37} \text{ erg s}^{-1}$ ) X-ray sources (Kundu, Maccarone & Zepf 2007). However, this might also be thought unlikely given the statistics of lower luminosity sources (Sarazin et al. 2003); a single high luminosity source is more likely than several lower luminosity ones.

Overall, 15 and 18 sources with luminosities  $> 8 \times 10^{38} \text{ erg s}^{-1}$  were detected in M87 and NGC 1399 respectively and all sources were detected in every observational epoch. Irwin (2006) estimated that the average outburst of these potential LMXBs would last  $\sim 50 \text{ yr}$ . This is strikingly similar to the predictions for the outburst length of GRS 1915+105 as predicted by Truss & Done (2006) and by my work in §4. If the duty cycles of the longer period systems are comparable to those of the short period systems (which

have  $t_{\text{out}} \sim 1$  month and  $t_{\text{q}} \sim 10$  yr) then the quiescence times for these objects will be long,  $> 1000$  yr.

The *Chandra* data used by Irwin (2006) showed no sources that could be identified as short period LMXBs. This may seem strange considering our Galaxy, in which GRS 1915+105 like objects are outnumbered 14-1 by shorter period LMXBs. However, the relatively short outbursts are likely to be missed by observations which last a matter of days. Irwin (2006) calculated that there were probably  $\sim 300$  short period LMXBs combined in the two galaxies. Considering the mass of M87 and NGC 1399 compared to that of our Galaxy this is reasonable. The ratio between the short and long period systems in both galaxies is 9, which is not inconsistent with our Galaxy considering the uncertainties associated with working with small number statistics. This is assuming the duty cycles of the longer period systems are comparable to their short period counterparts. Other studies (e.g. Ivanova & Kalogera (2006), Kim & Fabbiano (2004)) have drawn similar conclusions and deduce that LMXBs are an important contribution to the X-ray luminosity function (XLF) of elliptical galaxies. knowing the duty cycles of LMXBs is a key issue when modelling the XLF of elliptical galaxies. The standard approach is generally to assume a constant duty cycle (typically a few percent) or use a simple *ad hoc* prescription involving the mass transfer rate. Additionally there are proposed LMXB candidates in the Sculptor dwarf spheroidal galaxy (Maccarone et al. 2005) further demonstrating the importance of LMXBs in the XLFs of objects in the local universe. Ideally it would be desirable to perform numerical simulations, similar to the work in §4, for other possible systems but the size of the parameter space makes this prohibitively time consuming. I will investigate these long period LMXBs with red giant donors using a simple analytical model and try to gain an understanding of how their behaviour varies with orbital period. The initial motivation of this work was the sources detected by Irwin (2006), however the following model could be applied to a variety of system types.

## 5.2 The outburst

The maximum available mass to fuel an outburst is the total mass of the accretion disc. To estimate the mass in the disc at the start of an outburst I need to assume a surface density profile for the disc. It would be desirable to estimate this from the mass transfer rate and the quiescence time. However uncertainties in  $-\dot{M}_2$  and more importantly quiescence times  $> 1000$  yr, similar to GRS 1915+105, render this impossible. Proceeding in a

manner similar to §4, the mass of the disc is approximated by

$$M_{\text{disc}} = \int_0^{R_{\text{disc}}} 2\pi R \Sigma(R) dR. \quad (5.1)$$

Finally, I make the simple assumption that the surface density immediately preceding an outburst is, for all radii, equal to the critical surface density, as already given by eq. (4.3), rewritten here for clarity

$$\Sigma_{\text{max}}(R) = 11.4 \alpha_c^{-0.86} M_1^{-0.35} R_{10}^{1.05} \text{ g cm}^{-2}. \quad (5.2)$$

Combing the two equations above gives the total mass of the disc

$$M_{\text{disc}} = 2.4 \times 10^{21} \alpha_c^{-0.86} M_1^{-0.35} R_{\text{disc},10}^{3.05} \text{ g}, \quad (5.3)$$

where  $R_{\text{disc},10}$  is the disc radius in units of  $10^{10}$  cm. This is the total mass in the disc and hence the maximum available mass to fuel an outburst. From the strong dependence on  $R_{\text{disc},10}$  in eq. (5.3) it is clear that to obtain a reasonably accurate estimate for the mass in the disc a solid estimate for its radius is required.

### 5.2.1 Determination of the disc radius, $R_{\text{disc}}$

For this work I need to find some way to estimate the size of the accretion disc in an LMXB. It seems likely that the disc is a fraction of the binary separation,  $a$ . Simply setting the radius of the disc equal to,  $R_{\text{disc}} = \kappa a$ , with  $\kappa < 1$ , is one possibility. This is fairly crude and a better estimate involves the circularisation radius. This concept was introduced in §1.3.1 and will be further developed here. Making the substitution  $v_{\perp} = R_{L_1} \omega$ , where  $\omega = 2\pi/P_{\text{orb}}$ , in eq. (1.40) gives

$$R_{\text{circ}} v_{\phi}(R_{\text{circ}}) = R_{L_1}^2 \frac{2\pi}{P_{\text{orb}}}. \quad (5.4)$$

Combining this with eq. (1.41) gives an expression for the circularisation radius

$$R_{\text{circ}} \left( \frac{GM_1}{R_{\text{circ}}} \right)^{1/2} = R_{L_1}^2 \frac{2\pi}{P_{\text{orb}}}. \quad (5.5)$$

It is convenient to express  $R_{\text{circ}}$  in term of the binary separation,

$$\frac{R_{\text{circ}}}{a} = \left( \frac{R_{L_1}}{a} \right)^4 \frac{4\pi^2}{P_{\text{orb}}^2} \frac{a^3}{GM_1} \quad (5.6)$$

and finally using eq. (1.35)

$$\frac{R_{\text{circ}}}{a} = \left( \frac{R_{L_1}}{a} \right)^4 (1 + q). \quad (5.7)$$

As can be seen from eq. (5.7) the circularisation radius is heavily dependant on the distance from the primary to the  $L_1$  point. There have been many approximate analytical formulae to calculate  $R_{L_1}$  some of which are listed in table 5.1. Using any of these in eq. (5.7) would give an approximation for the circularisation radius. With regards to the size of the disc itself, Shahbaz, Charles & King (1998) used conservation of angular momentum arguments to show that when there is negligible accretion onto the primary the radius of the disc is  $R_{\text{disc}} \sim 1.36R_{\text{circ}}$  or  $\sim 0.7R_1$ . The value  $R_1$  is an approximation of the size of the Roche lobe of the black hole. Due to the form of eq. (1.36) the lobes are not spherical. A common approximation is to consider a sphere of radius  $R_1$  with the same volume as the lobe. The non trivial nature of eq. (1.36) means there is no exact formula describing  $R_1$ , but Eggleton (1983) describes a analytic approximation for all values of  $q$  (see table 5.1). A similar formula for the secondary star can be obtained by replacing  $q$  with  $q^{-1}$  (see §1.3.1). Truss & Done (2006) use a value for the circularisation radius given in Hessman & Hopp (1990) (again see table 5.1). All of the methods to calculate the disc radius detailed above are listed in table 5.1 and displayed in fig. 5.1. In LMXBs the mass ratio of the binary is often  $\sim 0.1$  and as such the expression for  $R_{L_1}$  from Plavec & Kratochvil (1964) appears to be unsuitable. The three remaining methods all give reasonable values for  $R_{\text{disc}}$  when compared to the numerical simulations of §4.

### 5.2.2 Outburst duration

Proceeding with the simple model discussed thus far, the disc of radius  $R_{\text{disc}}$  and mass  $M_{\text{disc}}$  goes into an outburst phase which lasts a time  $t_{\text{out}}$ . The outburst time is of the order of the viscous timescale at the disc outer radius. From Pringle (1981)

$$t_{\text{visc}}(R) = \frac{1}{\alpha \Omega_k (H/R)^2}, \quad (5.8)$$

at  $R_{\text{disc}}$ ,

$$t_{\text{out}} = t_{\text{visc}}(R_{\text{disc}}) = \frac{1}{\alpha} \left( \frac{R_{\text{disc}}^3}{GM_1} \right)^{1/2} \left( \frac{R}{H} \right)^2. \quad (5.9)$$

A typical value for  $H/R \sim 10^{-2}$  (Mayer & Pringle 2007) and  $\alpha = \alpha_h = 0.1$ . The total mass of the disc is accreted on this time scale giving a time-averaged mass accretion rate

Table 5.1. Analytic formula for the Roche lobe geometry

Estimates for distance from $M_1$ to $L_1$ <sup>a</sup>		
$\frac{R_{L_1}}{a} = 0.5 - 0.277 \log(q)$	$0.1 \leq q \leq 10$	Plavec & Kratochvil (1964)
$\frac{R_{L_1}}{a} = (1.0015 + q^{0.4056})^{-1}$	$0.04 \leq q \leq 1$	Silber (1992)
Estimates for the Roche lobe sphere <sup>b</sup>		
$\frac{R_1}{a} = \frac{0.49q^{-2/3}}{0.6q^{-2/3} + \ln(1 + q^{-1/3})}$	$0 < q < \infty$	Eggleton (1983)
Estimates for $R_{\text{circ}}$		
$\frac{R_{\text{circ}}}{a} = 0.0859q^{-0.426}$	$0.05 \leq q < 1$	Hessman & Hopp (1990)

<sup>a</sup> The distance from the centre of the primary to the  $L_1$  point in the binary.

<sup>b</sup> The sphere equal in volume to the Roche lobe of a star.

onto the primary  $\dot{M}_1 = M_{\text{disc}}/t_{\text{out}}$ . Using the formulation for  $R_{\text{disc}}$  of Hessman & Hopp (1990) and setting  $M_1 = 10 M_{\odot}$ ,  $M_2 = 1 M_{\odot}$  produces the dotted line in fig. 5.2. In this simple model the disc radius is proportional to the binary separation, which in turn varies as  $a \propto P_{\text{orb}}^{2/3}$  (see eq. (1.35)). Using this  $R_{\text{disc}} \propto P_{\text{orb}}^{2/3}$  in eq. (5.9) gives a simple relation for the outburst time,

$$t_{\text{out}}(\text{yrs}) \sim 8P_{\text{orb}}(\text{days}). \quad (5.10)$$

In the model detailed above, the disc is assumed to be entirely consumed in the outburst. This may be appropriate in the smaller discs of short period systems but as shown in §4, in longer period systems such as GRS 1915+105 the outer disc remains after an outburst. In comparison with the outbursts predicted in §4 which were on the order of  $\sim 25$  yr; this model predicts outbursts of  $\sim 300$  yr for a GRS 1915+105 like system. In the simulations carried out in §4 the outburst was typically triggered at a radius in the disc of  $R_{\text{trig}} \sim 0.1 - 0.2R_{\text{disc}}$ . This would reduce the outburst times predicted by eq. (5.10) by an order of magnitude. This begins a trend in this work, using information from the detailed model of GRS 1915+105 and generalising to other systems. It is known that X-ray radiation heating the disc can prolong an outburst (eg. Dubus et al. (2001), King & Ritter (1998)). This was discussed in §4.2.2 but for convenience the equation

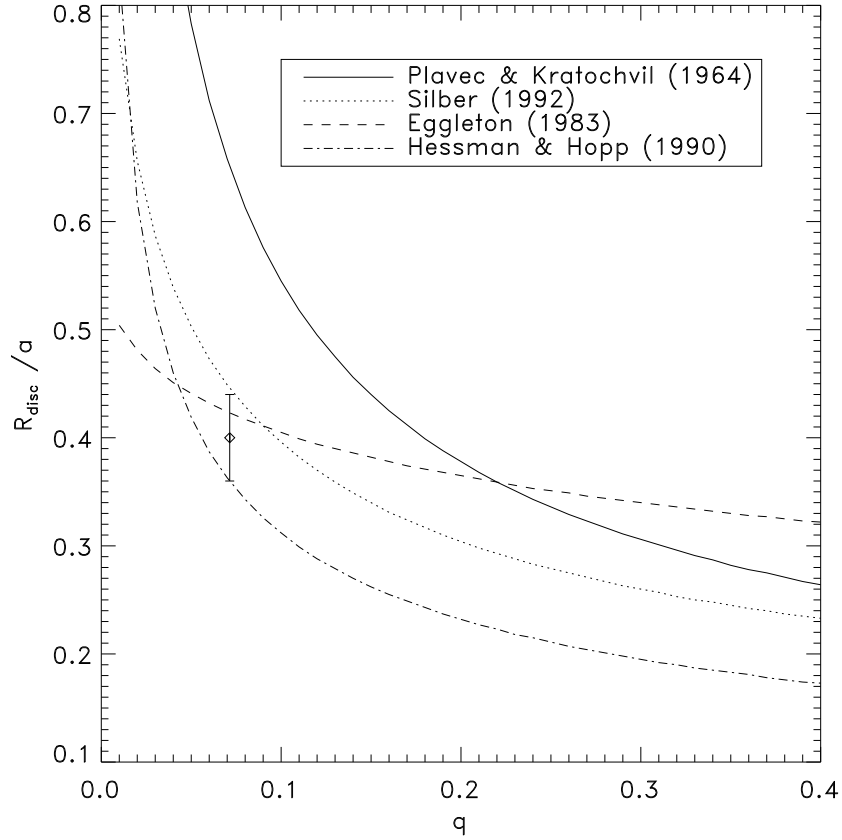


FIGURE 5.1. Different models for the radius for the disc. Solid line and dotted line use the  $R_{L_1}$  estimates from Plavec & Kratochvil (1964) and Silber (1992) respectively in eq. (5.7) to calculate  $R_{\text{disc}} = 1.36R_{\text{circ}}$ . The dashed line is  $R_{\text{disc}} = 0.7R_1$ , where  $R_1$  is estimate from Eggleton (1983). The dotted-dashed line is the  $R_{\text{disc}}$  used in Hessman & Hopp (1990). For reference a typical disc radius from simulations of GRS1915+105 ( $q = 1/14$ ) is shown as a diamond (see fig. 4.6)

describing the irradiation radius is repeated here,

$$R_{\text{irr}} = 2.7 \times 10^{11} \left( \frac{\epsilon}{10^{-3}} \right)^{1/2} \left( \frac{\eta}{0.1} \right)^{1/2} \dot{M}_{18}^{1/2} \text{ cm.} \quad (5.11)$$

Again  $\epsilon$  is the irradiation efficiency,  $\eta$  is the accretion efficiency and  $\dot{M}_{18}$  is the central accretion rate in units of  $10^{18} \text{ g s}^{-1}$ .

As discussed in §1.2.2 the Eddington limit caps the accretion rate onto any object. While the Eddington limit is only an estimate, significantly exceeding it over an extended period of time is unlikely. The result is a limit on the irradiation radius and an upper limit on the outburst time. If the outburst is triggered at some point in the disc,  $R_{\text{trig}} = \xi R_{\text{disc}}$  where  $\xi$  is a free parameter less than 1, the mass within this radius will fuel an outburst.

This mass will be accreted in a time  $t_{\text{visc}}(R_{\text{trig}})$ . The resulting average  $\dot{M}_1$  will cause a portion of the disc to be irradiated. This gives a new outer radius for the outburst  $R_{\text{irr}}$ , within which all of the mass will be accreted on a time scale  $t_{\text{visc}}(R_{\text{irr}})$ . This then gives an updated value for the average mass accretion rate. A simple model may be built where this proceeds iteratively until the central accretion rate converges (generally taking no more than 5 iterations). Figure 5.2 shows the result of adding the Eddington limit to the calculations of eq. (5.10). The irradiation efficiency was set to  $\epsilon = 10^{-3}$  and  $\xi = 0.1$ . The outburst time initially rises as  $R_{\text{disc}}$  the mass accretion rate onto the primary and the irradiation efficiency are such that the entire disc is irradiated and is accreted in the outburst. It is only when the period of the binary  $\sim 10$  days that the radius of the disc exceeds  $R_{\text{Edd}}$  (where  $R_{\text{Edd}} = R_{\text{irr}}(\dot{M}_{\text{Edd}})$ ) and  $t_{\text{out}}$  plateaus.

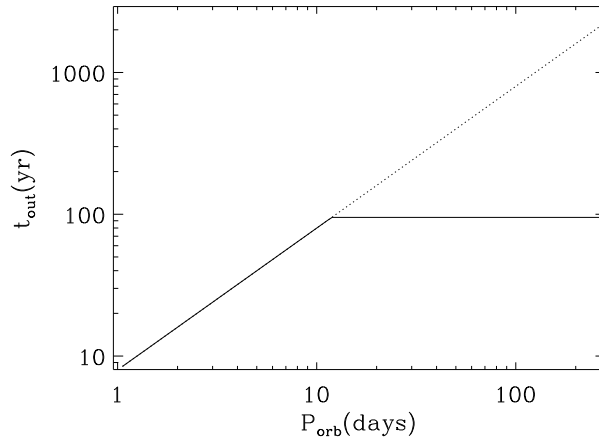


FIGURE 5.2. Plot of  $t_{\text{out}}$  varying with orbital period. Solid line is a model that includes the Eddington limit and has an outburst triggered in the inner disc. Dotted line is a model where the disc is totally consumed in the outburst.

### 5.2.3 A Different model for the disc surface density profile

The model assumed for the disc thus far is by no means the only one possible. Indeed it will likely be an over estimate of the disc mass. Truss & Done (2006) use a model for the disc of GRS 1915+105 that follows work by Dubus et al. (2001). The one-dimensional models carried out predict the surface density of a disc will follow  $\Sigma_{\text{max}}$  for the inner  $\sim 10\%$  of the disc,  $R_{\text{max}} = 0.1R_{\text{disc}}$ . In the outer disc the surface density plateaus resulting in a significantly less massive disc than detailed previously. From now on this model for the disc will be referred to as Model 2, while the model detailed previously will be referred to as Model 1. The mass of the disc is then as follows

$$M_{\text{disc}} = M(R < R_{\text{max}}) + M(R > R_{\text{max}}). \quad (5.12)$$

I assume the outburst is triggered at  $R_{\max}$  where  $\Sigma(R_{\max}) = \Sigma_{\max}(R_{\max})$ . The mass in the inner disc,  $M_{\max}$ , is given by

$$M_{\max} = M(R < R_{\max}) = \int_0^{R_{\max}} 2\pi R \Sigma_{\max}(R) dR, \quad (5.13)$$

with  $\Sigma_{\max}$  again given by eq. (5.2). Once again this mass is accreted on the viscous time (Pringle 1981) at  $0.1R_{\text{disc}}$ ,

$$t_{\text{visc}}(R_{\max}) = \frac{1}{\alpha} \left( \frac{10^{-3} R_{\text{disc}}^3}{GM_1} \right)^{1/2} \left( \frac{R}{H} \right)^2 \quad (5.14)$$

I now proceed in a manner the same as before. The mass of the inner disc and the viscous time provide an average  $\dot{M}_1$  for accretion onto the central object

$$\dot{M}_1 = \frac{M_{\max}}{t_{\text{visc}}(R_{\max})}. \quad (5.15)$$

Heating by X-ray radiation produced by the central object can push more of the disc into the hot state. If  $R_{\text{irr}}$  is greater than  $R_{\max}$  then the outer disc will be involved in the outburst. The extra mass beyond  $R_{\max}$  which is being kept in the hot state through irradiation is denoted by  $M_{\text{irr}}$ ,

$$\begin{aligned} M_{\text{irr}} &= M(R_{\max} < R < R_{\text{irr}}) = \int_{R_{\max}}^{R_{\text{irr}}} 2\pi R \Sigma_{\max}(R_{\max}) dR \\ &= \pi \Sigma_{\max}(R_{\max}) [R_{\text{irr}}^2 - R_{\max}^2]. \end{aligned} \quad (5.16)$$

This process is carried out iteratively until the central accretion rate converges. In the event that  $R_{\text{irr}} < R_{\max}$  then no additional disc mass enters the hot state and the outburst time is defined by  $t_{\text{visc}}(R_{\max})$ . I now define the value  $M_{\text{out}}$  as being the mass lost from the disc during an outburst. In Model 2  $M_{\text{out}}$  is given by

$$M_{\text{out}} = \begin{cases} M_{\max} + M_{\text{irr}} & \text{where } R_{\text{irr}} > R_{\max} \\ M_{\max} & \text{where } R_{\text{irr}} < R_{\max}, \end{cases} \quad (5.17)$$

while  $M_{\text{out}}$  for Model 1 is given by

$$M_{\text{out}} = \max [M(R < \xi R_{\text{disc}}), M(R < R_{\text{irr}})]. \quad (5.18)$$

For clarification fig. 5.3 displays the important characteristics of Model 2.

Figure 5.4 displays the mass lost in an outburst changing with orbital period for both

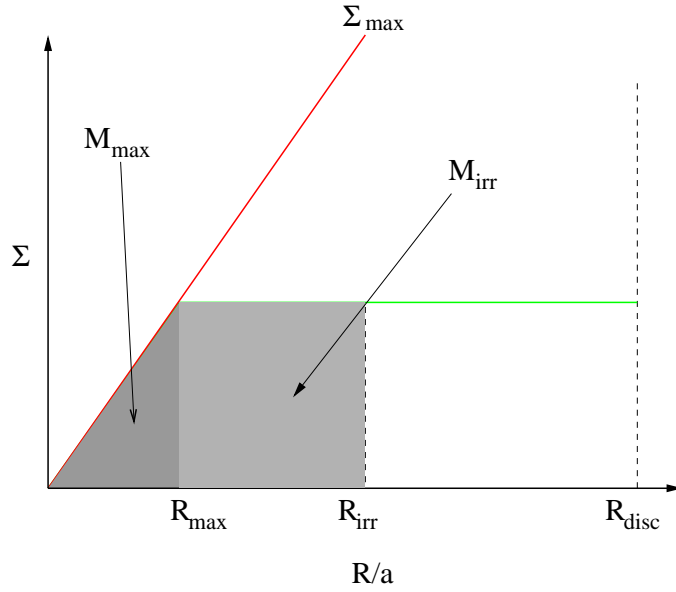


FIGURE 5.3. Diagram depicting Model 2. The green line is the surface density of the disc. N.B.  $R_{\text{irr}}$  can be less than  $R_{\text{max}}$ , in which case  $M_{\text{irr}} = 0$ .

models of the disc. In Model 1  $\dot{M}_1$  and  $\epsilon$  are such that  $R_{\text{irr}} > R_{\text{disc}}$  and the entire disc is irradiated. This continues until  $P_{\text{orb}} \sim 10$  days when  $R_{\text{irr}}$  has reached its Eddington limited value. The outburst time will remain constant until  $R_{\text{max}} > R_{\text{irr}}$  for longer orbital periods. For Model 2 the mass lost in the outburst is initially dominated by the irradiated portion of the disc, i.e.  $M_{\text{out}} \sim M_{\text{irr}}$ . The reduced mass in the disc however results in a smaller  $\dot{M}_1$  than in Model 1, hence an irradiation radius less than  $R_{\text{disc}}$ . This continues until  $P_{\text{orb}} \sim 100$  days, where the Eddington limit takes effect and the irradiation radius has reached its maximum value. From this point onwards  $M_{\text{out}}$  can no longer be considered to comprise solely of  $M_{\text{irr}}$ . The mass contained within  $R_{\text{max}}$  is now a significant fraction of  $M_{\text{out}}$ . When  $P_{\text{orb}} > 200$  days,  $R_{\text{max}} \rightarrow R_{\text{irr}}$  and the two models converge to the same mass lost in the outburst. To aid the discussion and prevent confusion several important definitions of both Model 1 and 2 are summarised in table 5.2

### 5.3 The quiescence time

The quiescence time is the time taken to replenish the mass lost from the disc during an outburst.

$$t_{\text{q}} = \frac{M_{\text{out}}}{-\dot{M}_2}, \quad (5.19)$$

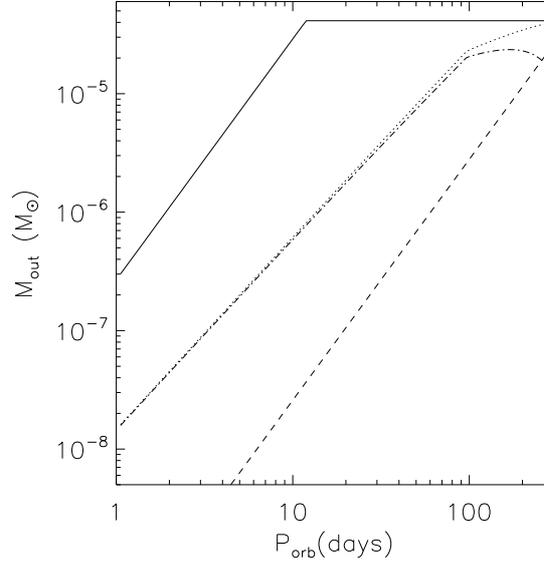


FIGURE 5.4. Plot of the mass lost from the disc in an outburst varying with orbital period. Solid line shows  $M_{\text{out}}$  for Model 1. The dotted line dashed line and the dotted-dashed line show  $M_{\text{out}}$ ,  $M_{\text{max}}$  and  $M_{\text{irr}}$  respectively for Model 2.

Table 5.2. Table of definitions used in both models of the disc

Model	Symbol	Definition
Model 1 & 2		
	$R_{\text{disc}}$	$1.36R_{\text{circ}}$ or $0.7R_1$
	$R_{\text{irr}}$	eq. (5.11)
	$R_{\text{Edd}}$	$R_{\text{irr}}(\dot{M}_{\text{Edd}})$
Model 1		
	$R_{\text{trig}}$	$\xi R_{\text{disc}}$
	$R_{\text{out}}$	$\max(R_{\text{irr}}, R_{\text{trig}})$
Model 2		
	$R_{\text{max}}$	$0.1R_{\text{disc}}$
	$R_{\text{trig}}$	$R_{\text{max}}$
	$R_{\text{out}}$	$\max(R_{\text{irr}}, R_{\text{max}})$

where  $-\dot{M}_2$  is the mass transfer from the secondary star. An estimate of the mass transfer rate over a wide range of orbital periods is needed.

### 5.3.1 Mass transfer rate

The purpose of this section is to show there is a link between the mass transfer rate and the binary orbital period. For this task I consider some numerical simulations by Webbink, Rappaport & Savonije (1983) and analytic work by King (1988), before finally considering more a recent paper by Ritter (1999). To obtain an expression for the mass transfer rate I follow the work by King (1988) who details the evolution of compact binaries and briefly focuses on likely scenarios for long period systems.

In the long period systems under scrutiny the secondary star losing mass to the primary must be a giant or subgiant star, as in GRS 1915+105 (see §4.1). When a main sequence star exhausts the hydrogen fuel in its core, nuclear reactions in the core stop, causing the core to contract. The core contains the products of the hydrogen burning process, i.e. helium. As the helium core collapses a shell surrounding the core, where hydrogen still remains, becomes hot enough to begin the fusion of hydrogen to helium. The higher temperatures lead to increasing reaction rates, producing enough energy to increase the star's luminosity and radius by several orders of magnitude. This increase in radius results in a much lower temperature at the stellar surface. The structure of the star is now somewhat different: a helium core is surrounded by a thin hydrogen-burning shell itself surrounded by an extended envelope. This envelope is now so tenuous that its impact on the properties of the star is negligible. The luminosity and radius of the star can be considered to be solely dependent on the core mass,  $M_c$ . Webbink et al. (1983) parameterises the luminosity and radius as a Taylor series:

$$\begin{aligned}\ln(L/L_\odot) &= 3.50 + 8.11y - 0.61y^2 + \dots \\ \ln(R/R_\odot) &= 2.53 + 5.10y - 0.05y^2 + \dots\end{aligned}\tag{5.20}$$

where  $y = \ln(M_c/0.25)$  (for the purpose of this section all masses are considered to be in solar mass units). If core masses in the range  $0.17 M_\odot < M_c < 0.45 M_\odot$  are considered then  $\ln|y| < 1$  and non linear terms in eq. (5.20) can be ignored. Combining eq. (1.39) with linearised version of eq. (5.20),

$$R \sim 12.6 R_\odot \left(\frac{M_c}{0.25}\right)^{5.1}\tag{5.21}$$

gives a relation between the binary orbital period, the total mass and the core mass of the secondary for a Roche lobe filling star:

$$P_{\text{orb}} \sim 16.5 \left(\frac{M_c}{0.25}\right)^{7.65} \left(\frac{1}{M_2}\right)^{1/2} \text{ days.}\tag{5.22}$$

As previously stated the luminosity of the star is provided by hydrogen burning in a shell surrounding the core. As the hydrogen is consumed, helium is added to the core, suggesting a link between  $L$  and  $\dot{M}_c$ . Hydrogen burns at  $4.19 \times 10^{18}$  erg g<sup>-1</sup>, therefore

$$\dot{M}_c = \frac{L}{4.19 \times 10^{18}} \sim \frac{33 L_\odot}{4.19 \times 10^{18}} \left( \frac{M_c}{0.25} \right)^{8.11}, \quad (5.23)$$

using eq. (5.20). Logarithmically differentiating eq. (5.20) gives

$$\frac{\dot{R}_2}{R_2} = 5.1 \frac{\dot{M}_c}{M_c} \quad (5.24)$$

which combined with eq. (1.46) for conservative mass transfer leads to

$$-\frac{\dot{M}_2}{M_2} \sim \frac{3\dot{M}_c}{M_c}. \quad (5.25)$$

A combination of the above and eq. (5.23) leads to an expression for the mass transfer rate,

$$-\dot{M}_2 \sim \frac{396 L_\odot}{4.19 \times 10^{18}} \left( \frac{M_c}{0.25} \right)^{7.11} M_2. \quad (5.26)$$

To express the mass transfer rate in terms of the orbital period, integrate eq. (5.25),

$$M_c = M_c^0 M_2^{-1/3}, \quad (5.27)$$

where  $M_c^0$  is defined to be the core mass for a solar mass star. The final mass of the star is equal to the final core mass,  $M_c^f = M_2^f$ , leaving  $M_c^f = M_2^f = (M_c^0)^{3/4}$ . Using this in eq. (5.22) results in relation between the orbital period at the end of the mass transfer process and  $M_c^0$ ,

$$P_{\text{orb}}^f = 394 \left( \frac{M_c^0}{0.25 M_\odot} \right)^{5.36} \text{ days}. \quad (5.28)$$

Using eq. (5.27) in eq. (5.22), the orbital period varies as  $P_{\text{orb}} \propto M_2^{-3.05}$ . From eq. (5.26) one then derives  $-\dot{M}_2 \propto P_{\text{orb}}^{0.45}$ . If  $M_2 = 1$  is assumed then eq. (5.22) gives the initial orbital period  $P_{\text{orb}}^i$  while eq. (5.28) gives the final orbital period  $P_{\text{orb}}^f$ . The ratio between the final and initial mass transfer rates is therefore

$$\frac{\dot{M}_2^f}{\dot{M}_2^i} = \left( \frac{P_{\text{orb}}^f}{P_{\text{orb}}^i} \right)^{0.45} \sim 4 \left( \frac{M_c^0}{0.25} \right)^{-1.03} \sim \frac{1}{M_c^0}. \quad (5.29)$$

Hence the value of  $-\dot{M}_2$  does not vary substantially as the orbital separation of the binary evolves. Indeed the average  $\dot{M}_2$  is set by the initial orbital period. Finally a combination

of eq. (5.22) and eq. (5.26) results in the desired relation between  $\dot{M}_2$  and  $P_{\text{orb}}$ ,

$$-\dot{M}_2 \sim 4 \times 10^{-10} P_{\text{orb}}^{0.93} (\text{d}) M_2^{1.47} M_{\odot} \text{yr}^{-1}. \quad (5.30)$$

The numerical calculations carried out by Webbink et al. (1983) are in good agreement with this result. More recent work has been carried out on binary evolution and mass transfer (Ritter 1999) which questions the constant mass transfer rate as the binary evolves. Ritter (1999) states that the most important factor is the core mass at the beginning of mass transfer. However the equation for  $-\dot{M}_2$  contains several other parameters such as initial primary and secondary masses as well as the core mass of the secondary. Using this work would expand the parameter space unnecessarily. Ritter (1999) compares his result for the mass transfer rate to that calculated by Webbink et al. (1983), shown in his figs. 3 and 4 (fig. 3 is reproduced here, see fig. 5.5). The two results differ by no more than 20% at the beginning of the mass transfer process, they are similar enough to warrant the use of eq. (5.30).

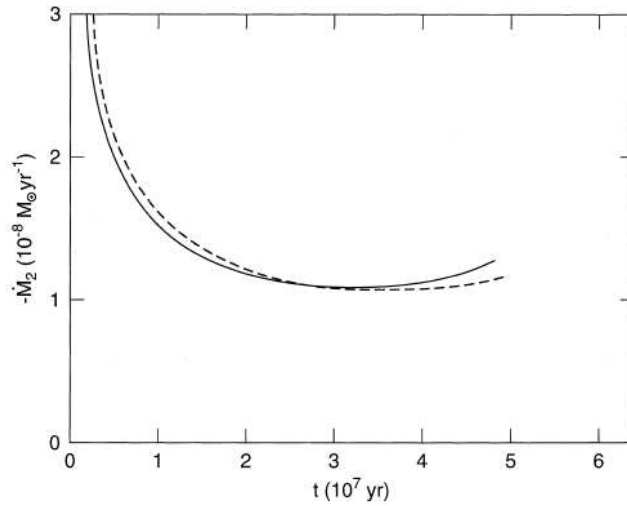


FIGURE 5.5. Mass loss rate as a function of time. Comparison between work by Ritter (solid line) and Webbink et al. (1983) (dashed line), taken from Ritter (1999).

### 5.3.2 Period range

The relations derived in §5.3.1 are not valid for the whole range of parameters. To ensure that eq. (5.20) could be linearised, a limit on the core mass was imposed, hence

$$\begin{aligned} 0.17 < M_c < 0.45 \\ M_c &\lesssim M_2 < \frac{5}{6} M_1. \end{aligned} \quad (5.31)$$

If  $M_1 \sim 10$  is assumed then using eq. (5.22) can impose limits upon the range of periods for which the relations in §5.3.1 are valid,

$$0.3 \text{ days} \lesssim P_{\text{orb}} \lesssim 6 \text{ yrs} \quad (5.32)$$

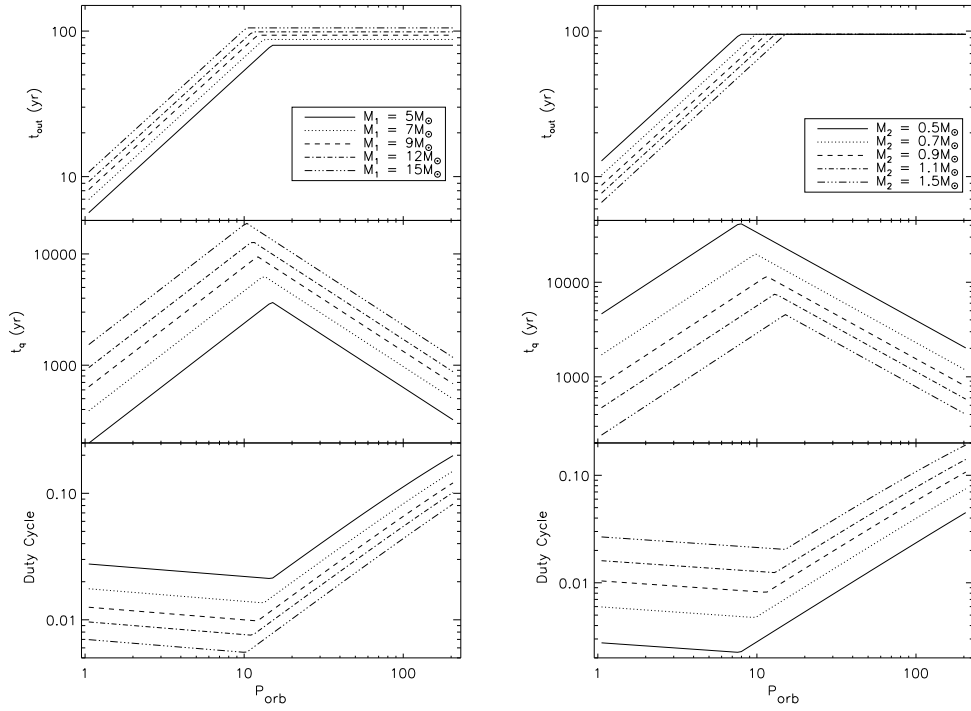
As previously stated Webbink et al. (1983) performed detailed calculations which are in agreement with eq. (5.30). Their binary evolution calculations were carried out in the (initial) orbital period range  $1 < P_{\text{orb}} < 200$  days. This is the range of orbital periods I will consider hereafter.

## 5.4 Exploring the parameter space

### 5.4.1 Model 1

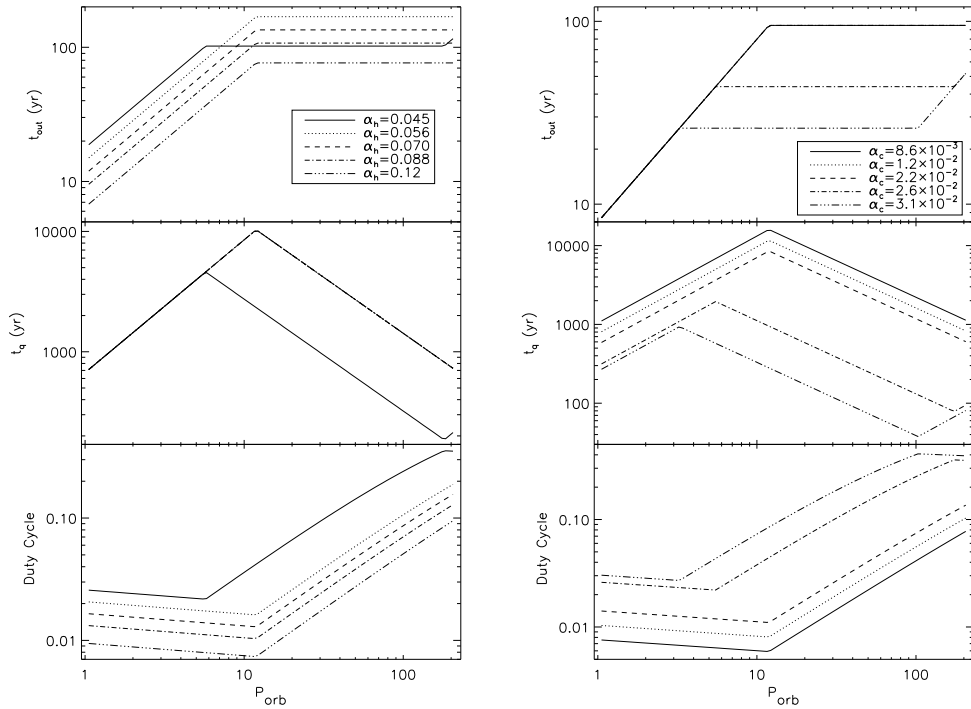
I shall start by examining the behaviour of the simplest of the models used for the surface density profile, Model 1. Unless stated otherwise the parameters for all of the figures are  $M_1 = 10 M_{\odot}$ ,  $M_2 = 1 M_{\odot}$ ,  $\alpha_h = 0.1$ ,  $\alpha_c = 0.01$ ,  $\epsilon = 1 \times 10^{-3}$ ,  $\eta = 0.1$ ,  $H/R = 0.01$ ,  $R_{\text{trig}} = 0.1 R_{\text{disc}}$  and  $R_{\text{max}} = 0.1 R_{\text{disc}}$ . The circularisation radius detailed by Hessman & Hopp (1990) was used. Model 1 can be regarded as an upper limit for the total mass of the disc. As a result the quiescence times using this model are particularly large  $\sim 10^3 - 10^4$  yr. Additionally mass accretion rates onto the primary are typically super Eddington at orbital periods of  $\sim 10$  days.

By examining fig. 5.6 and 5.7, a general trend can be observed in the behaviour of  $t_{\text{out}}$ ,  $t_{\text{q}}$  and the duty cycle. Initially the outburst time is directly proportional to  $P_{\text{orb}}$  (see §5.2.2). The choice of parameters has resulted in an  $\dot{M}_1$  which irradiates the entire disc and the Eddington limit is reached at  $\sim 7$  days. This behaviour continues until  $R_{\text{disc}} > R_{\text{Edd}}$  at  $P_{\text{orb}} \sim 10$  days, hence the mass lost from the disc during outburst is constant, irrespective of the size of the disc. However the mass transfer rate still increases with orbital period (see eq. (5.30)). When the entire disc is irradiated  $R_{\text{out}} = R_{\text{disc}} \propto P_{\text{orb}}^{2/3}$ , this in turn means  $\dot{M}_{\text{disc}} \propto P_{\text{orb}}^{2.03}$ . Hence, eq. (5.30) results in the quiescence time obeying a power law of  $\sim 1.1$  when the disc is totally consumed in outburst. When  $R_{\text{out}} = R_{\text{Edd}}$  the mass  $\dot{M}_{\text{out}}$  is constant, hence  $t_{\text{q}}$  obeys the relation  $\propto P_{\text{orb}}^{-0.93}$ . The effects on the duty cycle are then straight forward to calculate (assuming  $t_{\text{q}} \gg t_{\text{out}}$ ): a power law of  $\sim -0.103$  when  $R_{\text{out}} = R_{\text{disc}}$  and a power law of  $\sim 0.93$  when  $R_{\text{out}} = R_{\text{Edd}}$ . This raises the possibility that the duty cycles of long period LMXBs may be larger than previously assumed.



(a) varying  $M_1$

(b) varying  $M_2$



(c) varying  $\alpha_h$

(d) varying  $\alpha_c$

FIGURE 5.6. Parameter study of Model 1.

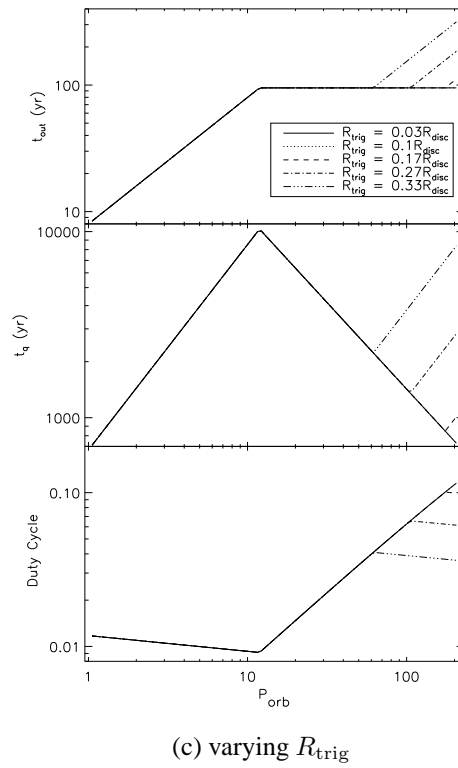
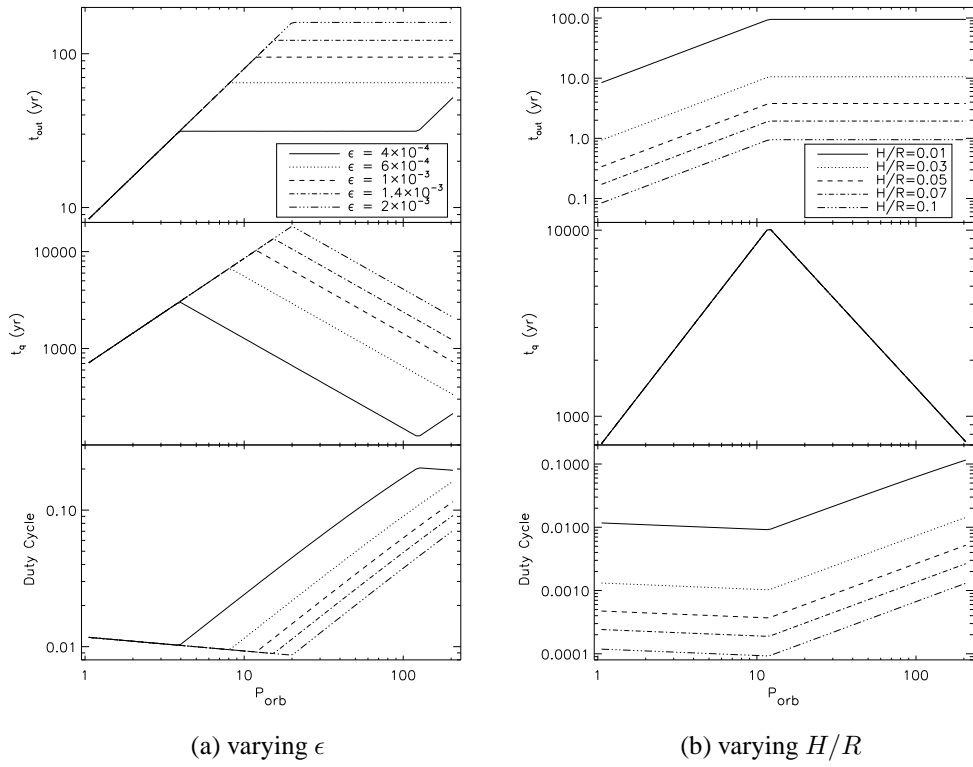


FIGURE 5.7. Parameter study of Model 1.

I will now briefly detail some of the specifics of the individual results of the parameter study.

**Figure 5.6a, varying  $M_1$**

Increasing the primary mass increases the orbital separation for a given period, resulting in a larger disc. The greater reservoir of mass results in the Eddington limit being reached at a smaller  $P_{\text{orb}}$  for a more massive black hole. Additionally the more massive the black hole the greater the Eddington luminosity. The maximum region of the disc which can be irradiated is greater, causing the increased outburst and quiescence times.

**Figure 5.6b, varying  $M_2$**

Once again changing the mass of a component in the binary changes the orbital separation for a given period. While increasing the secondary mass does increase the binary separation it also reduces  $R_{L_1}$  and the circularisation radius around the primary (see the form of  $R_{\text{circ}}$  in table 5.1). This reduction in the radius of the disc means that  $R_{\text{out}} = R_{\text{Edd}} < R_{\text{disc}}$  at shorter orbital periods. A larger  $M_2$  also increases  $-\dot{M}_2$  which in combination with the reduced  $R_{\text{disc}}$  reduces  $t_{\text{q}}$ .

**Figure 5.6c, varying  $\alpha_h$**

With the exception of  $\alpha_h = 0.045$  all of the trials behave in a similar way. The mass accretion rate is high enough to irradiate the entire disc until  $P_{\text{orb}} \sim 12$  days when  $R_{\text{disc}} > R_{\text{Edd}}$  and  $t_{\text{out}}$  plateaus. The viscous time at  $R_{\text{irr}}$  is reduced for larger values of  $\alpha_h$  but the same mass is accreted. When  $\alpha_h = 0.045$  however, the viscous time at  $R_{\text{irr}}$  is such that  $\dot{M}_1$  never reaches the Eddington limit, due to the low viscosity in the hot state and the resulting long outburst time. Thus, once  $P_{\text{orb}} \sim 6$  days the disc becomes larger than  $R_{\text{irr}}$  but the Eddington limit has not been reached.

**Figure 5.6d, varying  $\alpha_c$**

From eq. (5.2), increasing  $\alpha_c$  reduces the mass in the disc. For  $\alpha_c > 2.2 \times 10^{-2}$  the disc mass is low enough so that  $\dot{M}_1$  is always sub Eddington. As  $\alpha_c$  is decreased, the outburst curve begins to approach that of the Eddington limited case with an outburst time of  $\sim 100$  yrs. Although the outburst times are identical for all  $P_{\text{orb}}$  when  $\alpha_c \leq 2.2 \times 10^{-2}$

the effect of the differing  $\alpha_c$  can be seen in the quiescence time. When  $\alpha_c \geq 2.6 \times 10^{-2}$   $t_{\text{out}}$  and  $t_{\text{q}}$  begin to increase again at orbital periods  $> 100$  days. This is caused by  $R_{\text{trig}} > R_{\text{irr}}$  and is seen in a number of the trials.

### Figure 5.7a, varying $\epsilon$

For larger values of  $\epsilon$  the irradiation radius at  $\dot{M}_{\text{Edd}}$  is increased, see eq. (5.11), resulting in a correspondingly larger  $t_{\text{out}}$  and  $t_{\text{q}}$  (as more mass is lost from the disc in the outburst). The only departure from this behaviour is when  $\epsilon = 4 \times 10^{-4}$ , when the  $t_{\text{out}}$  curve once again starts to obey the power law of the pre Eddington limit, due to  $R_{\text{trig}} > R_{\text{irr}}$ . The trigger radius increases with the disc radius and so the power law is  $\sim 1$  due to the argument in §5.2.2.

### Figure 5.7b, varying $H/R$

The aspect ratio of the disc is varied between 0.01-0.1: these are values generally assumed to be reasonable (King, Kolb & Burderi 1996, Mayer & Pringle 2007). The effect on  $t_{\text{out}}$  is similar to that when varying  $\alpha_h$ , as  $H/R$  is increased the outburst time decreases, due to eq. (5.8). The amount of mass involved in the outburst is constant with changing  $H/R$  in the range chosen.

### Figure 5.7c, varying $R_{\text{trig}}$

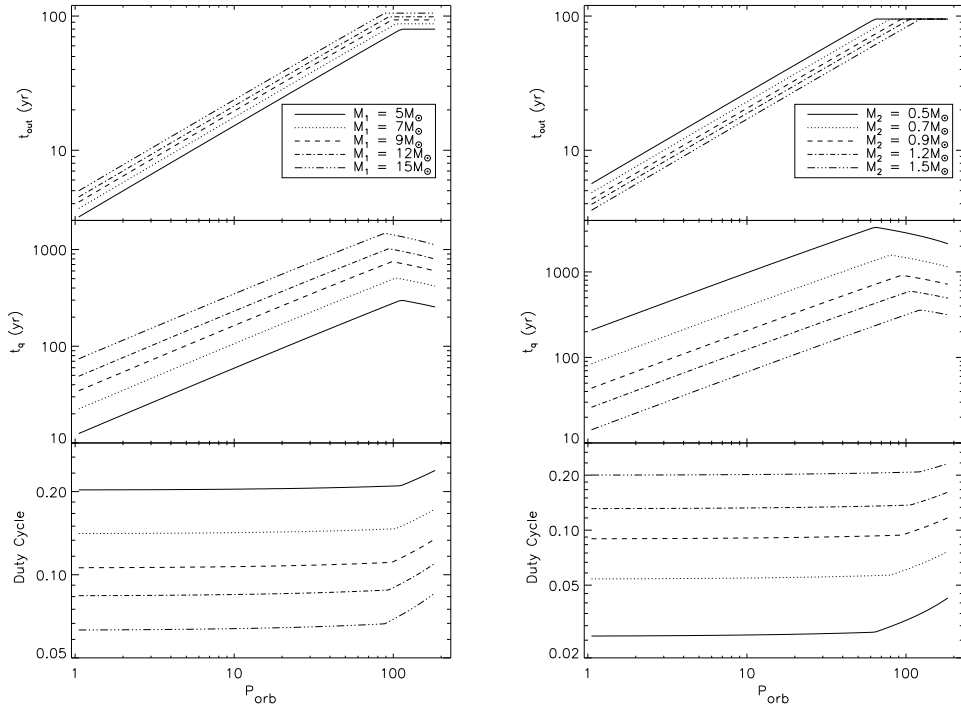
The only significant effect of changing  $R_{\text{trig}}$  is the value of  $P_{\text{orb}}$  for which  $R_{\text{trig}} > R_{\text{irr}}$ , the effect of which is described in the discussion of fig. 5.7a.

### Varying $\eta$

The results were found to be independent of  $\eta$  when  $\eta > 0.05$ . Values  $< 0.05$  are needed to influence the amount of the disc that is irradiated.

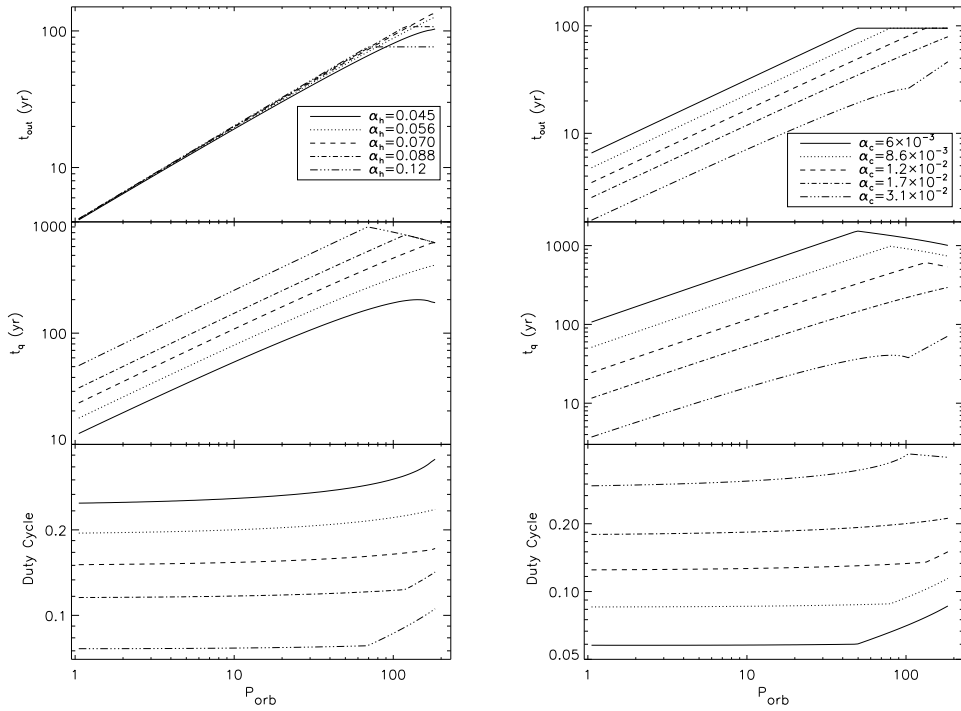
## 5.4.2 Model 2

The behaviour of the second model for the mass in the disc can be best understood by using the example of Model 1. The general form of the two models is similar: both  $t_{\text{out}}$  and  $t_{\text{q}}$  increase with  $P_{\text{orb}}$  until  $\dot{M}_{\text{Edd}}$  is reached, whereupon  $t_{\text{out}}$  plateaus and  $t_{\text{q}}$



(a) varying  $M_1$

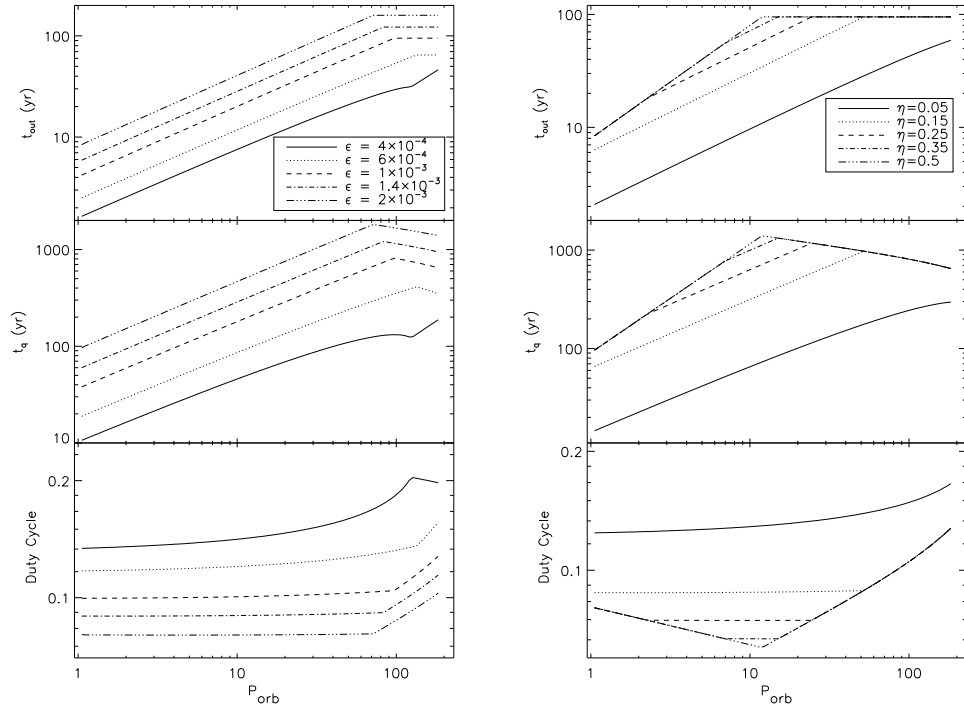
(b) varying  $M_2$



(c) varying  $\alpha_h$

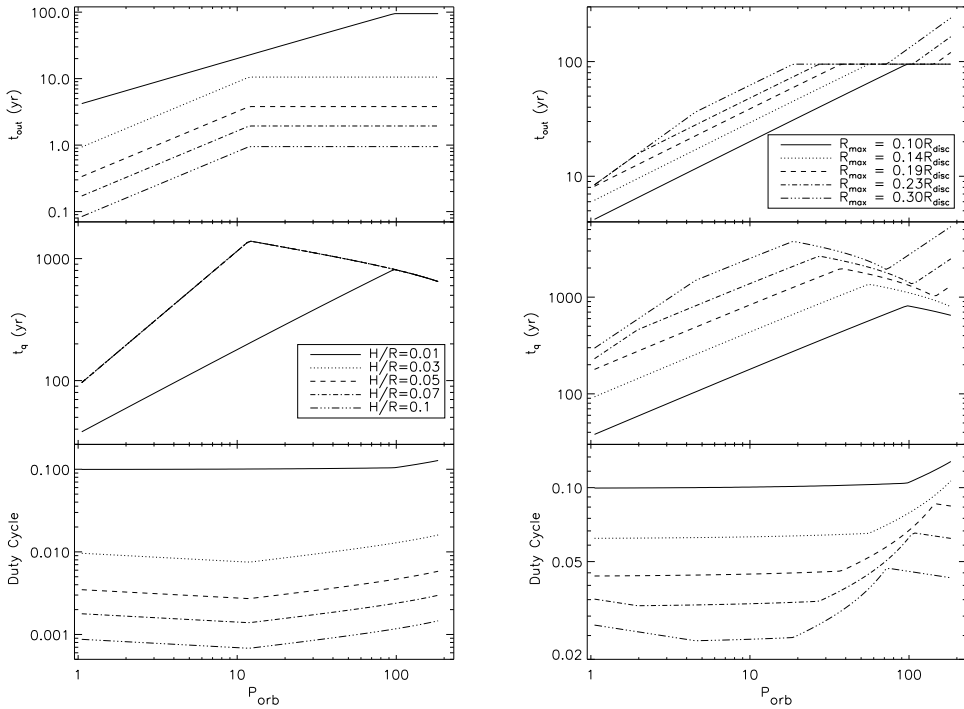
(d) varying  $\alpha_c$

FIGURE 5.8. Parameter study of Model 2.



(a) varying  $\epsilon$

(b) varying  $\eta$



(c) varying  $H/R$

(d) varying  $R_{\text{max}}$

FIGURE 5.9. Parameter study of Model 2.

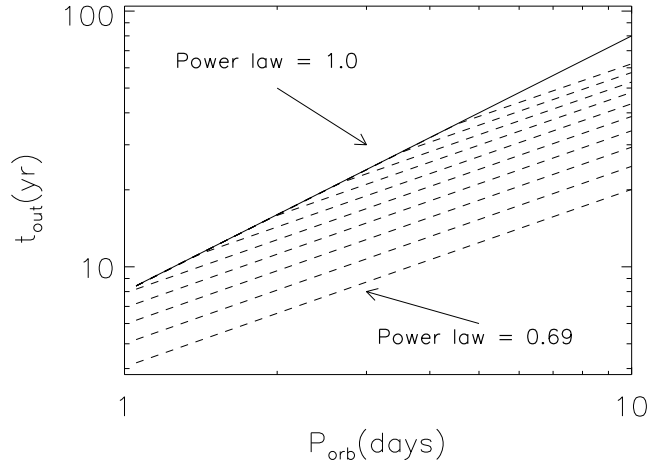


FIGURE 5.10. Figure showing the convergence to a power law of 1. Dashed lines are differing values of  $R_{\max}$  starting at  $0.1R_{\text{disc}}$  and increasing in increments of  $0.03R_{\text{disc}}$ .

begins to decrease. Compared with Model 1 the mass in the disc is reduced, therefore the Eddington limit is reached at larger  $P_{\text{orb}}$ , typically  $P_{\text{orb}} \sim 100$  days. A further consequence of the reduced disc mass is the reduced  $t_q$ . The form of  $t_q$  is generally not a simple power law for high values of  $P_{\text{orb}}$ , due to the more complicated expression for the disc mass (see eq. (5.17)). When  $P_{\text{orb}} > 100$  days  $M_{\text{irr}}$  is no longer the only significant constituent of  $M_{\text{out}}$  (see fig. 5.4). The resulting outburst time in Model 2 does not follow the same power law as in Model 1 at short orbital periods, indicating the disc is not totally irradiated and taking part in the outburst. The power law in the outburst times for  $P_{\text{orb}} < 100$  days is particularly evident in fig. 5.9a and can be explained by the model for the disc surface density profile. To illustrate this I will follow an example iteration series.

- Initially an outburst is triggered at  $R_{\max}$ . The mass contained within this radius is given by eq. (5.13). For a fixed  $M_1$  and  $M_2$ ,  $R_{\max} \propto P_{\text{orb}}^{2/3}$ . Hence the mass within  $R_{\max}$  contains within it mass proportional to  $P_{\text{orb}}^{2.03}$ .
- Using the expression for the viscous time (eq. (5.8)) at  $R_{\max}$  results in  $t_{\text{visc}}(R_{\max}) \propto P_{\text{orb}}$ . This gives an initial average mass transfer rate onto the black hole,  $\dot{M}_{\text{ini}} = M_{\max}/t_{\text{visc}}(R_{\max}) \propto P_{\text{orb}}^{1.03}$ .
- This initial average mass transfer rate results in irradiation of the disc following eq. (5.11), therefore  $R_{\text{irr}} \propto (\dot{M}_{\text{ini}})^{1/2}$  which in turn gives a dependence on the orbital

period  $R_{\text{irr}} \propto P_{\text{orb}}^{0.516}$ .

- Making the assumption that  $R_{\text{irr}} > R_{\text{max}}$ , which is possible in low period high  $\epsilon$  tests, the mass of the disc can be approximated by using eq. (5.16),  $M_{\text{out}} \sim 2\pi\Sigma(R_{\text{max}})R_{\text{irr}}^2$ . From eq. (5.2),  $\Sigma(R_{\text{max}})$  is approximately proportional to  $P_{\text{orb}}^{2/3}$  and using the above  $M_{\text{out}} \propto P_{\text{orb}}^{1.7}$ .
- The average mass accretion rate is now recalculated from the new outburst mass and the viscous time at the irradiation radius. From the above it is known that  $M_{\text{out}} \propto P_{\text{orb}}^{1.7}$  and  $R_{\text{irr}} \propto P_{\text{orb}}^{0.516}$ . Hence the updated average mass accretion rate is  $\dot{M}_1 \propto P_{\text{orb}}^{0.94}$ .
- The updated irradiation radius is now calculated from the new  $\dot{M}_1$ ,  $R_{\text{irr}} \propto P_{\text{orb}}^{0.46}$ . A new outburst time is now calculated from this irradiation radius, again using eq. (5.8), resulting in  $t_{\text{out}} = t_{\text{visc}}(R_{\text{irr}}) \propto P_{\text{orb}}^{0.69}$ . All subsequent iterations converge to this result and this power law is seen in several of the figures in this section.
- In a similar fashion for the quiescence time, the new mass of the outburst is given by  $M_{\text{out}} \sim 2\pi\Sigma(R_{\text{max}})R_{\text{irr}}^2$ . From the arguments above  $\Sigma(R_{\text{max}}) \propto P_{\text{orb}}^{2/3}$  and  $R_{\text{irr}} \propto P_{\text{orb}}^{0.46}$ , resulting in  $M_{\text{out}} \propto P_{\text{orb}}^{1.59}$ . Using eq. (5.30) ensures that the quiescence time obeys  $t_{\text{q}} \propto P_{\text{orb}}^{0.67}$ .

The transition between the two power laws in the outburst time can be seen in fig. 5.9d and in more detail in fig. 5.10. As the inner radius is increased the amount of mass in the disc increases, which can provide the necessary outburst mass and hence  $\dot{M}_1$  to irradiate the whole disc. This results in a power law for  $t_{\text{out}}$  of 1, i.e.  $t_{\text{out}}$  is proportional to  $P_{\text{orb}}$  (see §5.2.2). If this is not the case a power law of  $\sim 0.69$  is the result.

At first glance the behaviour of fig. 5.8c is surprising. An increase in  $\alpha_h$  should decrease  $t_{\text{out}}$ , however this fails to take into account the resultant increase in  $\dot{M}_1$  has on the irradiation radius ( $\propto \alpha_h^{1/2}$ ). Combined with eq. 5.16 (given  $R_{\text{irr}} \gg R_{\text{max}}$ ) results in the outburst time having no dependence on the viscosity in the hot state. The only remaining variable is the size of the disc. Figure 5.11 displays  $t_{\text{out}}$ ,  $t_{\text{q}}$  and duty cycle when the disc radii from Silber (1992), Eggleton (1983) and Hessman & Hopp (1990) are used in Model 2. The form of the resultant curves are qualitatively the same. When  $q = 0.1$  Silber (1992) and Eggleton (1983) predict a comparable  $R_{\text{disc}}$  (see fig. 5.1), which is larger than that predicted by Hessman & Hopp (1990). Hence they predict similar results and larger outburst and quiescence time.

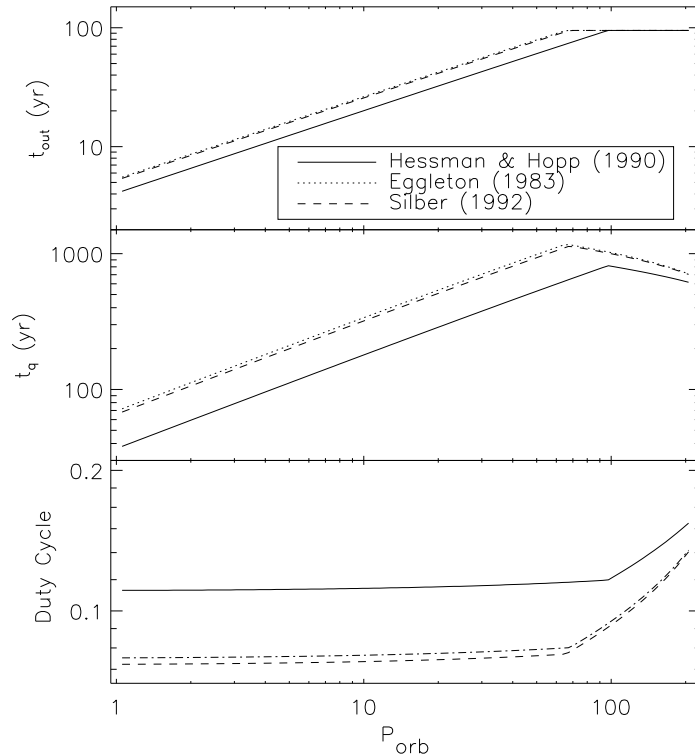


FIGURE 5.11. Outburst quiescence time and duty cycle as a function of orbital period. Model 2 is used with different expressions for  $R_{\text{disc}}$ .

## 5.5 Comparisons with observations

Before proceeding any further, it would be useful to compare the predictions made from the models against observed LMXBs. As previously stated there are only 15 confirmed Galactic black hole binaries. The majority of which have an orbital period on the order of one day; GRS 1915+105 is the longest period LMXB known. The history of X-ray astronomy is limited to only  $\sim 40$  yrs. This coupled with the quiescence times of even the shorter period system being of the order  $\sim 10$  yrs means there is a lack of observational data for comparison. This is further hampered by the total lack of data on the long period systems with outbursts lasting decades and quiescent periods lasting thousands of years. I will have to extrapolate the behaviour of the longer period systems based on the observation of their short period counterparts.

The criteria used to select the black hole LMXB were as follows: a giant or sub giant secondary, a known orbital period preferably several days long, known primary and secondary masses and a source that has had several outbursts. As can be seen in table 4.1 in McClintock & Remillard (2006) the ratio of LMXBs known with main sequence donor stars to those with giant/subgiant donors is approximately 2:1, further reducing possible

Table 5.3. Table of LMXB system parameters, typical outburst times and quiescence times

Name	$P_{\text{orb}}$ (days)	$M_1 (M_{\odot})$	$M_2 (M_{\odot})$	$t_{\text{out}}$ (months)	$t_{\text{q}}$ (yrs)
V1033 ScO	2.62 <sup>a</sup>	6.59 <sup>b</sup>	2.76 <sup>b</sup>	8-16 <sup>c</sup>	7 <sup>c</sup>
BW Cir	2.54 <sup>d</sup>	>7.83 <sup>d</sup>	>1.02 <sup>d</sup>	5-6 <sup>e</sup>	10 <sup>de</sup>
V404 Cyg	6.21 <sup>f</sup>	10 <sup>g</sup>	0.65 <sup>h</sup>	6 <sup>i</sup>	18-33 <sup>j</sup>

<sup>a</sup> González Hernández, Rebolo & Israelian (2008)

<sup>b</sup> Shahbaz (2003)

<sup>c</sup> Saito et al. (2007)

<sup>d</sup> Casares et al. (2004)

<sup>e</sup> Brocksopp et al. (2001)

<sup>f</sup> Casares et al. (1993)

<sup>g</sup> Shahbaz et al. (1996)

<sup>h</sup> Shahbaz et al. (1994)

<sup>i</sup> Życki, Done & Smith (1999)

<sup>j</sup> Richter (1989)

candidates. The selected sources are shown in table 5.3. They are all typical of the shorter (relative to GRS 1915+105) period LMXBs, outbursts lasting a few months and quiescent periods lasting a decade or so. By comparing these objects to the predictions of the model, I will be able to better constrain some of the parameters used, particularly the disc scale height and the irradiation efficiency. Another focus of this section will be to determine which of the models for the surface density in the disc provides the best match to the observations.

To constrain the parameters used in the model a search through the parameter space was conducted. The mass of the constituents of the system have been fixed, therefore the following parameters remain:  $\alpha_{h/c}$ ,  $H/R$ ,  $\epsilon$  and  $\eta$ . While  $\alpha_{h/c}$  are ways of parameterising our uncertainty regarding the viscosity in accretion discs, deviating too far from their “accepted” canonical values is undesirable. The parameters that had the greatest influence on the predicted outburst and quiescence times were  $H/R$  and  $\epsilon$ . These parameters have the greatest uncertainty associated with them, with accepted values for  $H/R$  from 0.1 to 0.01 while  $\epsilon$  can be expressed as (King & Ritter 1998)

$$\epsilon = (1 - \beta) \left( \frac{H}{R} \right)^n \left[ \frac{d \ln H}{d \ln R} - 1 \right], \quad (5.33)$$

where  $\beta$  is the albedo of the gas in the disc and the index  $n$  has a value of 1 or 2. The uncertainties of each of the constituents of  $\epsilon$  motivated the use of the single parameter to describe the irradiation efficiency. Figure 5.12 shows how the relative error between

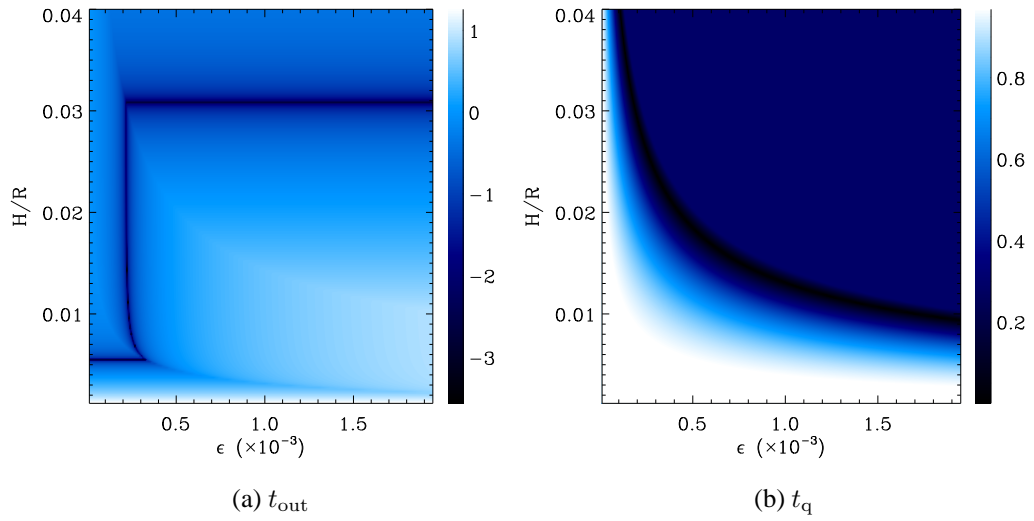


FIGURE 5.12. Plot of the relative error between the observed and predicted outburst and quiescence times (Model 2) for the system V1033 ScO as a function of  $\epsilon$  and  $H/R$ . Colour scale denotes the  $\log_{10}$  of relative error, which is minimised for both  $t_{\text{out}}$  and  $t_{\text{q}}$  when  $H/R = 0.03$  and  $\epsilon = 0.2 \times 10^{-3}$ .

the predicted and observed  $t_{\text{out}}$  and  $t_{\text{q}}$  varies when  $\epsilon$  and  $H/R$  are allowed to change for V1033 ScO. The error is minimised for both  $t_{\text{out}}$  and  $t_{\text{q}}$  when values of  $H/R \sim 0.031$  and  $\epsilon \sim 2 \times 10^{-4}$  are adopted.

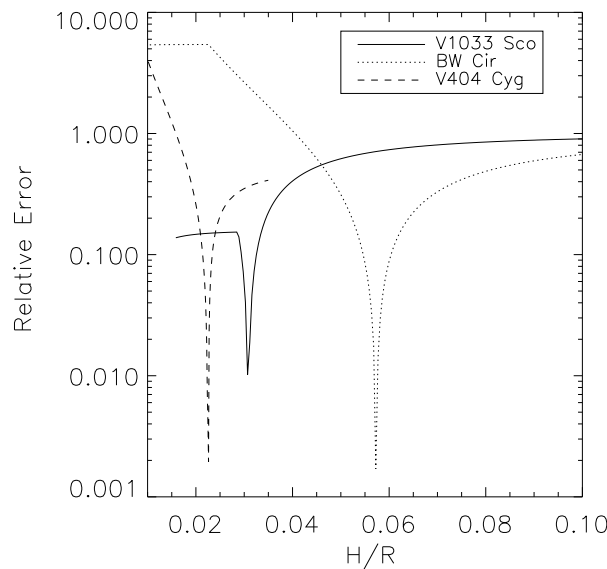


FIGURE 5.13. Plot of the relative error between observations of the outburst times and results of Model 2 against  $H/R$

Table 5.4. Table of LMXB system parameters, typical outburst times and quiescence times. Parameters are  $\eta = 0.1$ ,  $\alpha_h = 0.1$  and  $\alpha_c = 0.01$ .

Model	Name	$H/R$	$\epsilon(\times 10^{-3})$	Predicted		Observed	
				$t_{\text{out}}$ (months)	$t_{\text{q}}$ (yrs)	$t_{\text{out}}$ (months)	$t_{\text{q}}$ (yrs)
Model 1	V1033 ScO	0.03	0.05	12	65	8-16	7
“	BW Cir	0.06	0.1	6	$\sim 1000$	5-6	10
“	V404 Cyg	0.02	0.035	5	15	6	18-33
Model 2	V1033 ScO	0.03	0.2	14	16	8-16	7
“	BW Cir	0.06	1.0	6	$\sim 150$	5-6	10
“	V404 Cyg	0.02	0.035	5	15	6	18-33

Figure 5.13 shows the relative error between results from Model 2 and the observed outburst times. The surface density profile adopted has little effect on the outburst times in these short period systems, hence Model 1 produced similar results. The value of the scale height needed to match the observations appears to be in the range 0.02-0.06. Table 5.4 gives the “best fit” values of  $H/R$  and  $\epsilon$  adopted for the systems. Both models predict the outburst times of all three systems well. Model 2 predicts a quiescence time for V1033 ScO that is within a factor of  $\sim 2$  of the observed value. The quiescence time of BW Cir is predicted to be a factor of 15 too large. This may be associated with the uncertainty in the mass of the secondary (Casares et al. 2004). From the orbital data a lower limit of  $1.02 M_{\odot}$  was placed on the secondary. However Casares et al. (2004) identified absorption features which correspond to a G0-5 III type star, which has a typical mass range of  $2.1 - 2.4 M_{\odot}$ . If the upper limit of this mass range for the secondary was adopted then the quiescence time predicted by Model 2 would reduce to  $\sim 40$  yrs. Given the other uncertainties in the system ( $M_1$ ) this is becoming consistent with observations. Model 2 under-predicts the quiescence time for V404 Cyg but not to any significant degree. Given the large time scales involved (first outburst in 1933) Richter (1989) could not rule out the possibility outbursts had been missed. Indeed there was some indication of an outburst in 1979, which would reduce the observed quiescence time to  $10 - 23$  yr. In summary Model 2 predicts the outburst times well but can over estimate the quiescence time by a factor of  $> 2$ .

Model 1 over-estimates the quiescence times of the systems V1033 ScO and BW Cir by a large margin. The value of  $\epsilon$  is somewhat immaterial, no matter the value the quiescence times are grossly over-estimated. Even assuming  $M_2 = 2.4 M_{\odot}$  in BW Cir which gives a revised quiescence time of 115 yrs, all of the systems are predicted to have  $t_{\text{q}}$  a factor  $\sim 6 - 10$  too long. This is unsurprising, as the surface density profile of Model 1 ensures the disc is more massive than that of Model 2 (see fig. 5.4). This would cause the longer quiescence times and also increase the mass accretion rate onto

the primary. From the form of eqs. (5.1) and (5.2), increasing the value of  $\alpha_c$  will reduce the disc mass. If the disc mass becomes comparable to that predicted by Model 2 then the quiescence times will match the observations more accurately. Figure 5.14 shows the mass involved in the outburst for Model 1 for two different values of  $\alpha_c$ . An extreme value of  $\alpha_c$  is needed for  $M_{\text{out}}$  to resemble that of Model 2. This does indeed reduce the quiescence times to values approaching those of the observations. However this necessitates that  $\alpha_c \sim \alpha_h$ , which renders the idea behind the disc instability model somewhat useless as a solution to explain outbursts in CVs and LMXBs. The whole concept depends on the idea that in the hot state the disc viscosity is significantly greater than it is in quiescence, thus explaining the increase in the mass accretion rate during an outburst. The extreme values that parameters in Model 1 have to take to match the observations renders this model for the disc unreliable in my view.

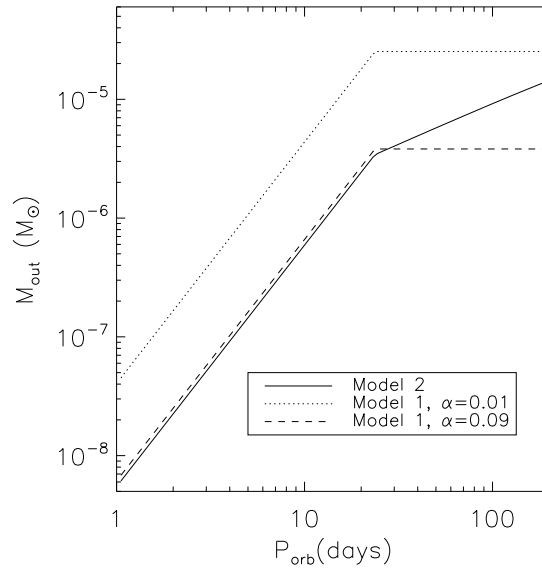


FIGURE 5.14. Plot of the mass involved in the outburst against orbital period, system masses follow V1033 ScOs,  $H/R = 0.03$  and  $\epsilon = 10^{-3}$ .

In contrast to V1033 ScO and BW Cir, Model 1 predicts the V404 Cyg well. This is due to the negligible irradiation efficiency needed for both Models 1 and 2. Without the irradiation of the outer disc and both models are essentially the same with the inner 10% of the disc being lost in the outburst. This conflicts with Życki et al. (1999) who suggest the entire disc is involved in an outburst, to explain the fast rise in the 1989 outburst. The discrepancy between the estimated mass transfer during quiescence and the disc mass lead Życki et al. (1999) to predict a model for the disc similar to my Model 2, by solving the vertical disc structure equations they find that the disc becomes unstable

at  $R_{\text{unst}} \sim 0.05R_{\text{disc}}$ . Beyond this point the disc does not fully build up in quiescence, i.e.  $R_{\text{unst}}$  is analogous to  $R_{\text{max}}$ .

### Varying $R_{\text{max}}$ in Model 2

If Model 2 does indeed represent the surface density in the disc more accurately of the two models, the “main” parameter defining this model  $R_{\text{max}}$  will need to be investigated, this was done briefly in §5.4.2 (see fig. 5.9d). Figure 5.15 depicts the effects on  $t_{\text{out}}$ ,  $t_{\text{q}}$  and duty cycle when  $R_{\text{max}}$  is allowed to vary for a given system, where  $M_1 = 10 M_{\odot}$ ,  $M_2 = 1 M_{\odot}$ ,  $H/R = 0.01$  and  $P_{\text{orb}} = 5$  days. The effects of this are dependent on the strength of the irradiation. With negligible irradiation,  $t_{\text{visc}}(R_{\text{max}})$  (eq. (5.8)) defines the outburst time

$$t_{\text{out}} \sim 40 \left( \frac{R_{\text{max}}}{R_{\text{disc}}} \right)^{3/2} \text{ yr.} \quad (5.34)$$

From eq. (5.13) and eq. (5.30) the quiescence time is given by,

$$t_{\text{q}} \sim 4000 \left( \frac{R_{\text{max}}}{R_{\text{disc}}} \right)^{3.05} \text{ yr.} \quad (5.35)$$

In contrast the outburst time with a high irradiation efficiency is controlled by  $t_{\text{visc}}(R_{\text{irr}})$ . There is sufficient mass in the disc to irradiate the whole disc when  $R_{\text{max}} > 0.3$  when  $\epsilon = 10^{-3}$ . Depending on the irradiation efficiency the change in the outburst and quiescence times when altering  $R_{\text{max}}$  by a factor of two can be as large as a factor of  $2^{3/2}$  and  $2^{3.05}$  from eq. (5.34) and eq. (5.35) respectively. Hence, the duty cycle can change by a factor of  $2^{-1.55}$ .

## 5.6 GRS 1915+105

All the information necessary to make some informed predictions for longer period systems is now in place. The temptation is to assume that the long period systems behave in the same way as their short period counterparts. This is by no means certain, as discussed in §5.5. Also fig. 5.13 shows a trend of decreasing disc aspect ratio with increasing orbital period. Additional information provided by the numerical simulations in §4 will be used to firm up some of the assumptions made. Figure 5.16 shows a similar exercise as in fig. 5.12 for the numerical results of §4. Typical values obtained in §4 are  $t_{\text{out}} = 25 \pm 5$  yr and  $t_{\text{q}} = 10^4 \pm 2 \times 10^3$  yr. From fig. 5.16 Model 1 requires parameters of  $H/R = 0.025$

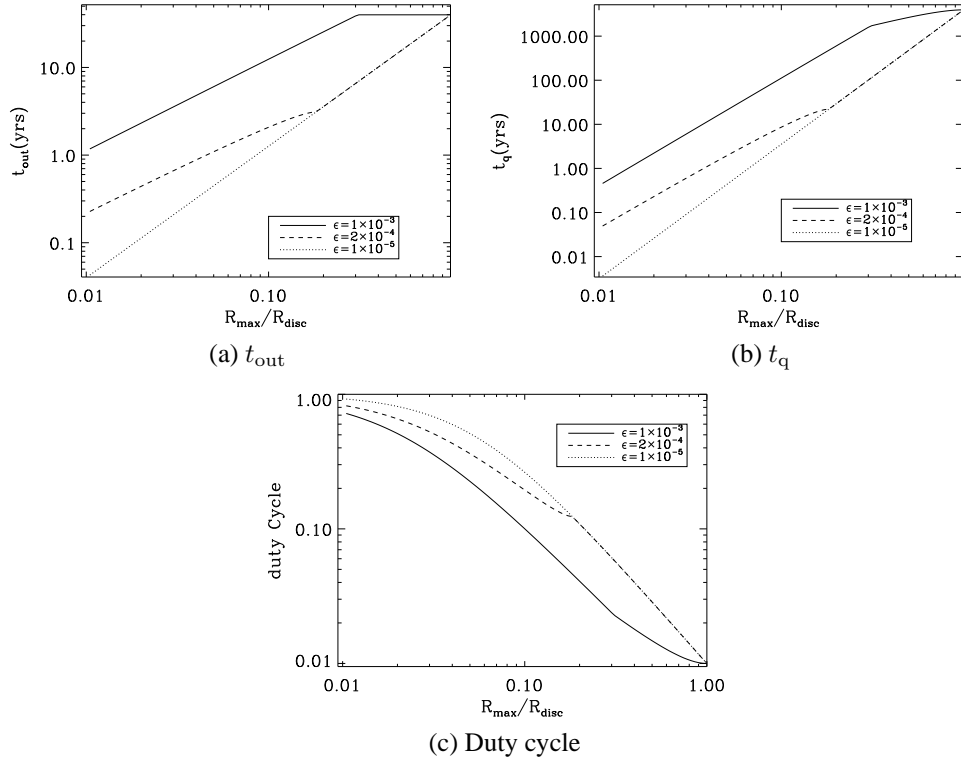


FIGURE 5.15. Plot of the outburst, quiescence times and duty cycle as a function of  $R_{\max}$  for different values of  $\epsilon$ . System parameters are:  $M_1 = 10 M_\odot$ ,  $M_2 = 1 M_\odot$  and  $P_{\text{orb}} = 5$  days.

and  $\epsilon = 1.5 \times 10^{-3}$  while Model 2 requires  $H/R = 0.036$  and  $\epsilon > 5 \times 10^{-3}$ . Both models can adequately reproduce the results from §4 as seen in fig. 5.17.

## 5.7 Discussion

A goal of this work is to make some prediction of the duty cycle of other long period LMXBs. From the comparisons with short period systems Model 1 can be ruled out due to its repeated over estimation of the quiescence time. Model 2 on the other hand can reproduce observations of short period LMXBs and the computer models of GRS 1915+105. To make general predictions of LMXBs I will need to constrain the parameter space somewhat. Assume that  $\eta$ ,  $\alpha_h$  and  $\alpha_c$  have their canonical values and that  $M_1 = 10 M_\odot$ . The value for  $M_1$  is arbitrary, within the range of possible masses for stellar mass black hole. From fig. 5.8a, the trend in the duty cycle does not change with  $M_1$  but merely changes magnitude. I am more interested in the changes in the duty cycle as orbital period changes therefore this assumption was justified. In a similar way the

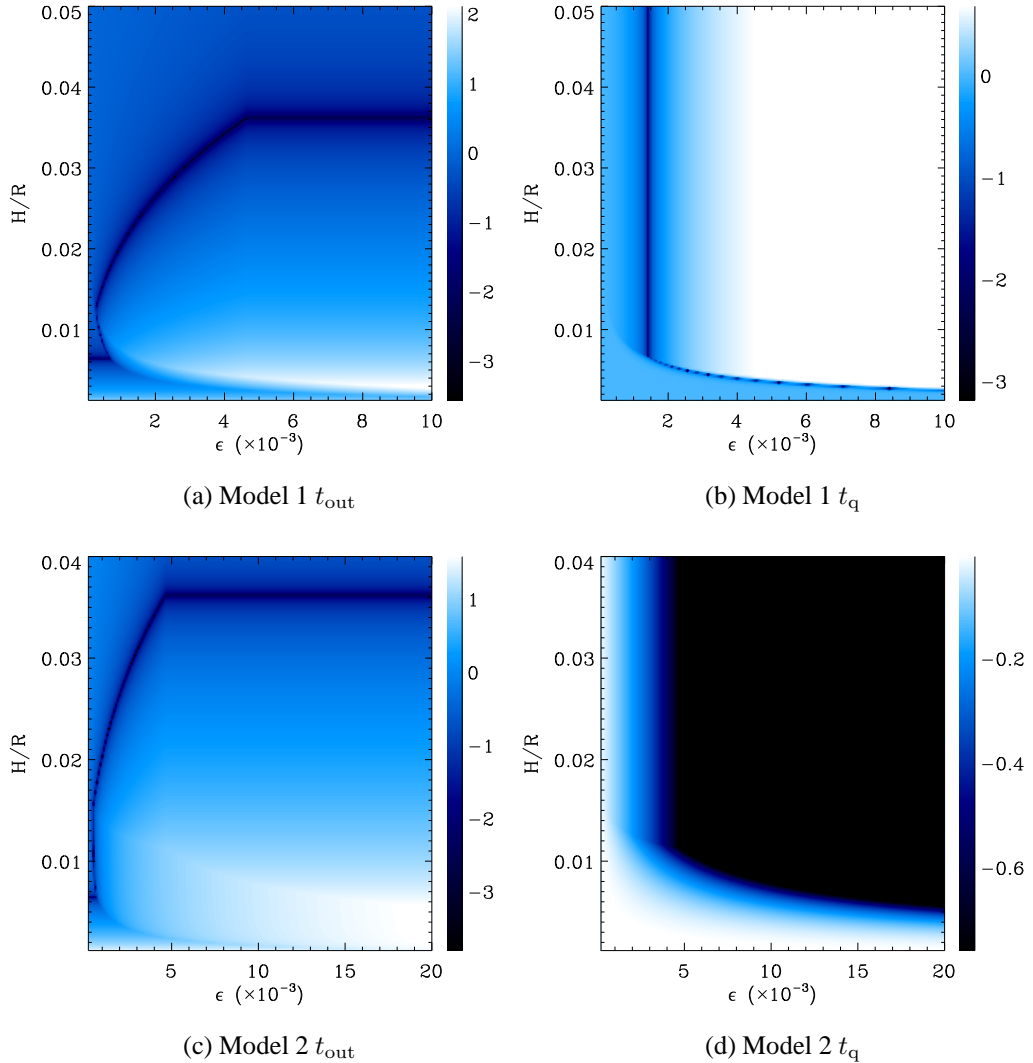


FIGURE 5.16. Plot of the relative error between the predictions of  $t_{\text{out}}$  and  $t_{\text{q}}$  from chapter 4 and this work as a function of  $\epsilon$  and  $H/R$ . Colour scale denotes the  $\log_{10}$  of relative error.

mass of the secondary was fixed at  $1 M_{\odot}$ . This had two motivations; the first follows the argument for  $M_1$  and the second is that a solar mass donor star would be typical in the old stellar population found in elliptical galaxies observed in Irwin (2006). In §5.5 the disc scale height has values between  $0.02 - 0.06$  while the above discussion of GRS 1915+105 implies  $H/R = 0.036$ . Figure 5.13 suggests that  $H/R$  decreases with orbital period in this model, therefore I will assume  $H/R$  has a value of approximately 0.03. The final parameter,  $\epsilon$ , has the weakest constraints with values ranging from  $10^{-5} - 10^{-3}$  in §5.5. Additionally the value of  $\epsilon$  can change the profile of the duty cycle v.s.  $P_{\text{orb}}$  plot (see fig. 5.9a). I made the decision to leave  $\epsilon$  as a free parameter and have it vary through three orders of magnitude to hopefully cover likely values for this parameter.

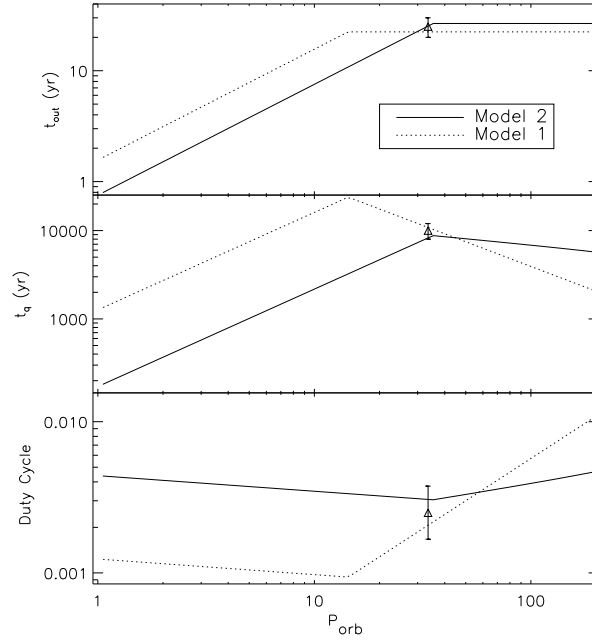


FIGURE 5.17. Comparison between Model 1 and 2 fitted to typical outburst and quiescence times of GRS 1915+105 generated from Chapter 4

Figure 5.18 shows the variation of the duty cycle with orbital period for the parameters described above for three different values of  $H/R$ . It appears the form of the duty cycle can be divided into three different regimes. The first (shaded green in fig. 5.19) can be identified as the low irradiation regime. In this region the duty cycle rises initially with orbital period until  $P_{\text{orb}}$  reaches a critical value where  $R_{\text{max}} > R_{\text{irr}}$  and hence  $t_{\text{out}} = t_{\text{visc}}(R_{\text{max}})$ . From this point onwards the duty cycle decreases with  $P_{\text{orb}}$ . Following the method outlined in §5.4.1 the duty cycle obeys

$$\begin{aligned}
 t_{\text{out}} &= 0.027 P_{\text{orb}}(\text{d}) \text{ yr} \\
 t_{\text{q}} &= 0.59 P_{\text{orb}}^{1.103}(\text{d}) \text{ yr} \\
 \text{duty cycle} &\sim 0.045 P_{\text{orb}}^{-0.103}(\text{d}),
 \end{aligned}
 \tag{5.36}$$

assuming that  $t_{\text{q}} \gg t_{\text{out}}$ . In the extreme case of no X-ray irradiation of the disc, the duty cycle will obey eq. (5.36) for the period range 1 – 200 days. Otherwise the duty cycle can increase by up to 60% in the range  $P_{\text{orb}} \sim 1 - 30$  days, before decreasing according to eq. (5.36). In the high X-ray irradiation regime (shaded light blue in fig. 5.19) most, if not all, the disc enters the hot state and is accreted during the outburst, resulting in smaller duty cycles that nevertheless show more variability with  $P_{\text{orb}}$ . When all of the disc is lost in the outburst the duty cycle again obeys  $\propto P_{\text{orb}}^{-0.103}$ , until the Eddington limit is reached. In this regime the duty cycle can increase by as much as a

factor of three when  $P_{\text{orb}}$  is increased from three days to 200 days. Immediately after the Eddington limit is reached the behaviour of the duty cycle is dominated by the changes in the quiescence time. In the limit where  $t_{\text{out}} \ll t_{\text{q}}$  and  $R_{\text{max}} \ll R_{\text{irr}}$  then eq. (5.16) and eq. (5.30) give the dependence  $\propto P_{\text{orb}}^{0.263}$  (for a constant  $R_{\text{irr}}$  and  $\Sigma(R_{\text{max}}) \propto P_{\text{orb}}^{2/3}$ ). The intermediate regime (shaded blue in fig. 5.19) has moderate irradiation of the accretion disc and is characterised by an initial constant duty cycle. It is caused by the power laws that  $t_{\text{out}}$  and  $t_{\text{q}}$  obey when the disc is partially irradiated: from §5.4.2  $t_{\text{out}} \propto P_{\text{orb}}^{0.69}$  and  $t_{\text{q}} \propto P_{\text{orb}}^{0.67}$ . Hence the duty cycle  $\propto P_{\text{orb}}^{0.02}$  i.e. nearly constant with orbital period. This behaviour continues until the Eddington limit is reached (red line in fig. 5.19) and  $t_{\text{out}}$  becomes constant, whereupon the power law of  $\propto P_{\text{orb}}^{0.263}$  takes over. Due to the form of eq. (5.16), when  $R_{\text{irr}} \sim R_{\text{max}}$  there is no simple power law to describe the duty cycle as seen in fig. 5.19. As stated above the red line shown in fig. 5.19 cuts through the intermediate regime where the Eddington limit is reached. The point at which  $\dot{M}_{\text{Edd}}$  is reached can be calculated by using the results of §5.4.2:  $M_{\text{out}} \propto P_{\text{orb}}^{1.7}$  and  $t_{\text{out}} \propto P_{\text{orb}}^{0.69}$ . Therefore the mass accretion rate varies as  $\sim P_{\text{orb}}$  (likewise for  $\dot{M}_{\text{Edd}}$ ).

To summarise, there appear to be three general trends in the duty cycle, the behaviour of which depends on the importance of  $R_{\text{irr}}$ . I have classified the regimes according to the extent of the irradiation in the disc when the Eddington limit is reached:

- $\mathbf{R}_{\text{irr}}(\dot{M}_{\text{Edd}}) < \mathbf{R}_{\text{max}}$ : A low irradiation of the accretion disc, characterised by an initial increase followed by a peak then a gradual decline with  $P_{\text{orb}}$ .
- $\mathbf{R}_{\text{max}} < \mathbf{R}_{\text{irr}}(\dot{M}_{\text{Edd}}) < \mathbf{R}_{\text{disc}}$ : Moderate irradiation of the accretion disc, characterised a constant duty cycle followed by an increase at higher orbital periods.
- $\mathbf{R}_{\text{irr}}(\dot{M}_{\text{Edd}}) = \mathbf{R}_{\text{disc}}$ : High irradiation of the accretion disc, characterised by an initial fall in duty cycle followed by a rapid increase at high orbital periods.

From fig. 5.18 the relative importance of each of the three regimes depends on how much of the disc is irradiated, with  $H/R$  changing  $\dot{M}_1$ , see eq. (5.11). To more accurately predict how the duty cycles of LMXBs change as a function of orbital period, an idea of the importance of X-ray irradiation is needed. From the discussion in §4.5 the length of the current outburst of GRS 1915+105 may be important in this understanding.

In existing models of black hole LMXBs the duty cycle is often assumed to be constant with a value of  $\sim 0.01$ . The model outlined in this section is equally valid for LMXBs with a neutron star primary which some estimates of the duty cycle have been made. In a study of cataclysmic variables Dobrotka, Lasota & Menou (2006) found a

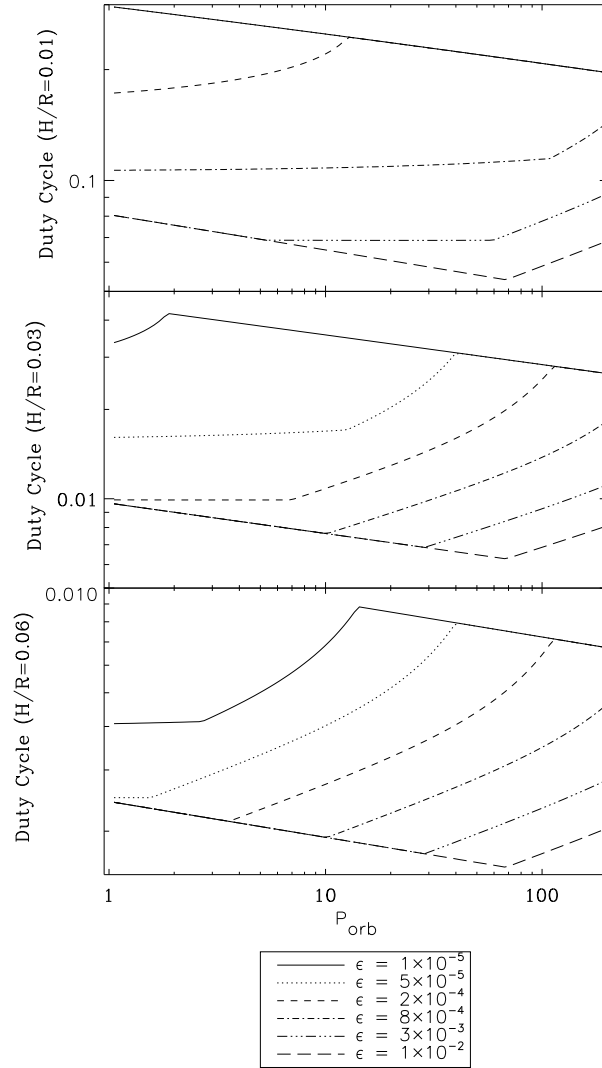


FIGURE 5.18. Variation of duty cycle with orbital period for three different values of  $H/R$  over a range of irradiation efficiencies.

relation between the duty cycle and the mass transfer rate from the secondary, approximately

$$\text{duty cycle} \sim \left( \frac{-\dot{M}_2}{\dot{M}_{\text{crit}}} \right)^2. \quad (5.37)$$

Where  $\dot{M}_{\text{crit}}$  is the critical mass accretion rate onto the primary ensuring all of the disc is irradiated (King et al. 1996). From eq. (4.6) one gets

$$\dot{M}_{\text{crit}} = \frac{4\pi\sigma T_H^4 R_{\text{disc}}^2}{\eta\epsilon c^2}. \quad (5.38)$$

Hence the duty cycle using this method varies approximately as  $\propto P_{\text{orb}}^{-0.81}$ . This model

was used by Fragos et al. (2008) for neutron stars, to simulate the XLF in Elliptical galaxies. The more complicated structure of the duty cycle dependence on the orbital period in the model presented in this work would likely influence their results. Depending on the importance of the irradiation of the disc the duty cycle can be expected to show three different types of behaviour as  $P_{\text{orb}}$  is increased. Assuming the model for the disc surface density is constant for all  $P_{\text{orb}}$ . The model described in this work is a more comprehensive method to describe the duty cycle of LMXBs than has been used in the past. However it is heavily dependant on the choice of parameters. These have been constrained to where possible by comparison to the few observations available and to detailed numerical simulations but much uncertainty remains. This toy model attempts to use the basic physics of accretion discs to reproduce their observed behaviour without resorting to a computationally expensive treatment similar to §4. It would be an ideal accompaniment for any studies looking at the X-ray luminosity in modelled star systems. Additionally, I have restricted myself to look at black hole LMXBs with giant companions. This analysis can be repeated in much the same way for main sequence donors and even extended to other classes of astrophysical objects such as CVs.

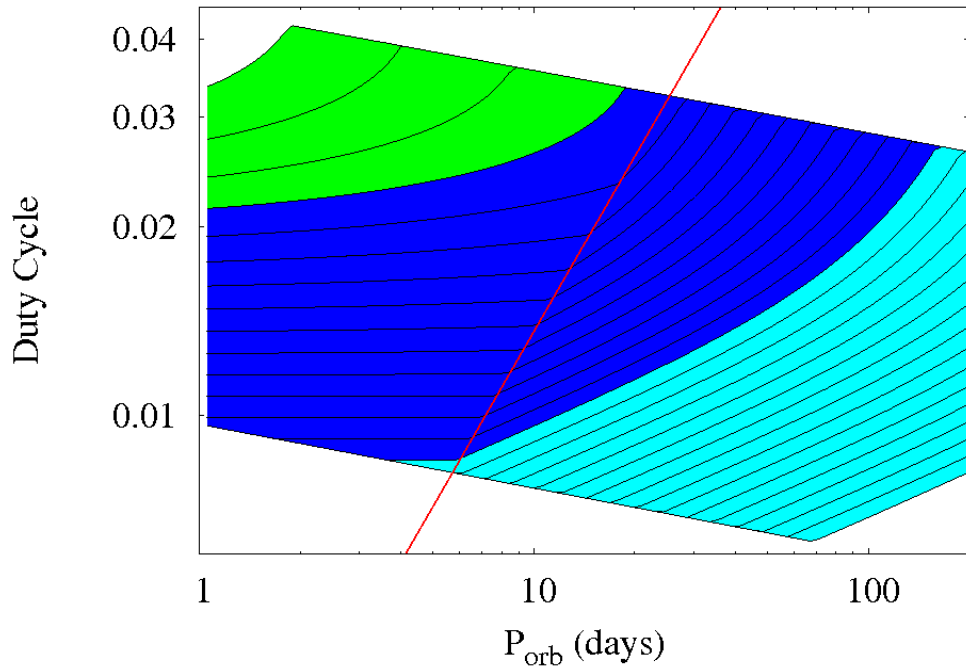
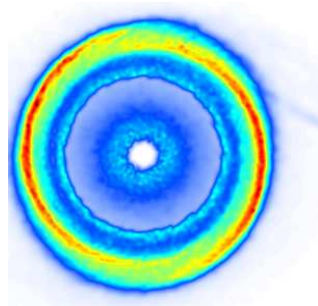


FIGURE 5.19. Depiction of the 3 different regimes in duty cycle  $P_{\text{orb}}$  parameter space as described in §5.7,  $\epsilon$  ranges from  $10^{-5} - 10^{-2}$ . If the top curve is characterised by  $i = 0$  then the efficiency of each curve  $i$  is given by  $\epsilon = 10^{-5} \times 1.26^i$ . The red line represents the points where the Eddington limit is reached in the moderate irradiation regime.

# Chapter 6

## *Conclusions*



“It don’t matter that some fool say he  
different...”  
- D’Angelo

*The Wire: All Prologue [2.06]*

In this thesis I have described accretion onto black holes in two scenarios: that of accretion from a diffuse medium in the Galactic centre and accretion in a binary system. Munro et al. (2005a) identified a LMXB candidate 0.1 parsec in projection from Sgr A\*, which due to its bright radio emission (Fender & Kuulkers 2001) they supposed contained a black hole. Alternatively, due to its faint X-ray luminosity there is the possibility that this binary may be accreting gas from the Minispiral and be a “fake LMXB” as described in §3.4.

In §3 and §4 I described objects in our own Galaxy, however observations described in §5 were the motivation for considering systems that could explain the X-ray emission in nearby galaxies. With the advent of the *Chandra* era there have been several studies of the X-ray emission of the Galaxy and its neighbours (for a review of extra galactic sources see Fabbiano (2006)). One of the most immediately noticeable features of LMXBs is their propensity to be found in globular clusters. In some elliptical galaxies the fraction of LMXBs associated with globular clusters is as high as 70% (Sarazin et al. 2003). LMXBs appear to be formed preferentially in globular clusters with a high collision rate (Peacock et al. 2009). Globular clusters have an unusually high stellar density and interactions between stars are far more likely than in the galactic field. This has led to the conclusion that LMXBs in globular clusters are formed by these interactions as opposed to the evolution of the binary system and/or the nuclear evolution of the stars. This alternative explanation for the formation of LMXBs has led some to conclude that most if not all LMXBs are formed in globular clusters (White, Sarazin & Kulkarni 2002). The LMXBs could be kicked out of the globular clusters which they were formed in due to the change in velocities experienced by a binary during the supernovae that forms the black hole/neutron star. Although this is refuted by Kundu et al. (2007), who find that the field LMXBs are associated with the underlying stellar population and are therefore likely formed in situ.

Whichever proves to be correct there are two distinct populations of LMXBs: those in globular clusters and those in the field. It has been proposed that LMXBs in globular clusters are primarily ultracompact X-ray binaries (Bildsten & Deloye 2004), i.e. a white dwarf secondary; while LMXBs in the field may be wide binaries with a red giant secondary (Piro & Bildsten 2002). Any binary with a large orbital period,  $P_{\text{orb}} \gtrsim 1$  day, would likely be disrupted by the frequent interactions in a globular cluster. However such binary systems could exist in the field. The formation mechanism of such binaries and LMXBs in general is still uncertain, with the possibility of the supernovae explosion destroying the binary. However there are other possible avenues: intermediate mass X-ray binaries which would be more likely to survive the supernovae (Podsiadlowski,

Rappaport & Pfahl 2002) and triple star systems, consisting of a high mass inner binary and a low mass companion (Eggleton & Verbunt 1986). However LMXBs are formed in the field, it appears likely that there are two different formation mechanisms for LMXBs that may result in differences in the system parameters, luminosity profiles, outburst and recurrence times. The observations of LMXBs with giant companions in the Sculptor dwarf spheroidal galaxy <sup>1</sup> (Maccarone et al. 2005) supports the idea that at least some of the field population comprises LMXBs with giant donors.

There have been several attempts to model the X-ray luminosity function (XLF) of elliptical galaxies, (Ivanova & Kalogera (2006) and Fragos et al. (2008)). The XLF is highly dependent on the population of X-ray binaries and models describing it are governed by the mass of the black hole /neutron star and the secondary type. Transient black hole X-ray binaries with red giant donors are particularly important when considering the high luminosity end of the XLF; while they may be less numerous than those with main sequence donors they are more luminous. A common problem when attempting to model the XLF of a particular galaxy is the lack of any constraints from theory or observations, on the duty cycles of X-ray transients. Ivanova & Kalogera (2006) report that the common assumption of a constant duty cycle for all systems fails to reproduce observations. Fragos et al. (2008) report that for certain parameters in their model a constant duty cycle of 1% could match observations, at the expense of removing the contribution of LMXBs from the XLF. Fragos et al. (2008) feel that a constant duty cycle of 1% is unrealistically low, however from §4 it may be appropriate for GRS 1915+105 like systems. The work presented in §4 and §5 is a step towards a understanding of long period black hole LMXBs which, as detailed above, are likely to reside in the field of galaxies and contribute significantly to the XLF.

Turning attention to our own Galaxy, of the confirmed 17 transient black hole LMXBs the longest period of 33.5 days is in GRS 1915+105. If the duty cycles of GRS 1915+105 like systems are as predicted in §4, it implies that there are potentially many more systems with similar orbital periods that are currently quiescent. Previous studies have assumed a constant duty cycle when estimating the number of these quiescent systems, however §5 has demonstrated that (depending on the model assumed for the accretion disc) longer period systems ( $P_{\text{orb}} \sim 10 - 100$  days) potentially spend less time in quiescence than previously assumed. Observation of quiescent black hole LMXBs in the Galaxy is challenging; they are  $\sim 100$  times less luminous than those containing a neutron star (Garcia et al. 2001), although longer period systems do appear to have

---

<sup>1</sup>low luminosity galaxies with little gas, dust or recent star formation, additionally they do not contain any globular clusters.

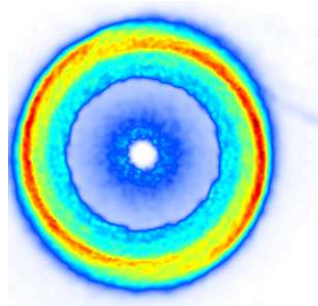
## Conclusions:

---

higher quiescent luminosities. Comparisons between the observed LMXBs in outburst and those in quiescence in the Galaxy would provide information on the duty cycles of these objects as well as the orbital period range. Improved estimates of the duty cycle and orbital period of LMXBs may allow the structure of the accretion disc to be inferred based on the models outlined in §5, improving any attempt to model the XLF of other galaxies.

# Appendix A

## *Results*



“....a little slow, a little late.”  
- Avon Barksdale

*The Wire: The Pager [1.05]*

Results:

---

In this appendix I detail all of the parameters used in the simulations described in §4 in table A.1. In table A.2 the raw data from the code is displayed along with the results post processing using the scaling method outlined in §4.3.6. The errors have been omitted from the tables for clarity but are shown on the figures in §4. The parameters were chosen so that  $\dot{M}_1 > -\dot{M}_2$  and the scaling method (see §4.3.6) was applicable (for discussion see §4.4.2).

Simulation Name	$\Sigma_{max}$	$\Sigma_{min}$	$\alpha_h^{\text{sph}}$	$\alpha_c^{\text{sph}}$	$\eta$	$\epsilon$	$\lambda$
base	55	4.7853	1.0	0.1	0.1	7e-4	1
irr 1	55	4.7853	1.0	0.1	0.1	3e-4	1
irr 2	55	4.7853	1.0	0.1	0.1	5e-4	1
irr 3	55	4.7853	1.0	0.1	0.1	9e-4	1
irr 4	55	4.7853	1.0	0.1	0.1	1.2e-3	1
sig max 1	40	4.7853	1.0	0.1	0.1	7e-4	1
sig max 2	47.5	4.7853	1.0	0.1	0.1	7e-4	1
sig max 3	62.7	4.7853	1.0	0.1	0.1	7e-4	1
sig max 4	70	4.7853	1.0	0.1	0.1	7e-4	1
sig min 1	55	3	1.0	0.1	0.1	7e-4	1
sig min 2	55	7	1.0	0.1	0.1	7e-4	1
sig min 3	55	10	1.0	0.1	0.1	7e-4	1
sig min 4	55	15	1.0	0.1	0.1	7e-4	1
alpha h 1	55	4.7853	0.5	0.1	0.1	7e-4	1
alpha h 2	55	4.7853	0.8	0.1	0.1	7e-4	1
alpha h 3	55	4.7853	1.3	0.1	0.1	7e-4	1
alpha h 4	55	4.7853	1.5	0.1	0.1	7e-4	1
alpha c 1	55	4.7853	1.0	0.05	0.1	7e-4	1
alpha c 2	55	4.7853	1.0	0.08	0.1	7e-4	1
alpha c 3	55	4.7853	1.0	0.15	0.1	7e-4	1
alpha c 4	55	4.7853	1.0	0.2	0.1	7e-4	1
wind 1	55	4.7853	1.0	0.1	0.1	7e-4	0.6
wind 2	55	4.7853	1.0	0.1	0.1	7e-4	0.8
wind 3	55	4.7853	1.0	0.1	0.1	7e-4	1.2
wind 4	55	4.7853	1.0	0.1	0.1	7e-4	1.4

Table A.1. Table detailing the parameters used in each simulation

Results:

Simulation Name	Out time (d)	Rec time (d)	$\dot{M}_1$ ( $10^{-8} M_{\odot} \text{ yr}^{-1}$ )	$\dot{M}_{\text{wind}}$	scaled Out time (yr)	scaled rec time (yr)	duty cycle
base	967	868	3.1	0.12	23.8	10722	0.00222
irr 1	974	873	3.1	0.09	24.0	10778	0.00223
irr 2	973	877	3.1	0.10	24.0	10829	0.00221
irr 3	978	864	3.1	0.11	24.1	10673	0.00226
irr 4	1044	850	2.9	0.16	26.2	10629	0.00246
sig max 1	924	582	2.7	0.03	22.8	7185	0.00317
sig max 2	904	769	3.0	0.06	22.3	9499	0.00235
sig max 3	1016	948	3.2	0.16	25.0	11715	0.00214
sig max 4	690-1040	650-990	1.8-3.9	0.09-0.5	17-26	8029-12229	**
sig min 1	1125	872	2.8	0.04	27.7	10772	0.00257
sig min 2	839	846	3.3	0.18	20.7	10454	0.00198
sig min 3	741	800	3.5	0.27	18.3	9882	0.00185
sig min 4	622	713	3.7	0.55	15.3	8801	0.00174
alpha h 1	1625	343	2.0	0.08	37.0	4241	0.00944
alpha h 2	1104	780	2.8	0.1	26.7	9635	0.00282
alpha h 3	733	825	3.5	0.36	18.1	10191	0.00177
alpha h 4	623	717	3.7	0.40	15.3	8853	0.00173
alpha c 1	974	934	3.1	0.15	24.0	21795	0.00117
alpha c 2	971	898	3.1	0.11	23.9	13716	0.00174
alpha c 3	1022	830	3.0	0.11	25.2	5565	0.00453
alpha c 4	**	**	**	**	**	**	**
wind 1	605-885	625-985	1.6-3.0	0.53-2.0	15-22	7720-12167	**
wind 2	970	908	2.9	0.46	23.9	11211	0.00213
wind 3	975	857	3.2	0.01	24.0	10582	0.00227
wind 4	976	865	3.2	0.00	24.1	10685	0.00225

Table A.2. Table containing the raw outburst and recurrence times and the final processed results. Errors have been suppressed for clarity. Simulations with \*\* never reached a steady state.

Results:

---

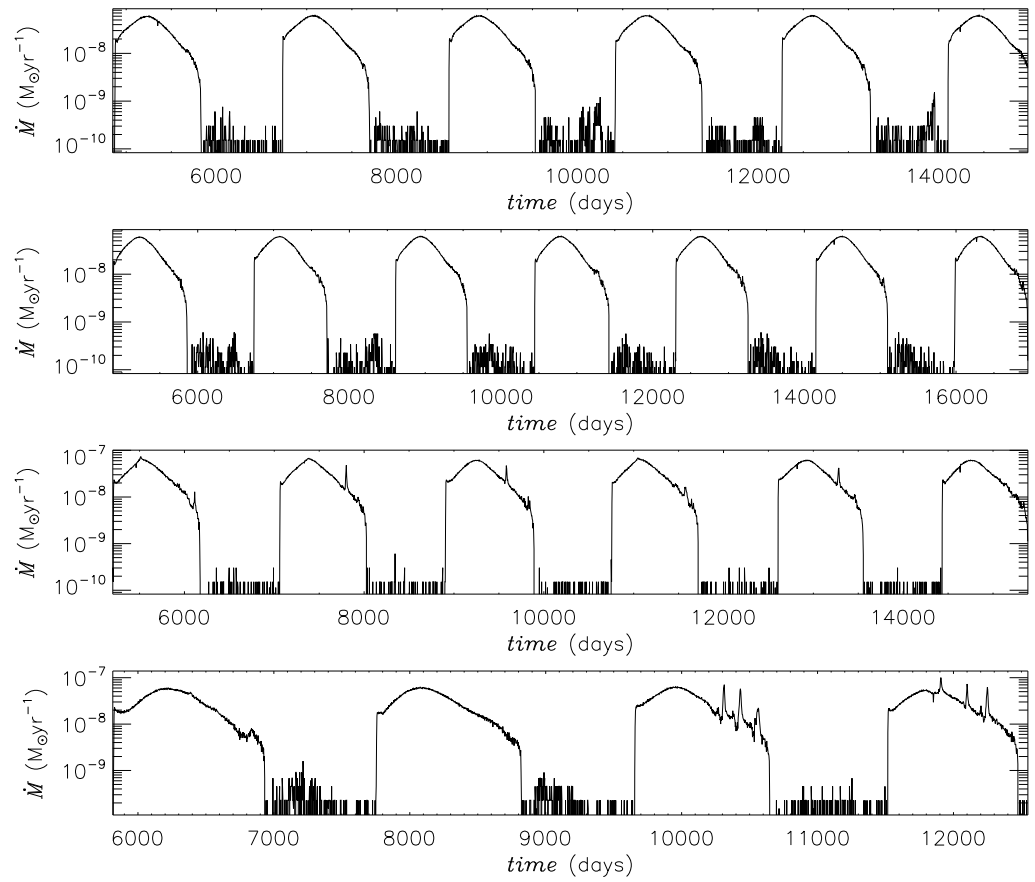


FIGURE A.1. Mass accretion rate as a function of time for the simulations irr 1, irr 2, irr 3 and irr 4 respectively.

## Results:

---

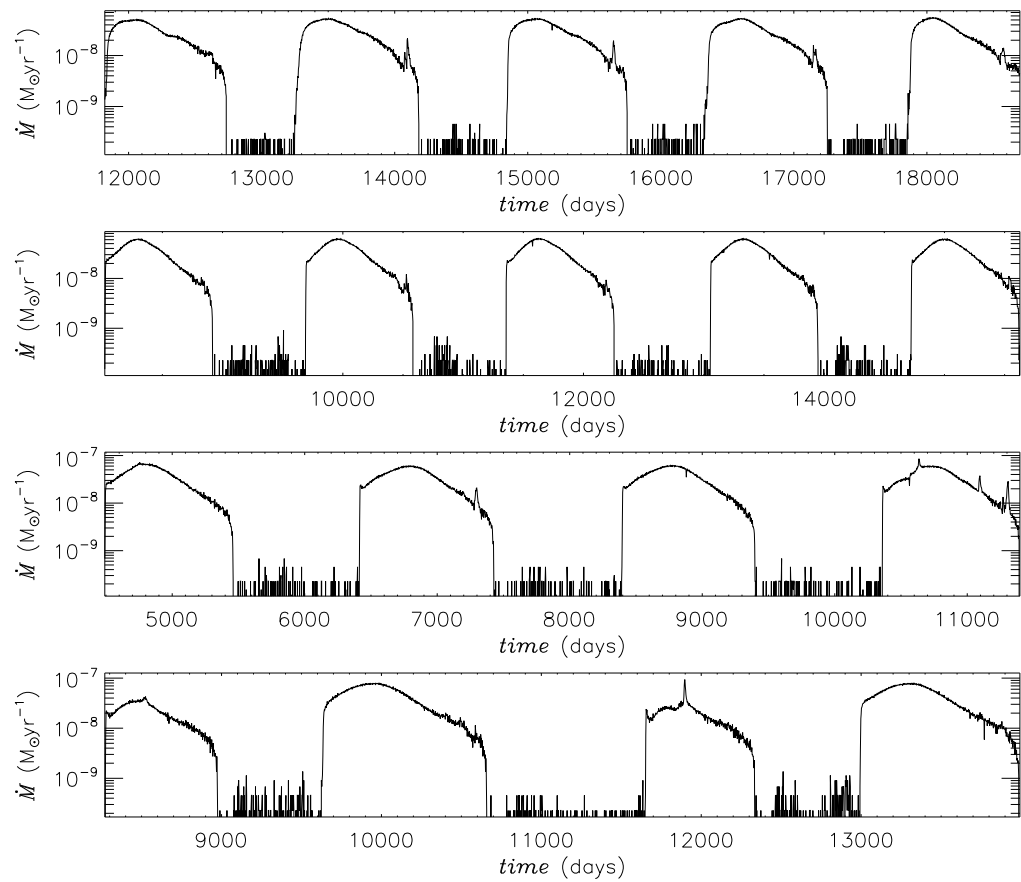


FIGURE A.2. Mass accretion rate as a function of time for the simulations sig max 1, sig max 2, sig max 3 and sig max 4 respectively.

Results:

---

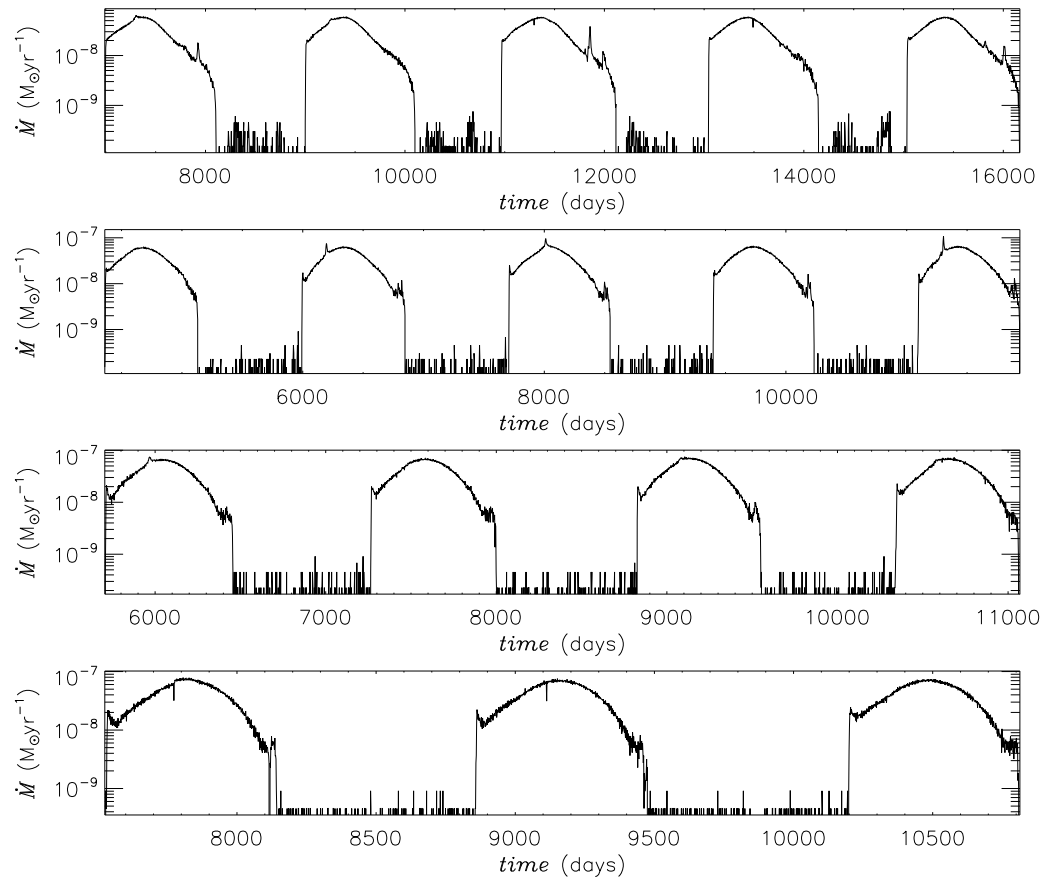


FIGURE A.3. Mass accretion rate as a function of time for the simulations sig min 1, sig min 2, sig min 3 and sig min 4 respectively.

## Results:

---

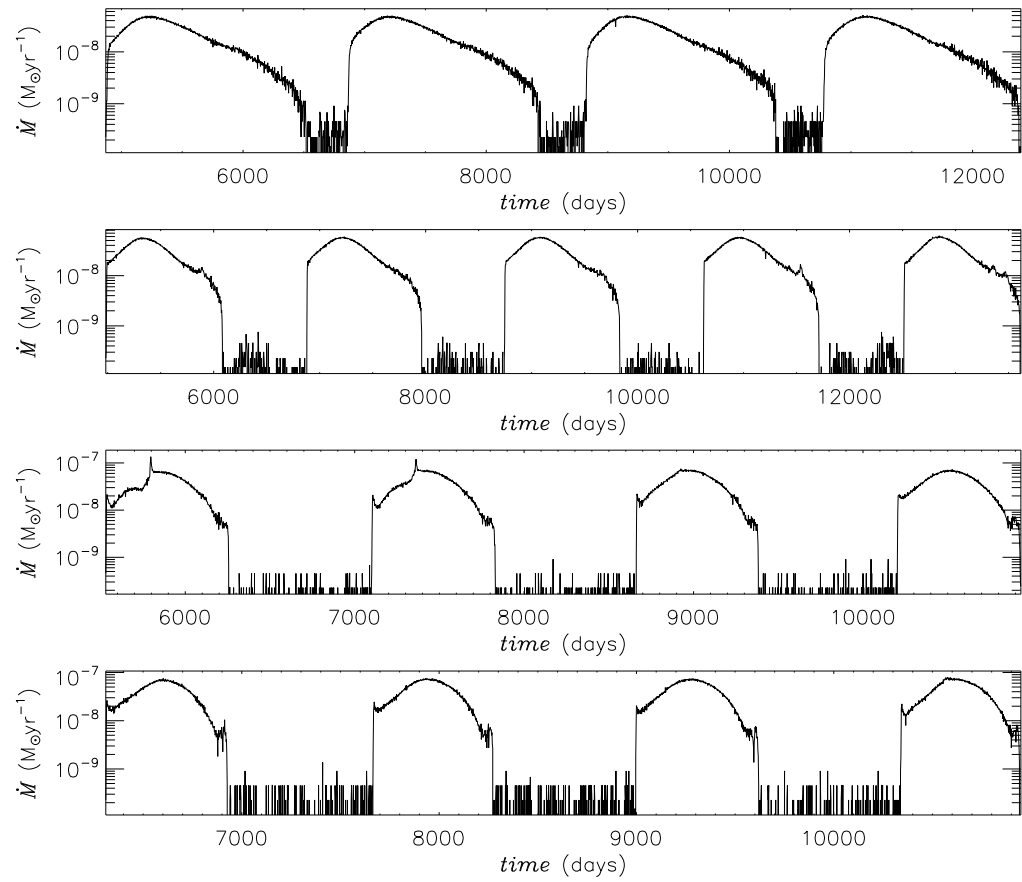


FIGURE A.4. Mass accretion rate as a function of time for the simulations alpha h 1, alpha h 2, alpha h 3 and alpha h 4 respectively.

## Results:

---

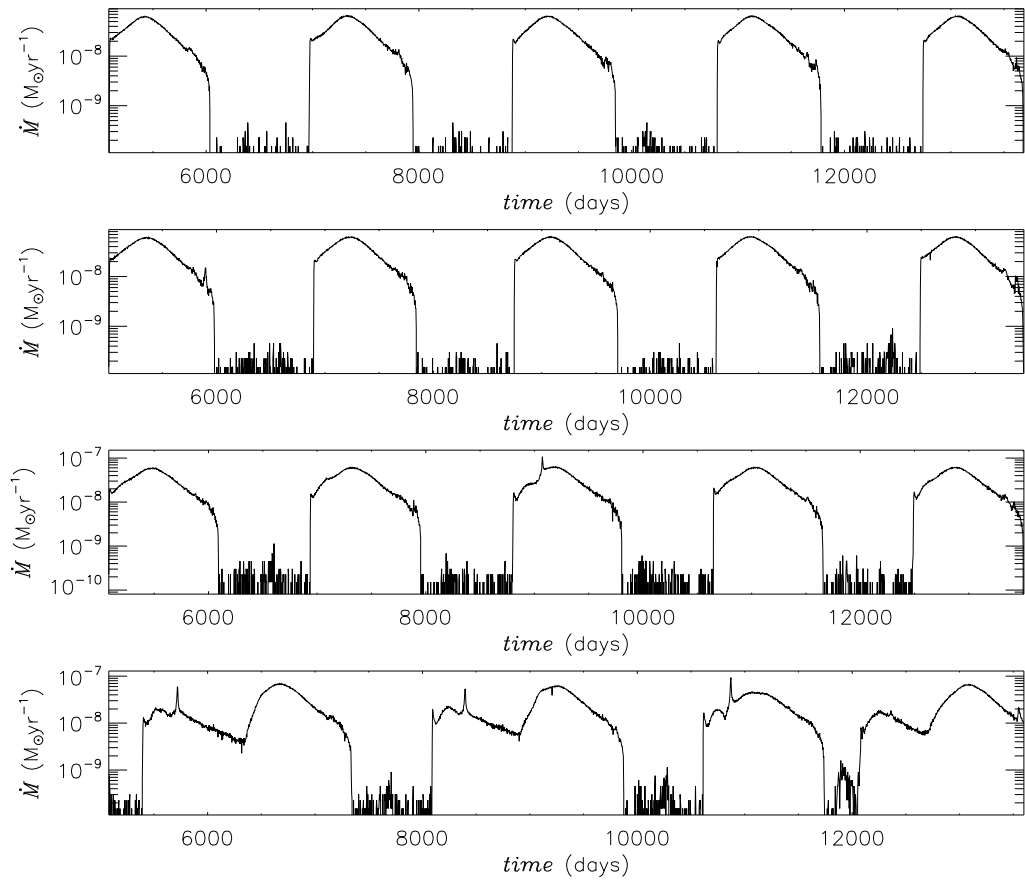


FIGURE A.5. Mass accretion rate as a function of time for the simulations alpha c 1, alpha c 2, alpha c 3 and alpha c 4 respectively.

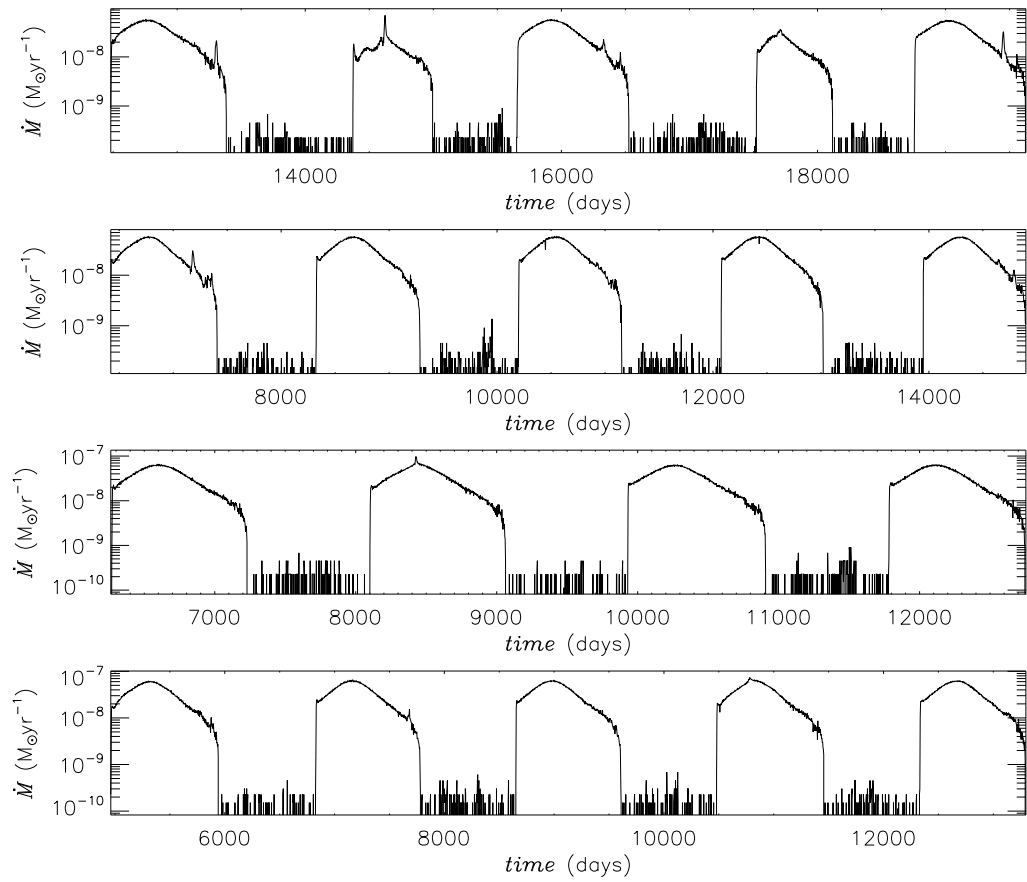


FIGURE A.6. Mass accretion rate as a function of time for the simulations wind 1, wind 2, wind 3 and wind 4 respectively.

## *Bibliography*

- Agol, E. & Kamionkowski, M. (2002), 'X-rays from isolated black holes in the Milky Way', *MNRAS* **334**, 553–562.
- Alexander, T. & Livio, M. (2004), 'Orbital Capture of Stars by a Massive Black Hole via Exchanges with Compact Remnants', *ApJL* **606**, L21–L24.
- Alexander, T. & Loeb, A. (2001), 'Enhanced Microlensing by Stars around the Black Hole in the Galactic Center', *ApJ* **551**, 223–230.
- Baganoff, F. K., Maeda, Y., Morris, M., Bautz, M. W., Brandt, W. N., Cui, W., Doty, J. P., Feigelson, E. D., Garmire, G. P., Pravdo, S. H., Ricker, G. R. & Townsley, L. K. (2003), 'Chandra X-Ray Spectroscopic Imaging of Sagittarius A\* and the Central Parsec of the Galaxy', *ApJ* **591**, 891–915.
- Bahcall, J. N. & Wolf, R. A. (1976), 'Star distribution around a massive black hole in a globular cluster', *ApJ* **209**, 214–232.
- Balbus, S. A. (2003), 'Enhanced Angular Momentum Transport in Accretion Disks', *AAR&A* **41**, 555–597.
- Balbus, S. A. & Hawley, J. F. (1991), 'A powerful local shear instability in weakly magnetized disks. I - Linear analysis. II - Nonlinear evolution', *ApJ* **376**, 214–233.
- Balbus, S. A. & Hawley, J. F. (2003), Numerical Simulations of MHD Turbulence in Accretion Disks, in E. Falgarone & T. Passot, eds, 'Turbulence and Magnetic Fields in Astrophysics', Vol. 614 of *Lecture Notes in Physics*, Berlin Springer Verlag, pp. 329–348.
- Balick, B. & Brown, R. L. (1974), 'Intense sub-arcsecond structure in the galactic center', *ApJ* **194**, 265–270.
- Belloni, T., Mendez, M., King, A. R., van der Klis, M. & van Paradijs, J. (1997), 'A Unified Model for the Spectral Variability in GRS 1915+105', *ApJL* **488**, L109+.
- Benz, W. (1990), Smooth Particle Hydrodynamics - a Review, in J. R. Buchler, ed., 'Numerical Modelling of Nonlinear Stellar Pulsations Problems and Prospects', pp. 269–+.

- Bildsten, L. & Deloye, C. J. (2004), ‘Ultracompact Binaries as Bright X-Ray Sources in Elliptical Galaxies’, *ApJL* **607**, L119–L122.
- Blaes, O. & Madau, P. (1993), ‘Can we observe accreting, isolated neutron stars?’, *ApJ* **403**, 690–705.
- Bolton, C. T. (1972), ‘Identification of Cygnus X-1 with HDE 226868’, *Nature* **235**, 271–273.
- Bondi, H. (1952), ‘On spherically symmetrical accretion’, *MNRAS* **112**, 195–+.
- Bondi, H. & Hoyle, F. (1944), ‘On the mechanism of accretion by stars’, *MNRAS* **104**, 273–+.
- Brocksopp, C., Jonker, P. G., Fender, R. P., Groot, P. J., van der Klis, M. & Tingay, S. J. (2001), ‘The 1997 hard-state outburst of the X-ray transient GS 1354-64/BW Cir’, *MNRAS* **323**, 517–528.
- Cannizzo, J. K., Shafter, A. W. & Wheeler, J. C. (1988), ‘On the outburst recurrence time for the accretion disk limit cycle mechanism in dwarf novae’, *ApJ* **333**, 227–235.
- Cannizzo, J. K. & Wheeler, J. C. (1984), ‘The vertical structure and stability of alpha model accretion disks’, *ApJS* **55**, 367–388.
- Casares, J., Charles, P. A., Naylor, T. & Pavlenko, E. P. (1993), ‘Optical Studies of V:404-CYGNI the X-Ray Transient GS:2023+338 - Part Three - the Secondary Star and Accretion Disc’, *MNRAS* **265**, 834–+.
- Casares, J., Zurita, C., Shahbaz, T., Charles, P. A. & Fender, R. P. (2004), ‘Evidence of a Black Hole in the X-Ray Transient GS 1354-64 (=BW Circini)’, *ApJL* **613**, L133–L136.
- Castro-Tirado, A. J., Brandt, S. & Lund, N. (1992), ‘GRS 1915+105’, *IAU Circ* **5590**, 2–+.
- Chanamé, J. & Gould, A. (2002), ‘Millisecond Pulsars as Probes of Mass Segregation in the Galactic Center’, *ApJ* **571**, 320–325.
- Chanamé, J., Gould, A. & Miralda-Escudé, J. (2001), ‘Microlensing by Stellar Black Holes around Sagittarius A\*’, *ApJ* **563**, 793–799.
- Clark, G. W. (1975), ‘X-ray binaries in globular clusters’, *ApJL* **199**, L143–L145.
- Cowley, A. P., Crampton, D., Hutchings, J. B., Remillard, R. & Penfold, J. E. (1983), ‘Discovery of a massive unseen star in LMC X-3’, *ApJ* **272**, 118–122.
- Cuadra, J., Nayakshin, S., Springel, V. & di Matteo, T. (2006), Accretion of Stellar Winds in the Galactic Centre, in ‘Revista Mexicana de Astronomia y Astrofisica Conference Series’, Vol. 26 of *Revista Mexicana de Astronomia y Astrofisica Conference Series*, pp. 139–140.

- Dobrotka, A., Lasota, J.-P. & Menou, K. (2006), ‘All Quiet in Globular Clusters’, *ApJ* **640**, 288–298.
- Dubus, G., Hameury, J.-M. & Lasota, J.-P. (2001), ‘The disc instability model for X-ray transients: Evidence for truncation and irradiation’, *A&A* **373**, 251–271.
- Duquennoy, A. & Mayor, M. (1991), ‘Multiplicity among solar-type stars in the solar neighbourhood. II - Distribution of the orbital elements in an unbiased sample’, *A&A* **248**, 485–524.
- Eckart, A. & Genzel, R. (1997), ‘Stellar proper motions in the central 0.1 PC of the Galaxy’, *MNRAS* **284**, 576–598.
- Eggleton, P. P. (1983), ‘Approximations to the radii of Roche lobes’, *ApJ* **268**, 368–+.
- Eggleton, P. P. & Verbunt, F. (1986), ‘Triple star evolution and the formation of short-period, low mass X-ray binaries’, *MNRAS* **220**, 13P–18P.
- Einstein, A. (1915), ‘Die Feldgleichungen der Gravitation’, *Sitzungsberichte der Königlich Preussischen Akademie der Wissenschaften (Berlin)*, Seite 844-847. pp. 844–847.
- Esin, A. A., McClintock, J. E. & Narayan, R. (1997), ‘Advection-dominated Accretion and the Spectral States of Black Hole X-Ray Binaries: Application to Nova MUS-CAE 1991’, *ApJ* **489**, 865–+.
- Fabbiano, G. (2006), ‘Populations of X-Ray Sources in Galaxies’, *AAR&A* **44**, 323–366.
- Fender, R. & Belloni, T. (2004), ‘GRS 1915+105 and the Disc-Jet Coupling in Accreting Black Hole Systems’, *AAR&A* **42**, 317–364.
- Fender, R. P. & Kuulkers, E. (2001), ‘On the peak radio and X-ray emission from neutron star and black hole candidate X-ray transients’, *MNRAS* **324**, 923–930.
- Fischer, D. A. & Marcy, G. W. (1992), ‘Multiplicity among M dwarfs’, *ApJ* **396**, 178–194.
- Fragos, T., Kalogera, V., Belczynski, K., Fabbiano, G., Kim, D.-W., Brassington, N. J., Angelini, L., Davies, R. L., Gallagher, J. S., King, A. R., Pellegrini, S., Trinchieri, G., Zepf, S. E., Kundu, A. & Zezas, A. (2008), ‘Models for Low-Mass X-Ray Binaries in the Elliptical Galaxies NGC 3379 and NGC 4278: Comparison with Observations’, *ApJ* **683**, 346–356.
- Frank, J., King, A. & Raine, D. J. (2002), *Accretion Power in Astrophysics: Third Edition*, Accretion Power in Astrophysics, by Juhan Frank and Andrew King and Derek Raine, pp. 398. ISBN 0521620538. Cambridge, UK: Cambridge University Press, February 2002.
- Freitag, M., Amaro-Seoane, P. & Kalogera, V. (2006), ‘Stellar Remnants in Galactic Nuclei: Mass Segregation’, *ApJ* **649**, 91–117.

- Garcia, M. R., McClintock, J. E., Narayan, R., Callanan, P., Barret, D. & Murray, S. S. (2001), 'New Evidence for Black Hole Event Horizons from Chandra', *ApJL* **553**, L47–L50.
- Ghez, A. M., Becklin, E., Duchjne, G., Hornstein, S., Morris, M., Salim, S. & Tanner, A. (2003), 'Full Three Dimensional Orbits For Multiple Stars on Close Approaches to the Central Supermassive Black Hole', *Astronomische Nachrichten Supplement* **324**, 527–533.
- Gingold, R. A. & Monaghan, J. J. (1977), 'Smoothed particle hydrodynamics - Theory and application to non-spherical stars', *MNRAS* **181**, 375–389.
- González Hernández, J. I., Rebolo, R. & Israelian, G. (2008), 'The black hole binary nova Scorpii 1994 (GRO J1655-40): an improved chemical analysis', *A&A* **478**, 203–217.
- Greiner, J., Cuby, J. G. & McCaughrean, M. J. (2001), 'An unusually massive stellar black hole in the Galaxy', *Nature* **414**, 522–525.
- Greiner, J., Cuby, J. G., McCaughrean, M. J., Castro-Tirado, A. J. & Mennickent, R. E. (2001), 'Identification of the donor in the X-ray binary GRS 1915+105', *A&A* **373**, L37–L40.
- Greiner, J., Morgan, E. H. & Remillard, R. A. (1996), 'Rossi X-Ray Timing Explorer Observations of GRS 1915+105', *ApJL* **473**, L107+.
- Grimm, H.-J., Gilfanov, M. & Sunyaev, R. (2003), 'X-ray binaries in the Milky Way and other galaxies', *Chinese Journal of Astronomy and Astrophysics Supplement* **3**, 257–269.
- Hōshi, R. (1979), 'Accretion Model for Outbursts of Dwarf Nova', *Progress of Theoretical Physics* **61**, 1307–1319.
- Hameury, J.-M., Menou, K., Dubus, G., Lasota, J.-P. & Hure, J.-M. (1998), 'Accretion disc outbursts: a new version of an old model', *MNRAS* **298**, 1048–1060.
- Hamilton, D. P. & Burns, J. A. (1991), 'Orbital stability zones about asteroids', *Icarus* **92**, 118–131.
- Harlaftis, E. T. & Greiner, J. (2004), 'The rotational broadening and the mass of the donor star of GRS 1915+105', *A&A* **414**, L13–L16.
- Hernquist, L. & Katz, N. (1989), 'TREESPH - A unification of SPH with the hierarchical tree method', *ApJS* **70**, 419–446.
- Hessman, F. V. & Hopp, U. (1990), 'The massive, nearly face-on cataclysmic variable GD 552', *A&A* **228**, 387–398.
- Hopman, C. & Alexander, T. (2006), 'The Effect of Mass Segregation on Gravitational Wave Sources near Massive Black Holes', *ApJL* **645**, L133–L136.

- Hoyle, F. & Lyttleton, R. A. (1939), The effect of interstellar matter on climatic variation, in 'Proceedings of the Cambridge Philosophical Society', Vol. 35 of *Proceedings of the Cambridge Philosophical Society*, pp. 405–+.
- Iorio, L. (2008), 'On the orbital and physical parameters of the HDE 226868/Cygnus X-1 binary system', *Astrophysics and Space Science* pp. 114–+.
- Irwin, J. A. (2006), 'The remarkable stability of probable black hole low-mass X-ray binaries in nearby galaxies', *MNRAS* **371**, 1903–1911.
- Ivanova, N. & Kalogera, V. (2006), 'The Brightest Point X-Ray Sources in Elliptical Galaxies and the Mass Spectrum of Accreting Black Holes', *ApJ* **636**, 985–994.
- Keek, L., in't Zand, J. J. M., Kuulkers, E., Cumming, A., Brown, E. F. & Suzuki, M. (2008), 'First superburst from a classical low-mass X-ray binary transient', *A&A* **479**, 177–188.
- Kim, D.-W. & Fabbiano, G. (2004), 'X-Ray Luminosity Function and Total Luminosity of Low-Mass X-Ray Binaries in Early-Type Galaxies', *ApJ* **611**, 846–857.
- King, A. R. (1988), 'The evolution of compact binaries', *QJRAS* **29**, 1–25.
- King, A. R., Kolb, U. & Burderi, L. (1996), 'Black Hole Binaries and X-Ray Transients', *ApJL* **464**, L127+.
- King, A. R. & Ritter, H. (1998), 'The light curves of soft X-ray transients', *MNRAS* **293**, L42–L48.
- Krabbe, A., Genzel, R., Eckart, A., Najarro, F., Lutz, D., Cameron, M., Kroker, H., Tacconi-Garman, L. E., Thatte, N., Weitzel, L., Drapatz, S., Geballe, T., Sternberg, A. & Kudritzki, R. (1995), 'The Nuclear Cluster of the Milky Way: Star Formation and Velocity Dispersion in the Central 0.5 Parsec', *ApJL* **447**, L95+.
- Kundu, A., Maccarone, T. J. & Zepf, S. E. (2007), 'Probing the Formation of Low-Mass X-Ray Binaries in Globular Clusters and the Field', *ApJ* **662**, 525–543.
- Lasota, J.-P. (2001), 'The disc instability model of dwarf novae and low-mass X-ray binary transients', *New Astronomy Review* **45**, 449–508.
- Lucy, L. B. (1977), 'A numerical approach to the testing of the fission hypothesis', *AJ* **82**, 1013–1024.
- Lynden-Bell, D. & Rees, M. J. (1971), 'On quasars, dust and the galactic centre', *MNRAS* **152**, 461–+.
- Maccarone, T. J., Kundu, A., Zepf, S. E., Piro, A. L. & Bildsten, L. (2005), 'The discovery of X-ray binaries in the Sculptor dwarf spheroidal galaxy', *MNRAS* **364**, L61–L65.

- Makishima, K., Takahashi, H., Yamada, S., Done, C., Kubota, A., Dotani, T., Ebisawa, K., Itoh, T., Kitamoto, S., Negoro, H., Ueda, Y. & Yamaoka, K. (2008), ‘Suzaku Results on Cygnus X-1 in the Low/Hard State’, *PASJ* **60**, 585–.
- Mayer, M. & Pringle, J. E. (2007), ‘Time-dependent models of two-phase accretion discs around black holes’, *MNRAS* **376**, 435–456.
- McClintock, J. E. & Remillard, R. A. (2006), *Black hole binaries*, Compact stellar X-ray sources, pp. 157–213.
- Menou, K., Esin, A. A., Narayan, R., Garcia, M. R., Lasota, J.-P. & McClintock, J. E. (1999), ‘Black Hole and Neutron Star Transients in Quiescence’, *ApJ* **520**, 276–291.
- Michell, J. (1784), ‘On the Means of Discovering the Distance, Magnitude, &c. of the Fixed Stars, in Consequence of the Diminution of the Velocity of Their Light, in Case Such a Diminution Should be Found to Take Place in any of Them, and Such Other Data Should be Procured from Observations, as Would be Farther Necessary for That Purpose. By the Rev. John Michell, B. D. F. R. S. In a Letter to Henry Cavendish, Esq. F. R. S. and A. S.’, *Philosophical Transactions Series I* **74**, 35–57.
- Mirabel, I. F., Duc, P. A., Teyssier, R., Paul, J., Claret, A., Rodríguez, L. F., Auriere, M., Golombek, D. & Martí, J. (1994), Multiwavelength observations of the possible soft gamma-ray burster GRS 1915+105., in C. E. Fichtel, N. Gehrels & J. P. Norris, eds, ‘American Institute of Physics Conference Series’, Vol. 304 of *American Institute of Physics Conference Series*, pp. 351–355.
- Mirabel, I. F. & Rodriguez, L. F. (1994), ‘A Superluminal Source in the Galaxy’, *Nature* **371**, 46–+.
- Mirabel, I. F., Rodriguez, L. F., Martí, J., Teyssier, R., Paul, J. & Auriere, M. (1993), ‘GRS 1915+105’, *IAU Circ* **5773**, 2–+.
- Miralda-Escudé, J. & Gould, A. (2000), ‘A Cluster of Black Holes at the Galactic Center’, *ApJ* **545**, 847–853.
- Monaghan, J. J. (1992), ‘Smoothed particle hydrodynamics’, *AAR&A* **30**, 543–574.
- Monaghan, J. J. & Lattanzio, J. C. (1985), ‘A refined particle method for astrophysical problems’, *A&A* **149**, 135–143.
- Morris, M. (1993), ‘Massive star formation near the Galactic center and the fate of the stellar remnants’, *ApJ* **408**, 496–506.
- Mouawad, N., Eckart, A., Pfalzner, S., Schödel, R., Moutaka, J. & Spurzem, R. (2005), ‘Weighing the cusp at the Galactic Centre’, *Astronomische Nachrichten* **326**, 83–95.
- Muno, M. P., Lu, J. R., Baganoff, F. K., Brandt, W. N., Garmire, G. P., Ghez, A. M., Hornstein, S. D. & Morris, M. R. (2005a), ‘A Remarkable Low-Mass X-Ray Binary within 0.1 Parsecs of the Galactic Center’, *ApJ* **633**, 228–239.

- Muno, M. P., Pfahl, E., Baganoff, F. K., Brandt, W. N., Ghez, A., Lu, J. & Morris, M. R. (2005*b*), ‘An Overabundance of Transient X-Ray Binaries within 1 Parsec of the Galactic Center’, *ApJL* **622**, L113–L116.
- Murray, J. R. (1995), ‘SPH simulations of accretion disks in cataclysmic variables.’, *Publications of the Astronomical Society of Australia* **12**, 272–273.
- Murray, J. R. (1996), ‘SPH simulations of tidally unstable accretion discs in cataclysmic variables’, *MNRAS* **279**, 402–414.
- Murray, J. R., Truss, M. R. & Wynn, G. A. (2002), Modelling unstable accretion discs, in B. T. Gänsicke, K. Beuermann & K. Reinsch, eds, ‘The Physics of Cataclysmic Variables and Related Objects’, Vol. 261 of *Astronomical Society of the Pacific Conference Series*, pp. 416–+.
- Nayakshin, S. & Sunyaev, R. (2007), ‘X-rays from cusps of compact remnants near galactic centres’, *MNRAS* **377**, 1647–1651.
- Oda, M., Gorenstein, P., Gursky, H., Kellogg, E., Schreier, E., Tananbaum, H. & Giacconi, R. (1971), ‘X-Ray Pulsations from Cygnus X-1 Observed from UHURU’, *ApJL* **166**, L1+.
- Oppenheimer, J. R. & Snyder, H. (1939), ‘On Continued Gravitational Contraction’, *Physical Review* **56**, 455–459.
- Oppenheimer, J. R. & Volkoff, G. M. (1939), ‘On Massive Neutron Cores’, *Physical Review* **55**, 374–381.
- Paczynski, B. (1971), ‘Evolutionary Processes in Close Binary Systems’, *AAR&A* **9**, 183–+.
- Paumard, T., Maillard, J.-P. & Morris, M. (2004), ‘Kinematic and structural analysis of the  $\zeta$ ASTROBJ<sub>1</sub>Minispiral/ $\zeta$ ASTROBJ<sub>2</sub> in the Galactic Center from BEAR spectro-imagery’, *A&A* **426**, 81–96.
- Peacock, M. B., Maccarone, T. J., Waters, C. Z., Kundu, A., Zepf, S. E., Knigge, C. & Zurek, D. R. (2009), ‘Wide Field CAMera survey of M31 globular clusters: low-mass X-ray binaries’, *MNRAS* **392**, L55–L59.
- Perna, R., Narayan, R., Rybicki, G., Stella, L. & Treves, A. (2003), ‘Bondi Accretion and the Problem of the Missing Isolated Neutron Stars’, *ApJ* **594**, 936–942.
- Pfahl, E. & Loeb, A. (2004), ‘Probing the Spacetime around Sagittarius A\* with Radio Pulsars’, *ApJ* **615**, 253–258.
- Piro, A. L. & Bildsten, L. (2002), ‘Transient X-Ray Binaries in Elliptical Galaxies’, *ApJL* **571**, L103–L106.
- Plavec, M. & Kratochvil, P. (1964), ‘Tables for the Roche model of close binaries’, *Bulletin of the Astronomical Institutes of Czechoslovakia* **15**, 165–+.

- Podsiadlowski, P., Rappaport, S. & Pfahl, E. D. (2002), ‘Evolutionary Sequences for Low- and Intermediate-Mass X-Ray Binaries’, *ApJ* **565**, 1107–1133.
- Press, W. H., Teukolsky, S. A., Vetterling, W. T. & Flannery, B. P. (1992), *Numerical recipes in FORTRAN. The art of scientific computing*, Cambridge: University Press, —c1992, 2nd ed.
- Pringle, J. E. (1981), ‘Accretion discs in astrophysics’, *AAR&A* **19**, 137–162.
- Richter, G. A. (1989), ‘V404 Cyg - a Further Outburst in 1956’, *Information Bulletin on Variable Stars* **3362**, 1–+.
- Ritter, H. (1999), ‘Analytical solution for the evolution of a binary with stable mass transfer from a giant’, *MNRAS* **309**, 360–372.
- Rubilar, G. F. & Eckart, A. (2001), ‘Periastron shifts of stellar orbits near the Galactic Center’, *A&A* **374**, 95–104.
- Saito, K., Homan, J., Yamaoka, K., Fukuyama, M., Miyakawa, T. G. & Yoshida, A. (2007), ‘RXTE spectra of the Galactic microquasar GRO J1655-40 during the 2005 outburst’, *ArXiv Astrophysics e-prints* .
- Sarazin, C. L., Kundu, A., Irwin, J. A., Sivakoff, G. R., Blanton, E. L. & Randall, S. W. (2003), ‘Low-Mass X-Ray Binaries and Globular Clusters in Early-Type Galaxies’, *ApJ* **595**, 743–759.
- Schödel, R., Ott, T., Genzel, R., Hofmann, R., Lehnert, M., Eckart, A., Mouawad, N., Alexander, T., Reid, M. J., Lenzen, R., Hartung, M., Lacombe, F., Rouan, D., Gendron, E., Rousset, G., Lagrange, A.-M., Brandner, W., Ageorges, N., Lidman, C., Moorwood, A. F. M., Spyromilio, J., Hubin, N. & Menten, K. M. (2002), ‘A star in a 15.2-year orbit around the supermassive black hole at the centre of the Milky Way’, *Nature* **419**, 694–696.
- Scoville, N. Z., Stolovy, S. R., Rieke, M., Christopher, M. & Yusef-Zadeh, F. (2003), ‘Hubble Space Telescope Pa $\alpha$  and 1.9 Micron Imaging of Sagittarius A West’, *ApJ* **594**, 294–311.
- Shahbaz, T. (2003), ‘Determining the spectroscopic mass ratio in interacting binaries: application to X-Ray Nova Sco 1994’, *MNRAS* **339**, 1031–1040.
- Shahbaz, T., Bandyopadhyay, R., Charles, P. A. & Naylor, T. (1996), ‘Infrared spectroscopy of V404 Cygni: limits on the accretion disc contamination’, *MNRAS* **282**, 977–981.
- Shahbaz, T., Charles, P. A. & King, A. R. (1998), ‘Soft X-ray transient light curves as standard candles: exponential versus linear decays’, *MNRAS* **301**, 382–388.
- Shahbaz, T., Ringwald, F. A., Bunn, J. C., Naylor, T., Charles, P. A. & Casares, J. (1994), ‘The mass of the black hole in V404 Cygni.’, *MNRAS* **271**, L10–L14.

- Shakura, N. I. & Sunyaev, R. A. (1973), 'Black holes in binary systems. Observational appearance.', *A&A* **24**, 337–355.
- Silber, A. D. (1992), Studies of an X-Ray Selected Sample of Cataclysmic Variables., PhD thesis, AA(MASSACHUSETTS INSTITUTE OF TECHNOLOGY).
- Smak, J. (1984), 'Outbursts of dwarf novae', *PASP* **96**, 5–18.
- Truss, M. & Done, C. (2006), 'The decline and fall of GRS 1915+105: the end is nigh?', *MNRAS* **368**, L25–L29.
- Truss, M. R., Murray, J. R., Wynn, G. A. & Edgar, R. G. (2000), 'The outbursts of dwarf novae', *MNRAS* **319**, 467–476.
- Truss, M. R. & Wynn, G. A. (2004), 'Long time-scale variability in GRS 1915+105', *MNRAS* **353**, 1048–1054.
- Ueda, Y., Yamaoka, K. & Remillard, R. (2009), 'GRS 1915+105 in "Soft State": Nature of Accretion Disk Wind and Origin of X-Ray Emission', *ArXiv e-prints* .
- Webbink, R. F., Rappaport, S. & Savonije, G. J. (1983), 'On the evolutionary status of bright, low-mass X-ray sources', *ApJ* **270**, 678–693.
- Webster, B. L. & Murdin, P. (1972), 'Cygnus X-1—a Spectroscopic Binary with a Heavy Companion?', *Nature* **235**, 37–+.
- White, III, R. E., Sarazin, C. L. & Kulkarni, S. R. (2002), 'X-Ray Binaries and Globular Clusters in Elliptical Galaxies', *ApJL* **571**, L23–L26.
- White, N. E., Nagase, F. & Parmar, A. N. (1995), The properties of X-ray binaries., in W. H. G. Lewin, J. van Paradijs & E. P. J. van den Heuvel, eds, 'X-ray binaries, p. 1 - 57', pp. 1–57.
- Yusef-Zadeh, F., Roberts, D. A. & Biretta, J. (1998), 'Proper Motions of Ionized Gas at the Galactic Center: Evidence for Unbound Orbiting Gas', *ApJL* **499**, L159+.
- Życki, P. T., Done, C. & Smith, D. A. (1999), 'The 1989 May outburst of the soft X-ray transient GS 2023+338 (V404 Cyg)', *MNRAS* **309**, 561–575.